Mode-locked fibre lasers for ultrafast gyroscopic measurements

Igor Kudelin
Doctor of Philosophy

Aston Institute of Photonic Technologies
Aston University
September 2021

Aston university

Mode-locked fibre lasers for ultrafast gyroscopic measurements

Igor Kudelin

Doctor of Philosophy, September 2021

Modern applications are constantly pushing the limits of current technologies, requiring further improvements in their precision. The advances in laser development significantly contribute to the achievements of modern technologies. One of the niches of precision technologies is gyroscopic measurements, where laser-based gyroscopes deliver unparalleled accuracy. Nonetheless, laser gyroscopes are subjected to the general limitation as *'lock-in'* effect, which restricts the lowest measurable angular velocity. The usage of pulsed laser sources, such as mode-locked lasers, can mitigate this deleterious effect and benefit the laser gyroscope development.The extensive studying of ultrafast lasers over the last few decades significantly improved their performance, extending their applications to extremely precise measurements such as optical clocks and telescope calibration. However, the usage of ultrafast lasers for the detection of angular rotations is still rudimentary and requires further studies.

In this manuscript, our goal is to contribute to the scientific achievements in the area of ultrashort pulses interferometry and, in particular, gyroscopic applications. We aim to deliver novel approaches for phase measurements at high data frequencies by using the recent advances in fast electronics and ultrafast measurement techniques. Firstly, we study bidirectional mode-locked fibre laser and its applicability for the detection of angular movements. Indicating the main obstacles to achieve continuous reliable results, in the following chapter we propose another interferometric setup, which provides the measurements of the pulse-to-pulse phase drift and can be used to characterise the phase noise of a pulse train or being exploited for interferometry. Finally, we demonstrate a passive gyro setup based on interferometric measurements, which inherits all the benefits of the usage of ultrashort pulses, while the phase noises of the laser source are significantly mitigated. We conclude that ultrashort pulses can benefit many phase-based applications, which require high resolution and high data rates, including but not limited to gyroscopic measurements.

Keywords and phrases: Laser gyroscope, fibre laser, mode-locking, ultrashort pulses, Dispersive Fourier Transformation.

Acknowledgements

That happened that during my PhD research I was supervised by three different people, and I would like to express my gratitude to all of them as their support made this work possible. First and foremost, I would like to thank Dr Maria Chernysheva for a warm welcome to the Aston Institute of Photonic Technologies (AiPT). Her support and helpful guidance undoubtedly helped me to realise myself as a researcher. I am also thankful to Dr Chernysheva for supporting my two-month stay at Leibniz Institute of Photonic Technology, Jena, Germany. I would like to thank my second supervisor Dr Srikanth Sugavanam, who accepted me at the end of my first year. Despite his busy schedule, he provided me with a great deal of advice and discussion. Though both of them have left Aston University during my PhD project, I am deeply grateful to them as they continue to guide me as external supervisors. Last but not least, I would like to thank Prof Sergei Turitsyn, who was my main supervisor during the final year of my PhD. He was supporting my work all along these three years of PhD, allowing me research freedom and opportunities for personal and professional growth. I am also grateful to my associated supervisor, Dr Egor Manuylovich, for all the fruitful discussions.

The PhD process could not be that enjoyable without the AiPT and PhD Student communities. I am very thankful to each member, some of whom have become close friends of mine. This friendly environment could not be overestimated, especially at this peculiar time of the global pandemic.

Finally, special gratitude I want to express to my Mother and friends, who were not near, but still provided me with priceless support and boosted my motivation.

Contents

List of Figures

List of Tables

List of Acronyms

ACF Autocorrelation function. 48–50, 58, 59, 61, 72–76, 78, 79, 111, 172

ARW Angular Random Walk. 30, 84, 95, 96, 101, 104, 117, 119, 130–132

CCW counter-clockwise. 53, 55, 58, 60, 61, 64, 66, 67, 72, 75, 77, 80, 81, 170–172

CEO Carrier-Envelope Offset. 33, 43, 84, 85, 87, 97, 101, 102, 104, 106, 109–112, 114, 116–120, 123, 124, 126, 129–132, 134–136

CEP Carrier-Envelope Phase. 33, 40

CW clock-wise. 53, 55, 58–61, 64, 66, 72, 76, 77, 80, 81, 110, 170–172

DFT Dispersive Fourier Transform. 46–50, 52, 56, 58, 61, 63, 64, 66, 68, 72, 74, 75, 78, 79, 86–89, 96–98, 101, 102, 108, 110, 111, 113, 114, 120, 121, 124, 128, 131–139, 164–166, 168, 169, 172, 176

DWs Dispersive Waves. 69, 78

FOG Fibre-Optic Gyroscope. 24, 27, 29, 30, 120, 138

FWHM Full Width at Half Maximum. 32, 39, 49, 60, 69, 72, 166

GDD Group Delay Dispersion. 37, 39, 47, 48, 58, 61, 86, 96, 164

GVD Group Velocity Dispersion. 32, 38, 47, 60, 164, 165, 169

MEMS Micro-Electro-Mechanical System. 22

MZI Mach-Zehnder Interferometer. 108, 110, 111, 115, 118–124, 126, 127, 130–132, 176

NALM Non-linear Amplifying Loop Mirror. 36, 53

NOLM Non-linear Optical Loop Mirror. 36, 53, 84

NPR Non-linear Polarisation Rotation. 36, 37, 53, 55, 57, 63, 69, 84

PC Polarisation Controllers. 58, 63, 65, 102, 110

PDF Probability Density Function. 98, 102, 112, 124

PSD Power Spectral Density. 40–42, 113, 126

QML Q-switched Mode-Locked. 56, 77

RF Radio Frequency. 28, 41–43, 57, 58

RIN Relative Intensity Noise. 42, 58

RLG Ring Laser Gyroscope. 23, 24, 27

SESAM Semiconductor Saturable Absorber Mirror. 35, 53, 55

SNR Signal-to-Noise Ratio. 41, 54, 55, 57, 85, 94–96, 100, 114, 117–119, 124, 129, 132, 138, 139, 166, 168

SPM Self-Phase Modulation. 32, 36–38, 46, 61

SWNTs Single-Walled Carbon Nanotubes. 35, 53, 55, 57, 61, 63, 65

TBP Time-Bandwidth Product. 32, 72

XPM Cross-Phase Modulation. 37, 56, 63

Chapter 1

Introduction

Measurements of angular movements, provided by gyroscopes, take a significant part of our everyday life. No inertial navigation system could be imaging without a gyroscope, which is an essential part in ships, submarines, aircraft, and spacecraft. As the market of auto-navigation systems is rapidly growing (unmanned cars, quadcopters, etc.), they impose higher requirements on data frequencies and resolution of measurements of angular velocity. Such applications are in need of reliable and compact gyroscopes. Among other types of gyroscopes, laser gyroscopes stand out due to their extremely high sensitivity to angular motion. Moreover, the whole gyroscope setup could be implemented in an optical fibre, that can be easily bent and coiled, resulting in a compact and robust setup. However, laser gyroscopes, utilizing continuous-wave generation, are suffered from a so called *'lock-in'* effect, which limits their performance at low angular velocities.

Mode-locked lasers inherit unique and attractive properties such as the ability to generate a robust train of pulses with duration of hundreds or even tens of femtoseconds (1 fs $= 10^{-15}$ s)[1]. Ultrafast lasers have been a revolutionary tool, which are now widely spread in industry, medicine, and many fields of science. Mode-locked lasers could be efficiently stabilised with frequency instability as low as 10^{-18} [6], which is required for various high-precision applications such as optical clocks and frequency metrology to name a few. Additionally, recent achievements in conjugate areas such as fast electronics strongly benefit the development of mode-locked lasers, opening a new avenue for potential applications.

The motivation for this work is to synergise the recent progress in the development of mode-locked fibre lasers and electronics to achieve accurate and high-speed gyroscopic measurements. At the moment of writing the thesis, only several works have been dedicated to gyroscopes based on mode-locking generation. However, it has been already demonstrated, both theoretically and experimentally, that such a device would inherit reduced *'lock-in'* effect by orders of magnitude or even completely eliminated. Additionally, to the best of our knowledge, there are no works on the single-shot measurement of angular rotation up to now. This gap can be filled by recently emerged time-stretching techniques,

[1]The term *ultrafast* is generally refer to a time scale of a few picoseconds and below (1 ps $= 10^{-12}$ s)

which proved their suitability for sensing applications and have a potential to substitute traditional methods for gyroscopic measurements. All in all, the lack of *'lock-in'* effect along with modern real-time measurement techniques constitute mode-locked fibre lasers as a good candidate to achieve high-precision measurements of angular velocity at high data rates.

1.1 Overview of the Thesis

This thesis is structured in the following way. In this *Chapter*, we introduce laser gyroscopes, their operational fundamentals, traditional measurement techniques, and limitations. Then, we describe the mechanisms for the generation of ultrashort pulses in fibre lasers and approaches to characterise such laser radiation. Recently emerged real-time techniques for characterisation of ultrashort pulse generation are also discussed.

Chapter 2 is dedicated to the development of bidirectional mode-locked fibre lasers. We begin by discussing their design features and recent progress in their applications for gyroscopic measurements. Further, we demonstrate experimental results on complex dynamics of counter-propagating pulses inside a laser cavity. The gyroscopic measurements obtained in a bidirectional mode-locked laser by using various real-time techniques are also presented.

In *Chapter* 3 we discuss a possibility to transit from the bidirectional to a uni-directional setup for gyroscopic measurement, based on ultrashort pulses and real-time measurement techniques. There, we propose a novel experimental setup, which allows us to provide pulse-to-pulse phase measurements. We begin by investigating the phase dynamics of the used free-running uni-directional mode-locked fibre laser. Then, we exploited the developed setup with the uni-directional laser for gyroscopic measurements. We finish the *Chapter* by indicating the further applications of the proposed setup for the pulse-to-pulse phase measurements.

Chapter 4 reports experimental results on gyroscopic measurements in a passive Sagnac interferometer, using an external source of the ultrashort pulse train. To the best of our knowledge, it is the first demonstration of a passive gyroscope based on ultrashort pulses. We evidence the system to be an ideal platform for synergising the ultrashort pulses and the real-time interferometric techniques for phase-based measurements. We also indicate the further amendments of the passive gyroscopic configuration to achieve and, hopefully, outperform traditional methodologies for gyroscopic measurements.

Finally, Chapter 5 concludes the thesis with a critical assessment of the application of ultrashort pulses in various gyro configurations and approaches for gyroscopic effect detection. The summarising table of all the presented results, using different schemes and configurations, with comparison to the previous works, is presented. We also consider a broader impact of the presented results on other phase-based applications, which would benefit from utilising the ultrashort pulses along with the real-time measurement

techniques.

1.2 List of publications

The presented results have been already published or in the process to be submitted to scientific journals or conference proceedings. The relevant list of published works is shows below:

Journal Publications

1. **I. Kudelin**, S. Sugavanam, M. Chernysheva, "Rotation Active Sensors Based on Ultrafast Fibre Lasers," *Sensors*, 21, 3530, 2021.

2. **I. Kudelin**, S. Sugavanam, M. Chernysheva, "Single-shot interferometric measurement of pulse-to-pulse stability of absolute phase using a time-stretch technique," *Optics Express* 29, 18734-18742, 2021.

3. **I. Kudelin**, S. Sugavanam, M. Chernysheva, "Pulse-onset dynamics in a bidirectional mode-locked fibre laser via instabilities," *Communication Physics* 3, 202, 2020.

4. **I. Kudelin**, S. Sugavanam, M. Chernysheva, "Build-up dynamics in bidirectional soliton fiber lasers," *Photonics Research* 8, 776-780, 2020.

Conference Publications

1. **I. Kudelin**, S. Sugavanam, M. Chernysheva, "Ultrafast gyroscopic measurements in a passive Mach-Zehnder interferometer via time-stretch technique," *Conference on Lasers and Electro-Optics Europe and European Quantum Electronics Conference*, Optical Society of America, paper cj_p_55, 2021.

2. **I. Kudelin**, S. Sugavanam, M. Chernysheva "Correlation of solitons in bidirectional mode-locked fibre laser," *Proceeding SPIE*, 11358, Nonlinear Optics and its Applications, 1135810, 2020.

3. **I. Kudelin**, s. Sugavanam, M. Chernysheva, "Real-time pulse dynamics in bidirectional mode-locked fibre lasers," 9^th International seminar on fibre lasers, pp. 85-85, 2020

4. **I. Kudelin**, S. Sugavanam, M. Chernysheva, "Build-Up of Bidirectional Ultrashort Pulse Laser Generation: from Q-Switched Instabilities to Mode-Locking," *Conference on Lasers and Electro-Optics Europe and European Quantum Electronics Conference*, Optical Society of America, paper cj_7_1, 2019.

5. **I. Kudelin**, S. Sugavanam, M. Chernysheva, "Real-time Observation of Soliton Build-up Dynamics in Bidirectional Mode-Locked Fibre Lasers," *Conference on Lasers and Electro-Optics*, Optical Society of America, paper STu3L.7, 2019.

During the PhD project, I have participated in other projects related to the development of mode-locking lasers, which eventually resulted in publications. These results are not presented in the Thesis, however, some of them are cited throughout the text. Therefore, it would be relevant to mention this additional contribution below:

1. D. Dvoretskiy, S. Sazonkin, **I. Kudelin**, I. Orekhov, A. Pnev, V. Karasik, L. Denisov, "Multibound Soliton Formation in an Erbium-Doped Ring Laser With a Highly Nonlinear Resonator," *IEEE Photonics Technology Letters*, vol. 32, no. 1, pp. 43-46, 2020.

2. **I. Kudelin**, "Collision dynamics of co-propagating solitons in mode-locked fibre laser with net-anomalous dispersion," *Proceeding SPIE, Real-time Measurements, Rogue Phenomena, and Single-Shot Applications VI*, 11671, 116710C, 2021.

3. I. Orekhov, **I. Kudelin**, D. Dvoretskiy, S. Sazonkin, A. Pnev, V. Karasik, L. Denisov, "Propagation Features of Multibound Solitons in Optical Fiber With Anomalous Dispersion in the Telecom Range," *Frontiers in Optics / Laser Science*, Optical Society of America, paper JTh4A.13, 2020.

4. Y. Ososkov, A. Chernutsky, D. Dvoretskiy, S. Sazonkin, **I. Kudelin**, I. Orekhov, A. Pnev, V. Karasik, "Fiber Optic Raman Distributed Temperature Sensor Based on an Ultrashort Pulse Mode-Locked Fiber Laser," *Optics and Spectroscopy*, 127, 664–668, 2019.

5. D. Dvoretskiy, S. Sazonkin, I. Orekhov, **I. Kudelin**, A. Pnev, V. Karasik, L. Denisov, V. Davydov, "Low-saturation-energy Ultrafast Saturable Absorption of High-density Well-aligned Single-walled Carbon Nanotubes," *Laser Congress*, Optical Society of America, paper JW2A.2, 2019.

6. K. Litvinova, M. Chernysheva, **I. Kudelin**, S. Khalimanenko, F. Leyva, "Experimental evaluation of pulse 1550 nm laser system for welding of heart tissue," *Conference on Lasers and Electro-Optics Europe and European Quantum Electronics Conference*, Optical Society of America, paper cl_p_17, 2019.

7. D. Dvoretskiy, S. Sazonkin, I. Orekhov, **I. Kudelin**, A. Pnev, V. Karasik, L. Denisov, "Controllable Generation of Ultrashort Multi-bound Solitons in a Mode-locked Erbium-doped Ring Laser with a Highly-nonlinear Resonator," *Conference on Lasers and Electro-Optics Europe and European Quantum Electronics Conference*, Optical Society of America, paper cj_p_55, 2019.

8. **I. Kudelin**, M. Chernysheva, "Square Pulse and Harmonic Ultrashort Pulse Generation in Semiconductor Optical Amplifier-Based Mamyshev Oscillator," *Conference on Lasers and Electro-Optics Europe and European Quantum Electronics Conference*, Optical Society of America, pp. 1-1, 2019.

9. **I. Kudelin**, S. Sugavanam, M. Chernysheva, "Real-time Observation of Soliton Build-up Dynamics in Bidirectional Mode-Locked Fibre Lasers," *Conference on Lasers and Electro-Optics*, Optical Society of America, paper STu3L.7, 2019.

10. D. Dvoretskiy, S. Sazonkin, **I. Kudelin**, I. Orekhov, A. Pnev, V. Karasik, L. Denisov, "Multibound solitons generation with a controllable number of bound states in a passive mode-locked all-fiber erbium-doped ring laser," *Nonlinear Optics and Applications XI*, Vol. 11026, p. 110260Q, 2019.

1.3 Contribution

Here, I want to acknowledge the collaboration and contribution during the provided research. Throughout my PhD project, I had two main collaborators who worked with me and helped me to achieve the goal of the provided research. The first collaborator is Dr Maria Chernysheva, who has a strong background in fibre optics and was my first supervisor from October 2018 to January 2019, and she is also responsible for designing the bidirectional mode-locked laser I used in the experiments. Another collaborator is Dr Srikanth Sugavanam, who was my main supervisor from January 2019 until August 2020. He guided me through the real-time measurement techniques and assisted me with the analytical derivations and helped to develop critical thinking. I would like to note that even after both collaborators left Aston University and the position of my main supervisor, they continued to provide invaluable support and discussion at all stages of the work. Additionally, I would like to mention the contribution done by my last main supervisor, Prof Sergei Turitsyn (from August 2020 till now), who supported and guided me through the last stage of my PhD work.

My contribution is the conceiving of various systems for real-time measurements, gathering the experimental results, and providing their analysis. To appreciate the contribution made by the mentioned collaborators, from now on in the Thesis I will address from the plural form.

1.4 Laser gyroscopes

The term *'gyroscope'* stands for 'precision motion', derived from the Ancient Greek language. The first genuine gyroscope was constructed by Johann Bohnenberger in 1817 and was based on a rotating massive sphere [7]. However, the full potential of the gyroscopes was realised only in 1852 by Léon Foucault, who used a gyroscope to estimate the Earth rotation [8]. Moreover, it was Foucault who introduced the device its modern name *'gyroscope'*. The next generation of gyroscopes utilised the advent of electric motors to maintain the rotation of a spinning mass (rotating massive sphere [9] or disk [10]). A typical mechanical gyroscope is schematically shown in Fig. 1.1. Two gimbals and the gyroscope frame are mounted in a way to allow the gyro rotate in all axes, while the rotor

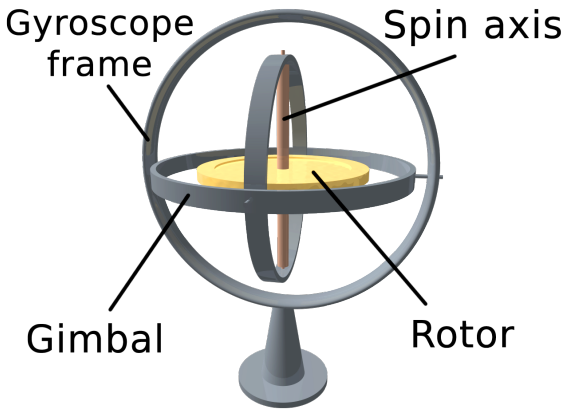

Figure 1.1: Schematic illustration of a mechanical gyroscope.

maintains its spin axis direction regardless of the orientation of the outer frame. Nowadays, mechanical gyroscopes are still of interest for applications requiring long-term high stability. However, their high cost and the presence of moving parts limit their range of applications.

We want to separately mention a Micro-Electro-Mechanical System (MEMS) gyroscope technology due to their significant difference from other mechanical gyroscopes. MEMS are motion sensors, based on Coriolis acceleration, measuring the angular motion of the object. The main advantage of the MEMS is their robustness and miniature sizes, ranging from 20 micrometers up to a millimeter. On the other hand, MEMS inherit high noises compared to other gyroscopes, which substantially limit their application in high-precision measurements. Due to their compactness, MEMS technology occupies the niche of consumer electronics, such as smartphones, drones, gyroscouters, and segways.

The primary focus of the *Thesis* is the field of optical gyroscopes. Almost all optical gyroscopes are based on the Sagnac effect. In 1913 George Sagnac provided his famous experiment by splitting input light into two counter-propagating directions of a ring interferometer (Sagnac interferometer), allowing the counter-propagating beams to interfere on the detector [11; 12]. When the plane of the interferometer spins, the counter-propagating beams cover different optical paths and arrive at the photodetector at different time. This inequality also manifests as a phase shift of counter-propagating beams, which could be observed from the interference. Thus, the effect of the time retardation between the counter-propagating beams due to angular rotation is known as the Sagnac Effect. Through, the original goal of the Sagnac experiment was to prove the existence of the aether, the Sagnac effect was perfectly consistent with Einstein's theory of special relativity [13], which discard the existence of the aether [14].

Optical gyroscopes commonly refer as laser gyroscopes, since gyroscope performance is strongly dependent on the coherence of the light source which makes laser radiation a perfect candidate. Laser gyroscope was demonstrated for the first time by Macek and Davis in 1963 [15], two years after the invention of the laser. The laser gyroscope develop-

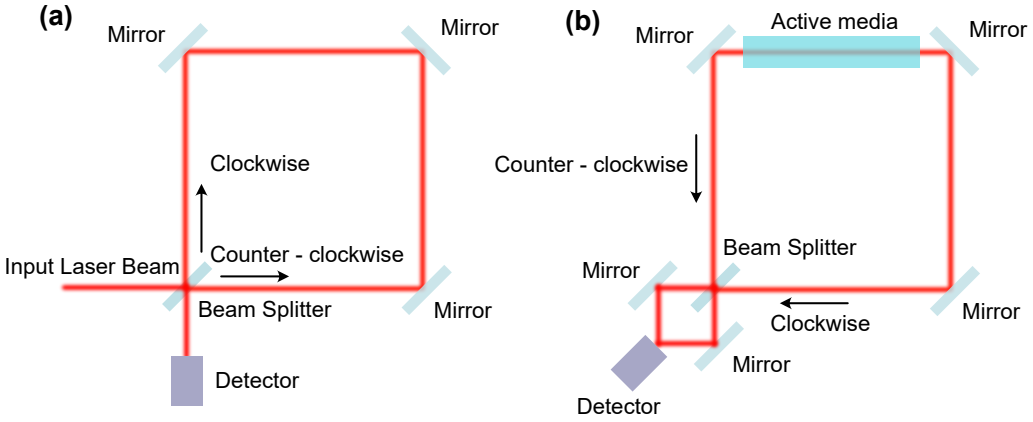

Figure 1.2: Schematic depiction of (**a**) passive Sagnac interferometer and (**b**) ring laser gyroscope.

ment has undergone significant changes and many different types of laser gyroscopes have been proposed. However, only laser gyroscopes operating with continuous-wave radiation achieve commercial maturity, while only a few works and patents have been dedicated to laser gyroscope with other generation regimes of the laser. Generally, laser gyroscopes are subdivided into passive and active configurations. In active gyroscopes[1], the active media is placed inside the Sagnac interferometer. While passive gyroscope configurations exploit a laser source with an external Sagnac interferometer. The principal schemes of passive and active laser gyroscope configurations are depicted in Fig. 1.2(a) and (b), respectively. Both configurations have their advantages and found a niche in commercial applications.

Active gyroscopes or Ring Laser Gyroscope (RLG) are usually constructed in a monolithic design and contain an active media such as He–Ne gas. He–Ne gas is a perfect active media to achieve single-mode operation with extremely narrow linewidth. However, as will be discussed in *Chapter 1.4.3*, the gaseous active media has several drawbacks, which motivate many research groups to substitute it with a solid-state gain medium. Moreover, RLGs have to maintain the generation in both counter-propagating directions, which restrict their cavity designs. The active gyroscope can also be designed in an all-fibre design, where the light propagates inside an optical fibre. RLGs demonstrate the most accurate rotation measurements and can detect precise rotational motions associated with seismic events [16], Chandler and Annual wobbles [17].

As was indicated before, the most dramatic obstacle in laser gyroscopes is the lock-in effect. This effect arises due to the back-scattering on reflecting surfaces. The back-scattered light is further amplified in the active media and can results in frequency synchronisation with a counter-propagating beam, so they could not be distinguished. The lock-in effect manifests at low rotation velocities below Ω_L, where the laser gyroscope cannot operate and is called a *'dead-band'*. The dead-band can be minimised, but not completely eliminated. The most straightforward solution is reducing the number of reflecting surfaces

[1]Active gyroscopes are commonly called just laser gyroscopes. Here and thereafter we will use the term laser gyroscope to refer to an active gyroscope.

(*e.g.* triangular-shaped cavity). The other approach to suppress the dead-band zone is to increase the quality of the reflecting surfaces by coating with high-reflective dielectrics [18]. Another mechanism, called optical dithering [19], is based on the presence of mechanically driven oscillations on the gyroscope platform. However, dithering introduces additional noises and complicates the total setup of a laser gyroscope. In optical fibres, the back-scattering light arises due to inherent Rayleigh scattering [20].

The field of passive gyroscopes is mostly occupied by the Fibre-Optic Gyroscope (FOG). An undeniable advantage of using optical fibre in passive gyroscopes is that fibre could be easily coiled multiple times, so the propagating light will pass longer distances and, as a consequence, accumulate a more prominent Sagnac effect. By coiling and bending the fibre, the complete device could be compact and economical. Another privilege of FOGs and all passive gyroscopes, in general, is that they do not suffer from the lock-in effect. Though FOGs are more durable, they still underperform RLGs in precision. The drawback of the passive gyroscopes is that light passes only once through the interferometer and the accumulated Sagnac effect is only sensitive to the derivative of the angular position (i.e. angular velocity). Nevertheless, the FOGs are the best choice for tactical grade applications, occupying more than 50% of the market [21].

1.4.1 Sagnac Effect

As was mentioned above, optical gyroscopes operate on the basis of the Sagnac effect, which relates the discrepancy in optical paths of counter-propagating beams ΔL to the angular rotation of the gyro platform. When the laser gyroscope platform rotates at an angular velocity ω rad/s in a clock-wise direction, single-roundtrip optical paths for counter-propagating beams could be expressed:

$$L_{CW} = L + R \cdot \omega \cdot T \qquad L_{CCW} = L - R \cdot \omega \cdot T \tag{1.1}$$

, where $L = 2\pi R$ is the interferometer optical length at rest, L_{CW} and L_{CCW} is optical paths for clock-wise and counter-clockwise directions, respectively. R is the radius of the interferometer and T is a roundtrip time $T = L/c$, where c is the speed of light. The additional terms in the equations refer to the effect of the angular rotation. This effect is quantitatively the same, but of different sign. Thus, the mismatch in optical paths between counter-propagating beams due to the angular rotation calculated as:

$$\Delta L = L_{CW} - L_{CCW} = 2 \cdot R \cdot \omega \cdot T = \frac{2 \cdot R \cdot L}{c}\omega = \frac{4\vec{\mathbf{A}}}{c}\vec{\omega} \tag{1.2}$$

, where $\vec{\mathbf{A}} = \pi R^2$ – is the oriented area of the laser gyroscope. The difference in the optical paths leads to a different time for counter-propagating beams to make a roundtrip through the interferometer:

$$\Delta t = \frac{\Delta L}{c} = \frac{4\vec{\mathbf{A}}}{c^2}\vec{\omega} \tag{1.3}$$

The Sagnac effect is also manifested as a phase shift between counter-propagating beams. The expression of the phase-time relationship is:

$$\phi = t \cdot \frac{2\pi c}{\lambda_c} \tag{1.4}$$

, where λ_c – is the carrier wavelength of the beam. By substituting the eq. 1.4 into the eq. 1.3 we can estimate the Sagnac-induced phase shift as:

$$\Delta\phi = \Delta t \cdot \frac{2\pi c}{\lambda_c} = \frac{8\pi\vec{\mathbf{A}}}{\lambda_c c}\vec{\omega} \tag{1.5}$$

The vector form is used in the above equations to indicate that the laser gyroscopes are sensitive only to the rotation in the plane of the gyro platform. The presented Sagnac equations 1.2-1.5 give a linear relationship between rotation velocity and parameters of the laser beams and could be applied for arbitrary gyroscope geometry. The fraction defining the ratio between the angular velocity and the beam parameters is known as a scale factor.

If light propagates in the medium with a refractive index n, the wave velocity in the fixed laboratory frame is retarded by the Fizeau drag coefficient α [22]:

$$V_{CW} = c/n + R \cdot \omega \cdot \alpha \qquad V_{CCW} = c/n - R \cdot \omega \cdot \alpha \tag{1.6}$$

and the temporal delay between counter-propagating beams in the medium Δt_m becomes:

$$\Delta t_m = \Delta t \cdot n^2 \cdot (1 - \alpha) \tag{1.7}$$

, where Δt is the temporal domain in a vacuum. Since the Fizeau drag coefficient $\alpha = 1 - \frac{1}{n^2}$ it compensate for the effect of the refractive index n [22].

The equations above derived for linear speed of the interferometer much less than the speed of light ($V_{linear} = \omega \cdot R << c$), that is always the case for real applications. However, the Sagnac effect is perfectly explained in the context of general relativity. The complete derivation of the Sagnac formula with special-relativistic analysis and corrections can be found in works [23; 24].

In the case of the active gyroscope, the angular movement results in an offset of the oscillation frequencies of counter-propagating beams. Basically, a laser cavity maintains generation only at integer numbers of propagating wavelengths, called longitudinal modes. The condition for longitudinal modes defined as the integer number of the wavelength should consist a cavity perimeter $L = n \cdot \lambda$. The corresponding oscillation frequencies are derived as $\nu = c/L$. Thus, according to the selection of the longitudinal modes, the difference in the optical paths, caused by the Sagnac effect, can be manifested through the change in the oscillation frequencies of counter-propagating beams. The associated

beat-note frequency or '*Sagnac frequency*' can be derived as:

$$\frac{\Delta\nu}{\nu} = \frac{\Delta L}{L} \qquad \Delta\nu = \frac{\Delta L \cdot \nu}{L} = \frac{4\vec{\mathbf{A}}}{L\lambda_c}\vec{\omega} \tag{1.8}$$

This equation illustrates that the longitudinal frequency modes experience shifts during the rotation of the platform. Another interpretation of this effect could be understood as a Doppler shift, caused by movements of the laser platform [25]. If the linear velocity of the interferometer is much less than the speed of light, the frequency shifts between counter-propagated beams due to the Doppler effect estimated as:

$$\Delta\nu = \frac{\Delta V_{linear}}{c}\nu_0 = \frac{2R\omega}{\lambda_c} = \frac{4\vec{\mathbf{A}}}{L\lambda_c}\vec{\omega} \tag{1.9}$$

, where ΔV_{linear} is the difference in linear velocity of counter-propagating directions of the interferometer. As was expected, the effect of frequency offset derived from the Doppler effect is perfectly matched with Eq. 1.8, based on the Sagnac effect.

The introduced equations for the Sagnac effect establish the basis for measurements of angular velocity in optical gyroscopes. Though, several modifications have been demonstrated to increase the response of the laser beam parameters to the Sagnac effect. For example, in 1981, A. Kaplan and P. Meystre proposed the implementation of a nonlinearly induced non-reciprocity in the laser cavity [26]. Other approaches are based on the concept of a *'slow light'* [27], which can be achieved by introducing a giant dispersion [28; 29; 30; 31; 32; 33]. A potential of 10^4-enhanced resolution of gyroscopic measurement in a microcavity has been discussed in Ref. [34]. Matthew J. Grant and Michel J. F. Digonnet reported about ∼2400 enhanced rotation sensing at exceptional points of a parity–time-symmetric gyroscope [35].

1.4.2 Measurement Techniques

Measurement techniques of the Sagnac effect in optical gyroscopes could be subdivided into 3 types, according to the Sagnac equations 1.3-1.8: temporal, phase, and spectral measurements. Here, we would like to note, that measurements of the Sagnac effect in the temporal domain require pulsed laser generation (e.g. mode-locked lasers), while spectral measurements could be provided only in active laser gyroscopes.

The most obvious approach is to measure the time retardation due to the Sagnac effect. However, the limited rise time of 15 ps in modern photodetectors severely restricts that approach. As an example, if we consider an interferometer with area of 1 m^2 (radius r $= \sqrt{1/\pi} \approx 0.56$ m), the Sagnac-induced time shift of 15 ps after one roundtrip will refer to a rotation velocity of $\sim 337.5 \cdot 10^3$ rad/s. At first glance it seems that this resolution is far beyond any applications, however, if we consider that laser beam can pass the interferometer multiple times, the accumulated Sagnac temporal shift is correspondingly enhanced by the value of the roundtrip number. If we divide the Sagnac Eq.1.3 by the

roundtrip bypass time $T = L/c$ and multiply by the integration time τ, the sensitivity of this method can be calculated:

$$\Delta t = \frac{4\mathbf{A}}{c^2} \cdot \frac{c \cdot \tau}{2\pi R}\omega = \frac{2R \cdot \tau}{c}\omega \tag{1.10}$$

By substituting the integration time equals to the cavity bypass time $\tau = L/c$, that is single-shot measurements after each roundtrip, it will result in the original Sagnac eq. 1.3. But, for the considered gyroscope the resolution could achieve $\sim 6 \cdot 10^{-3}$ rad/s for integration time of 1 s. So, the resolution of temporal measurements of Sagnac effect could be further increased multiple time at the cost of reducing data frequency. Thus, this approach has a trade-off between the data frequency and the resolution. However, the main advantage of the approach is that it can potentially achieve high data frequencies in the MHz range and beyond in a simple setup.

The phase-based measurements are based on the interference between counter-propagating beams. The interference could be easily obtained by overlapping both beams at the detector. During rotation of the gyro platform, the counter-propagating beams experience additional Sagnac-induced phases of different signs, displacing the interferometric pattern accordingly. The Sagnac-induced phase shift can be also treated as a movement of a standing wave inside the interferometer. Thus, the positions of nodes and antinodes are fixed if the gyroscope is at rest. When the gyroscope experience angular rotation, the photoreceivers measure the rotation angle by counting the interference fringes running over them. Figure 1.3 schematically illustrates the interferometric patterns when the gyroscope is at rest and experiences phase shift due to rotation. As an example, if the photodetector can resolve the shift of interference by $2\pi/100$, the gyroscope with an area of 1 m^2 will resolve the angular velocity of 0.75 rad/s. The disadvantage of the approach is that it limits the maximum rotation velocity. If the angular velocity will shift the interferometric pattern by more than π during one integration period, it would not be possible to unequivocally reconstruct the angular velocity since the interferometric pattern has a period of 2π.

The described phase-based detection of the Sagnac effect is a dominant methodology in FOGs. In passive gyroscopes the light passes the interferometer only once (open-loop), the Sagnac-induced phase shift is not accumulated from one roundtrip to another as it happens in active gyroscopes, where the beams can circulate for multiple roundtrips. In other words, the recorded interferometric pattern is sensitive only to a variation of the angular velocity, i.e. derivative of the angular rotations. Therefore, FOGs, generally, provide lower sensitivity than RLGs.

Alternatively, the combination of two oscillation frequencies will result in a beat frequency, equals to the difference between the oscillation frequencies of the incident radiation. Initially, when the laser platform is at rest, the oscillation frequencies of the counter-propagating beams are perfectly matched. During rotation of the gyro platform, the oscillation frequencies of counter-propagating beams experience shifts according to

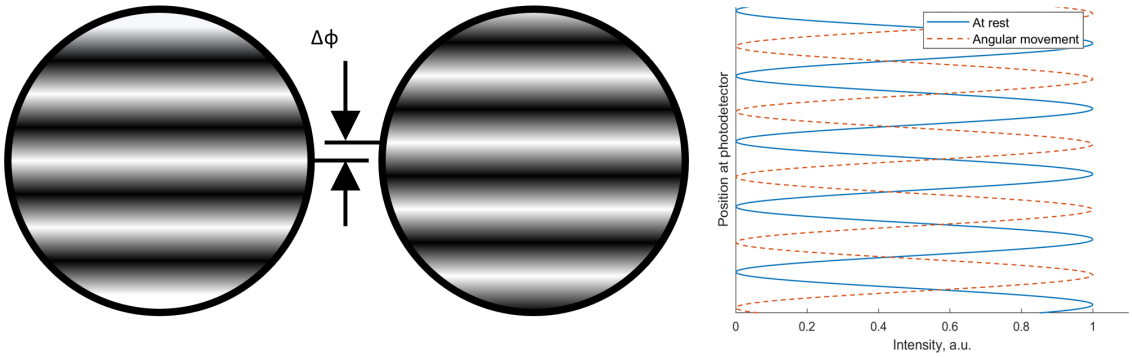

Figure 1.3: The interference of the counter-propagation beams on the photodetector, when the gyroscope at rest and experience angular rotation.

the Sagnac eq. 1.8 and the Sagnac frequency can be further accurately retrieved from the Radio Frequency (RF) spectrum of the signal from the photodetector. The resolution of the approach is determined by the line-width of the oscillation frequency, which is limited by the irreducible quantum noise [36; 37]. Generally, this method provides the most accurate measurements of the Sagnac effect and allows to achieve a sensitivity of $1.2 \cdot 10^{-11}$ rad/s/$\sqrt{Hz}$ and resolve a rotation rate of 10^{-12} rad/s ($5 \cdot 10^{-6}$ deg/h) at 1000 s integration time [38].

Since the feature of oscillation modes is a characteristic of laser cavities, the measurement of the Sagnac frequency could be observed only in the laser cavity. However, in 1977 Ezekiel and Balsamo proposed a new architecture of a passive resonator laser gyroscope by introducing a closed-loop optical path inside an interferometer [39]. The inserted closed loop, e.g. the Fabry-Perot interferometer, introduces the condition for longitudinal mode selection and, therefore, allows the frequency splitting of the resonance optical modes due to the Sagnac effect while mitigating the lock-in effect. A similar approach was used in Ref. [40; 41], where the passive resonator was implemented as a ring microresonator. Though passive resonator laser gyroscopes have the potential to achieve performance comparable with active laser gyroscopes, they still underperform [42].

1.4.3 Errors in Laser Gyroscopes

Here, we will consider effects, which induce errors in the measurements of angular velocity and limit the performance of optical gyroscopes. As was discussed earlier, the most deleterious effect in laser gyros is the lock-in effect and corresponding dead-band zone. Apart from it, laser gyroscopes inherit the following errors in defining the angular rate:

- *Gas degradation.* He-Ne lasers generate the most desirable narrow-band radiation, which is crucial for precision gyroscopic measurements. However, gas lasers suffer from leaking of the gas media from the cavity enclosure, which reduces the laser gain and, therefore, affects the scale factor of the gyroscope. Moreover, the scale factor and the laser gain are further reduced due to contamination of the laser

gas with hydrogen, oxygen, nitrogen, and water vapour [43; 44]. Besides, laser gyroscopes with gaseous active media experience bias due to gas flow caused by temperature fluctuations or ionic flow due to electric discharge [45]. These effects of gas degradation limit the long-term performance of the gyroscope and cause a transition to using solid-state gain mediums.

- *Variation of the scale factor.* Under the influence of external conditions such as temperature and pressure, the scale factor tends to fluctuate in time, inducing uncertainty in the determination of the angular velocity. The intracavity conditions, including instabilities of the laser gain and losses, also affect the scale factor of the gyroscope. In FOGs, time-dependent fluctuations of temperature and pressure lead to variations in travel time along the same sections of optical fibre for counter-propagating beams (known as the Shupe effect [46]), causing an additional parasitic difference in their optical paths.

- *Intracavity non-reciprocal effects.* The most significant among which are Magneto-optic effects [47; 48] and Kerr effect. The presence of a magnetic field (e.g. the magnetic field of the Earth) causes an additional phase difference of counter-propagating beams and is known as a Faraday effect. This parasitic effect could be significantly reduced by using polarisation-maintaining fibres [49]. Moreover, owing to very small silica fibre core and long distances in fibre interferometers, even a small mismatch in intensity between the counter-propagating beams results in an additional accumulated Kerr-induced phase shift [50]. However, by using a hollow-core fibre in the interferometer, this effect could be mitigated [51].

- *Optical frequency fluctuations.* All free-running lasers experience dynamic fluctuations of the oscillation frequency of the laser radiation. One of the approaches to overcome this obstacle is to apply a feedback loop with piezoelectric actuators [52]. For a long-term operation, the oscillation frequency could be efficiently stabilised via a beat-note with an actively stabilised reference laser as a feedback reference signal [53].

- *Polarisation instability.* Counter-propagating beams can experience polarisation instability, leading to a variation of the optical paths caused by the birefringence of optical components. The effect of polarisation instability could be mitigated by introducing a polariser inside the interferometer. In FOGs, the accuracy of angular rate measurements could also be enhanced by using a polarisation-maintaining fibre or polarising single-mode fibre [54].

- *Acoustic noise and vibrations.* It is known, that optical fibres are sensitive to acoustic noises, which are converted to phase noises through photo-elastic effect [55]. Vibrations and input shock, which are intrinsic to many industrial applications, introduce

an additional noise and bias offset during measurements. However, by constructing the gyro in a rigid monolithic design the effect of the environmental perturbations on gyro performance could be minimised.

All aforementioned parameters define the stability and performance of the laser gyro. The gyroscope performance is usually assessed by the Allan deviation of the Sagnac frequency (more information on the Allan deviation is presented in *Section* 1.5.2). The stability of the gyroscopic measurements for long-term operations is usually defined as an Angular Random Walk (ARW) and estimated as an Allan deviation at 1 s integration time with units of rad/s/$\sqrt{Hz}$ or deg /$\sqrt{h}$. In other words, the ARW characterise the fluctuations of the beat-note frequency over time due to noises. Another way to estimate the ARW through the various noise specifications was shown in works [56; 57] as:

$$ARW(\tau) = \sqrt{PSD/\tau} \qquad [\text{deg}/\sqrt{h}] \tag{1.11}$$

In FOGs, the ARW is limited mainly by the intensity noise of the laser generation [58] and can be reduced down to 0.008 deg /$\sqrt{h}$ [59].

Another one of the most critical factors of a gyroscope performance is bias instability. The bias instability is usually characterised as the lowest value of the Allan deviation and expressed in degrees per hour. The bias instability determines the lowest angular velocity which could be measured by the gyroscope. The integration time, at which the bias instability occurred, corresponds to the optimal averaging time period when the white noise could be effectively averaged out and before other noises start to dominate. This integration time also determines the data frequency at which the highest resolution can be achieved. Depending on the type of the gyroscope, the bias instability can range from 1000 deg/h down to 0.0001 deg/h [21].

All in all, to minimise the effect of noises on gyroscope performance, the whole device should be constructed in a rigid monolithic design. Meanwhile, FOGs should be based on polarisation maintaining or hollow-core fibres. Additionally, a feedback loop for active control of the laser generation is also highly preferred.

1.5 Ultrafast Fibre Lasers

One of the most significant characteristics of a laser is its operation regime, such as continuous-wave, Q-switched or mode-locked. The Q-switched technique allows obtaining pulses of huge energies up to 0.8 J [60] and duration, ranging from μs to ns. However, the term ultrafast is usually referred to sub-picosecond pulse duration, which could be achieved by locking of longitudinal modes of a laser. This technique is called mode-locking and has been realised for the first time in a He–Ne laser, generating 2.5 ns pulses, in 1964 [61]. Nowadays, modern ultrafast laser can achieve the generation of pulses as short as 5 fs in bulk lasers [62] and 24 fs in ultrafast fibre laser [63] directly from the laser cavity. Due

to short pulse duration, mode-locked laser systems deliver extremely high peak powers with a potential to achieve 100 PW [64], enabling investigations of relativistic effects and extremely high-field physics [65; 66; 67]. The spectral features of ultrafast pulse train, known as a frequency comb [68], are widely used for fast spectroscopy [69; 70] and frequency metrology [71; 72]. Additionally, mode-locked fibre lasers demonstrated a high stability performance with frequency instability of 10^{-18}-10^{-19} [73], that is widely utilised in high-performance optical clocks [74; 75; 76] and for calibration of astronomical spectrographs [77; 78; 79]. Ultrafast lasers also found a great niche in sensing applications [80; 81].

1.5.1 Mode-locking Mechanism

As was stated above, the mode-locking is a phase synchronisation of the longitudinal modes of the laser. The frequency separation between longitudinal modes is governed by the optical length of the laser cavity and calculated as $c/(nL)$ for a ring cavity and $c/(2nL)$ for a linear cavity, where n is the refractive index. This value is usually relatively small to be resolved by the optical spectrum analyser. A typical Gaussian emission spectrum is shown in Fig. 1.4(a). If no selective elements are applied, laser tends to emit quasi-continuous-wave radiation, featuring chaotic intensity fluctuations as a superposition of numerous longitudinal modes with random phases. Figure 1.4(b) demonstrate the intensity profile in the temporal domain for a Gaussian spectrum with random phases. However, a real free-running laser will emit only at particular longitudinal modes due to intracavity dynamics such as mode competition and the resulting spectra will significantly differ from the one presented in Fig. 1.4(a). Figure 1.4(c) demonstrates the laser emission in the temporal domain when the optical modes, depicted in Fig. 1.4(A), are partially locked. This pattern inherits a more prominent intensity spike. If the entire optical spec-

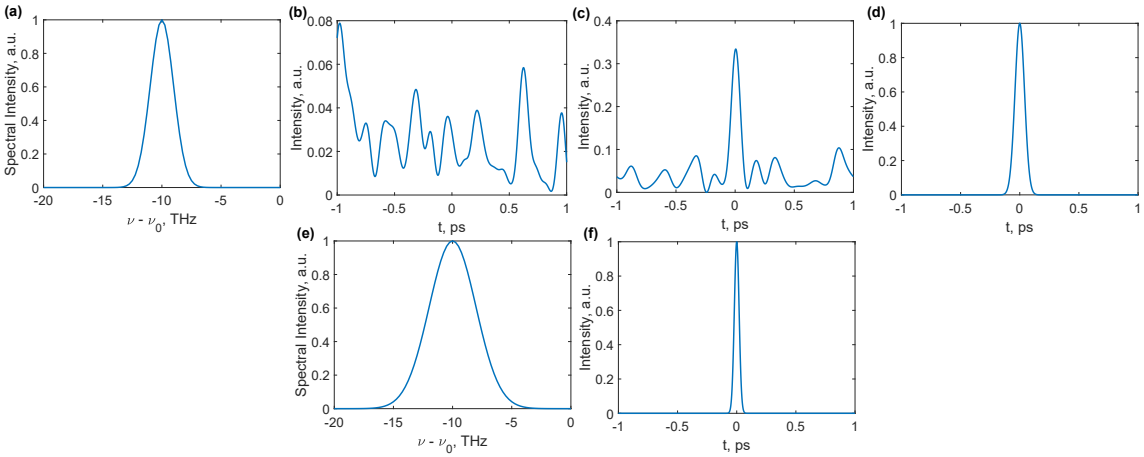

Figure 1.4: **(a)** A typical optical spectral profile with corresponding temporal intensity profiles, when the longitudinal modes are: **(b)** not phase-locked, **(c)** partially phase-locked and **(c)** fully phase-locked (a transform-limited pulse with duration of 100 fs). **(e)** An optical spectra with doubled spectral width, which corresponds to a **(f)** transfrom-limited pulse duration of 50 fs.

trum is phase-locked (synchronised), in the temporal domain it results in one energetic intensity peak (pulse), circulating in the laser cavity. These figures are presented here to schematically demonstrate the significance of the spectral phase on the resulting intensity profile in the temporal domain.

When all longitudinal modes are synchronised, the pulse is known to be transform-limited. The duration of the transform-limited pulse depends on the width and the shape of the corresponding optical spectra. It is useful to introduce the Time-Bandwidth Product (TBP) $= \Delta\tau \cdot \Delta\nu$, where $\Delta\tau$ is pulse temporal duration at Full Width at Half Maximum (FWHM) and $\Delta\nu$ is corresponding spectral FWHM. The TBP indicates how close a pulse duration to the transform-limited one (*e.g.* TBP$\approx$ 0.315 for a $sech^2$-shaped pulse and ≈ 0.44 for a Gaussian-shape pulse). As an example, Figure 1.4(e) shows a broader pulse spectra, compared to Fig. 1.4(a), which corresponds to a limited pulse duration of 50 fs, shown in Fig. 1.4(f). To generate a $sech^2$-shaped pulse with a duration of 50 fs, the bandwidth should exceed 6.3 THz, that is 50.8 nm for a central wavelength of 1555 nm. Thus, active media with broader emission spectra is preferred to achieve shorter pulse durations.

Mode-locking generation

The process of ultrashort pulse formation in mode-locked lasers with a parabolic gain profile can be best described in the temporal domain as a function of distance by the modified nonlinear Schrödinger equation [82; 83]:

$$\frac{\partial A}{\partial z} = -\frac{i}{2}\left(\beta_2 + i\frac{g}{\Omega_g^2}\right)\frac{\partial^2 A}{\partial t^2} + i\gamma|A|^2 A + \frac{1}{2}(g-l)A \tag{1.12}$$

, where A is the slowly varying electric field moving at the group velocity along the propagation distance z, β^2 is the Group Velocity Dispersion (GVD), Ω_g is the parabolic bandwidth of the gain, g and l are the gain and loss coefficients correspondingly. Note, that this model does not take into account the gain dynamics of the active medium (details on the numerical approaches for accounting the gain dynamics could be found in Ref. [84]). $\gamma = 2\pi n_2/\lambda A_{eff}$ is the nonlinear coefficient responsible for the Self-Phase Modulation, where λ is the operational wavelength, A_{eff} is effective fibre mode area, and n_2 is the nonlinear refractive index of fibre ($n_2 = 3.2\cdot10^{-20}$ m^2/W for the standard silica fibre [85]).

Figure 1.5 demonstrates a typical picture of mode-locking generation in the temporal and frequency domains. If the longitudinal modes of the laser are synchronised, the output radiation consists of equidistant pulses, which are commonly referred as a pulse train. In the temporal domain, the pulse train is characterised by the pulse duration, the temporal separation between consecutive pulses, and the absolute phase. The temporal pulse spacing T_R is governed by the cavity length as $T_R = Ln/c$ and ranges from hundreds of picoseconds to hundreds of microseconds. This pulse repetition rate is known as a fundamental repetition frequency $f_{rep} = 1/T_R = c/(Ln)$ and equals to the inter-mode

separation of the laser cavity, ranging from kHz to GHz.

The absolute phase is defined as the difference between the optical phase of the carrier wave with respect to the envelope and is also called a Carrier-Envelope Phase (CEP) ϕ_{ce} (Fig. 1.5(a)). The CEP arises due to a mismatch between the group and phase velocity of the wave packet [86]. The CEP is normally not important for pulses with duration longer than several carrier-wave cycles. However, the absolute phase becomes relevant for pulses of duration of a few optical cycles, affecting the pulse electric field, which is crucial for application in extreme high-field physics [87; 88].

In the frequency domain, the pulse train presents as equidistant narrow lines, which are longitudinal modes of the laser cavity, and usually are referred to as a frequency comb. The frequency separation between individual lines is governed by the laser cavity and equals the repetition frequency of the pulses $\Delta f = c/Ln = f_{rep} = 1/T_R$. The entire comb is shifted from the zero frequency by the Carrier-Envelope Offset (CEO) frequency f_{CEO}, which is the pulse-to-pulse slippage of the CEP of a pulse train. The CEO frequency relates to the CEO phase as: $f_{ceo} = f_{rep} \cdot mod(\phi_{ce}, 2\pi)/2\pi$. In other words, the CEO frequency (or phase) emerges when the accumulated absolute phase per single cavity roundtrip is not an integer multiple of 2π. If the carrier slips through the envelope by an integer multiple of 2π through single roundtrip, no pulse-to-pulse phase shift occurs and the frequencies are not shifted from the zero value ($f_{ceo} = 0$). For example, the pulse train depicted in Fig. 1.5 has a CEO phase of π and correcponds to the CEO frequency of $f_{ceo} = f_{rep}/2$. Thus, the entire frequency comb can be fully described by two values $\nu_n = f_{ceo} + n \cdot f_{rep}$ (has only two degrees of freedom).

The mode-locking mechanism has been intensively studied for several decades [83; 89; 90; 91]. The mode-locking can be achieved by inserting an intensity-selective element (active or passive), which introduces additional losses for low-intensity light and, thus, supporting propagation only of high-intensity spikes.

The first mode-locking generation was achieved by using an intensity modulator, operating at a frequency equals to the mode spacing [61]. The usage of an active element, such as an acousto-optic or electro-optic modulator, is known as an active mode-locking. The amplitude modulator inside the laser cavity is acting as a transmission gating at the cavity roundtrip frequency. An intensity spike, arriving at the maximum transmission, is passed with relatively low loss, while another radiation is significantly attenuated [92]. The main drawback of active mode-locking is that it produces pulses with picosecond durations [91].

A passive mode-locking technique is able to produce pulses with a duration of 5 fs [62]. The passive mode-locking relies on the usage of a saturable absorber inside the laser cavity. The saturable absorber acts as an intensity discriminator by transmitting high-intensity spikes and suppressing low-intensity radiation. Nowadays, there is a big diversity of saturable absorbers, which could be divided as a *real* and *artificial*.

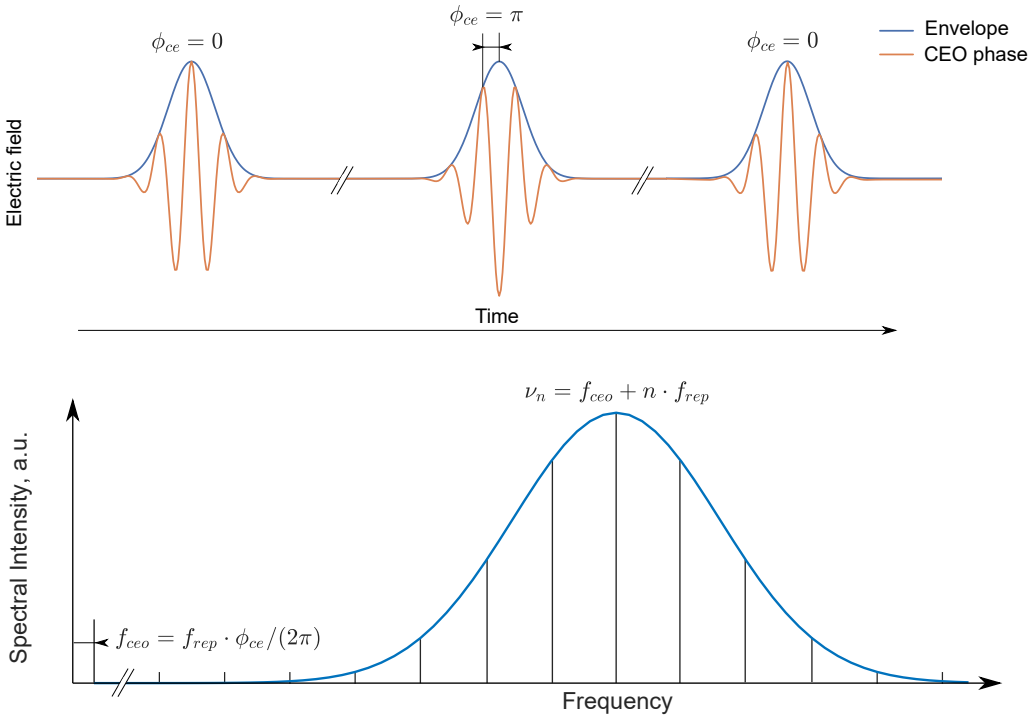

Figure 1.5: A typical picture of mode-locking generation in the time and frequency domains. The frequency mode separation is shown for a better illustration, while the real spectrum can contain thousands of modes and even more.

Real saturable absorbers

Real saturable absorber is a material, which inhibits highly-nonlinear behaviour. A perfect saturable absorber can be understood as a material with two-level energy states: the incident low-intensity light excites electrons to the upper energy states, and, as a consequence, is strongly attenuated, while high-energy spikes are able to excite all electrons to the upper states and be transmitted with much less attenuation. Numerically, the attenuation of a saturable absorber can be simulated:

$$q(t) = \frac{q_0}{1 + \frac{P_{in}}{P_{sat}}} + q_{ns} \tag{1.13}$$

, where q_0 is the modulation depth, q_{ns} is the non-saturable loss, P_{in} is the input peak power, and P_{sat} is the saturation peak power at which the absorption coefficient is half of the non-saturable value. The modulation depth, non-saturable losses, and saturation power define the quality of the saturable absorber. Figure 1.6 shows the effect of a saturable absorber on the input radiation taken from Fig. 1.4(b-d). It can be seen, that the lower-intensity spikes are strongly attenuated, while the single energetic pulse passes the saturable absorber with an attenuation close to the non-saturable coefficient. Moreover, the saturable absorber tends to shorten the pulse duration, since the intensity wings of the pulse experience stronger attenuation than the peak.

Equation 1.13 presents a simplified model of a saturable absorber when the excited

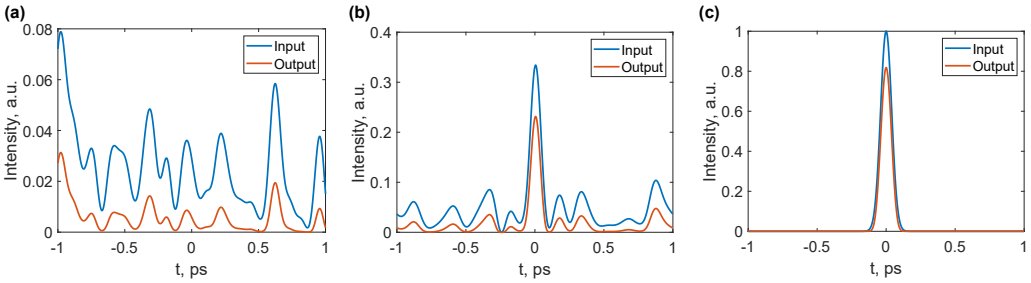

Figure 1.6: **(a - c)** Transmitted intensity after the action of a saturable absorber on the input intensity, corresponding to the Fig. 1.4(b-d). The saturable absorber parameters are: modulation depth $q_0 = 0.9$, non-saturable absorption $q_{ns} = 0.1$ and the saturation power $P_{sat} = 0.1$ a.u.

electrons are instantly decaying to the ground state. A real saturable absorber has a relaxation time, which ranges from sub-picosecond to tens of picoseconds [93]. Nonetheless, real saturable absorbers allow to generate pulses with a duration much shorter than the inherited relaxation time.

Active media, such as dyes, were the first known materials exhibiting saturable absorption properties [94; 95]. However, dyes require elaborated design and their optical properties experience degradation over time. A breakthrough design consisted of multiple-quantum-well absorber and Bragg mirror, have been introduced in 1992 by U. Keller [93; 96]. This design, Semiconductor Saturable Absorber Mirror (SESAM), allows to carefully manipulate the optical parameters of the saturable absorber. The limitations of the SESAMs are their relatively long relaxation time (from a few to tens of picoseconds) [97] and limited modulation depth (∼20% [98]) with narrow optical bandwidth and degradation under strong incident radiation.

Another material, inheriting strong saturable absorption, is Single-Walled Carbon Nanotubes (SWNTs). SWNTs were first applied as a saturable absorber in an Erbium-doped fibre laser in 2003 [99]. Carbon nanotubes have broad operational bandwidth, fast relaxation time (∼200 fs [100]) and the modulation depth can reach the value of 64% [101]. However, carbon nanotubes inherit low uniformity and repeatability of optical properties, which limit their commercial production.

The development of a cost-effective material with high non-linearity and ultrafast relaxation time is of interest of many research groups world-wide. For the last decade, numerous new materials have emerged: graphene [102; 103], topological insulators [104], transition metal dichalcogenides [105; 106], metallic MXene[107; 108], and black phosphorous [109; 110]. Recently, Wang et al. have demonstrated that plasmonic metasurfaces also exhibit saturable properties [111].

Artificial saturable absorbers

Artificial saturable absorbers are based on non-linearity of the refractive index due to the Kerr effect. The non-linear refractive index in glass has the response time of the order of

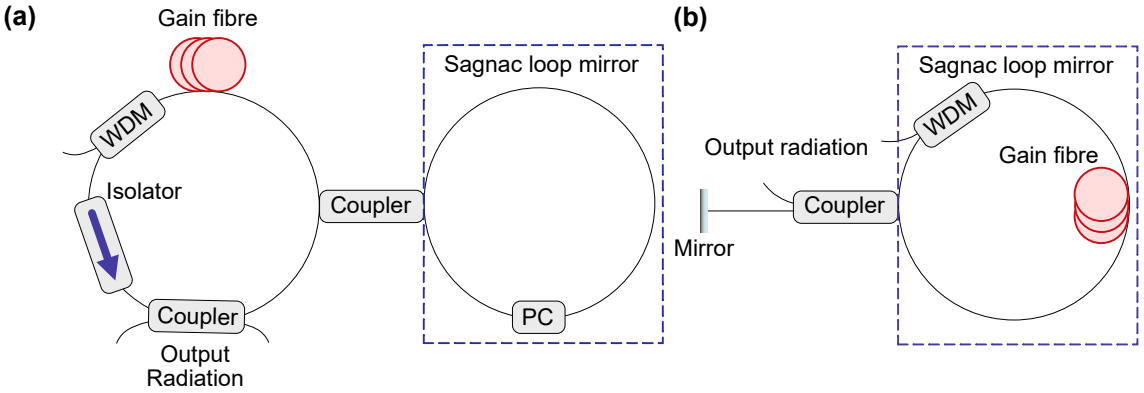

Figure 1.7: Typical implementation of: **(a)** figure-of-8 laser with a Non-linear Optical Loop Mirror and **(b)** figure-of-9 laser with a Non-linear Amplifying Loop Mirror.

a few femtoseconds [112], thus, artificial saturable absorbers are usually referred to as a fast saturable absorber. Among the most prominent techniques utilizing non-linear properties of the refractive index are Non-linear Polarisation Rotation (NPR) [113], Non-linear Optical Loop Mirror (NOLM) [114], Non-linear Amplifying Loop Mirror (NALM) [115] in optical fibre and Kerr-lens mode-locking [116] in bulk lasers.

The operational principle of the NOLM is based on destructive interference of the low-intensity beam and constructive interference for high-intensity radiation. The NOLM consists of a Sagnac loop mirror, where the incoming beams from a gain media are divided into two counter-propagating beams in the input optical coupler. Since both counter-propagating pulses pass the same optical paths, they accumulate equal phase shifts. To achieve a non-identical phase shift, the input coupler is set to transmit beams of different intensities in counter-propagating directions. Thus, counter-propagating beams will acquire different phase shifts associated with the Kerr non-linearity. Onwards, the loop transmittance will vary depending on the accumulated phase difference between the counter-propagating beams. By choosing the coupler division ratio and controlling the polarisation states of the counter-propagating beams, it becomes possible to achieve intensity selection as required for a saturable absorber. An example of the laser cavity with the NOLM is presented in Fig. 1.7(a) and called a figure-of-8 laser. The polarisation controller is used inside the loop mirror to produce an additional phase shift between counter-propagating pulses. A modification of this approach includes an active gain media inside the Sagnac loop mirror to increase the difference in the accumulated non-linear phase shifts of counter-propagating pulses [117]. This technique is known as a NALM and its implementation in a figure-of-8 laser is shown in Fig. 1.7(b).

The mechanism of the NPR is shown in Fig. 1.8 and can be explained as follows. Firstly, an input pulse is linearly polarised after passing the first polariser. The first waveplate adjusts the polarisation state to an elliptical one. The elliptically polarised pulse propagates through a non-linear Kerr media, where the different parts of the pulse (wings and the peak) experience different phase shifts due to the Self-Phase Modulation

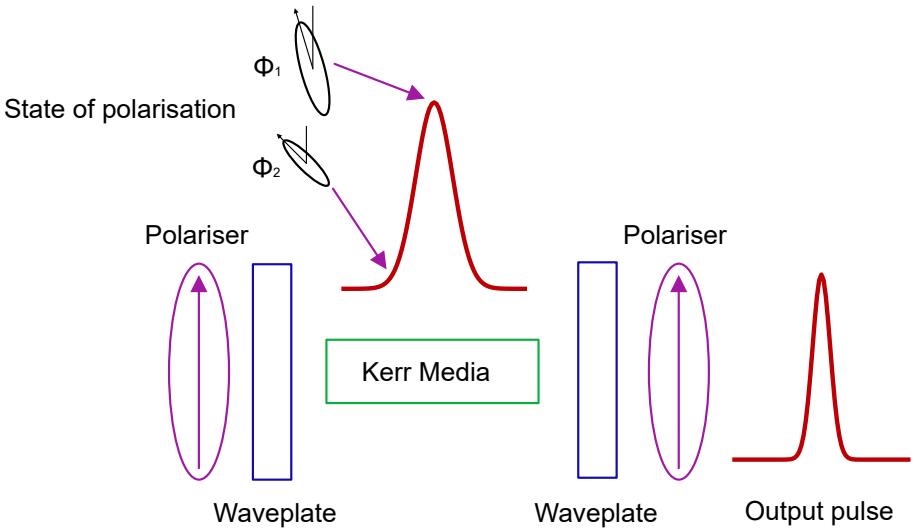

Figure 1.8: Mechanism of the Non-linear Polarisation Rotation.

(SPM) and Cross-Phase Modulation (XPM). Thus, after propagating in the Kerr media, the pulse has a non-uniform state of polarisation across the pulse envelope in the time domain. The second waveplate adjusts the polarisation state of the peak of the pulse to linear, so it matches the following polariser and the pulse peak will be transmitted with a high coefficient, while the wings of the pulse, featuring different states of the polarisation, are suppressed.

Severe disadvantages of the NPR are that the polarisation settings drift with temperature and that it is troublesome to experimentally find and reproduce the appropriate state of the polarisation. Moreover, this technique requires higher intensities, which make it difficult to obtain a stable self-starting generation. The mode-locking generation obtained via the NPR also inherit higher instabilities and noises. However, artificial saturable absorbers demonstrate better timing jitter than fibre laser mode-locked by a real saturable absorber [118].

To overcome obstacles of each real and artificial saturable absorbers a hybrid mode-locking was proposed [119]. While the slow saturable absorber is responsible for a reliable self-starting generation, the fast saturable absorber shortens the pulse duration. Additionally, hybrid mode-locking generation results in a better noise performance [120].

Generation regimes in mode-locked fibre lasers

Mode-locked laser experience a big variety of generated pulses, depending on intracavity parameters such as gain, losses, and net intracavity dispersion map. Figure 1.9 demonstrates some of the most established generation regimes defined by the intracavity Group Delay Dispersion (GDD).

One of the best-studied and the first observed operation regime in mode-locked fibre lasers is the generation of conventional solitons[1] [122; 123]. Solitons are formed as a result

[1]The definitions we use here are widespread in the fibre laser community, while slightly different

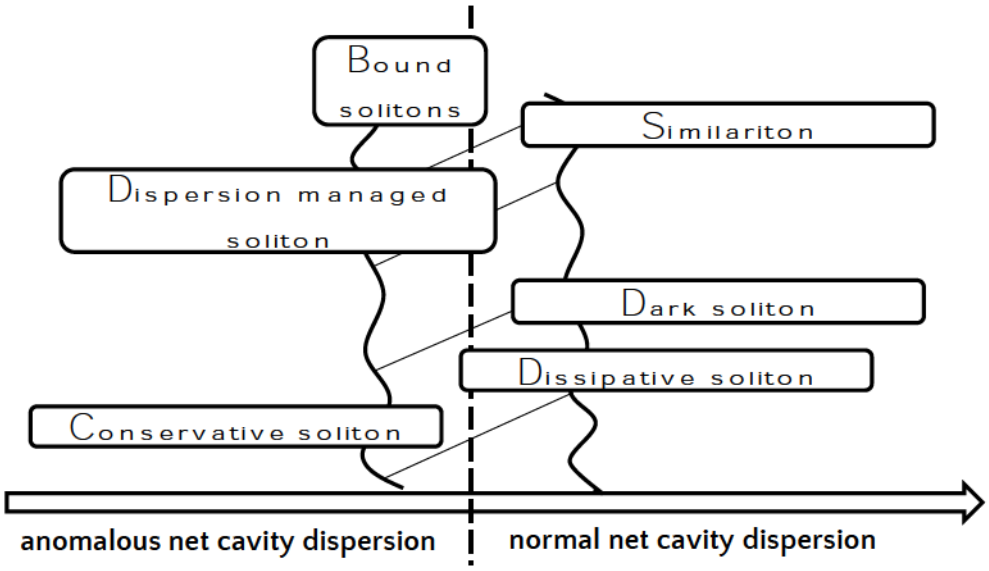

Figure 1.9: Generation regimes of ultrashort pulses sorted by the net cavity Group Delay Dispersion.

of the balance between anomalous dispersion and nonlinear-induced phase, due to the SPM. Note, that this mechanism of soliton formation is predominant only If the gain spectrum is much larger than the pulse spectrum. Solitons obey the soliton area theorem $E = 2|\beta_2|/(\tau \cdot \gamma)$, where E is the soliton energy, β_2 is the GVD, τ is the soliton duration, and γ is the non-linear parameter of the fibre. Thus, for a given fibre with fixed dispersion and non-linear parameters, the duration of the pulse is inversely proportional to the pulse energy. However, due to periodically occurring disturbances in the laser cavity, such as local gain and losses, the soliton tends to emit co-propagating dispersive waves. Due to a resonant coupling between the soliton and the emitted dispersion waves, the soliton spectra inherent parasitic peaks at certain wavelengths known as Kelly sidebands [124]. The temporal shape of the soliton is expressed as $sech^2(t/\tau)$, and it is preserved due to the mutual annihilation of the Kerr non-linearity and anomalous dispersion. The generation of solitons is very stable against perturbations and relatively easy to achieve since the pulse strives to the solitonic shape in fibre with anomalous dispersion. But, when the soliton accumulates a critical non-linear phase it may experience instability dynamics with wave-breaking [125] or split apart and transit into multi-pulse regime.

By creating a dispersion map in the laser cavity, consisted of sections with normal and anomalous dispersion, the generation of so called dispersion-managed solitons can be achieved if the resulting net cavity dispersion has close-to-zero value [126]. The sections with alternating dispersion cause the pulse duration to temporally stretch and compress by orders of magnitude over each roundtrip. This breathing dynamics significantly reduce the roundtrip non-linear phase and allow to achieve pulse energy 100-fold higher than the energy of conventional solitons. Notably, owing to a close-to-zero net cavity dispersion,

definitions of various types of solitons can be also used (for example as presented in Ref. [121])

stretched-pulse fibre lasers demonstrate the lowest level of timing jitter, intensity and frequency noises [127; 128]. Mover, the dispersion-managed solitons do not inherit spectral Kelly sidebands.

Generation of self-similar pulses (or similaritons) can be achieved by introducing high positive dispersion in the laser cavity [129]. Similaritons have a parabolic pulse shape with a linear chirp and experience remarkable breathing dynamics and do not reach transform-limited duration inside the cavity. The transform-limited pulse duration can be achieved by extra-cavity de-chirping. Self-similar pulsed generation pulses do not undergo wave-breaking and provide even higher pulse energies [130].

Theoretically, the pulse energy of similaritons rapidly scales up with normal net cavity Group Delay Dispersion [131]. This leads to the advent of the all-normal dispersion cavity with a generation of dissipative solitons [132]. Lasers, generating the dissipative soliton, are able to deliver higher pulse energies than any other types of ultrashort pulses [121].

A particularly different generation regime is a generation of dark solitons [133], which, contrary to the bright pulses, manifest as a train of intensity dips at the fundamental repetition rate in a continuous-wave radiation [134]. Dark solitons can be formed under appropriate laser operation conditions such as the normal net-cavity dispersion and, sometimes, the anti-saturable absorber effect (negative cavity feedback) [135]. The fundamental dark solitons have a $\tanh^2$ shape, reaching a zero intensity at the centre of the pulse with a phase shift of π. Numerical works have demonstrated that dark solitons are less sensitive to the noise [136], fibre losses [137], and dark soliton interactions [138]. However, a stable generation of dark solitons is more sophisticated and harder to achieve compared to the generation of bright solitons.

1.5.2 Characterisation of Mode-locking Generation

Any laser source can be characterised by a number of parameters. The following equations provide the full energy description of a pulsed laser generation:

$$P_{av.} = \lim_{t\to\infty} \frac{\int_{-\infty}^{+\infty} A^2 dt}{t} \approx \frac{\int_0^{T_R} A^2 dt}{T_R} = \frac{E_{pulse}}{T_R} \qquad \text{[Watt]} \tag{1.14}$$

$$E_{pulse} = P_{av.} \cdot T_R = \frac{P_{av.}}{f_{rep.}} \qquad \text{[Joule]} \tag{1.15}$$

$$P_{peak} = \eta \frac{E_{pulse}}{\tau_{FWHM}} \qquad \text{[Watt]} \tag{1.16}$$

where, $P_{av.}$ is the average power of the laser generation, A is the pulse amplitude, E_{pulse} is the pulse energy, P_{peak} is the peak power (the pulse energy over the pulse duration), τ_{FWHM} is the FWHM pulse duration, T_R is the time interval between consecutive pulses (roundtrip time), and $f_{rep.} = 1/T_R$ is the repetition rate. η is the conversion constant, that depends on the temporal shape of the pulse and equals 0.88 for the sech^2-shape and

0.94 for Gaussian-shaped pulses.

One of the trickiest parts of pulse characterisation is to measure its temporal duration. Unfortunately, even the fastest modern photodetectors cannot provide direct measurements of the duration of ultrashort pulses due to the limited rise time of 15 ps. One of the most established methods to characterise the ultrashort pulse duration is based on the autocorrelation of the pulses, i.e. the strobing of a pulse with itself [139]. This device, called an autocorrelator, provides an autocorrelation of the pulse, from which the temporal duration of the pulse could be extracted, while other parameters such as the pulse chirp (time variation of the instantaneous frequency $\nu_{inst} = \partial\phi/\partial t$) or the CEP remain unknown. Note, that the autocorrelator cannot unequivocally reconstruct the temporal profile of the pulse and the temporal duration is estimated for the presumptive pulse shape. The pulse chirp could be also understood as a non-flat spectral phase and is accumulated due to dispersion and self-phase modulation [140], affecting the pulse shape and duration. Thus, an unchirped pulse corresponds to the transform-limited shape. To enhance the discrimination between the pulse and background noise, autocorrelators employ nonlinear effects, such as second-harmonic generation (most common), third-harmonic generation, and dual-photon absorption [141]. In general, autocorrelators provide the best time resolution of a few femtoseconds. Nowadays, various commercially available devices, based on the self-strobing of the pulse, provide a full-field characterisation of a ultrashort pulse, which includes the pulse temporal, spectral, and phase profiles (FROG [142], GRENOUILLE [143], SPIDER [144]).

To provide any precision measurements it is important to provide a characterisation of the noise performance of the mode-locking generation. The pulse train in the presence of noise can be numerically described as [145]:

$$A(t) = [A_0 + \Delta A(t)] \sum_{n=-\infty}^{\infty} a(t - nT_R + \Delta T_R(t)) exp\{i[2\pi\nu_c t + n\phi_{ce} + \Delta\Phi(t)]\} \quad (1.17)$$

where A_0 is the electric field amplitude, and $\Delta A(t)$ is the amplitude fluctuations, which is responsible for intensity noise (fluctuations in average power). $a(t)$ is the pulse envelope in time, T_R is the temporal spacing between pulses, and $\Delta T_R(t)$ is the time deviation of the pulse envelope position in the time domain from its perfectly periodic position (the timing jitter). ν_c is the oscillation frequency, ϕ_{ce} is the CEP, and $\Delta\Phi(t)$ is the phase fluctuations of the field.

Timing jitter

Characterisation of the timing jitter is of particular importance for gyroscopic measurements as the uncertainty in pulse position directly converts to uncertainty in the angular velocity. In the frequency domain, the PSD of the timing jitter can be treated as the phase

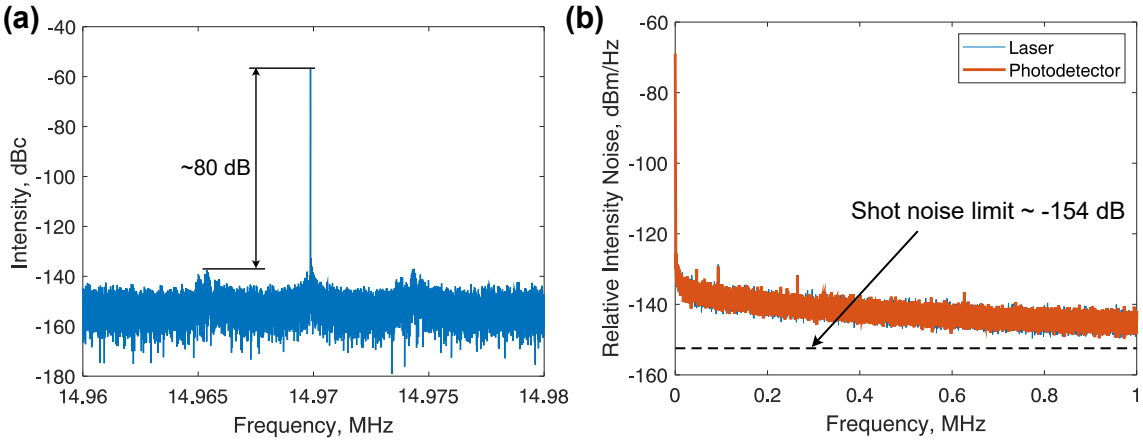

Figure 1.10: Examples of the experimental results on noise measurements of a free-running mode-locking generation. **(a)** RF spectra at the fundamental frequency and **(b)** the Power Spectral Density of the Relative Intensity Noise.

noise PSD of the repetition frequency f_{rep}. One of the methods to estimate the timing jitter of the pulse train is the evaluation of the shape and width of the repetition frequency f_{rep} by analysing the RF spectrum of the signal from photodetector [146]. Numerically, the timing jitter can be estimated as:

$$\frac{\Delta T_R}{T_R} = \frac{1}{2\pi n} \cdot \left(\frac{\Delta f}{\Delta P \cdot f_{res}}\right)^{1/2} \tag{1.18}$$

here ΔT_R is the timing jitter, T_R is the temporal spacing between the pulses, n is the order of the frequency component, f_{res} is the frequency resolution of the RF spectrum, ΔP is the Signal-to-Noise Ratio (SNR), and Δf is the width of the frequency peak. For a given fundamental repetition frequency (n = 1) of a used mode-locked fibre laser, depicted in Fig. 1.10(a), with the SNR of 80 dB, Δf = 31 Hz and the resolution of 1 Hz, the estimated timing jitter is $\approx$ 0.0089% or 5.9 ps for the T_R = 66.67 ns. By estimating the higher orders of the frequency peaks (n > 1), it is possible to evaluate the timing jitter at higher frequencies. Unfortunately, this method does not characterise the timing jitter at low frequencies due to the non-repetitive dynamics of mode-locked lasers [147]. Other methods, based on optical heterodyne techniques [148] or balanced optical cross-correlation [149], demonstrated the measurements of the timing jitter with attosecond precision.

Intensity noise

Firstly, it is important to evaluate the Signal-to-Noise Ratio of the mode-locking generation. The SNR can be evaluated from the RF spectra of the signal at the fundamental repetition frequency. An example of an RF spectrum at the fundamental repetition frequency of the used mode-locked laser generation is shown in Fig. 1.10(a). The Signal-to-Noise Ratio (SNR) at the fundamental repetition frequency is ~80 dB, limited by the formation of the parasitic sidebands, which correspond to intensity instabilities.

Similar to the continuous-wave lasers, the intensity noise of the pulse train can be characterised as the Relative Intensity Noise (RIN). The RIN is a ratio of the average mean-square fluctuations of the optical power $\langle \delta P(t)^2 \rangle$ to the square of the average optical power $\langle P(t) \rangle^2$ over different time span T [146; 150; 151]:

$$RIN = \frac{\langle \delta P(t)^2 \rangle_T}{\langle P(t) \rangle_T^2} \tag{1.19}$$

In the Fourier frequency domain, the Power Spectral Density (PSD) of the RIN can be represented as:

$$S_{RIN}(f) = \frac{2}{\overline{P^2}} \int_{-\infty}^{+\infty} \langle \delta P(t) \delta P(t+\tau) \rangle exp(i2\pi f \tau) d\tau \qquad [\mathrm{Hz}^{-1}] \tag{1.20}$$

here $\overline{P}$ is the average optical power. The RIN PSD can be easily obtained from the Radio Frequency (RF) spectrum of the signal from the detector. A root mean square value of the intensity noise can be derived by integrating over a frequency interval:

$$\frac{\delta P(t)}{\overline{P}}|_{rms} = \sqrt{\int_{f_1}^{f_2} S(f) df} \tag{1.21}$$

In Ref. [152] Authors studied the influence of the intensity noise on the timing jitter and indicated the following coupling mechanisms: slow saturable absorber, Kramers–Krönig-related phase change, Kerr non-linearity and Raman self-frequency shift. The RIN is limited by the shot noise, which can be exressed as:

$$S = \frac{2h\nu}{\overline{P}} \tag{1.22}$$

where h is Planck's constant and ν is the oscillation frequency of the wave. The RIN, limited by the shot noise, is frequency independent, owing to the nature of the shot noise. As an example, a laser generation at the central wavelength of 1550 nm with average power of 1 mW have shot noise limit of the RIN of $2.46 \cdot 10^{-16} Hz^{-1}$ or -156 dBc/Hz. Figure 1.10(b) presents the RIN PSDs for the mode-locked generation in a free-running laser and the noise floor of the used photodetector. As can be seen, the intensity noise in the provided experiment were lower or comparable to the intensity noise of the used photodetector.

Frequency noise

The frequency noises are fluctuations of the comb lines, which could be fully characterised by two values f_{ceo} and f_{rep}. The stability of an oscillation frequency is usually assessed as an Allan deviation [153]. The Allan deviation is a square root of the Allan variance and can be estimated as follows:

$$\sigma_y^2(\tau) = \frac{1}{2} < (\overline{y_{n+1}} - \overline{y_n})^2 >= \frac{1}{2\tau^2} < (y_{n+2} - 2y_{n+1} + y_n)^2 > \tag{1.23}$$

where $\sigma_y(\tau)$ is the Allan deviation with units $1/\sqrt{Hz}$, $\overline{y}$ is the averaged value over the integration time τ. The Allan deviation characterises the average difference between two averaged consecutive measurements, which makes it distinctive from the standard deviation, which estimates the deviation from the mean value. In mode-locked lasers, the Allan deviation is usually assessed for the repetition frequency f_{rep}. Generally, the Allan deviation numerically estimates the ability of the measured frequency to remain unchanged at different integration times. The Allan deviation at integration time below ∼0.4 s is mostly governed by the laser system stability. While, at the integration time above ∼0.4 s the Allan deviation starts to diverge due to environmental fluctuations [154; 155]. Nowadays, modern mode-locked laser systems are able to achieve the uncertainty of the frequency at the level of 10^{-15} at the integration time of 1 s [154; 156]. In the case of laser gyroscopes, the Allan deviation is measured for the Sagnac frequency and defines the performance of the gyroscope.

The carrier-envelope offset frequency characterises the phase stability of the pulse train and has a significant impact on the overall performance of the generated frequency comb. The first attempt to measure the carrier-envelope phase was demonstrated in 1996 by *Xu et al.* [157]. This approach was based on the cross-correlation of consequtive pulses and provided only relative changes. For the absolute measurements of the CEO frequency a $f-2f$ interferometer have been proposed [74; 158]. In the $f-2f$ interferometer, an octave-spanning supercontinuum is generated in a highly non-linear fiber to achieve two oscillation frequencies $\nu_n = f_{ceo} + n \cdot f_{rep}$ and $\nu_{2n} = f_{ceo} + 2 \cdot n \cdot f_{rep}$. Then, the n^{th} comb line is frequency-doubled in a highly nonlinear fibre to achieve the oscillation frequency of $2 \cdot \nu_n = 2 \cdot f_{ceo} + 2 \cdot n \cdot f_{rep}$. Thus, the beat note between $2 \cdot \nu_n$ and ν_{2n} corresponds to the f_{ceo}. Figure 1.11 demonstrate this technique in the frequency domain and an experimental setup with an in-line all-fibre $f-2f$ interferometer.

Another method to measure the absolute value of the CEO frequency is based on the ionization of an isotropic medium [159; 160]. However, both approaches require a complex setup, high peak power, and short pulse duration of less than ≈200 fs. In bidirectional mode-locked lasers with matched repetition rates between counter-propagating pulse trains, the relative difference between CEO frequencies can be easily estimated from the RF spectrum [161].

The CEO frequency is very sensitive to the intensity noises of the pump source [162] and environmental perturbations [163]. Moreover, the stability of the CEO frequency depends on the net cavity dispersion and, as a consequence, on the operation regime of ultrashort pulses [120]. Thus, the fluctuations of the CEO frequency can be minimised by designing the laser cavity with a close-to-zero net cavity dispersion [164]. The stability of the CEO frequency is fundamentally limited by the amplified spontaneous emission of the used laser [165].

The great advantage of the frequency comb is that it can be fully described by two values f_{rep} and f_{ceo}. Since both these frequencies lay in the microwave range, they can

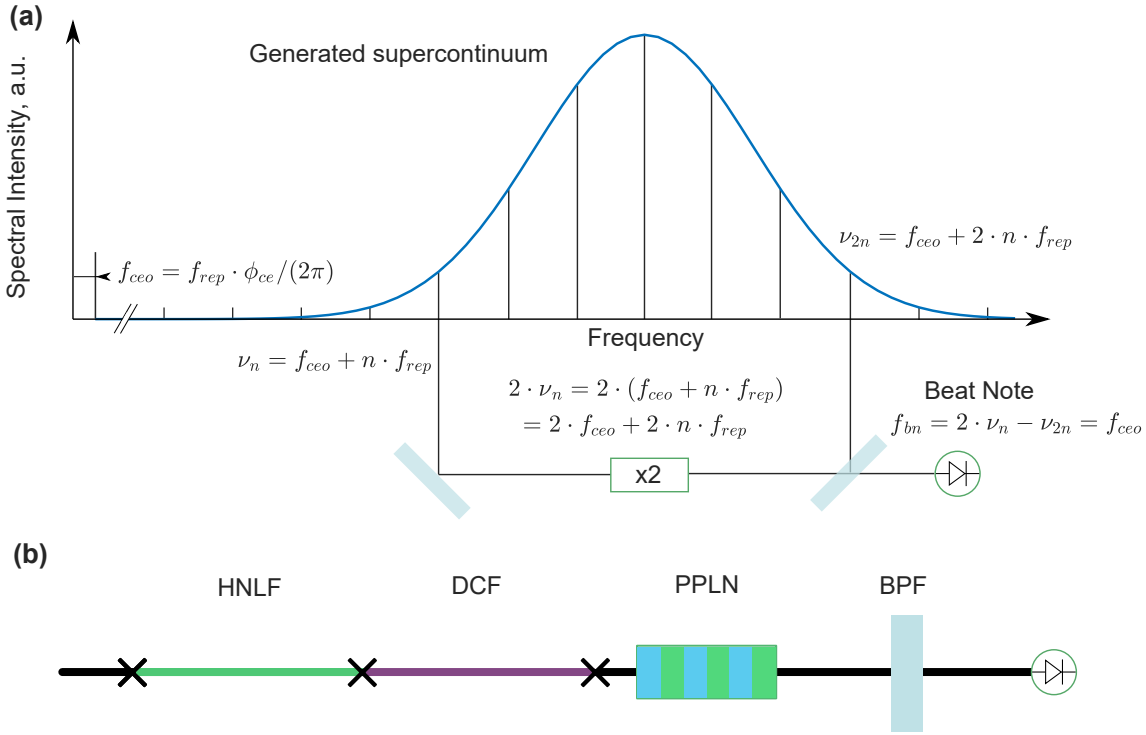

Figure 1.11: **(a)** Detection of the f_{ceo} in a $f-2f$ interferometer. **(b)** Schematic demonstration of an all-fibre $f-2f$ interferometer with common path. HNLF – highly non-linear fiber; DCF – dispersion compensating fiber; PPLN – periodically poled lithium niobate $LiNbO_3$; BPF – band-pass filter.

be efficiently stabilised through beating with a frequency standard based on atomic transitions [86; 166].

1.6 Real-time Measurement Techniques

The previously described methods are used to measure time-averaged parameters of a pulse train, which is useful to characterise the long-term performance. However, mode-locked fibre lasers inherit non-linear instability dynamics at the time scale of the cavity roundtrip, which is far beyond the bandwidth of the traditional techniques. Single-shot observation of these fast non-repetitive dynamics is crucial for the investigation of the ultrafast nonlinear processes in lasers and provides a broad avenue for application with increased data rates. Here we will discuss the latest achievements in the real-time measurement techniques and their potential applications.[1]

1.6.1 Spatio-temporal measurements

The intensity dynamics of the pulse train in a time domain at each subsequent roundtrip is known as the spatio-temporal measurements [167]. Modern oscilloscopes allow providing real-time observations of laser dynamics over the time scales of tens and even hundreds

[1]Here, by the real-time measurements, we mean single-shot measurements. And while the data analysis is performed after the recording, these measurements have the potential to be processed in real-time.

of thousands of round trips. The continuous picture of the time domain can be further segmented over a time window of the roundtrip time and stacked into a two-dimensional matrix, forming a spatio-temporal representation of the laser dynamics for every subsequent roundtrip [167]. Such a 2D map helps to investigate the evolution of the laser generation with a complex temporal profile such as in Raman lasers [168] and partially mode-locked lasers [167]. Figure 1.12 demonstrates the principle of spatio-temporal colliding dynamics of two periodic pulses in a mode-locked fibre laser cavity.

The challenge to capture the pulse dynamics in the intensity domain is the limited response time of used oscilloscopes and photodetectors, which is much longer compared to the duration of an ultrashort pulse. The temporal resolution of the spatio-temporal measurement can be estimated by the following expression [169]:

$$t_{FWHM} = \sqrt{{t_{FWHM}}^2{}_{PD} + {t_{FWHM}}^2{}_{DSO}} \tag{1.24}$$

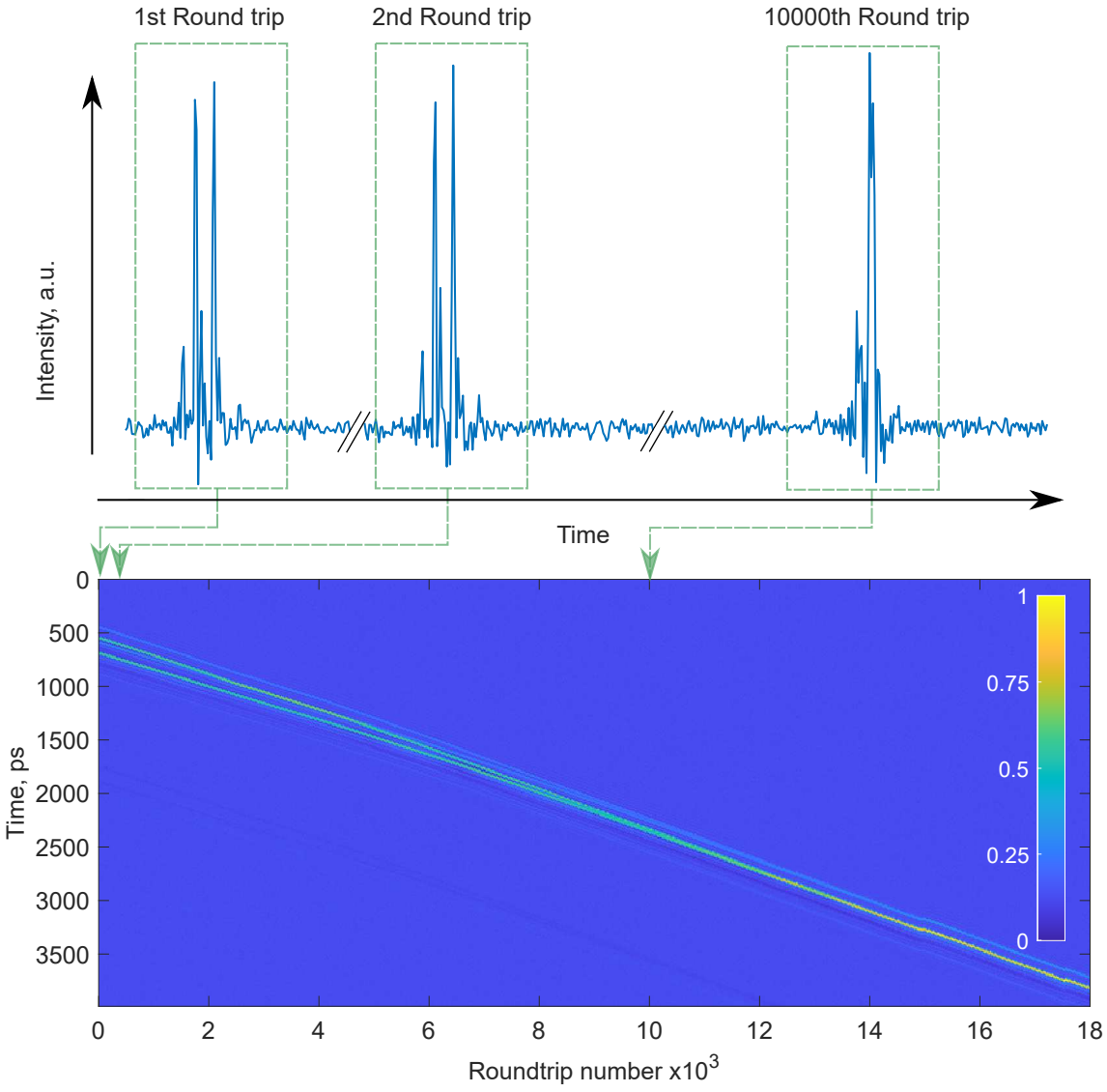

Figure 1.12: Principle of the spatio-temporal measurements. The 1D trace of a train of coupled solitons is converted to a 2D evolution map with window of the round trip time.

where $t_{FWHM\,PD}$ and $t_{FWHM\,DSO}$ are the impulse response time of the photodetector and the digital storage oscilloscope correspondingly. The response time relates to the rise time t_R as $t_{FWHM} = 0.915 \cdot t_R$. Currently, modern combinations of commercially available fast photodetectors and digital-storage oscilloscopes are limited by the time resolution of a few tens of picoseconds.

The spatio-temporal technique has demonstrated its efficiency observing the laminar-turbulent transitions [170], interaction of quasi-stationary localized structures [167] and rogue wave events [171]. More recently, the method was used in the investigation of the onset dynamics of laser generation in mode-locked lasers [172; 173]. This method is a linear approach to capture single-shot fast-evolving dynamics, resulting in a simple measurement configuration.

The limited temporal resolution of the above method can be efficiently surpassed by applying a quadratic phase shift across the temporal envelope of the pulse [174]. By further propagation of the chirped pulse in a dispersive media it will be temporally magnified, preserving its original temporal shape. This mechanism is equivalent to the action of a thin lens on a laser beam in space and is known as a *time-lens*. The quadratic phase can be efficiently applied by using a phase modulator or by exploiting non-linear effects, such as the Self-Phase Modulation and four-wave mixing. In Ref [175] Authors used a commercial available PicoLuz Ultrafast Temporal Magnifier (Thorlabs) with a temporal magnification of 76.4 and the resulting temporal resolution of 400 fs for investigation of spontaneous breathers and rogue wave events. A new heterodyne time-lens based on the a temporal-holography have been demonstrated in 2018 for the full-field characterisation of the complex ultrashort signals with a temporal resolution of ∼80 fs [176]. With this setup Authors recently investigated the modulation instability and Akhmediev breather-like patterns [177]. All in all, the spatio-temporal technique along with time-lens can be effectively enhance the resolution of the Sagnac effect measurements in the time domain.

1.6.2 Dispersive Fourier Transformation

Another technique, based on the time-stretching, is the Dispersive Fourier Transform (DFT) [178; 179]. The DFT technique allows single-shot recording of an optical spectrum of the pulse directly from the oscilloscope trace. Dissimilar to the traditional tools for measuring optical spectra such as optical spectra analysers, which require long integration time scales providing the maximum data acquisition speeds in the order of a few Hz, the DFT technique provides single-shot measurements achieving data rates of tens and hundreds MHz. Like the time-lens, the DFT exploits the space-time duality and is an analogue of the paraxial diffraction.

Figure 1.13 schematically demonstrates the operational principle of the DFT. Here, a pulse is sent through a dispersive element, allowing it to acquire a linear chirp and disperse in the temporal domain. Thus, the different spectral element delayed by different amount

of time due to the Group Velocity Dispersion (GVD), forming a spectral profile in the temporal domain (Fig 1.14(a)). Onwards a 2D map of optical spectra dynamics can be obtained analogously to the spatio-temporal map (Fig 1.14(c)). In the case of a income pulse with a complex temporal profile, the DFT technique is able to efficiently capture the interference pattern.

The dispersive element could be implemented as an arrayed waveguide grating [180], optical diffraction gratings, and through chromo-modal excitation in a multimode waveguide [179; 181]. However, the use of an optical fibre is preferable and the most widespread approach due to its simplicity and the capability to provide giant GDD. The acquiring temporal delay Δt due to the dispersion can be estimated as:

$$\Delta t = Dz\Delta\lambda + \frac{1}{2}\frac{dD}{d\lambda}z(\Delta\lambda)^2 \tag{1.25}$$

here D and z is the dispersion and the length of optical fibre, correspondingly. λ and $\Delta\lambda$ is the central wavelength and the wavelength shift from the central wavelength respectively. The second term of the equation refers to the higher-order dispersion, which is not linearly dependent on the wavelengths and, thus, is deleterious. The other maleficent effect which induces uncertainty in the DFT spectra is the non-linearity of the fibre, which distorts the optical spectra of the pulse, propagating in the non-linear media. Thus, the perfect dispersion element should possess a giant GDD and lack the higher-order dispersion and non-linearities.

Similar to the spatio-temporal analysis, the resolution of the DFT measurements is determined by the temporal resolution of the used oscilloscope and photodetector. Thus, by using equations 1.24 and 1.25 we can estimate the spectral resolution, limited by the measurement equipment as:

$$\delta\lambda = \frac{t_{FWHM}}{Dz} = \frac{\sqrt{{t_{FWHM}}^2{}_{PD} + {t_{FWHM}}^2{}_{DSO}}}{Dz} \tag{1.26}$$

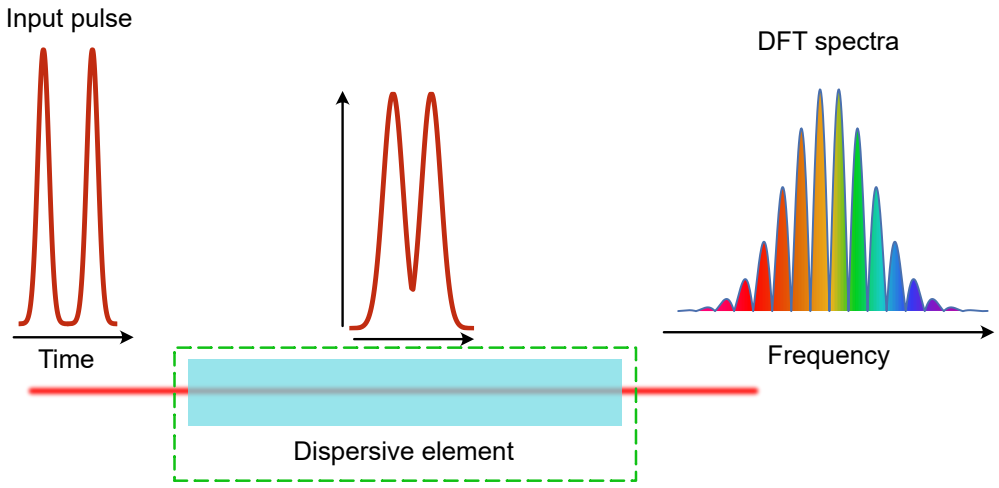

Figure 1.13: Principle of the Dispersive Fourier Transformation technique.

Here, we have neglected the higher order dispersion. Since the DFT technique is the temporal analogue of the far-field diffraction, where the minimal beam radius is limited by the width of the slit and a viewing distance, the spectral resolution of the DFT is also limited by the total accumulated GDD as [178]:

$$\delta\lambda_{GDD} = \lambda_c\sqrt{2(c|D|z)^{-1}} \tag{1.27}$$

where λ_c is the central wavelength and c is the speed of light in vacuum. It seems reasonable to increase the accumulated GDD, however, to avoid the overlapping between spectra of consecutive pulses, the following relation should be satisfied: $Dz\Delta\lambda < T_R$. More discussion on the DFT resolution in the presence of noises is presented in *Appendix* A.

The mathematical properties of the Fourier transform can be further exploited to obtain a pulse-resolved field Autocorrelation function (ACF), known as the first-order ACF or the temporal coherence function. The Wiener-Khinchin theorem states that the single-shot first-order ACF could be obtained by applying the Fourier transform of the individual single-shot power spectrum. However, since the DFT technique does not provide the spectral phase information, the numerically obtained ACF is chirp-free (i.e. assuming that the spectral phase is constant over the wavelengths). Thus, the numerically obtained ACF can be interpreted as a chirpless analogue of the real first-order ACF. In other words, the interpretation of the numerical ACF needs the assumption that the measured ultrashort pulses have a negligible chirp. Nevertheless, the obtained first-order ACF contains the information on the temporal separations between pulses independent of their chirp.

The single-shot ACF attains particular interest for investigating complex dynamics of coherent structures such as multiple coupled solitons. Numerically, the ACF of two identical bound solitons can be expressed as [182]:

$$R(\tau') = 2\int I_0(\omega)e^{i\omega\tau'}d\omega + e^{-i\phi}\int I_0(\omega)e^{i\omega(\tau+\tau')}d\omega + e^{i\phi}\int I_0(\omega)e^{i\omega(\tau-\tau')}d\omega \tag{1.28}$$

where $I_0(\omega)$ is the optical spectrum of a single pulse, τ is the time separation between pulses, and ϕ is the relative phase. Thus, data on the relative pulse separation and phase, retrieved from the interferometric pattern, could be further exploited in many applications as will be discussed later. An example of a numerically-obtained single-shot ACF of two closely-separated pulses is shown in Fig.1.14(b) and its 2D map in Fig.1.14(d). This technique is very accurate for bandwidth-limited pulses, however, it also is able to provide the data of energy distributions for highly-chirped pulses. In order to spectrally resolve the two-pulse interference, the spacing between the pulses τ should lie in the following range:

$$2/\Delta\nu_{FWHM} < \tau < 1/2\nu_{res} \tag{1.29}$$

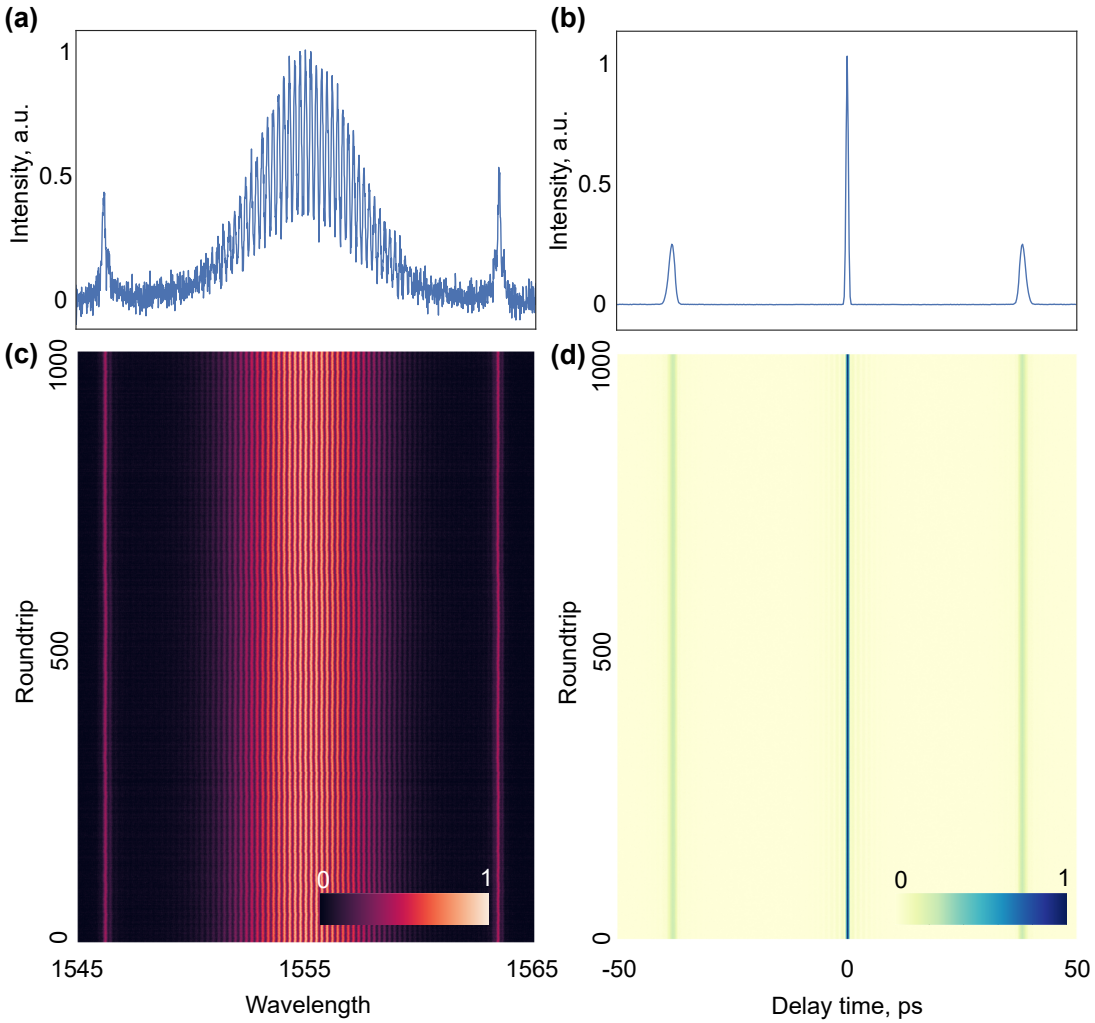

Figure 1.14: A single-shot **(a)** DFT spectra and **(b)** a corresponding first-order autocorrelation function. 2D maps of **(c)** spectral evolution and **(d)** corresponding autocorrelation function of two solitons.

where $\Delta\nu_{FWHM}$ is the FWHM bandwidth of the pulse spectra and ν_{res} is the frequency resolution of the DFT measurements. The left-hand side of the equation denotes that at least two modulation periods should be fitted in the FWHM interferogram. While one modulation period should be enough to recognize the interference, practically, the interferometric pattern could not be uniquely distinguished since the modulation occurred mainly at the wings of the interferometric spectra, which could be distorted due to the presence of noises. The right-hand side restricts the maximum pulse spacing due to the spectral resolution of the DFT measurements.

Due to the Fourier Transform properties, the resolution of the numerically obtained ACF $\delta\tau$ is inversely proportional to the covered wavelength span:

$$\delta\tau = \frac{\lambda_c^2 Dz}{c \cdot T_R} \tag{1.30}$$

where c is the speed of light in vacuum and λ_c is the central wavelength. This equa-

tion provide a trade-off between the resolution of the DFT and the ACF due to limited roundtrip time T_R. However, the resolution of the ACF can be numerically increased by using a zero-padding method. On the other hand, the maximum delay time of the ACF is inversely proportional to the resolution of the DFT:

$$\Delta\tau = \frac{\lambda_c^2 Dz}{c \cdot t_{FWHM}} \tag{1.31}$$

The Dispersive Fourier Transform technique opened a great avenue for investigation of many high-speed and non-repetitive processes such as build-up dynamics of conventional solitons in Ti:Sapphire lasers [172], fibre lasers [173], and dissipative solitons [183], Q-switched instabilities [184], and bound solitons [185]. This real-time measurements also revealed many ultrashort dynamics which are *invisible* for the traditional measurement techniques, including soliton pulsations [186; 187] and soliton-similariton dynamics [188]. By extracting the relative phase and temporal spacing between the coherent structures from the interferometric pattern, internal dynamics of soliton molecules and optical soliton molecular complexes have been experimentally revealed [182; 189]. By combining both the time-lens and the DFT it is possible to characterise the full-field of the pulses by using the iterative Gerchberg Saxton algorithm [190]. Other techniques have been also reported to reconstruct the full-field of the ultrashort pulses based on the DFT measurements [191; 192]. Moreover, since the DFT measurements provide a continuous set of useful data, it becomes possible to control and predict the mode-locked generation via emerging data processing techniques such as Machine Learning [193; 194; 195].

Apart from the fundamental interest in non-linear fibre optics, many sensing capabilities of the DFT technique with high acquisition rates have been demonstrated, e.g. displacement sensing and barcode reading [196], cellular imaging [197], imaging of ultrafast laser ablation [198], and microfluidic flow imaging [199]. Recently, a spectrally scanning LiDAR system with line rate in MHz range has been presented [200]. All these make the Dispersive Fourier Transform technique a very powerful tool both for fundamental science and real-world applications.

1.7 Summary

This *Chapter* has outlined the major historical developments in the areas of laser gyroscopes and ultrafast fibre lasers. We discussed operation basics for detection of angular velocity via laser beams and provided the main measurements techniques, indicating their advantages and limitations. We also reviewed the source of noises in laser gyroscopes. The underlying mechanisms of mode-locking generation and various saturable absorbers are also provided. We also included a broad discussion on the characterisation of mode-locking generation in terms of stability, such as intensity and frequency noises. We introduced recently emerged real-time measurement techniques, describing their operation

principles, and outlined their perspectives in further applications. In the following chapters, we intend to demonstrate that the real-time techniques alongside with mode-locked fibre lasers can be powerful tools in gyroscopic and other phase-based applications.

Chapter 2

Bidirectional Mode-locked Fibre Lasers for Gyroscopic Measurements

Ultrafast fibre lasers offer a big variety of cavity designs. One of the most peculiar designs is the bidirectional laser cavity, which allows a generation of two counter-propagating pulse trains. The bidirectional mode-locked lasers provide the best solution when two pulse trains are required for such applications as dual-comb spectroscopy and gyroscopic measurements. However, the bidirectional generation inherits unique pulse dynamics and imposes several restrictions on the laser cavity. In *Section* 2.1 we review the bidirectional cavity designs, their advantages, and the possibility to observe the Sagnac effect.

Counter-propagating solitons, generated in a bidirectional laser, undergo complex dynamics due to their continuous interactions in the laser cavity. In *Section 2.2* we provide an experimental results on the pulse onset dynamics in bidirectional laser cavity recorded via the Dispersive Fourier Transform (DFT) technique. We demonstrate that counter-propagating beams experience complex energy interchange between counter-propagating channels, which strongly affects the laser generation regime at the steady state operation.

Section 2.3 focus on gyroscopic capabilities of bidirectional mode-locked fibre lasers. We discuss the up-to-date results on measurements of angular velocity by using bidirectional mode-locked lasers. Then, we demonstrate experimental results on gyro measurements by using the spatio-temporal technique to observe the temporal Sagnac effect, and the DFT technique for investigation of the relative phase dynamics between counter-propagating pulses.

2.1 Design of Bidirectional Mode-Locked Fibre Lasers

The realisation of a bidirectional mode-locking generation in a ring cavity imposes several fundamental restrictions due to continuous interactions between counter-propagating

beams. The presence of a real saturable absorber in the bidirectional laser cavity initiates a mechanism of colliding mode-locking. This mechanism was firstly introduced in a bulk laser in 1981 [201] and refers to the interaction of two oppositely directed pulses in the saturable absorber. Since both counter-propagating beams saturate the absorber by crossing the absorber at the same time, the colliding mode-locking substantially reduces the threshold of the laser generation. This mechanism also enforces counter-propagating pulses to collide in the saturable absorber, synchronising the repetition rates of counter-propagating pulses. Moreover, Authors in Ref. [201] indicated that pulses formed owing to the colliding mode-locking, inherit shorter durations and better stability. This mechanism is crucial in bidirectional mode-locked lasers in which both counter-propagating pulses excite the same saturable absorber. However, colliding mode-locking can be avoided by designing the laser cavity in a way to violate cavity symmetry in opposite directions and introducing an additional saturable absorber.

Firstly, we consider the NOLM/NALM cavity configuration. This design attracts the interest since it has a linear cavity design and does not support a truly bidirectional laser generation. However, it contains a Sagnac loop mirror with two counter-propagating beams inside, allowing to provide gyroscopic measurements. The cavity designs of the NOLM/NALM are shown in Fig. 1.7. The advantage of this setup is that it does not require any further modifications. Moreover, NALM-based fiber lasers, implemented with a polarisation maintaining fiber, demonstrated outstanding timing jitter and noise performances [202; 203].

The simplest cavity design, able to maintain a bidirectional mode-locked generation, is a common ring cavity configuration with the use of a single saturable absorber. In 2008 this cavity setup was firstly used to demonstrate the bidirectional mode-locked fibre laser in Ref. [1] and is schematically shown in Fig. 2.1(a). In this work Authors used SWNTs as a saturable absorber and achieved pulses with duration of 640 fs and 597 fs in the clock-wise (CW) and counter-clockwise (CCW) directions. In other work [204] Authors used a similar cavity setup to produced ultrashort pulses with durations of 2.6 ps and 2 ps in the clock-wise (CW) and counter-clockwise (CCW) directions, respectively. The Authors demonstrated that by adjusting the intracavity birefringence it is possible to control the parameters of the output pulses and, particularly, perfectly match the central wavelengths and the repetition rates of the counter-propagating pulses. Other saturable absorbers operating in a transmission regime can be also used for achieving the bidirectional mode-locking generation in a similar cavity design. Recently, *B. Li et al.* reported on the bidirectional mode-locking generation achieved by solely exploiting the Non-linear Polarisation Rotation (NPR) technique in a fibre laser [205].

Abdukerim et al. demonstrated another all-fibre cavity design for bidirectional mode-locked generation, shown in Fig. 2.1(b) [2]. The mode-locking generation was achieved by the co-action of the NPR effect and a single SESAM. Authors presented a generation of ultrashort pulses with durations of 2.4 ps and 3.2 ps in the CW and CCW directions,

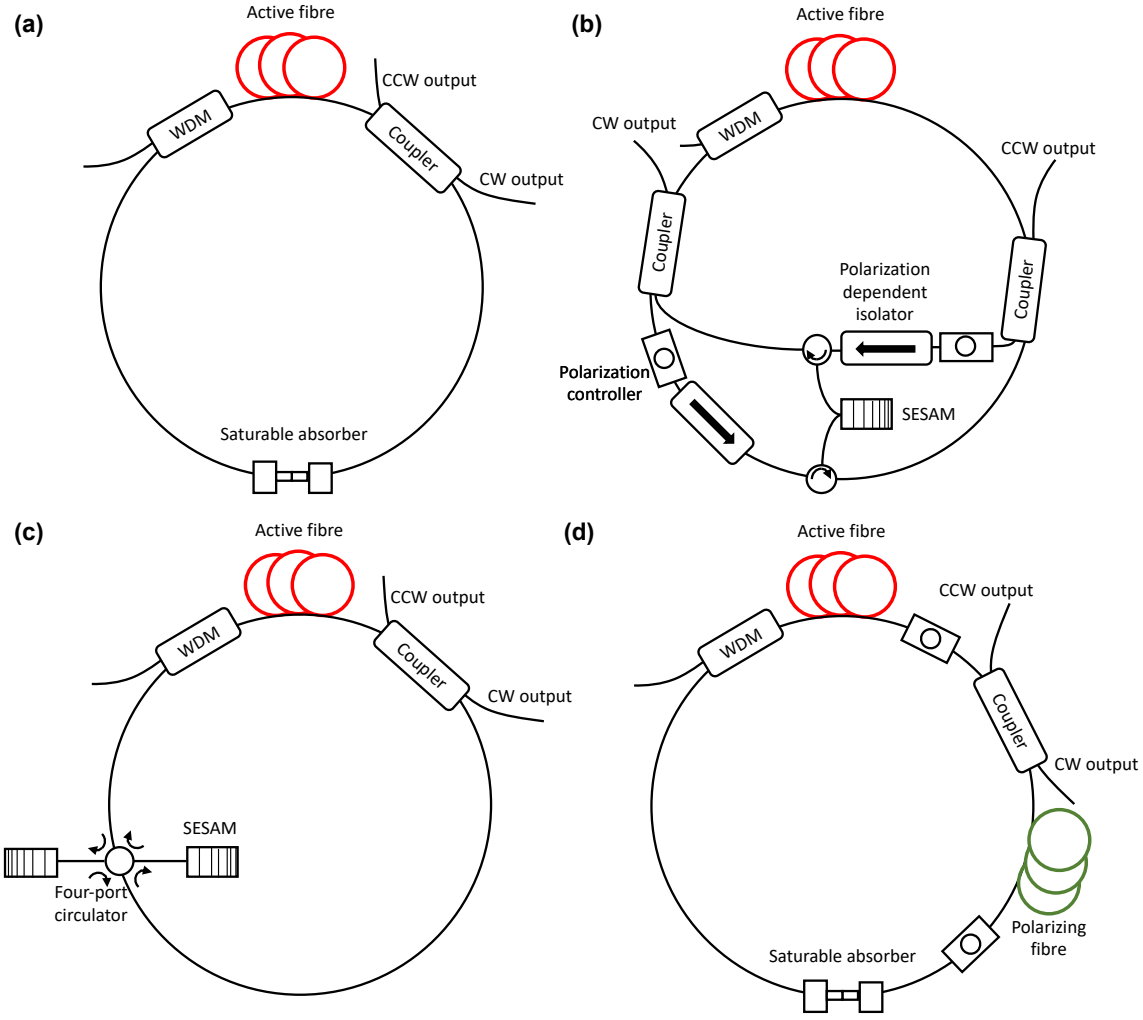

Figure 2.1: Bidirectional mode-locked fibre laser designs: a) Simple ring cavity with a saturable absorber [1], b) Ring cavity with two optical circulators, isolators and a SESAM [2], c) Cavity setup with four-port circulator and two SESAMs [3], d) Ring cavity with a hybrid mode-locking, basen on real saturable absorber and the Non-linear Polarisation Rotation [4; 5]

correspondingly. However, this approach demonstrated relatively low SNR of ∼40 dB. Moreover, this laser cavity inherits higher losses due to the presence of two optical couplers inside the laser cavity. Due to different optical paths for counter-propagating beams, a difference in the repetition rates can be achieved, while the central wavelength of the counter-propagating pulses could be independently controlled by adjusting the polarisation controllers. An important feature of this cavity setup is that the different paths of counter-propagating pulses allow to independently adjust the generation in opposite directions and to provide an active feedback for pulse stabilisation.

Another design of a bidirectional mode-locked laser cavity with a four-port circulator has been reported by Ouyang et al. [3] (Fig. 2.1(c)). By introducing a four-port circulator in the laser cavity, the pulses had different optical paths and do not share the saturable absorber. Thus, this cavity configuration does not inherit the mechanism of the colliding mode-locking. Moreover, the total cavity setup is less cost-efficient due to the use of an

additional SESAM. Authors reported generation of conventional solitons with duration of 138 fs and 318 fs in the CW and CCW directions, correspondingly. The SNRs at the fundamental repetition rate in both directions were greater than 80 dB, which indicates about high stability of the laser generation.

Figure 2.1(d) presents another cavity configuration for bidirectional mode-locking generation. This setup is similar to the traditional uni-directional ring-cavity setups with the hybrid mode-locking, except for the absence of an optical isolator. Such a cavity configuration has been used to achieve bidirectional mode-locking in Ref. [4; 5]. Both mentioned works exploited hybrid mode-locking with the use of the SWNTs and the NPR effect. To achieve the NPR effect in the opposite directions in an all-fibre cavity, Authors used a highly-bent polirising fibre, which induces a polarisation-dependent losses [206]. Authors of Ref. [4] investigated various generation regimes in such a laser cavity. For a conventional soliton generation, they reported on pulse duration of 502 fs and 524 fs for the CW and the CCW directions with the corresponding SNR exceeding 60 dB in both directions. Moreover, Authors demonstrated that this duration was lower than the pulse duration in the same laser, operated in the unidirectional regime, which highlights the significance of the colliding mode-locking.

A general drawback of laser cavities, where counter-propagating beams pass exactly the same optical paths, is that it complicates the implementation of an active stabilisation of the laser generation in counter-propagating directions. Only a few works have been reported on the stabilisation of the bidirectional mode-locking generation [207; 208] and more investigations are required for efficient stabilisation of counter-propagating beams for gyroscopic measurements. Additionally, the stability of the bidirectional mode-locking generation can be improved owing to the colliding mode-locking. On the other hand, the colliding mode-locking induces a complex synchronisation dynamics forcing the pulses to always collide in the saturable absorber, which may obstruct the gyroscopic measurements since the Sagnac effect manifests as a temporal shift. Additionally, a shared active media also induces a complex energy exchange between counter-propagating waves. Owing to this energy exchange dynamics, one of the directions may become dominant with an extinction ratio of up to 10 dB, leading to a quasi-unidirectional generation [209; 210], Q-switched instability, or multi-soliton generation [211]. Thus, it is crucial to investigate the pulse dynamics in bidirectional mode-locked lasers.

2.2 Dynamics of Counter-propagating Waveforms in Bidirectional Mode-locked Laser

In this *Section* we present experimental results on complex dynamics of counter-propagating waves inside the ring all-fibre mode-locked laser. Previously demonstrated works had a sharp focus on conventional mode-locked Ti:sapphire or unidirectional fiber lasers,

and studied pulse interactions such as repulsion and attraction or phase change in co-propagating soliton complexes, e.g., soliton molecules [182; 212]. Still, the lack of experimental and theoretical studies of underlying soliton dynamics in bidirectional mode-locked lasers presents a significant restriction toward the advancement of bidirectional ultrafast laser generation for their further applications. Moreover, bidirectional fibre lasers present unique systems allowing directionally uninhibited generation, resulting in complex dynamics and interactions between counter-propagating beams. The interactions of counter-propagating waves are a result of two mechanisms: direct soliton-soliton interactions through collision owing to the Cross-Phase Modulation (XPM); and indirect interaction owing to intracavity components with parameters varying in time such as the saturable absorber and the gain media. As an example, the collision of both pulses in a saturable absorber leads to the formation of the transient grating in the saturable absorber and is responsible for colliding mode-locking [201]. In turn, the colliding mode-locking may result in a synchronisation dynamics of counter-propagating pulses. Another type of indirect interactions of the pulses arises owing to the dynamics of the gain media. The pulse arriving first in the active media may experience stronger gain, depleting the population inversion and reducing the gain for the counter-propagating wave. These interactions may lead to instability dynamics of the laser generation and affect the usage of the bidirectional mode-locked lasers. These interactions and underlying physical processes significantly stand out from interactions of co-propagating pulses [213] or, for example, within bound soliton states [189]. Optical effects in bidirectional mode-locked cavities were scantily studied experimentally [214; 215; 215], while considered theoretically only outside laser cavities [216; 217]. However, the bidirectional mode-locked lasers are still lacked theoretical investigations due to computational complexity and more experimental works are required.

Here, we present the mutual switch-on dynamics of counter-propagating solitons with synchronised and unsynchronised repetition rates in a bidirectional hybrid mode-locked Erbium-doped ring fibre laser using the spatio-temporal and the DFT measurements. We demonstrate the formation of counter-propagated pulses from the modulation instability and the Q-switched Mode-Locked (QML) pulses through beating dynamics. Moreover, we indicate the role of the QML in further pulse evolution, including the formation of multi-soliton structures. Coherent complexes of two and three solitons are obtained, involving complex dynamics such as collisions with the emission of the dispersive waves. For a better understanding, we present the pulse-to-pulse energy variations and define a new localisation parameter to track shot-to-shot energy redistribution for each of the counter-propagating pulses. We demonstrate that redistribution of energy between the counter-propagating channels takes a key role in the formation of persistent bidirectional mode-locked generation. These results shed light on the further understanding of nonlinear dynamics in bidirectional soliton systems and other non-linear systems with colliding and interacting ultrashort pulses.

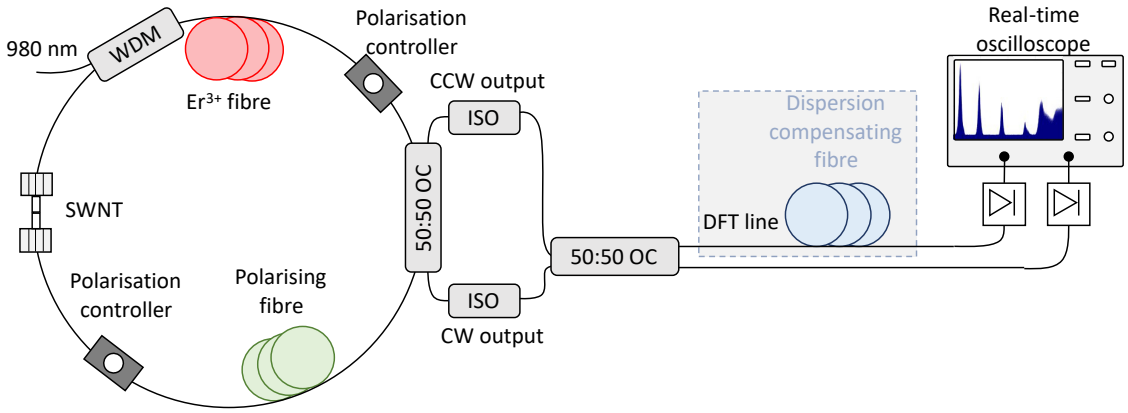

Figure 2.2: The experimental setup of the bidirectional mode-locked ring fibre laser for the Dispersive Fourier Transformation and spatio-temporal measurements; SWNT - single-walled carbon nanotubes, ISO - optical isolator, OC - optical coupler, WDM - wavelength division multiplexer.

2.2.1 Experimental setup

The laser used for the investigation of the pulse dynamics is schematically shown in Fig. 2.2 and is presented in details in Ref. [5]. A 2-m erbium-doped fibre (Liekki Er30-4/125), pumped via a laser diode at 980 nm trough 980/1550 wavelength division multiplexor, was used inside the cavity as an active media. A hybrid mode-locking was realised via a co-action of Single-Walled Carbon Nanotubess and the Non-linear Polarisation Rotation effect. A 6-m of polarising fibre with the bow-tie geometry, bent in a ring with a radius of 5 cm, was used as a reciprocal polarisation-selective element with an extinction ratio of 30 dB to perform the NPR effect in opposite directions. Two polarisation controllers were used for accurate adjustment of the operation regime. The total cavity length was 13.4 m with anomalous dispersion, which allowed the bidirectional generation of conventional solitons at the repetition frequency of ∼15 MHz. This cavity configuration allowed two types of generation: when the repetition rates of counter-propagating pulses are synchronised; and when the counter-propagated pulses have slightly different repetition rates in the range of 20-100 Hz, which could be managed via the polarisation controllers. The pump power was set at 97 mW, which was the threshold of the colliding mode-locked generation. The bidirectional mode-locked fibre laser in the steady-state generates near transform-limited 570 fs and 790 fs soliton pulses at 1555 nm central wavelength with synchronised repetition rate of 14.78 MHz in both directions. The phenomenon of identical central wavelengths of counter-propagating solitons refers to the colliding mode-locking and the equal optical paths in opposite directions [1; 218]. The output power was 1 mW in a clockwise direction, and 0.4 mW in a counter-clockwise direction. However, the direction with the highest energy was governed by the adjustment of the PCs, that highlights the influence of NPR effect on the pulse formation [5]. However, one direction always dominated, and no generation with equal pulse energies was obtained during our experiments. The RF spectrum of the fundamental repetition rate with SNR of 80 dB is shown

in Fig. 1.10(a). The timing jitter, evaluated from the RF spectrum, assessed to a value less than ∼0.87 ps. Figure 1.10(b) shows the RIN of the laser generation, which indicates low intensity noises.

The experimental setup for simultaneous observations of the spectral and the temporal evolution is shown in Fig. 2.2. A 2X2 3-dB coupler is used as an output coupler for observation of both counter-propagating waves. To avoid spurious back-reflections into the laser cavity, both output beams pass polarisation-insensitive isolators. For simultaneous recordings of the bidirectional generation in the spectral and the temporal domains we used the following strategy: both output beams are combined in another 3 dB coupler with a temporal spacing close to the half of the pulse period in order to avoid overlapping; one arm of the latter 3-dB coupler directly connected to a photodetector for recording of the spatio-temporal measurements; while the other output passes the DFT line before being made incident on another photodetector. The measurement equipment consisted of 33 GHz Digital-storage oscilloscope (Agilent DSOX93204A) and two 50 GHz photodetectors. The DFT line was realised as a 11 km of dispersion compensating fibre with GDD of -1200 ps/nm. Using the expressions 1.26 and 1.24, the calculated resolution estimated as 0.021 nm and 25 ps for the DFT and the spatio-temporal measurements, respectively. This spectral resolution of the substantially exceeds the typical spectral resolution in previous works of 0.1 nm [172; 188; 190], which allows us to observe the spectral dynamics in more details. Moreover, high spectral resolution provides a high maximum temporal delay of the numerically obtained ACF of 330 ps. More discussion on the DFT resolution is presented in *Appendix* A.

2.2.2 Build-up dynamics of unsynchronised pulses in bidirectional mode-locked fibre laser

Figure 2.3 demonstrates the experimental results on typical formation dynamics of both clock-wise and counter-clockwise pulses, recorded over the complete build-up process using the DFT technique. To register the build-up dynamics we followed the following procedure: firstly we adjusted the Polarisation Controllers (PC) to generate unsynchronised ultrashort pulses in opposite directions and set the oscilloscope trigger to the level of the stable pulse generation; then, we slightly detuned the PC to transit back to the generation of the continuous wave; finally, by adjusting the PC to the state when we observed the bidirectional generation, the newly-generated pulses trigger the oscilloscope to capture single measurements, allowing us to register the pulse formation dynamics. The electronic PC we used could be controlled from the computer with high precision, allowing adjustment to the exact state when the bidirectional generation was observed. Note, that this dynamics was observed by changing the intracavity polarisation states rather than changing the pump power.

The complete build-up dynamics in both directions, measured via the DFT, is shown

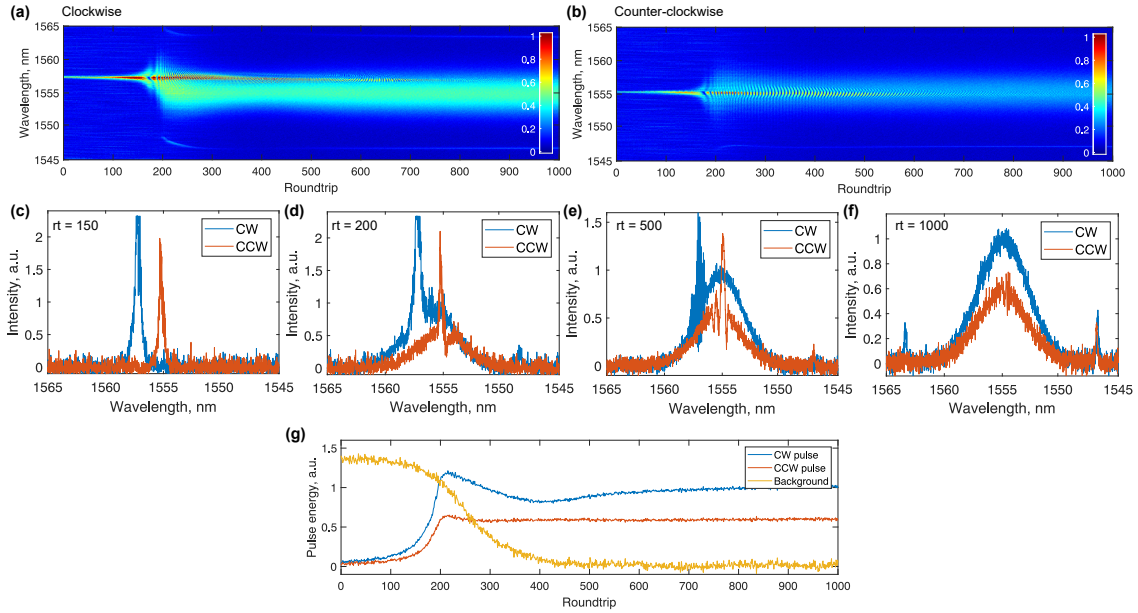

Figure 2.3: Experimental results of the spectral build-up of bidirectional solitons: (a) clockwise (CW) and (b) counter-clockwise (CCW). The spectra crops from the DFT measurements at (c) 150th, (d) 200th, (e) 500th, and (f) 1000th roundtrip. (g) Dynamics of the energy of counter-propagating pulses and the energy of background radiation (continuous-wave).

in Fig. 2.3(a-f). The formation dynamics features four transition stages, starting from modulation instability, sequentially undergoing through beating dynamics, and further formation of final steady bidirectional mode-locking generation through multi-peak structures.

Alongside with the spectral information, it is important to investigate the energy distribution between the opposite-circulating beams. To calculate the pulse energy we integrate its spectral profile over wavelengths, which according to Parseval's theorem corresponds to pulse energy and is demonstrated in Fig. 2.3(g). To calculate the background radiation or the energy preserved as the continuous-wave radiation, we integrated the noise background floor. The energy units were normalised to the energy of the pulse in the CW direction during the stable bidirectional mode-locking generation.

By exploiting the Wiener–Khinchin theorem as was described in *Section* 1.6.2, we obtain the single-shot first-order Autocorrelation function (ACF). Since the generated solitonic pulses are close to their bandwidth-limited durations, we can assume that both pulses inherit only a negligible chirp. This fact allows us to interpret the numerically obtained ACF to investigate the pulse dynamics. Figure 2.4 shows the evolution of the numerically obtained ACFs, corresponding to the spectra, displayed in Fig. 2.3. From the ACF it is possible to distinguish all stages of the pulse formation.

We are staring our discussion with modulation instability, since it plays a crucial role in the pulse formation from intensity background noise. Modulation instability is a feature of non-linear systems with periodic perturbations, leading to a rapid growth of localised

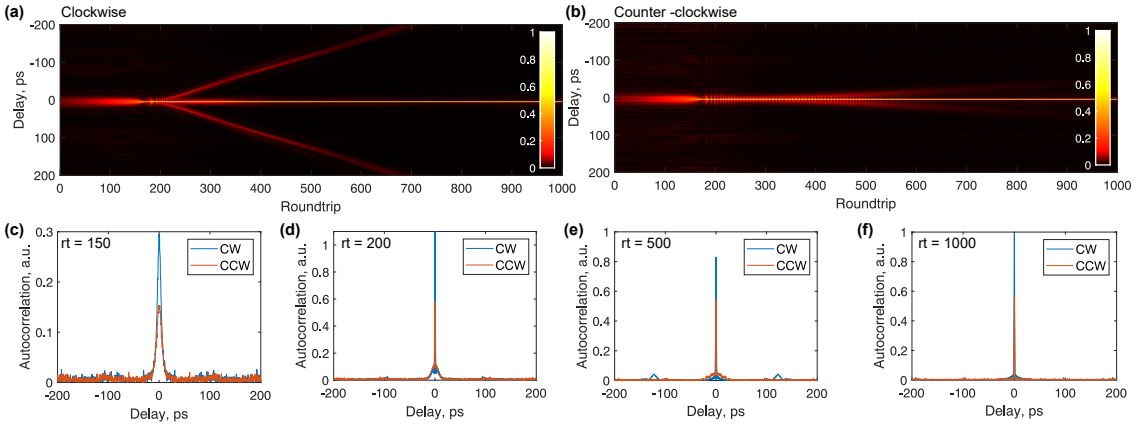

Figure 2.4: The first-order autocorrelation function of the build-up of bidirectional solitons: (a) clockwise (CW) and (b) counter-clockwise (CCW). The crops from the autocorrelation function at (c) 150th, (d) 200th, (e) 500th, and (f) 1000th roundtrip.

intensity structures from an initial wave with nearly constant amplitude [219; 220; 221]. The modulation instability is a general concept and have been observed in various physical systems such as hydrodynamics [222], plasma waves [223], Bose-Einstein condensates [224] and optics [219]. In our observations, the narrow-band modulation instabilities (Fig. 2.3(c) and 2.4(c)) were originated in both directions from an intensity noise floor with an exponential growth of their energy until the energy reaches the level of the soliton energy in the steady state at ∼200 roundtrip (Fig. 2.3(g)). Due to higher peak intensity of modulation instabilities compared to the continuous-wave radiation, they experience lower intracavity losses due to the saturation of the saturable absorbers, which induce substantial growth of the energy of modulation instabilities in both directions. Hence, the energy of the background continuous-wave radiation started to decrease (Fig. 2.3(g)) due to the limited energy stored in the gain media. The narrow temporal duration of the modulation instabilities correspond to time-bandwidth-limited durations at the FWHM of 10 ps and 15 ps in the CW and CCW directions respectively with the peak intensity ∼3-times lower compared to the stable soliton.

The spectral dynamics of the generation of the modulation instability in the CW direction is shown in Fig. 2.5(a). As can be seen, the modulation instability inherit strong spectral wings. The spectral offset of the spectral wings at maximum gain from the seeding intensity peak can be calculated as [225]:

$$\Omega_{max} = \sqrt{2\gamma P_0/|\beta_2|} = \sqrt{2/(|\beta_2|L_{NL})} \tag{2.1}$$

where γ is the nonlinear parameter of the medium (2.2 mrad/W for optical fibre at 1550 nm), P_0 is the optical power, $|\beta_2|$ is the Group Velocity Dispersion, and $L_{NL} = (\gamma P_0)^{-1}$ is the nonlinear length. According to this equation by using the bandwidth-limited duration of the intensity peak of 10 ps and average power of 1 mW, the spectral separation $\Omega_{max} \approx$ 36 GHz (0.3 nm). This numerical value is well matched with the experimental results

as shown by the arrow in Fig. 2.5(a). Note, that this frequency offset of the maximum gain is obtained for the average power of 1 mW, which is the average power during the stable soliton generation. As can be seen from Fig. 2.3(g), during the build-up dynamics, the energy of the modulation instability varies from noise floor to ∼1.2 mW. For the energies below 1 mW, the frequency offset of the gain is less than the spectral width of the modulation instability and exhibited as a spectral broadening of the modulation instability (red line in Fig. 2.5(a)).

Starting from the ∼160th roundtrip, the energy of the modulation instabilities reach the level to excite non-linear effects and the modulation instabilities started to spectrally broaden due to the Self-Phase Modulation (SPM) (Fig. 2.3(d)). During the broadening dynamics, both counter-propagating pulses undergo breathing dynamics in the spectral and temporal domains. The breathing dynamics was preserved for ∼30 and ∼150 roundtrips in the CW and CCW directions respectively and shown in Fig. 2.5. This breathing dynamics is attributed to the beating between the seeded modulation instability and the newly-formed pulse, which is similar to the one in bulk Kerr-lens mode-locked lasers [172]. Notable, that both counter-propagation pulses experienced similar dynamics during these roundtrips with the temporal spacing between the seeded modulation instability and the nascent pulse of less than the duration of the pulses (Fig. 2.4(d)). It is worth noting, that the peak intensity of the seeding modulation instability was decreased by ∼85% after the formation of the ultrashort pulses, meaning that almost all energy was transformed to the broadband pulse from the modulation instability. The broadband ultrashort pulse inherits further reduction of the intracavity losses compared to the modulation instability since its duration is less or comparable to the relaxation time of the SWNTs.

During the beating dynamics and the pulse spectral broadening, the counter-propagating pulses experienced a shift in their central wavelengths. The total differences in the central wavelength between the seeding modulation instability and the broadband pulses was estimated from their interference from the DFT spectra, shown in Fig. 2.3(e), to be ∼1.84 nm and -0.25 nm in the CW and the CCW directions respectively. The following shift of the central wavelength of the pulses occurred mainly due to the intracavity conditions for the stable bidirectional mode-locking generation. Furthermore, the intracavity GDD affects the temporal dynamics of the pulses with different central wavelengths. Thus, due to the difference in the central wavelength and the intracavity dispersion, the seeded modulation instability and the generated ultrashort pulse diverge from each other. The divergence rate in the CW direction, estimated from the ACF, was ∼ 405 fs per roundtrip. Consider the difference in the central wavelength of 1.84 nm and the cavity length of 13.3 m, the divergence rate corresponds to the average intracavity dispersion parameter of 16.6 fs/nm/m, which is in good agreement with the experimental setup. In the CCW direction, the divergence rate was much smaller due to the smaller difference in the central wavelength between the modulation instability and the formed broadband pulse.

With the spectral broadening of both counter-propagated pulses, pronounced Kelly

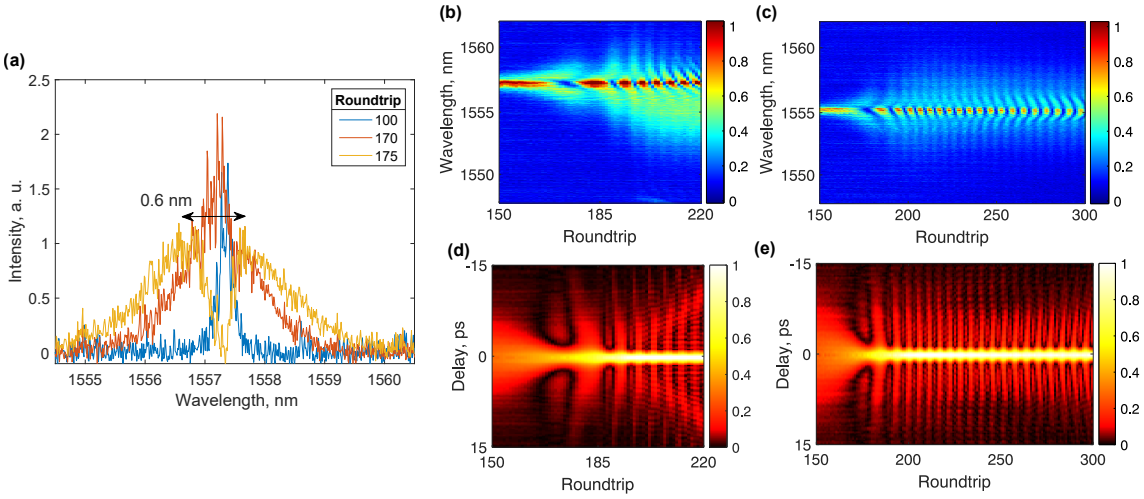

Figure 2.5: **(a)** The single-shot DFT spectra of the generation of the modulation instability in the CW direction at different roundtrips. The arrow indicates the spectral width of 0.6 nm.The subsequent beating dynamics: **(b - c)** the DFT spectra and **(d - e)** first-order autocorrelation function of the clockwise and counter-clockwise pulses correspondingly.

sidebands also rapidly originated, which confirm the generation of the conventional solitons (Fig. 2.3(f)). Moreover, the Kelly sidebands demonstrated a strong variation of the central wavelength, following the central wavelength of the main solitons. The emitted dispersive waves follow the dynamics of the central wavelength of the soliton in order to maintain the phase-matching conditions for efficient radiation of synchronised resonant dispersive waves [226].

The residual long pulses after the pulse splitting were preserved for ∼450 roundtrips and were annihilated almost simultaneously in both counter-propagating directions. The simultaneous annihilation of the residual sub-pulses in both directions highlights the importance of the saturable absorber on the pulse dynamics. The residual pulses, as well as the seeded modulation instability, have synchronised repetition rates in both directions with a collision point in the saturable absorber, and the extinction of one pulse results in higher losses in the saturable absorber for the counter-propagated pulse and its subsequent annihilation consequently.

The presence of the residual broad pulse in bidirectional mode-locked lasers for several hundred roundtrips is a noticeable difference from unidirectional mode-locked lasers, where the seeded pulse can totally evolve into an ultrashort pulse [173] or may be rapidly attenuated by the saturable absorber [172]. However, in unidirectional fibre lasers, mode-locked via a real saturable absorber, the beating dynamics can be also extended if the central wavelength of the seeded pulse is close to the formed ultrashort pulse [227]. The proximity of their central wavelengths induces a low divergent rate and together with a relatively long relaxation time of the real saturable absorber allows the seeded pulse to 'tail' the stronger pulse, which saturates the absorber, for several hundred roundtrips. In contrast, in the bidirectional mode-locked laser, the counter-propagated seeded pulses are

synchronised with the collision point in the saturable absorber, which significantly reduces the threshold and, thus, extends their presence for several hundreds of roundtrips.

Finally, after the annihilation of the residual pulses, a stable bidirectional generation of conventional solitons was achieved (Fig. 2.3(c) and 2.4(c)). The formation process lasted for the same amount of time in both opposite directions and took around 1000 roundtrips (66.7 μs) from the first intensity spike to the stable ultrashort pulse. Nearly the same amount of roundtrips are required for the generation of dissipative solitons in a unidirectional fibre laser [173], while in bulk lasers the pulse formation from the modulation instability takes less time, but the bulk laser can emit intensity fluctuations for a substantial amount of time before the formation of the seeding modulation instability [172]. The achieved generation regime was stable and lasted for at least several hours.

By analysing the arrival time of the counter-propagating pulses on the photodetector from the intensity dynamics (Fig. 2.6) and mapping the events to the laser setup geometry, we confirmed that both pulses originated with one of the collision point in the SWNTs saturable absorber, as predicted in other investigations [214; 215]. The second collision point located symmetrically opposite, slightly shifted from the output coupler. Both collision points inside the laser cavity were static during the modulation instability. However, after the formation of the broadband pulses in both directions, their relative trajectories started to diverge, indicating that the colliding points start moving through the laser cavity by the value of $\Delta f / f_{rep} \cdot L$, where Δf is the difference of repetition rates between counter-propagating pulses and L is the optical length of the laser cavity. We refer this mismatch to the intensity discriminated transmission of the NPR effect and the birefringence of the optical fibre. The settings of the PCs in the laser cavity create a difference in the polarisation states of the counter-propagating pulse and, therefore, distinct effective refractive indices due to birefringence and, in the end, a difference of the optical paths in opposite directions. In Ref. [5] Authors demonstrated that for the bidirectional generation with matched repetition rates, generation in both directions has almost coinciding state of polarisation. However they do not present measurement of the state of polarisation for the bidirectional generation with unsynchronised repetition rates, which could experience different polarisation. This conclusion is supported by the fact, that we could not obtain an apprehensible interference of the counter-propagated pulses at the output from the laser via the DFT measurements, which can take place if both counter-propagating pulses inherit different polarisation states. Additionally, counter-propagating pulses with different polarisation states do not form a periodic grating in the saturable absorber and are less subject to interact inside the laser cavity since the Cross-Phase Modulation is 3 times less effective for cross-polarised beams [225].

The comprehensive understanding of the soliton formations and their interactions inside a bidirectional laser cavity lacks efficient and adequate numerical models. Few discrete studies discussed the nature of collision of counter-propagating ultrashort pulses inside a media [216; 228]. These theoretical works demonstrated that interactions of counter-

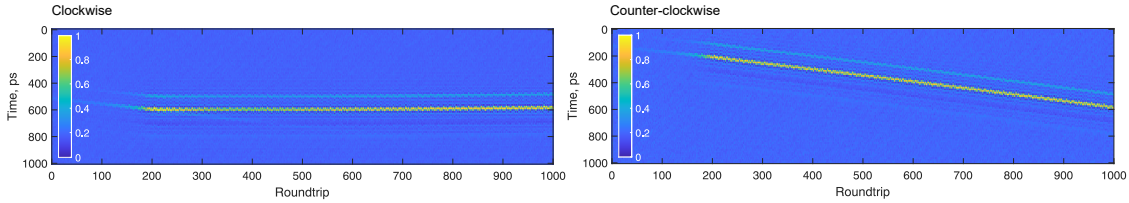

Figure 2.6: The spatio-temporal dynamics during the pulse build-up in clockwise and counter-clockwise directions.

propagating pulses are non-integrable and, therefore, do not produce a soliton solution. The final result of the pulse collision is strongly dependent on the initial conditions of each counter-propagating pulse, such as the pulse duration and the peak intensity or group velocity, as well as their relative polarisation. Thus, Afanas'ev et al. have determined the result of ultrashort pulse collision in a resonant two-level medium in regards to their peak powers, demonstrating that low-intensity components got annihilated, while collision of relatively high-peak-power pulses leads to a portion of their energy to transfer to low-intensity secondary diverging pulses, as an oscillating 'tails' of the primary pulse [216]. This numerical work confirms our experimental observation of the pulse evolution, where the secondary weak pulse 'tailed' the main soliton. In Ref. [228] the Authors considered the dependence of the colliding dynamics at different polarisation states of the counter-propagating solitons. They numerically predicted a formation of secondary solitary waves for colliding pulses with orthogonal polarisation states and a formation of population grating in the interaction region if the colliding pulses have parallel states of polarisation. Our experimental studies verify this theoretical observation by the demonstration of different build-up dynamics of counter-propagating pulses, depending on the initial conditions (compared to Ref. [211]). We assert that the collision of counter-propagating pulses and the crossing point in the laser cavity plays a pivotal role in the formation of multi-soliton structures and their further annihilation during the build-up process of a steady-state mode-locking in a bidirectional fiber laser. Therefore, counter-propagating pulses with evolving intensities and polarisation states experience different formation dynamics in the cavity.

Summary

In summary, here we demonstrated the real-time formation dynamics of counter-propagating solitons with different repetition rates in the bidirectional mode-locked erbium-doped fiber laser. By using the DFT and the spatio-temporal techniques, we have analysed the fast transient dynamics during soliton build-up toward the stable bidirectional mode-locking regime. Although counter-propagating pulses experience a similar evolution pattern, they undergo through each evolution stage over different time periods. The difference in the evolution matches the difference in intensities: domination of the clock-wise bean and suppression of counter-clockwise pulses. Therefore, we can conclude that the pulse for-

mation at the early stage in each direction is strongly relying on the counter-propagating beam owing to the colliding mode-locking. Once the pulse with broad spectra was formed, it propagates with less dependency on the counter-propagating pulse, leading to the unsynchronisation of counter-propagated pulses. Additionally, though counter-propagating pulses were seeded by the modulation instability at different central wavelengths, both of the pulses subsequently evolve to have broad spectrum located at almost matched central wavelengths. The mismatch of the repetition rates is related to the mismatch of intensities of counter-propagating pulses and the birefringence of the optical fibre.

We experimentally observed that the primary pulse in each direction is formed from modulation instability transitions through beating dynamics into conventional stable solitons similar to the unidirectional mode-locked fibre lasers [172; 173]. Contrary, in comparison to earlier demonstrated results on unidirectional pulse formation [172; 173], soliton molecules structures were not observed in either of the directions. In contrast, residual satellite intensity peaks are present in the formation dynamics for several hundreds of roundtrips. When the intensity of such pulses reaches the threshold, they simultaneously annihilate in both directions, leaving the main pulses propagating in the cavity.

Our findings also demonstrate that the net cavity dispersion is an important factor in the formation dynamics. Thus, the earlier work of Yu et al. discussed the build-up process in the net-normal dispersion bidirectional lasers and demonstrated the similarities between dynamics of counter-propagated beams during their build-up [215]. Additionally, Authors indicated the crucial role of the real saturable absorber on the synchronisation of counter-propagating pulses. These studies provide the basis for further investigation of pulse formation and evolution in non-linear bidirectional laser systems. Moreover, this observations contribute to the development of bidirectional systems for their further usage for dual-comb spectroscopy or gyroscopic measurements.

2.2.3 Pulse onset dynamics of synchronised pulses in bidirectional mode-locked fibre laser

In this section, we consider another build-up dynamics intrinsic to the generation of counter-propagating pulses with synchronised repetition rates in the bidirectional mode-locked fibre laser. The synchronised repetition rates underline the importance of the colliding mode-locking on the pulsed generation. In the time domain, that means that the counter-propagating pulses are directly interacting always in the same two locations inside the laser cavity, and, as we discuss later in this *Section*, one of these crossing points is in the real saturable absorber (SWNTs). In the frequency domain, the synchronised repetition rates denote that the inter-modal frequency separation of the generated combs is also matched. Another distinctive feature from the results presented in the previous *Section* is that these dynamics have been recorded directly by switching on the pump laser. At first, we adjusted the PCs for the stable synchronised mode-locking generation

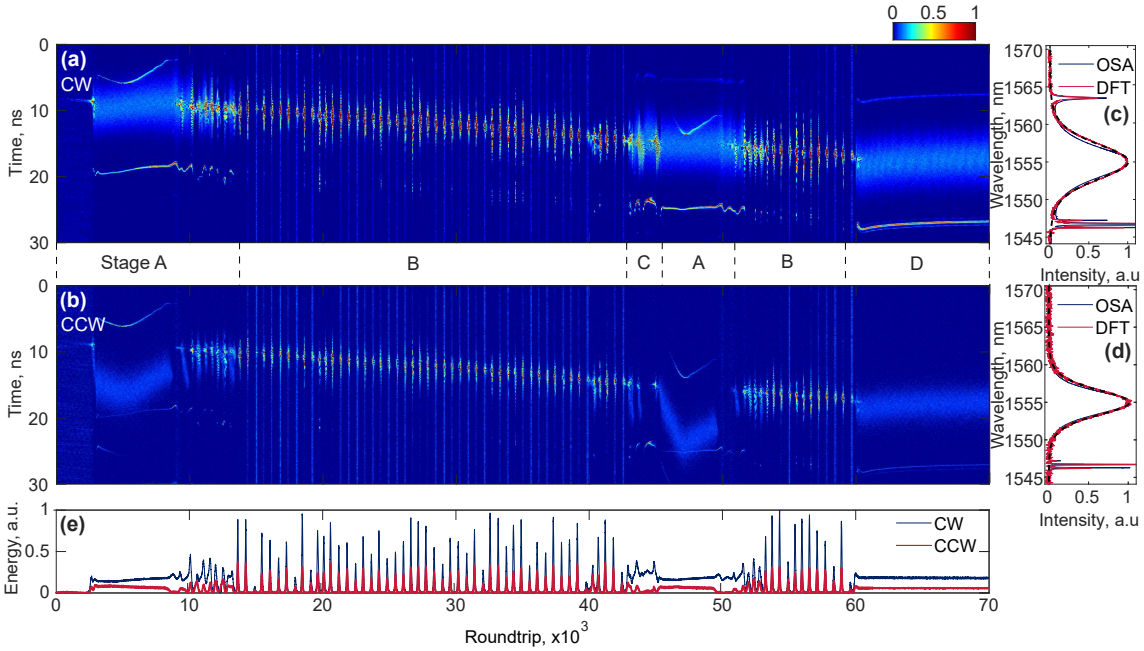

Figure 2.7: Spectral switch-on dynamics in bidirectional mode-locked laser: **(a)** clockwise (CW) and **(b)** counter-clockwise (CCW) directions. Averaged over 100 roundtrips DFT spectra with sech^2-function approximation (black dashed line), and spectra from optical spectrum analyser (OSA) are depicted for **(c)** clockwise and **(d)** counter-clockwise directions. **(e)** Dynamics of the round trip pulse energies.

and set the oscilloscope trigger. After that, we switched the pump power off and then, the recorded dynamics was recorded by switching on the pump laser. Thus, we observed a non-trivial dynamics through Q-switched instabilities with many accompanying ultrafast phenomena. All these make the results presented here distinguished from the previous dynamics.

Figures 2.7(a-b) demonstrate the complete picture of the build-up dynamics of the clock-wise (CW) and counter-clockwise (CCW) pulses in the bidirectional mode-locked fibre laser, recorded via the DFT technique. Figures 2.7 (c-d) show the optical spectra, recorded with an optical spectrum analyser (Yokogawa) and the DFT measurements with averaging over 10 roundtrips with a $sech^2$-function approximation. Both measurements and their approximation indicates a good correlation with each other. Figure 2.7 (e) shows the evolution of the pulse energies over the round trips. Pulse establishment in both directions took approximately 70 thousand round trips (4.8 ms), where the following events could be distinguished: formation of an unstable mode-locked pulse with a following spectra blue-shift, soliton breakup with a transition into Q-switched instabilities generation, the formation of soliton complexes and soliton collision, and the final evolution to the stable mode-locked generation from a Q-switched pulse. Similar to unidirectional mode-locked lasers and the previous results, the pulse formation was always initialised through the modulation instability. To justify our conclusion, we have recorded several dozens of switch-on dynamics, which demonstrate similar features, but there has been no preferred

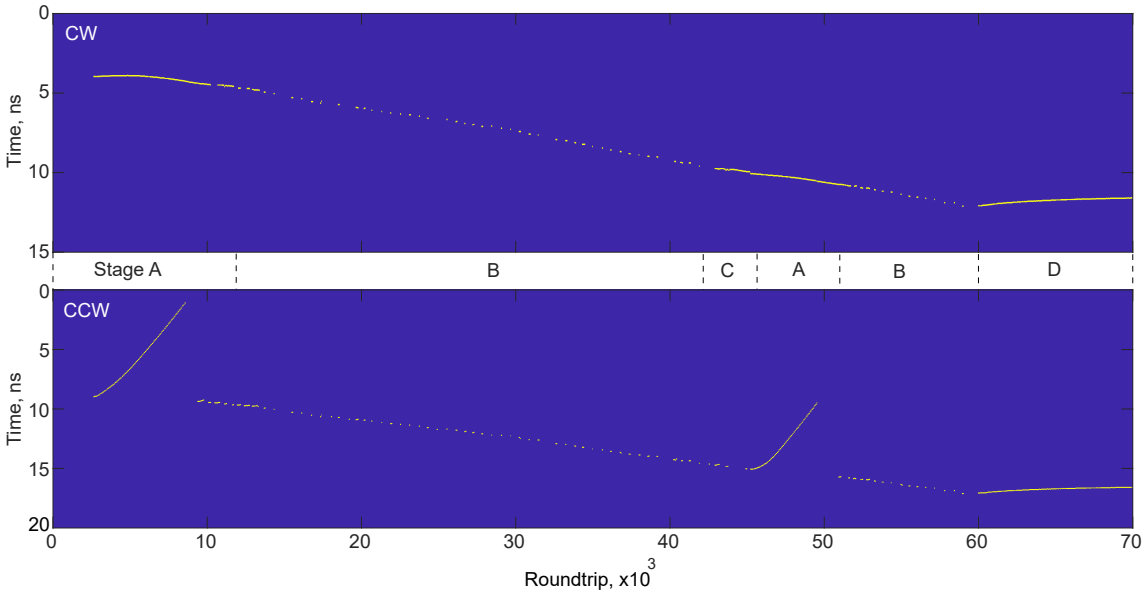

Figure 2.8: Spatio-temporal trajectories of the counter-propagating pulses, where Stage A - Q-switched instabilities, B - formation of soliton complexes and soliton collision, C - soliton spectra blue-shift, D - final formation of stable mode-locked pulses. Top: CW - clockwise direction; Bottom: CCW - counter-clockwise direction.

sequence of events or a single pathway to the stable mode-locking generation. Since no preferred sequence of events has been observed, we divide the entire dynamics into stages which we will discuss separately, indicating their relation to other observed events. Although we presented only one build-up dynamics here that is the most representative, the following analysis and inferences are applicable to observed build-up dynamics in general. More data on the pulse build-up dynamics is presented in *Appendix* B.

Figure 2.8 shows the spatio-temporal trajectories of the counter-propagating pulses. It should be noted that the repetition rates are slightly different during the Q-switched instabilities compared to the mode-locked generation owing to the effect of the nonlinear refractive index and a slight offset of the central wavelength of the Q-switched instabilities. The repetition rates of the counter-propagating pulses have been synchronised except for the stage when the CCW soliton experienced a spectra blue-shift and its spatio-temporal trajectory experienced a strong deviation at 0-10 and 45-50 thousand roundtrips. The time deviation constituted 7.9 and 5.7 ns. The time deviations correspond to the shift of pulse collision point inside the laser cavity by 1.57 and 1.14 meters respectively.

Stage A. Central wavelength drift

We are starting the discussion on the pulse build-up dynamics with the phenomena of the central wavelength drift. We have observed this phenomenon multiple times during the single build-up process. The most sustainable shifts have appeared after the first pulse formation from the intensity spike (3 - 10 thousand roundtrips) and secondly at 45-50 thousand roundtrips. Figure 2.9 shows the second central wavelength shift as it was more

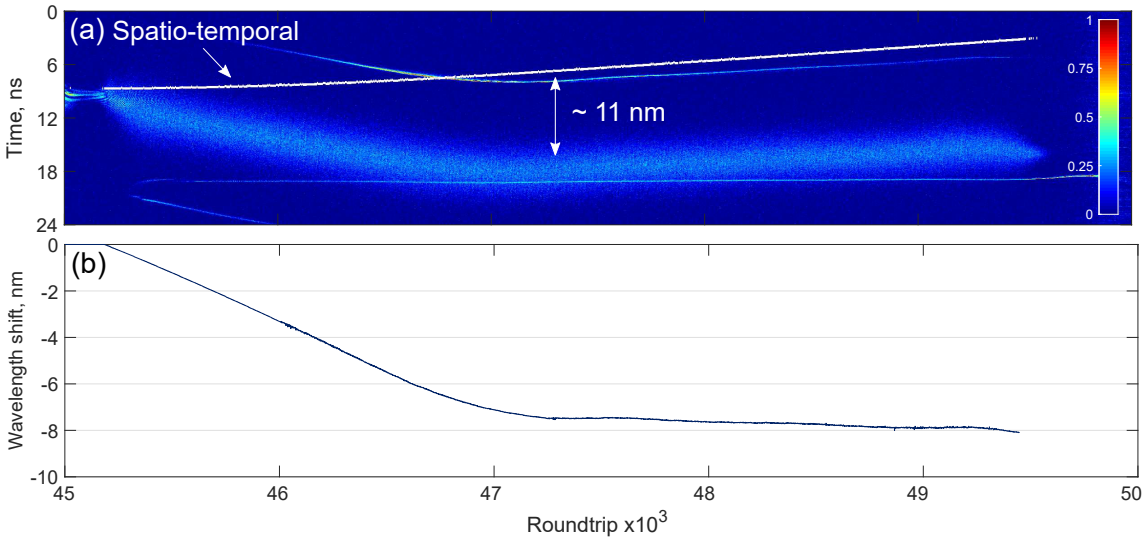

Figure 2.9: Dynamics of the central wavelength in the counter-clockwise (CCW) direction. **(a)** Dispersive Fourier transform (DFT) spectra, where the white line represents the pulse intensity dynamics. **(b)** Real-time central wavelength offset from 1555 nm, defined by the discrepancy between central wavelength of the DFT spectra and spatio-temporal dynamics.

prominent, though the dynamics remains the same. The shift of the central wavelength was occurring only at the early stages of the pulse formation, after the broadening of the seeded instability. Moreover, this dynamics manifested only in the less energetic direction. The measurement technique of the central wavelength, recorded via the DFT is discussed in *Appendix* A and B.1. As can be seen from Fig. 2.9(b) the central wavelength was linearly shifting at a velocity of 0.04 nm per roundtrip. After the pulse was shifted by ∼7.5 nm after the 47 thousand round trip, the velocity of the central wavelength shift slowed down. The total wavelength blue-shift was almost 9 nm, which is significantly higher than was previously demonstrated [172; 229].

Initially, before the occurrence of the soliton blue-shift, the repetition rates in both directions were the same. Therefore, the counter-propagating pulses always collided at the same two points inside the laser cavity. These interaction points can be derived from the knowledge of the time delay between the counter-propagating pulses. By taking these parameters into account, we can conclude that the counter-propagating pulses have interacted in the saturable absorber. The central wavelength drift induces a difference in the repetition rate of the counter-clockwise pulse and, thus, their de-synchronisation (Fig. 2.8). Consequently, the points of soliton collision inside the laser cavity started to move along the laser cavity. From the spatio-temporal dynamics shown in Fig. 2.8, we calculated a total shift of 1.57 m (7.9 ns) and 1.14 m (5.7 ns) from the original interaction point in the saturable absorber before the counter-clockwise pulse disappeared during the first and the second appearance of this effect. When the counter-propagating pulses are not crossing in the real saturable absorber, the colliding mode-locking does not occur and the pulses experience additional losses. Onward, the less energetic pulse is further decreased

in energy and vanished. The following generation in the less energetic direction, obtained after the soliton blue-shift, is occurred at wavelengths close to 1555 nm with synchronised repetition rates and has the collision point in the saturable absorber. This dynamics indicates that colliding mode-locking is a dominant factor over the pulse formation and governs the synchronised regime through the steady-state bidirectional generation.

The lack of simulation models of bidirectional mode-locked lasers does not allow an explicit investigation of the underlying phenomenon of the observed spectral blue-shift of the less energetic pulse. It is known, that interaction of co-propagating solitons or soliton with a co-propagating continuous-wave radiation can lead to the soliton deceleration or acceleration [213; 230; 231]. A similar dynamics could be observed in a counter-propagating collision, however, its manifestation is less pronounced due to smaller interaction length. Our experiments demonstrate that the counter-clockwise soliton experiences acceleration (decrease in cavity round-trip time) during blue-shift in net-anomalous dispersion cavity ($dn/d\omega < 0$), which can be induced by interacting with the counter-propagating soliton and the emitted Dispersive Waves (DWs).

Additionally, the 9-nm-shift in the central wavelength can be caused by the gain saturation [232], and gain competition effects in the Erbium-doped fibre [233]. The effect of the central wavelength shift was accompanied by a loss of the pulse energy, while in the counter-propagating direction the surplus energy accumulated due to the law of total energy conservation (Fig 2.7e). This phenomenon highlights a complex interrelation between energies of the counter-propagating beams that is mediated by the gain saturation and gain dynamics. Additionally, the fact that the soliton shift was always observed only in the less energetic direction indicates that the less energetic direction is more sensitive to soliton perturbation, including central wavelength changes. The central wavelength shift may also result in an inability to maintain the conditions for the NPR effect. All these, accompanied with a higher loss in the saturable absorber due to suppression of the colliding mode-locking, eventually lead to a decrease in the pulse energy and its dissipation and disappearance. The breakup of the pulse after the central wavelength shift induces an excess energy in the counter-propagating direction that was observed to lead to two different scenarios: Stage B – break-up of the more energetic pulse and transition to the generation of Q-switched instabilities or Stage C – formation of multiple solitons.

Stage B. Q-switched instabilities

Stage B featuring Q-switched instabilities, observed after the first breakup of the mode-locking generation at around the 12 thousandth roundtrip. The Q-switched instabilities occurred in both directions and lasted for approximately 40 thousand round trips (2.7 ms) in total. The Q-switch repetition rate was 25 kHz (which corresponds to the repetition period of 40 μs) with a FWHM duration of 4 μs, i.e. approximately equivalent to 60 roundtrips of the steady-state mode-locked regime. Here, the laser is operating in

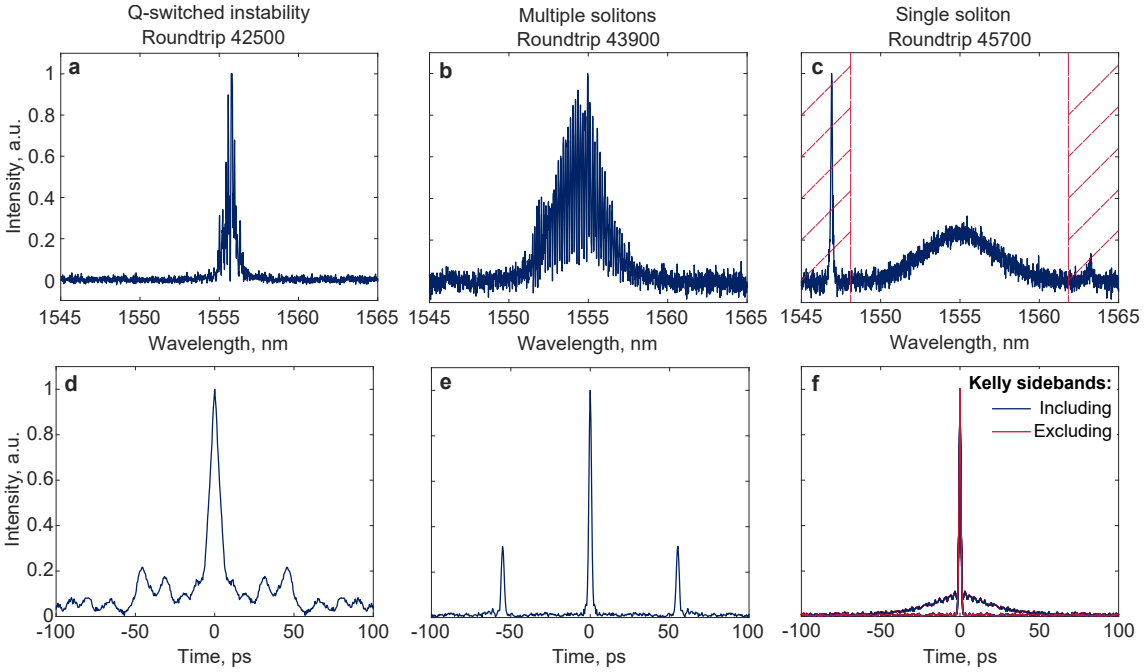

Figure 2.10: Single-shot DFT spectra of typical events during build-up dynamics in the clockwise direction: **(a)** Q-switched instability, **(b)** two solitons and **(c)** single soliton; and **(d-f)** corresponding first-order autocorrelation functions, numerically obtained from the DFT spectra via application of the Wiener-Khinchin theorem. Shaded part in **(c)** presents the zone which we zero-padded to exclude the Kelly sidebands.

the Q-switched mode-locking regime, i.e. the radiation have an intensity envelope of a Q-switched pulse with high peak intensity (5-6 times more intensive than the soliton maximum intensity) and filled with ultrashort pulses [234; 235]. Part of the energy during the Q-switched instabilities was concentrating in a quasi-continuous-wave radiation (usual Q-switched pulse with a duration much longer than the round-trip time) that preceded the localised ultrashort structures (*Appendix* B.2). A typical spectrum of an ultrashort pulse during the Q-switched instability is shown in Fig. 2.10(a). In general, Q-switched instabilities are caused by relaxation oscillations of the gain media and due to the long upper-state lifetime of Er3+ ions in silica fibre [235]. Another mechanism of Q-switched instabilities is referred to the polarisation instability due to desynchronisation of the polarisation states [236; 237]. The occurrence of such instabilities indicates that the laser was operating close to the lasing threshold [238]. Unlike the other work [229], where the transition from Q-switch to mode-locking was achieved by increasing the pump power, the transition dynamics observed here occurred naturally without any further changes in pump power or adjustments of the polarisation controllers. Q-switched instabilities are not a necessary step for obtaining the bidirectional mode-locking operation, but it appears after strong modulation of the background radiation (quasi-continuous-wave radiation) or after the breakup of a quasi-stable mode-locking generation.

Figure 2.11 demonstrates the distribution of the energies of the Q-switched instabilities versus the time interval between pulses. This Figure indicates that Q-switched

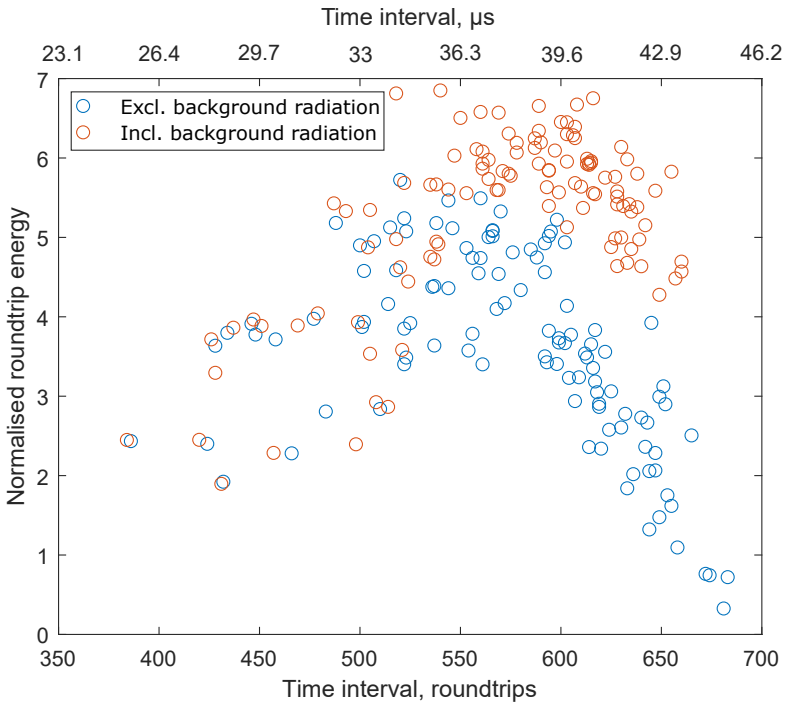

Figure 2.11: Distribution of the energies of Q-switched instabilities versus time interval between them. The errors in the roundtrip energy could arise due to photodiode noises that were much smaller compared to the Q-switched pulse energy and so the errors are too small to be visible on the graph.

pulses with less temporal intervals have less energy due to the limited energy, stored in the active media. The substantial discrepancy between both data at the right-hand side of the figure indicates that the pulses with a longer temporal interval emit more energy as a quasi-continuous-wave radiation. In other words, Q-switched pulses at lower repetition rates tend to emit more energy as a *common* relatively long Q-switched pulse with less localised ultrafast structures. Moreover, the shift into lower time intervals of the Q-switched instabilities with higher energies in a quasi-continuous-wave radiation shows that the quasi-continuous-wave radiation preceded the localised ultrafast structures (Q-switched instability), as shown in *Appendix* B.2. Hence, the localised structures started to form when the long Q-switched pulse reached the threshold of quasi-mode-locking generation.

However, we have not found a relation between the parameters of the Q-switched instabilities prior to the stable pulse formation. In some scenarios, the Q-switched instabilities completely evolve into the quasi-continuous wave operation (usual Q-switched operation without any localized structures at the time scales shorter than the roundtrip time). This generation regime experienced a decline in maximum energy with the growth of the energy contained in the continuous-wave radiation.

Stage C. Formation of soliton complexes

Stage C corresponding to the formation of soliton complexes, observed between 42 and 45 thousand round trips and displayed in Fig. 2.12. A prerequisite for the multi-soliton formation is a presence of an excessive energy in the dominant direction after a Q-switched burst or intensity spike. In contrast, the counter-propagating pulse lacks enough energy for pulse formation, and it disappears shortly after the central wavelength shift. The observed dynamics of soliton complexes is resemble the observations, made in unidirectional lasers [173], but the underlying principles are different.

For a closer look at the pulse characteristics, we exploit the Wiener-Khinchin theorem and calculated the round-trip-resolved field autocorrelation function from the inverse Fourier transform of the single-shot spectra measured by the DFT technique [188; 190; 227]. Figures 2.10(a-c) and (d-f) present the real-time spectra of Q-switched instability, bound solitons, single soliton and corresponding ACFs, respectively. Although the real-time field autocorrelation is not sensitive to the spectral phase, it presents the overall dynamics of energy distribution and relative phases. This technique can be used with a high degree of accuracy for almost bandwidth-limited pulses (Time-Bandwidth Product: 0.37 for CW, 0.335 for counter-clockwise [5], and 0.315 for fundamental solitons). Note, that the FWHM of the field ACF is 2.5 times broader than the actual pulse duration for soliton-shape pulses, which provides appropriate accuracy in order to investigate pulse-to-pulse dynamics. The ACFs for the multi-soliton case (Fig. 2.10b, e) are seen to be significantly different from the single-soliton case, exemplify that the single-shot spectra can provide information about the internal pulse temporal structure and the relative phase of the pulse complexes that remains unresolved in the intensity domain measurements [182]. Figures 2.12(a, b) show the spectral evolution and the round-trip resolved ACF between 42-45 thousand round trips, respectively. These dynamics clearly show a formation of multi-soliton structures at different stages. Figure 2.12 presents the analysis only of the clockwise pulse, as the counter-clockwise pulse was highly attenuated at these round-trips (Fig. 2.7(a, e)). The observed high-contrast spectral modulation further confirms a good pulse coherence of the multi-soliton complexes (Fig. 2.10b).

Localisation parameter. From Parseval's theorem by integrating the single-shot spectra from the DFT measurements, one can obtain the data on the pulse energy variation per roundtrip. To confirm the formation of stable solitons and the establishment of the steady-state mode-locking, it is important to analyse how this energy is distributed across the round-trip span and how much of it is contained in the main pulse. To this end, we define a localisation parameter L as:

$$L = \frac{ACF(\tau = 0) \cdot t_{res}}{\int\limits_{-\tau_{max}}^{\tau_{max}} ACF(\tau) d\tau} \tag{2.2}$$

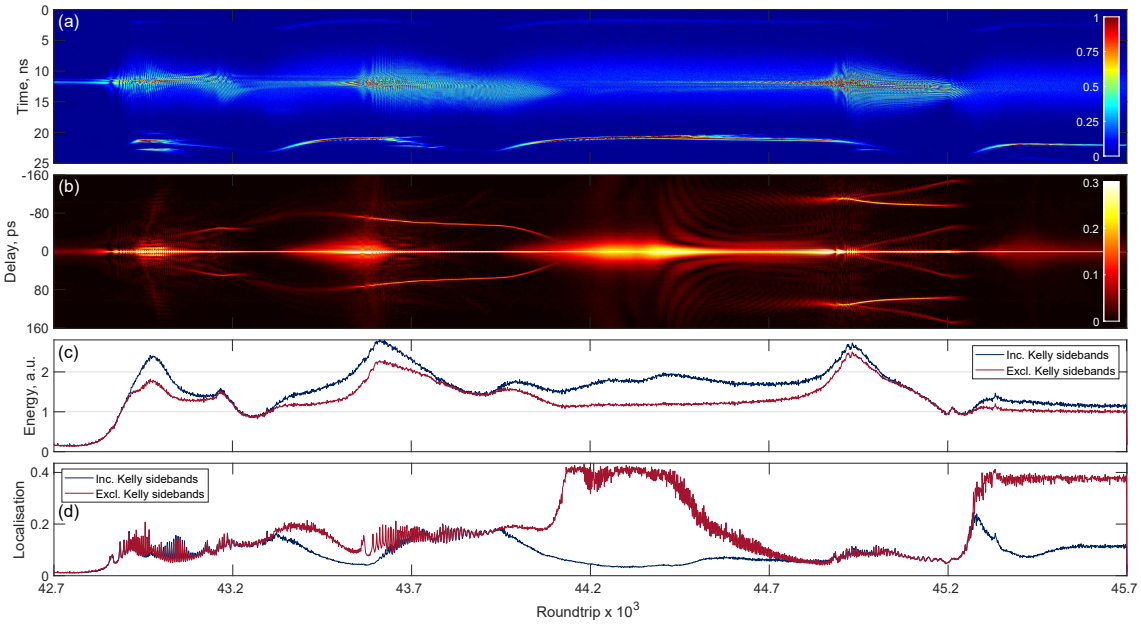

Figure 2.12: Formation and internal dynamics of soliton complexes in the clockwise direction. **(a)** Dispersion Fourier Transform spectra and **(b)** the corresponding first-order autocorrelation function. **(c)** Shot-to-shot variation of the pulse energy normalised to the singe-soliton energy in the steady-state, and **(d)** evolution of the localisation parameter. The grey lines show the pulse energy and the localisation parameter for mode-locking operation in the steady-state.

where

$$ACF(\tau) = \int_{-T/2}^{T/2} E(t) \cdot E(t+\tau)dt \tag{2.3}$$

and as follows from Fubini's theorem:

$$\int_{-\tau_{max}}^{\tau_{max}} ACF(\tau)d\tau = \int_{-T/2}^{T/2} E(t)dt \cdot \int_{-T/2}^{T/2} E(t)dt = (\int_{-T/2}^{T/2} E(t)dt)^2 \tag{2.4}$$

here, E is the pulse electric field, t is the time, τ is the ACF time delay and T is the round trip time, t_{res} and τ_{max} is the ACF temporal resolution and the maximum time delay, correspondingly. By the definition, the ACF at $\tau = 0$ (the overlap of the pulse intensity profiles) is calculated as $ACF(\tau = 0) = \int_{-T/2}^{T/2} |E(t)|^2 dt$ and represents the energy per round trip (see Fig. 2.12c). Thus, the localisation parameter is less or equal to 1.

The calculated localisation parameter for each round trip is depicted in Fig. 2.12(d). L equals unity only when all the energy per round trip is concentrated in the temporal duration, shorter than the temporal resolution of the ACF, and approaches zero if all the energy is equally distributed over time during a roundtrip. In other words, such a parameter shows the extent to which the energy is accumulated at one specific point in time. This parameter is normalised and does not depend on the pulse intensity but its duration or shape. Thus, the theoretical value of the localisation parameter L for a $sech^2$-

shaped pulses for a given ACF resolution and the pulse duration is 0.4. This parameter helps for further analyse of the pulse dynamics and the energy distribution during complex multi-structured pulses.

Additionally, in the formation of bound states of multiple solitons a dispersive wave radiation plays a crucial role [239] by providing attractive or repulsive forces between neighbouring solitons [240; 241; 242]. In mode-locked lasers, these waves manifest in the form of the Kelly spectral sidebands [124]. Here, we use the real-time DFT spectra and the ACF to investigate the role of the Kelly sidebands in the formation of soliton complexes. We calculated the round-trip resolved pulse energies and the localisation parameter L for two cases – when we include the Kelly sidebands in the calculation and when we excluded them. To exclude the Kelly sidebands from the calculation without influence on the ACF time span or the resolution, we zero-padded them in the DFT data (Fig. 2.10(c)). In the spatial domain, Kelly sidebands appear as quasi-continuous-waves beside the main pulses (Fig. 2.10(f)). So, the energy variation of Kelly sidebands could be retrieved by the difference of graphs in Fig. 2.12(c). *Appendix* B.3 presents the calculated first-order ACF for the case when we excluded Kelly sidebands from our calculations.

Firstly, we calculated the localisation parameter and the pulse energy corresponding to the mode-locking operation in the steady-state, which are shown by the grey lines in Fig. 2.12(c, d). When the contribution of the Kelly sidebands was removed, the observed localisation parameter L for the stable mode-locked pulses was close to the theoretical value of 0.4. Generally, the value of the localisation parameter drops significantly if we include Kelly sidebands into the calculations due to the non-localised nature of the dispersive waves. Certain roundtrips demonstrate the agreement of the values of the localisation factor L when they have been estimated with or without consideration of the Kelly sidebands. Such dynamics was observed in two cases: when the localisation of the pulse itself is low and matches the L value of the sidebands or when the energy of Kelly sidebands is negligible compared to the pulse energy and does not significantly affect the L value.

The ACF in Fig. 2.12(b) shows a tendency to form a multi-pulse structure in the clockwise direction. Unidirectional generation of multiple pulses arises due to uneven distribution of energies between opposite directions, *i.e.* when the majority of the intracavity energy is concentrated in one direction. Such a presence of the excess energy, after the Q-switched instability or intensity spike, tends to operate in the multi-soliton regime due to the soliton energy quantisation effect [243; 244]. The soliton energy quantisation effect dictates that the multiple solitons could be formed when the intracavity energy exceeds the energy of the fundamental soliton, which is limited by the soliton area theorem. *Appendix* B.4 shows that a stable bidirectional mode-locked operation can be achieved after the multi-soliton stage if the energy is more evenly reallocated between both directions.

Another dynamics we have observed during the generation of multiple solitons is the emission of the dispersion waves with increased energy. Ref. [245] theoretically demonstrated that collisions of co-propagating solitons can induce a generation of extremely

energetic DWs, similar to what we have observed experimentally here in the real-time time scale. Each time prior to the formation of the multi-soliton complexes, the total energy and energy in Kelly sidebands had substantially increased. At roundtrip numbers near 43.5 thousand, we observed a two-soliton complex, with a decreasing inter-soliton separation over the propagation due to the unbalanced attraction forces caused by the dispersive waves, until they collide. After the pulse collision, the energy localised in the Kelly sidebands increased more than 6 times and almost reached the level of the single soliton pulse energy. At the same time, the soliton energy at these round-trips was increased by 15% with a corresponding compression of the pulse duration by ∼8%. The reduction in pulse duration has been also confirmed by the higher localisation values and is in agreement with the soliton area theorem. In other words, the collision of two co-propagating solitons results in the production of one more energetic soliton of a shorter duration with an extra emission of the dispersive waves. A similar dynamics recorded via the DFT technique have been also demonstrated in Ref. [242].

During these round-trips, we had also noticed a higher background radiation which confirms the increased energy of the dispersive waves. After that, starting from 44.4 thousand round trip, the energy of the main pulse continued to rise, while the localisation started decreasing due to the formation of satellite sub-peaks. After 400 round-trips, when the total energy significantly increased, intensity spikes evolved into a pulse with further splitting into a 1+2 soliton complex, similar to the one if Ref. [182]. These dynamics emerge due to the presence of excess energy and soliton energy quantisation effect, theoretically described in Ref. [243; 244]. The amplitude ratio of solitons in the complex is 4:4:1 with a time separation of 52 ps and 42 ps. The soliton complex experiences a reduction in the energy and decays at the 45200 roundtrip. Right after that, we observe quasi-stable single-soliton generation with an intrinsic sharp increase of the localisation parameter.

Soliton breakup and transition from mode-locking to Q-switched instabilities

Alongside with the interest to the soliton formation, the conception of circumstances when the mode-locking generation experiences perturbations and evolves into instability operation also gains much interest. In Ref [246] Authors have been shown that the instability during soliton propagation can be induced by the continuous-wave radiation. Here we show the experimental result of soliton breakup and transition dynamics into Q-switched instabilities in the presence of an energetic dispersive waves. This transition has been observed two times (8 - 11 and 49 - 52 thousand roundtrips) after the soliton central wavelength shift and decaying of the CCW pulse in both cases. Here we will describe only the second occurrence due to the more pronounced dynamics.

Figures 2.13(a, b) demonstrate the DFT and the corresponding ACF traces during the pulse break-up. Figures 2.13(c, d) provide the dynamics of the pulse energy and the

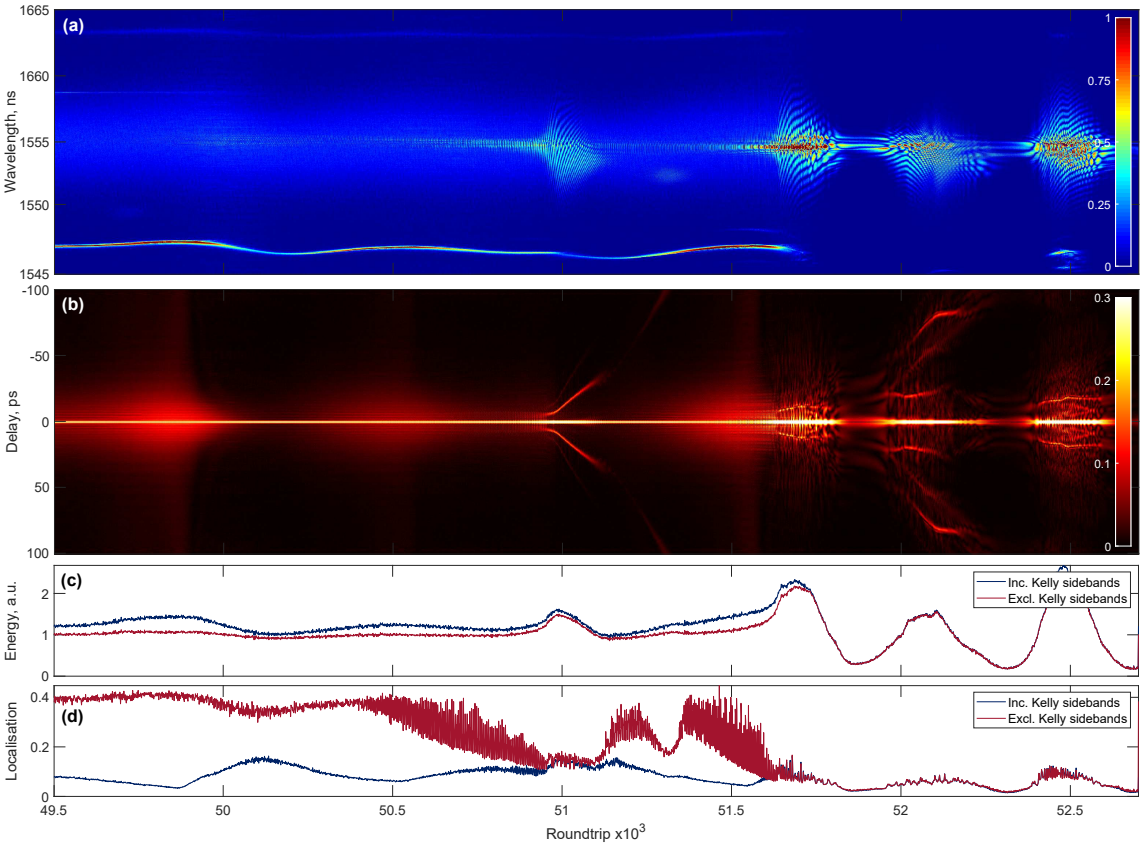

Figure 2.13: Formation and internal dynamics of the soliton break-up in the clockwise direction. **(a)** Real-time DFT measurements, **(b)** the corresponding field ACF, **(c)** the pulse energy and **(d)** the localisation parameter of transition from mode-locked generation to Q-switched instabilities.

localisation parameter for two cases: when we take into account Kelly sidebands and when we exclude the Kelly sidebands from the calculations. The pulse instability appeared in a periodic modulation of the energy of dispersive waves after the CCW pulse disappeared, which induced a perturbation of energy in the CW direction. The first fluctuations arise at roundtrips between 49500 and 50000 when the energy of the Kelly sidebands increases two times and consistently dropped almost to zero. These fluctuations affect the pulse energy, which also experienced a decrease in energy by 10%. The localisation parameter drops after the first energy fluctuation, indicating an increase in the pulse duration. After 500 more roundtrips, the sideband energy rose again with a downward trend of the localisation value with modulation of 5 roundtrips which was caused by beating dynamics between the main pulse and newly-formed sub-peaks. The low value of the localisation parameter and the modulated spectrum clearly evidence about the multi-soliton formation, which is resolved in the ACF, where a born of a new pulse from the intensity spikes is shown. After the 51.5 thousandth roundtrip, the pulse emitted additional dispersive waves and eventually evolves into a multi-structured Q-switched mode-locked pulse. Note, when the pulse energy after modulation instability reaches the single soliton energy level, further recession in the pulse energy below this level will undoubtedly result in a translation into

Q-switched instability.

By analysing the real-time soliton dynamics, we can confirm that the energy of the surrounding quasi-continuous waves emitted by the soliton as the dispersive waves can induce instabilities into the soliton propagation. Since the Kelly sidebands are related to the gain and the losses, experienced by the soliton during one roundtrip across the laser cavity, the increase of their energy relates to a violation of the gain-loss equilibrium of the soliton. The gain-loss conditions could be caused by the annihilation of the counter-propagated pulse, which provides more energy and the higher gain in the CW direction, however, due to the soliton are theorem, this additional energy could not be accumulated by the single soliton, inducing multi-pulse generation. Moreover, the annihilation of the CCW pulse induced more losses in the CW direction, caused by the threshold of the saturable absorber according to the colliding mode-locking. The modulation frequency of the amplification of the dispersive waves is closed to the repetition frequency of the Q-switched instability (25 kHz), indicating the influence of the relaxation dynamics of the active media on the generated pulse. This dynamics highlight the significance of the colliding mode-locking on the pulse dynamics, the dependence of the CW pulse on the counter-propagating pulse, and that the pulse break-up dynamics, similar to the pulse formation, can also experience the multi-soliton stage and excess emission of dispersive waves.

Stage D. Final formation and propagation dynamics of the stable bidirectional soliton generation.

Now we consider the final formation of the counter-propagating mode-locked pulses from the Q-switched generation and its further propagation. Since at this stage both pulses have experienced dynamics with common features, we show the single-shot spectra (Fig 2.14(a)) and ACF (Fig 2.14(b)) evolution only for the clockwise pulse (see *Appendix* B.5 for the counter-clockwise pulse). At first, the localisation parameter slightly increased during the preceding QML pulse with intense continuous-wave radiation and was maintained at the same level due to the presence of a low-intensity broad residual pulse. A picosecond pulse originated from the Q-switched instability and continued to propagate further, seeding the mode-locking generation. Pulses in both directions originated from the residual picosecond pulses after the following increase of the energy due to the relaxation oscillations of the active media. The pulses further evolved through the modulation instability with further spectral broadening and a sharp increase of the localisation. Similar build-up dynamics were observed in Ref. [247], where the soliton was formed from subnanosecond intensity spikes on the usual Q-switched envelope via the spectral broadening and beating dynamics. Onward, both pulses experienced a strong beating pattern due to the interference between the main pulse and the moving aside subordinate intensity spikes (Fig 2.14(b)), which were induced by the nonlinear refractive index and the intracavity dispersion [247], similar to

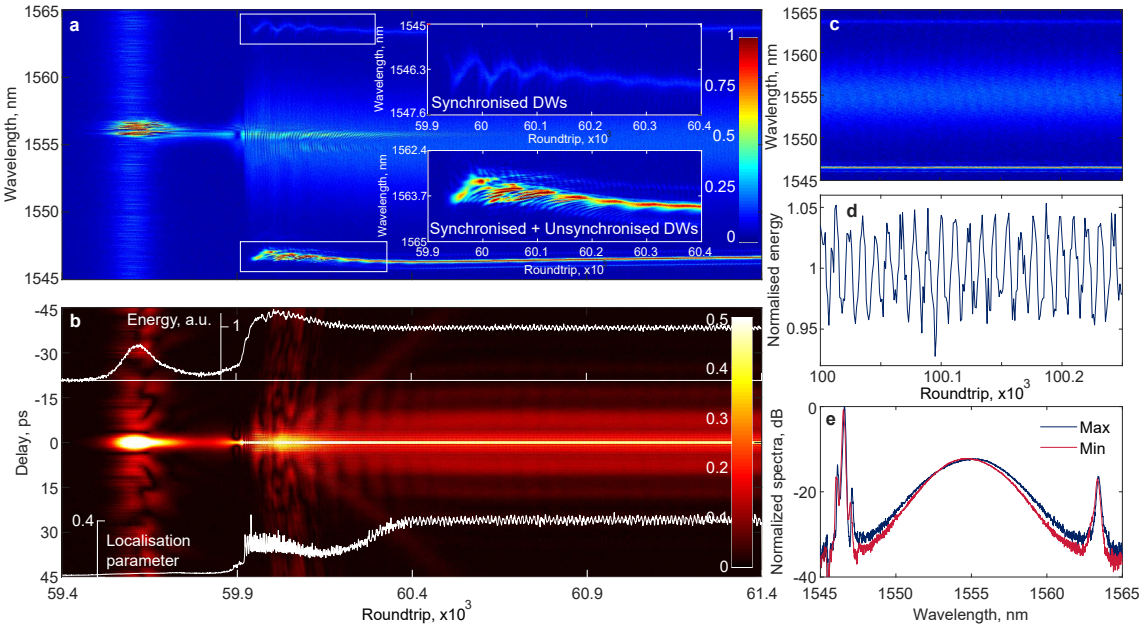

Figure 2.14: Final formation and propagation of the steady mode-locked pulse in the clockwise direction. **(a)** Dispersion Fourier transform spectra and **(b)** the corresponding first-order autocorrelation function during the transition from Q-switched instability into the mode-locked generation. Insets: **(a)** formation of synchronised and unsynchronised dispersive waves, **b** the pulse energy and the localisation parameter, superimposed on the evolution of autocorrelation function over round trips. **(c)** spectra pulsation during stable pulse generation with corresponding energy oscillation in **(d)**. **(e)** Spectra of pulses corresponding to the maximum and the minimum energies.

the previously shown results. The beating dynamics inherit a different time period in opposite directions. Strong oscillations near the main pulse at the ACF are related to the co-propagating dispersive waves. Similar to other results on pulse build-up dynamics [173; 227; 248] and our previous results, we also observed the generation of satellite pulse with more than 10 times lower intensity.

Dissimilar to all previous works, here, at the early stage of the formation of the ultra-short pulses we experimentally observed synchronised and unsynchronised resonant DWs (see insets in Fig. 2.14(a)) [226]. The synchronised and unsynchronised resonant DWs were only recently theoretically predicted and could not be experimentally observed by using traditional spectral measurements. Thus, by using the DFT technique we detected the synchronised and unsynchronised resonant DWs for the first time to the best of our knowledge. As we discuss earlier, solitons emit dispersive waves due to periodic gain and losses inside the laser cavity [124]. Due to the wavelength oscillations during the pulse formation, synchronised dispersive waves repeat the behaviour of the soliton spectra to maintain the phase-matching conditions with the soliton. At the same time, the dynamics of the unsynchronised dispersive waves differ from the oscillation of the central wavelength of the pulse, which prevents the phase-matching conditions [226]. Insets in Fig. 2.14(a) clearly show the synchronisation between the pulse spectra oscillations and the emitted dispersive waves at longer wavelengths, while at shorter wavelengths the dispersive waves

exhibit complex dynamics different from the spectra oscillation. Such dynamics confirm the generation of the predicted unsynchronised dispersive waves. During the pulse formation and further stable propagation, we have observed the central wavelength oscillations. At the same time, the Kelly sidebands continued to propagate undisturbed, and only a minor amount of energy is traveling between multiple-structured Kelly sidebands. The generation of unsynchronised resonant dispersive waves was observed on both edges of the short-wavelength Kelly sideband with a separation of 60 GHz (0.5 nm). As seen in Fig. 2.14(a), unsynchronised dispersive waves have been formed during strong spectra oscillation at the early stage of the soliton formation and continue to propagate further. The energy dissipation from the main pulse, related to the generation of strong unsynchronised dispersive waves, can be seen in the ACF.

This behaviour of unsynchronised dispersive waves agrees with theoretical predictions, described in Ref. [226]. In this work, the unsynchronised dispersive waves were observed only at the short-wavelength side. At the same time, the Kelly sidebands at the longer wavelength had a lower intensity, which may refer to the gain spectrum of the Erbium-doped fibre and the third-order dispersion. The complex multiple-spike structure of the dispersive waves was also detected by an optical spectrum analyser, as depicted in Fig. 2.7(f). In this laser setup, unsynchronised resonant dispersive waves were only observed when the build-up dynamics experienced strong instabilities at the certain alignment of the polarisation controllers, and when the energy of Kelly sidebands was extremely high. When pulses undergo through simpler build-up dynamics, discussed in *Section* 2.2.2, no unsynchronised resonant dispersive waves were observed. The results presented here indicate that unsynchronised resonant dispersive waves are dependent on the initial conditions of the pulse formation. Additionally, since the emitted unsynchronised dispersive waves propagate separately from the pulse, they do not satisfy phase-matched conditions, and, thus, requiring higher energy and gain compared to the synchronised dispersive waves.

Figure 2.14(c) shows the DFT spectra obtained when the laser operates in the stable state. The measured DFT spectra demonstrate weak spectral pulsations in the clockwise direction. Concisely, the pulse dynamics in the more energetic clockwise direction during the stable propagation is as follows: the energetic pulse is getting spectrally more narrow while moving to the shorter wavelengths by 0.5 nm with a 10%-decrease in energy, next the process reverses and repeats periodically within 11 round trips (Fig. 2.14(e, d)). According to the soliton area theorem, this leads to the pulse duration oscillations, which are well observed in the ACF and the localisation evolution (Fig. 2.14(b)). The oscillation range of the central wavelength has matched the spectral separation between multiple-structured Kelly sidebands so that the soliton is able to maintain the phase-matched condition with complex sidebands.

Soliton pulsations have been theoretically observed for many operation regimes [249; 250] and have been recently experimentally revealed with the help of the DFT technique [251; 252]. These soliton pulsations are related to the period-doubling bifurcations

at specific values of the system [253]. They indicate that the soliton has a strange attractor and cannot be reproduced by one cavity bypass [254]. Importantly, no pulsations were observed for a bidirectional generation with different pulse repetitions rates in counter-propagating directions [255]. The fact that switching between generation regimes with equal and different pulse repetitions rates is achieved by adjusting the polarisation controllers suggests that the bifurcation points arise at a particular intracavity polarisation state. So, the soliton pulsations could arise to maintain the synchronisation of the counter-propagating pulses. The synchronisation of the repetition rates of counter-propagating solitons was also observed in other non-linear systems such as microresonators [256].

By analysing dozens of build-up dynamics, we have concluded that the energy allocation between opposite directions is the key factor rather than the localisation parameter for the formation of a stable bidirectional mode-locking generation. If the energy in the dominating direction does not drop by more than 10% after the Q-switched pulse or intensity spike, it will lead to the multi-soliton formation in the dominating direction and the annihilation of the pulse in the less energetic direction (*Appendix* B.4). This means that the stable bidirectional mode-locking is more reliant on the energy distribution between counter-propagating channels rather than on the initial pulse shape. Moreover, counter-propagating pulses eventually evolve into almost identical stable states, even if the preceding dynamics is particularly different.

Cross-correlation of counter-propagating solitons

To reveal the differences in the build-up dynamics between the counter-propagating beams, we provide a cross-correlation analysis of the counter-propagating pulse spectra during the final pulse formation. Clearly, a better understanding can be obtained with more robust numerical solutions. However, the cross-correlation analysis can help to indicate the dependency between counter-propagating pulses and periodic patterns, governed by the intracavity dynamics.

To estimate the degree of the similarity we calculated the cross-correlation of their spectra and show it in Fig. 2.15. The cross-correlation has been calculated only for 59.7 - 61 thousand roundtrips since at the earlier roundtrips the cross-correlation does not provide a substantial information due to the very narrow spectra and uniqueness of the Q-switched pulses. The cross-correlation was calculated as:

$$CC(T_{CW}, T_{CCW}) = \frac{[\int I_{CW}(\lambda, T_{CW}) \cdot I_{CCW}(\lambda, T_{CCW}) d\lambda]^2}{\int [I_{CW}(\lambda, T_{CW})]^2 d\lambda \cdot \int [I_{CCW}(\lambda, T_{CCW})]^2 d\lambda} \tag{2.5}$$

where CC is the cross-correlation value, T_{CW} and T_{CCW} is the roundtrip number of the CW and the CCW pulse respectively, and λ is the wavelength. We want to note that the cross-correlation value is normalised, thus it does not depend on the spectra amplitude but on its shape and the central wavelength.

After 400 roundtrips, when both counter-propagated pulses spectrally broadened, the

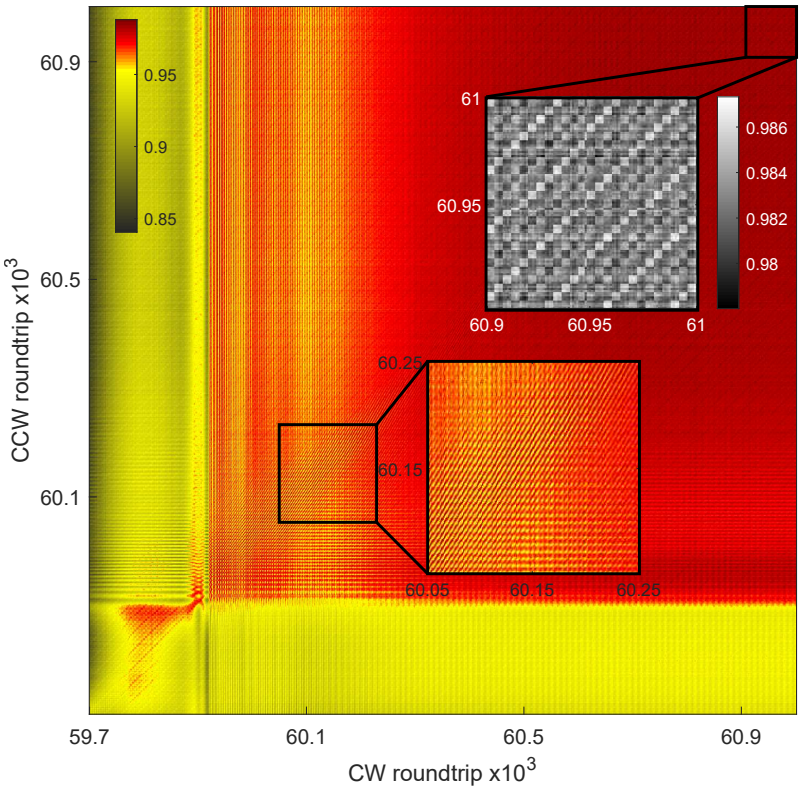

Figure 2.15: The spectral cross-correlation of the counter-propagating pulses.

cross-correlation increased to 98% and shown a high degree of similarity between the pulse spectra. A yellow frame located at the south and the west refers to the correlation between the pulse at the early stage of formation (modulation instability) and the counter-propagated pulse spectra at different stages of the pulse formation, from modulation instability to the stable soliton propagation. This part contains a relatively low correlation value due to the narrow spectra of the relatively long seed pulse. In the same segment of the cross-correlation map, we observed a periodicity of 11 roundtrips. This behavior evidences the pulse spectral pulsation and the beating dynamics [190]. During the pulse broadening (59.9 thousand round trip) we also observed a modulation of a few roundtrips. After 200 roundtrips the pulsation in CCW direction have disappeared and no pulsations were observed in this direction in the steady state. The spectral pulsation appeared in the CCW direction even in the steady state of the mode-locked operation with a period of 11 roundtrips. This dynamics reveals the behavior of the pulse periodicity before coming to the stable bidirectional mode-locking generation.

Another short-term periodicity of 5-7 roundtrips was revealed at the early stage of the pulse formation dynamics right after the pulse spectral broadening at 59.9 thousandth roundtrip. The highest correlation of 0.96 was observed for a roundtrip difference of ± 50. The modulation depth of such periodic pattern was 6.3%. Notably, that the periodic pattern has a slope α of 57.3 degrees. Slopes that differ to 45 degrees mean that spectrum of the CW pulse at the roundtrip of T_{CW} does not have the highest correlation with counter-propagating spectra at the same roundtrip, but correlates with the counter-propagated

pulse at a shifted roundtrip. This pattern indicates that both counter-propagated pulses have experienced similar periodical dynamics with different periods. This is a particular case during the beating and breathing dynamics, which was observed at these roundtrips. This periodicity lasted for 400 roundtrips with a further increase of the cross-correlation to the higher values.

The longest time period we observed from the cross-correlation analysis is 28 roundtrips or 1.9 μs (grey inset in Fig. 2.15). Such a relatively long time can refer to the active fibre dynamics such as the pump level decay time (10 μs [257]) or the laser diode instabilities. Interestingly, that the maximum of the cross-correlation is shifted and achieved when T_{CW} is not equal to T_{CCW} with a slope of 45 degrees.

In general, the correlation pattern is not symmetric over the line $T_{CW} = T_{CCW}$ which emphasizes the different build-up processes of the counter-propagated pulses in the bidirectional mode-locked laser.

Summary

Here we have demonstrated the complex switch-on dynamics experienced by unsynchronised counter-propagating ultrashort pulses during formation in the fibre cavity. Generally, the counter-propagating pulses experienced different build-up dynamics, while their mutual interactions in the fibre laser allowed the formation of eventually almost identical solitons. After 70 thousand round trips from the first intensity spike observed, a stable bidirectional mode-locked generation, evolving from Q-switched instabilities, has been achieved. The obtained bidirectional mode-locked generation was stable and inherit exactly matched repetition rates in opposite directions for several hours.

The demonstrated formation dynamics is rich with phenomena and nonlinear processes, which make it stand out when compared to the earlier demonstrated evolution in uni- and bidirectional mode-locked lasers. The demonstrated dynamics highlight the interconnection between both directions. Owing to the colliding mode-locking, the pulses have always originated with the collision point in the saturable absorber that allows saturation at lower intensities. In this work, we have also indicated the interrelation and underlying dynamics between different stages. We have revealed that the complex interchange of the intracavity energy between counter-propagating beams, mediated by the active media, plays a vital role in the formation of the stable bidirectional mode-locked generation. This is similar to the results presented in Ref. [229] where Authors indicated the role of the energy distribution after the Q-switched pulse on the generation regime in a unidirectional laser. While our results revealed that the deflections in the energy allocation lead to different discussed stages such as quasi-stable pulse formation with a following shift in the central wavelength or unidirectional multi-soliton formation in the dominated direction. Additional dynamics, presented in *Appendix* B, feature similar stages and confirm the repeatability of the observations, albeit their sequence and duration may substantially vary

each time we switched on the pump power. Such behaviour indicates that the complex dynamics arise due to the sophisticated operation regime that depends on a variety of underlying conditions.

To analyse the similarities between the spectra of the counter-propagating pulses we provided the cross-correlation analysis. The cross-correlation analysis reveals complex periodic processes at different stages of the pulse formation between both pulses, ranging from a few to 30 roundtrips, emphasizing varying dynamics at different stages. In addition, this analysis helped to understand the formation of spectral pulsation of the solitons.

We also introduced a new evaluation parameter for numerical estimation of the energy localisation for roundtrip-resolved measurements. The localisation parameter provides the basis for comprehensive analysis of the role of dispersive waves on pulse break-up and the multi-soliton complexes formation and their interactions. We provided a method for the absolute pulse-to-pulse measurements of the deviation in the central wavelength and have shown a pronounced blue-shift of the central wavelength. Moreover, these results experimentally reveal the existence of synchronised and unsynchronised dispersion waves and show their origination from complex pulse spectra behaviour. While numerical simulations of bidirectional mode-locked lasers are complicated, we believe that such simulations can be supported by experimental observations obtained via the presented real-time measurements. Together numerical and experimental studies can help to reveal the true nature of the underlying mechanisms giving rise to the observed phenomena like the wavelength drifts, or even pulse formation from Q-switched instabilities. Compared to the previous studies of bidirectional generations in fibre cavities, we have investigated conventional solitons in the all-fibre anomalous-net dispersion cavity in details, featuring more complex dynamics. These observations open up a great avenue towards versatile manipulation of the nonlinear soliton dynamics. We believe the obtained results would constitute a basis for the further investigations of the counter-propagating soliton dynamics and their interactions in complex systems and the role of the emitted dispersive waves and the Q-switched instabilities on mode-locking generation. At last but not least, these results are significant for further practical applications of fibre lasers with colliding mode-locking such as dual-comb spectroscopy and gyroscopic measurements.

2.3 Gyroscopic Measurements

2.3.1 Historical perspective

The interest in using the mode-locked laser for measurements of angular velocity originated from the work in 1989 by Chesnoy, who numerically demonstrated that the lock-in effect could be mitigated by using ultrashort pulses [258]. Indeed, ultrashort pulses feature small spatial length ($\sim$0.3μm per fs in vacuum) and interact apace only in two points inside the closed-loop. Moreover, in mode-locked lasers, the low-intensity back-scattered light would

be further attenuated in the intensity-selective element such as a saturable absorber. Thus, the implementation of the gyroscopic measurements in mode-locked lasers is less subjected to the lock-in synchronisation.

The first gyro-type response in a bidirectional mode-locked dye laser was demonstrated in 1990 [259]. Two years later in 1992, *Gnass et. al.* presented the first genuine measurements of the Sagnac effect in a bidirectional laser [260]. Both works indicated a significantly reduced lock-in effect, which provided a new avenue for gyroscopic measurements. Although the focus of the thesis is concentrated on the gyroscopic measurements in mode-locked fibre lasers, we would like to note that modern bidirectional mode-locked bulk lasers have the potential to provide the gyroscopic resolution of 10^{-5}deg/s [25].

In a mode-locked fibre laser, the first experimental results on gyroscopic measurements have been presented in the NOLM-cavity configuration in 1993 [261]. The laser cavity comprised Neodymium-doped double-clad fibre, pumped with a diode array. The Sagnac loop mirror had a length of 600 m, coiled in a spool with a radius of 8 cm. To achieve mode-locking generation Authors used an active technique, based on the phase modulator. By measuring the temporal separation between the output pulses, the Sagnac effect has been evaluated. In addition, the Authors demonstrated that the Sagnac effect could be further enhanced by controlling the amplitude of the phase modulator. Later, the same group has reported an advanced noise performance, decreasing the ARW down to 0.06 deg/$\sqrt{h}$ by inserting an intracavity polariser and exploiting polarisation-maintaining fibre [262]. Importantly, in Ref. [263] Authors demonstrated gyroscopic measurements of dynamic rotation input. Moreover, they improve the long-term stability of the bias instability down to 20 deg/h by implementing a lock-in amplifier in the laser system. Here, we would like to note that although the gyroscopic measurements were provided inside the laser cavity, the Sagnac effect was not accumulated through consecutive roundtrips, which makes this approach similar to the passive gyroscope and significantly limits the overall gyroscope capabilities.

Later, *Braga et al.* presented beat-note measurements in a bidirectional mode-locked fibre laser [208]. Although the response of the beat-note was not associated with the Sagnac effect, the phase shift similar to the one experienced by laser beams under rotation exposure on the laser platform was induced by the intracavity phase modulator. In this work, the mode-locked mechanism was based on the NPR effect, combined with two amplitude modulators. The intracavity modulators were acting as temporal gates and allowed to control the repetition rates and the crossing point of the counter-propagating beams inside the laser cavity, which is essential for mitigation of the synchronisation between them. Moreover, both modulators provided an efficient feedback for stabilisation of the repetition rate and, as a consequence, reduce the bias instability.

As was mentioned before, while the gyroscope is at rest, the beat-note frequency between the counter-propagating pulses refers to the difference of the corresponding Carrier-Envelope Offset (CEO) frequencies [161]. This *'rest'* beat-note (at zero rotation) can

be finely tuned by managing polarisation controllers and varying the pump power. This feature allows to completely eliminate the lock-in effect by setting the rest beat-note sufficiently apart.

The first genuine measurements of the Sagnac frequency via ultrafast fibre laser were reported by *Krylov et al.* in 2017 [214]. The laser gyroscope setup was built in a ring configuration shown in Fig. 2.1(d). The laser gyroscope presented as a single fibre coil with a diameter of ∼1 m and a total area of 0.79 m^2. An external delay line with a fine tuning has been used to overlap the pulses in the temporal domain. The 'rest' beat-note frequency was set to 1.61 MHz with the SNR of ∼30 dB. The Sagnac frequency response demonstrated a linear relation to the applied rotation velocity with a scale factor of 7 kHz/(deg/s), which was in good agreement with the Sagnac equation 1.8. The resolution was estimated based on the bias frequency drift and constituted 0.01 deg/s. This work has demonstrated that traditional technique for measurements of the Sagnac effect could be efficiently applied in mode-locked fibre lasers. However, the Authors noted a high sensitivity of the Sagnac frequency to the relative CEO frequency, which has a deleterious effect on the bias instability, since the CEO frequency tends to rapidly fluctuate. The CEO frequency could be independently measured by the $f-2f$ interferometer and be efficiently stabilised. Moreover, as was discussed in *Chapter 1.5.2*, the stability of the CEO frequency could be increased by constructing the laser cavity with close-to-zero net cavity dispersion with the generation of the dispersion-managed solitons [120]. Nonetheless, an efficient and simultaneous stabilisation of the counter-propagating pulses in such a cavity setup for gyroscopic measurements could be very sophisticated.

In 2019 *Zhang et al.* proposed to use another ultrafast generation regime known as 'dark' solitons for measurements of the angular rotation based on the beat-note methodology [264]. The dark solitons are contrary to *'bright'* pulses and manifest as a train of ultrashort dips in a continuous-wave radiation [134]. The interest of the usage of the dark solitons in precision measurements is owing to the numerical investigations, which have shown that dark solitons are less sensitive to noise [136], fibre losses [137] and interactions between neighbouring dark solitons [138], compared to the bright counterparts. Moreover, the generation of dark soliton also inherits the advantages of both conventional solitons and continuous-wave radiation and, therefore, there is no need in an additional external delay line for overlapping of counter-propagating dark solitons. In Ref [264] the Authors have used two rare-earth-doped optical fibres inside the laser cavity: an Erbium-doped fibre, pumped by a diode laser, served as a gain media, while a 0.8 mm of Thulium-doped fibre with strong absorption at 1550 nm acted as a saturable absorber. Similar to the conventional solitons, the dark solitons also inherit the 'rest' beat-note corresponding to the CEO frequency at zero angular rotation. The beat-note frequency peak had a linewidth of 169 Hz and the SNR of ∼7.5 dB. The laser gyroscope was coiled up to 18 turns in a ring shape with a radius of 0.3 m. The total length and enclosed area were 69.5 m and 5.22 m^2, respectively. The gyroscope scale factor was numerically estimated to be 3.35

kHz/(deg/s), which was confirmed by experimental results of 3.31±0.09 kHz/(deg/s). The corresponding resolution of the gyroscopic measurement was 0.05 deg/s. The bias drift was estimated by 10 hours measurements of the zero frequency and constitute 143 Hz. These results demonstrate that gyroscopic measurements are not limited to conventional solitons, while other generation regimes of ultrashort pulses could be more beneficial for gyroscopic applications. For example, other work demonstrated increased stability of multi-bound soliton generation in a free-running fibre laser [265], which could benefit the performance of the overall gyroscopic performance.

As we discussed in *Section 1.6.2*, the real-time measurements provided new insights on many applications, including gyroscopic measurements [266]. In Ref. [266], the laser cavity was similar to the one used in Ref. [214] and is schematically shown in Fig. 2.1(d) with the brief discussion in *Section 2.2.1*. The laser features are discussed in more detail in Ref. [5]. A distinctive feature of this laser is that it is able to generate pulses with synchronised and unsynchronised repetition rates by adjusting the intracavity polarisation state. The optical Sagnac effect in this cavity setup was evaluated using two real-time techniques for both operation regimes: spatio-temporal and the DFT measurements.

For investigation of the Sagnac effect in the temporal domain, the Authors used the generation regime with unsynchronised repetition frequencies of counter-propagating waves. A 33 GHz oscilloscope and a 50 GHz photodiode with a rise time of 12.5 ps have been used, which results in the temporal resolution of 25 ps according to the Eq. 1.24. The difference in the repetition rates Δf of counter-propagating pulses can be also understood as a moving crossing point along the laser cavity. The temporal shift per each roundtrips can be estimated as $\Delta l = \frac{\Delta f}{f_{rep}} L$. In that case, the gyroscopic effect can be estimated through the change in the angle between pulse spatio-temporal trajectories. The Sagnac effect was evaluated by comparing the temporal spacing between the counter-propagated solitons at 10^4 roundtrip after the crossing point in regards to the pulse separation when the platform is at rest. The experimentally obtained scale factor was 0.885 deg/s/ns, corresponding to the gyroscopic resolution of 0.022 deg/s at a data frequency of 1.5 kHz. However, the resolution could be further increased by acquisition over a larger window of roundtrip at the cost of reduced data frequency. The upper limit of the roundtrip window and the resolution were dedicated by the limited temporal response of the photodetector and the memory of the used oscilloscope.

The approach based on the Dispersive Fourier Transform measurements requires synchronised repetition rates in both directions in order to record the pulse-to-pulse dynamics of the interferometric pattern. The lengths of the output arms were adjusted to achieve the temporal separation in the range, governed by the Eq. 1.31. The DFT line was realised using an 11 km of dispersion-compensating fibre with the Group Delay Dispersion of -1200 ps/nm. Similar to the 'zero' beat-note frequency, when the gyroscopes is at rest the relative phase between counter-propagating pulses was rapidly changing accordingly to the relative carrier-envelope phase. The Sagnac effect appeared as an additional phase

shift, changing the tilt of the interferometric pattern. The angle was extracted by applying the fast Fourier transformation across the roundtrip window. The window was set to 5000 roundtrips which corresponds to the data frequency of 3 kHz. The experimental resolution of the gyroscopic measurements limited by the using equipment and the measurement technique reached 7.2 mdeg/s with the scale factor of 17.2 mdeg/s/kHz. Similar to other real-time methods, the resolution could be further increased at the cost of the acquisition rate by setting a larger window. Moreover, this phase-based technique could also be further extended for other applications, not limiting to the gyroscopic.

Overall, the real-time measurement techniques surpass the current acquisition rates of the state-of-the-art gyroscopes by several orders of magnitude, demonstrating great potential for further investigations.

On the other hand, as we have demonstrated in *Section* 2.2, bidirectional ring-cavity mode-locked lasers feature complex nonlinear dynamics of counter-propagating waves, involving interactions in gain media and continuous collisions in the saturable absorber. Another approach for fiber laser cavity design has been suggested in Ref. [161], based on parametric generation, eliminating the complex energy dynamics in a gain medium. The seed signal from a mode-locked laser is split in a 3-dB coupler and used for bidirectional parametric generation in a Sagnac loop, based on the four-wave mixing in polarisation-maintaining dispersion compensation fibre. Onwards, a beat-note measurement technique was applied for observation of the Sagnac frequency. However, the demonstrated settings inherit strong frequency oscillations by tens of kHz due to the high sensitivity of the parametric oscillations to the environmental perturbations and instabilities of the pump laser. Despite that the Authors did not provide gyroscopic measurements, the presented gyroscope concept has further potential in measurements of angular velocity.

Another potential way to avoid the synchronisation dynamics between counter-propagating pulses is to measure the Sagnac effect in a passive interferometer with an external source of the ultrashort pulse train. However, no works have been reported on passive gyroscopic measurement via ultrafast lasers. The main reason for that is, as we have shown, most works have been focused on the measurement of the beat-note frequency, which could not be obtained in passive interferometers. Since the dominating technique in passive gyroscopes is based on the phase measurements, the DFT technique could serve as an excellent tool to fill this gap.

All in all, this *Section* comprehensively overviewed the up-to-date development of laser gyroscopes based on ultrashort pulse generation. The experimental results confirmed the strong mitigation of the lock-in effect in such laser gyroscopes. However, the discussed works have not achieved results comparable to the traditional laser gyroscopes. The main observed limitation to achieve higher resolution was related to the strong oscillations of the CEO phase. Moreover, most of the described work exploit traditional techniques adopted from the laser gyroscopes based on generation of continuous wave, which do not allow to extract the full potential of the ultrashort pulses such as high data rates. Among other

techniques, the real-time measurements such as the DFT demonstrated a potential to achieve both high resolution and the data rates. But, further research is required due to the lack of comprehensive studies of the ultrashort pulse response to the angular rotations.

2.3.2 Experimental results

In this section, we present experimental results on gyroscopic measurements in a bidirectional mode-locked fibre laser. The laser we used was described in *Chapter 2.2.1.* The laser was placed on the rotation platform with a radius of 0.305 m, which results in a total enclosed area of 1.24 m^2. The rotation platform was connected to a stepper motor, which was used as a source of discrete angular movements. Since the data rate of the proposed methods significantly exceeds the data rates of the traditional gyroscopes we were able to detect the irregularities in the angular rotations of the DC motors. Thus, we use the stepper motor which allows us to apply angular rotations with an apriori known angular step size.

Stepper motors are brushless electric motors that provide an angular rotation in discrete steps. Stepper motors have multiple electromagnets arranged as a stator around a central rotor. A simplified setup of a bipolar stepper motor with two winding is shown in Fig. A.1. The electromagnets are activated by an external circuit through two windings. By applying a current through A-A', the electromagnets are activated and attract the gear's poles, rotating the motor shaft accordingly (Fig. A.1(a)). Then, the applying voltage over the winding B activates the other pair of electromagnets, which attracts the rotor, producing the next step (Fig. A.1(b)). Onwards, the electromagnets A are consecutively energised and the process is repeated. The main advantage of the stepper motor is that it can be precisely controlled with a known step size with high repeatability. Moreover, the step angle could be further reduced by using the microstepping technique.

In our measurements, we used an RS PRO Hybrid Stepper Stepper Motor with a four-wire bipolar winding. Hybrid stepper motors usually have teeth that are offset on two different cups around the outside of the magnet rotor, providing better precision and higher torque. The used motor has a step angle of 0.9 degrees (400 full steps per single

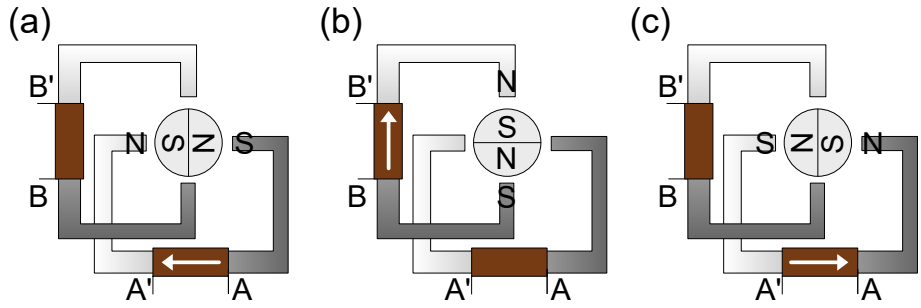

Figure 2.16: Schematic representation of the working principles of a stepper motor. The winding are energised in the following order: **(a)** from A to A', **(b)** from B to B', **(a)** from A' to A.

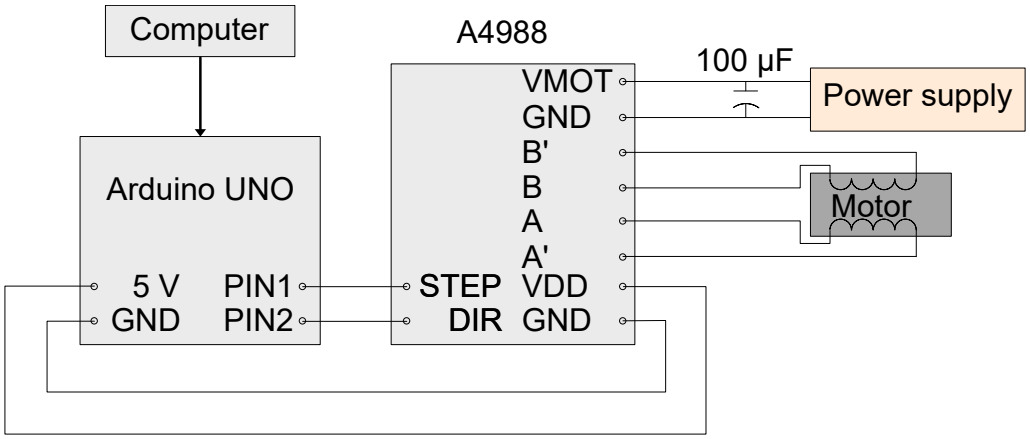

Figure 2.17: Schematic illustration of the experimental scheme to control the stepper motor.

revolution) and a shaft diameter of 5 mm. The step angle accuracy at full step with no load is in the range of ±5%. The holding torque is 0.44 N·m. The stepper motor was controlled via an Arduino UNO using the A4988 driver and the Stepper Library. The whole scheme is schematically demonstrated in Fig. 2.17. The used driver allows to simply implement the microstepping with the step angle of a half-step, quarter-step, eighth-step, and sixteenth-step. By setting through Arduino the required steps per seconds and the step size we were able to manage the average angular velocity of the motor.

The transmission ratio between the laser platform and the stepper motor is calculated as a ratio between their radiuses and results in $M = 8.2 \cdot 10^{-3}$. Hence, the single full-size step of the motor rotates the laser platform by 7.4 mdeg (128.8 μrad) and can be further reduced by microstepping method down to 46.1 μdeg (8 μrad), which is 1/16 of the full step-size. In order to resolve at least one step in time, the minimum motor speed was 80 steps per second and limited by the oscilloscope memory, which allows recording a temporal window of 26 ms.

Moreover, the stepper motor produces a dynamic angular velocity (from zero angular velocity to twice the average angular velocity), that allows to simultaneously investigate an effect of a broad range of the applied angular velocities on the ultrashort pulses. The detection of dynamic Sagnac effect have been demonstrated previously by using a mode-locked laser [267], however these measurements were associated with a phase modulation which are, in principle, similar to the angular rotations. The sinusoidal angular rotation have been also applied to investigate the Sagnac effect in microresonators [40]. For the out-of-lab applications it is important that the gyroscope is able to capture fast angular oscillations, which do not affect the mode-locking operation.

Since the Sagnac frequency response to the applied angular velocity in mode-locked lasers has been demonstrated before [25; 208; 214; 264; 268], here we focus on measurements of the Sagnac effect by exploiting real-time measurement techniques such as the DFT and spatio-temporal dynamics. Firstly, these techniques allow us to particularly

investigate the dynamics of the generation regimes and their peculiarities. Additionally, these techniques provide both high resolution of the phase measurements and high data rates, limited by the repetition rate of the laser source of 15 MHz. Dissimilar to the previous work [266], here we are using a more advanced method for phase extraction from the interferometric pattern, allowing single-shot measurements. Moreover, here we provide gyroscopic measurements of dynamics angular rotations that are more significant for real applications and for investigation of the pulse response to varying angular velocities.

Spatio-temporal measurements

Figure 2.18(a) shows the measurement setup for evaluation of the Sagnac temporal shift by using the spatio-temporal technique. Radiation from both counter-propagating outputs of the laser gyro was recorded by two 50 GHz photodetectors, which were connected to the 33 GHz oscilloscope. For these measurements, we achieved the generation regime with different repetition rates of the counter-propagating pulses. The spatio-temporal dynamics of the counter-propagating pulses when the laser platform was at rest are presented in Fig 2.18(b). To estimate the Sagnac effect by using the spatio-temporal measurements we calculated a temporal shift between the trajectories of the counter-propagating pulses. The inset in Fig 2.18(b) demonstrates the calculated temporal spacing between the pulses at rest. According to the Sagnac effect, the temporal separation between counter-propagating pulses should change when the angular velocity is applied.

Unlike the measurement setup in the Ref. [266], we used two different channels for each direction in order to avoid the pulse overlapping on the photodetector. The temporal overlapping of the counter-propagating pulses induces an uncertainty in the evaluation of the temporal position of each pulse. Moreover, the pulse overlapping at the output from

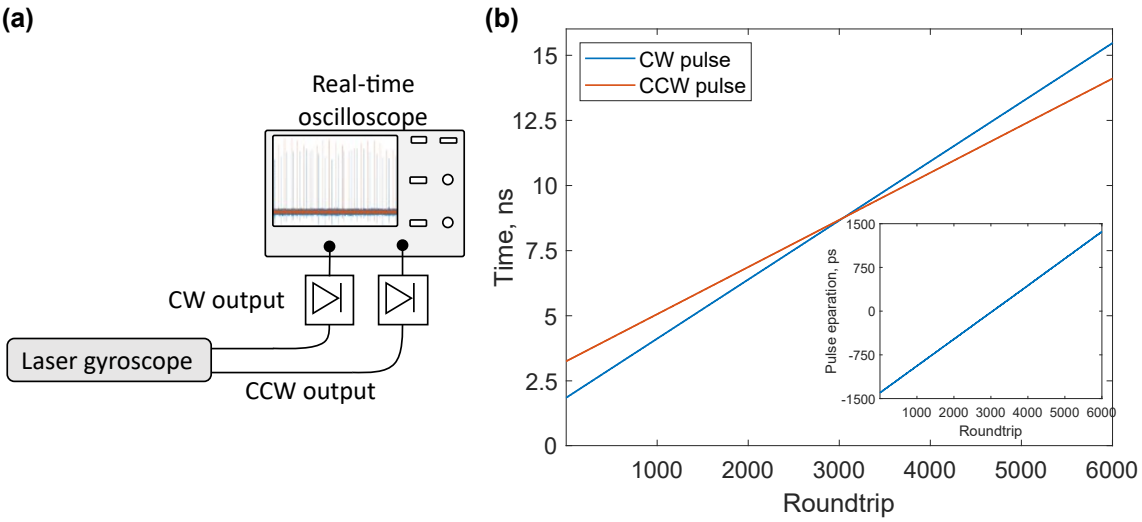

Figure 2.18: **(a)** The measurement setup for gyroscopic measurements by using the spatio-temporal technique. **(b)** The spatio-temporal dynamics of the counter-propagating pulses at zero angular rotation. Inset: the temporal spacing between the counter-propagating pulses.

the laser cavity can result in additional perturbations of the solitons due to the interaction of co-propagating pulses [242; 269; 270].

To evaluate the Sagnac temporal shift we, firstly, provided reference measurements by recording the temporal dynamics of the counter-propagating pulses when the gyroscope platform was at rest. The reference measurements provide the data on the pulse divergence rate, which is the difference in the repetition rate. Then, we recorded the spatio-temporal dynamics of the counter-propagating pulses with a rotating gyroscope platform by the stepper motor. The Sagnac effect in such configuration manifests as an additional timing shift of the pulse spatio-temporal position to the reference measurements. Thus, the resulting data on the Sagnac induced temporal shift is evaluated as the difference between both measurements.

Figure 2.19(a) demonstrates the experimental results on the pulse temporal spacing during the rotation exposure, after we subtracted the reference measurements. The stepper motor was set to produce 100 steps per second at the full-step size (blue line) and half-step size (orange line). As can be seen, the temporal shift due to the Sagnac effect was accumulated through consecutive roundtrips, which is characteristic of the active gyroscopes. In order to estimate the Sagnac effect in real-time (pulse-to-pulse variations), we should differentiate the temporal shift in time. The corresponding differentiation of the gyroscopic measurements for both step-sizes with a moving averaging window of 1000 roundtrips is shown in Fig. 2.19(b). The averaging of the results is necessary to increase the resolution of the pulse spatio-temporal position due to the limited temporal response of the used measurement equipment. The results demonstrate a good temporal agreement with the set step duration of the motor of 10 ms. Additionally, if the gyroscope will rotate in the opposite direction, the relative time separation between the pulses will start to decrease, allowing to uniquely determine the rotation direction.

The resulting scale factor of the laser gyroscope, evaluated from the experimental data, is shown in Fig. 2.20(a). This scale factor was estimated for a difference in the repetition frequencies of the counter-propagating pulses of 22.5 Hz, which corresponds to the divergence rate of ∼100 fs per roundtrip. The experimental relation between the relative pulse separation per roundtrip and the applied angular velocity is in relatively good agreement with the linear approximation. The residual deviations from the perfect linear approximation refer to the limited resolution of the setup and the slippage between the rotation platform and the motor. The experimental scale factor was estimated to a value of 8.42 fs/(deg/s). We would like to note that we did not observe any synchronisation dynamics even at the lowest measured angular velocity of 0.037 deg/s (0.64 $\mu rad/s$). The lack of synchronization is explained by the fact that even at the zero rotation velocity, the counter-propagating pulses are far from synchronisation, so the lock-in effect is completely eliminated.

On the other hand, at high angular velocities or at a low divergence rate between the counter-propagating pulses, the effect of the Sagnac-induced temporal shift can be com-

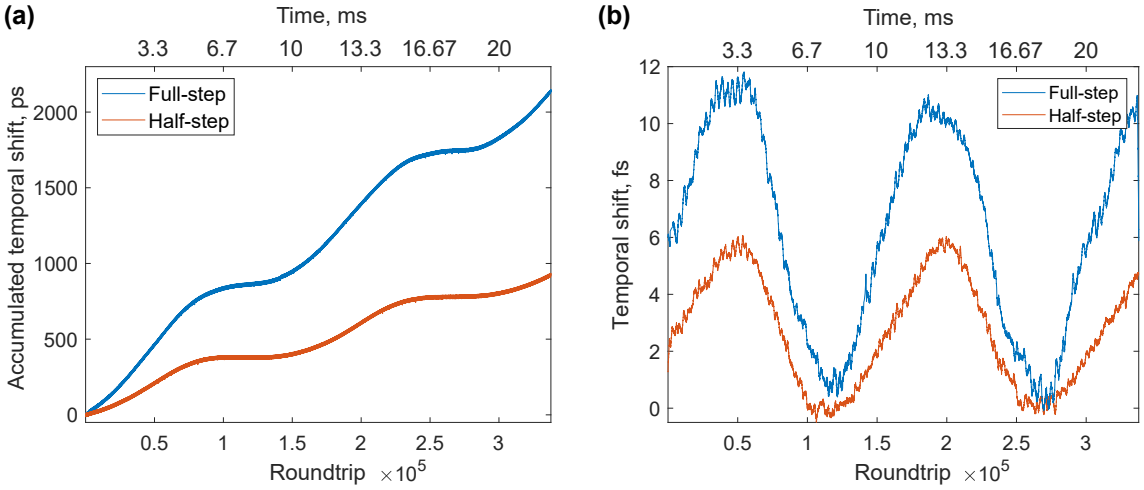

Figure 2.19: **(a)** The accumulated Sagnac-induced temporal shift between counter-propagating pulse when the stepper motor was set to produce 100 steps per second (10 ms 150000 roundtrips per step) with full-step (blue line) and half-step size (orange line). **(b)** The corresponding differentiation of the accumulated temporal shift with averaging window of 1000 roundtrips.

pared to the divergence rate and may lead to their synchronisation. That is confirmed by our experimental observations where we observed a relation between the scale factor of the gyroscope and the initial divergence rate between counter-propagating pulses. The dependence of the scale factor on the difference in the repetition rate is shown in Fig. 2.20(b). The approximation of the experimental results we adopted from the traditional lock-in effect [271]:

$$S = S_0 \frac{\sqrt{(\frac{\Delta\nu}{\Delta\nu_0})^2 - 1}}{\frac{\Delta\nu}{\Delta\nu_0}} \tag{2.6}$$

where S is the resulting scale factor, S_0 is the asymptotic scale factor. $\Delta\nu = \Delta\nu_{CW} - \Delta\nu_{CCW}$ is the difference in the repetition rates of the counter-propagated pulses (divergence rate), $\Delta\nu_0$ is the minimum difference in the repetition rates at which the Sagnac effect can be observed. The approximated values of the asymptotic scale factor and the minimum divergence rate is $S_0 = 10.85 fs/(deg/s)$ and $\Delta\nu_0 = 14.19$ Hz, correspondingly. The approximation is shown in the Fig. 2.20(b) as a dotted black line. However, this approximation does not provide the best fit for the experimental data mainly due to the reason that the mechanism of synchronisation between the counter-propagating pulses in mode-locked lasers is different from the traditional lock-in effect. Hence, we use a different approximation with saturation properties as:

$$S = \frac{S_0}{1 + \frac{\Delta\nu_{sat} - \Delta\nu_0}{\Delta\nu - \Delta\nu_0}} \tag{2.7}$$

here $\Delta\nu_{sat}$ is the saturation frequency, at which the maximum Scale factor S_0 decreased by two times. The approximation values are: $S_0 = 11.63 fs/(deg/s)$, $\Delta\nu_0 = 9.54$ Hz,

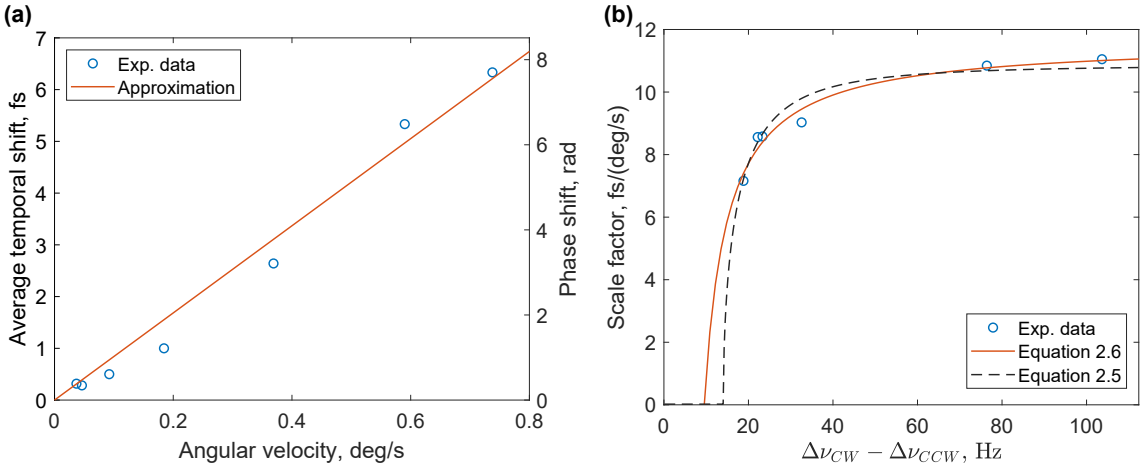

Figure 2.20: **(a)** The relation between the average pulse temporal shift per roundtrip and the applied angular velocity (blue dots) with linear approximation (orange line). **(b)** The relation between the experimental scale factor and the difference in the repetition rate between counter-propagating pulses (blue dots) with approximations (orange and black lines).

and $\Delta\nu_{sat} = 14.83$ Hz. As demonstrated in the Fig. 2.20(b), this approximation provides a better agreement with the experimental data. Though both approximations provide only slightly different results, they both revealed an important conclusion, that while no traditional lock-in has been observed at low angular velocities, the repetition rates of the counter-propagated pulse could be synchronised, limiting the gyroscopic measurements. This agrees with our experimental investigations, that no bidirectional mode-locked generation with unsynchronised repetition rates was observed with a difference in the repetition rates less than ~18 Hz. The explanation of the reduced scale factor can be understood as the counter-propagating pulses with close repetition rates start to synchronise and which reduces the effect of the Sagnac-induced temporal shift. Moreover, a temporal shift per roundtrip at a low divergence rate is comparable to the Sagnac-induced temporal shift. As an example, a divergence rate of 10 Hz corresponds to the temporal shift of fewer than 50 fs, which is less than 5 times more than the Sagnac temporal shift at an angular velocity of 1 deg/s. Thus, it is desirable to achieve a high divergence rate for reliable gyroscopic measurements. Moreover, as we will discuss later, only a negligible temporal shift, induced by the angular rotations, was observed during the generation regime with synchronised repetition rates of counter-propagating pulses.

Since eq. 2.7 provides a better fitting to the experimental results we will use the asymptotic scale factor of 11.63 fs/(deg/s) in our further discussion. This experimentally obtained asymptotic scale factor substantially exceeds the theoretical scale factor of $S_{theor} = 0.0014 fs/(deg/s)$, based on the classical Sagnac Eq. 1.3. However, previous works have demonstrated a potential to substantially increase the response of the gyroscopic measurements by introducing an anomalous dispersion [28; 29; 30; 32; 272]. The enhancement factor of such light dragging in a dispersive medium, according to the

Lorentz's prediction, can reach up to $\sim 10^4$ [34]. While our results demonstrate the enhancement of $\sim$ 7825 times. This enhancement factor indicates that the response of the wave pockets, such as ultrashort pulses, to the applied angular velocity, is higher than predicted by the classical Sagnac equation and so they have a significant potential for gyroscopic applications. However, further work is required in order to comprehensively understand this phenomenon.

On the other hand, this experimental scale factor is smaller than the one observed in Ref. [266] in a similar experimental setup. However, here we used a different approach to estimate the scale factor. Firstly, we based our results on almost 390 thousand consecutive roundtrips, compared to 10 thousand in Ref. [266], which allows us to obtain a higher resolution. Moreover, the pulse dynamics in each direction was measured in two separate channels to exclude pulse interaction outside the laser cavity. And lastly, in Ref. [266] Authors measure the pulse separation after overlapping of counter-propagating pulses on the photodetector. This approach may induce additional uncertainty, due to the relatively low resolution of the measurement equipment compared to the pulse duration, so that the counter-propagating pulse could not be distinguished for several hundreds of roundtrips. Thus, our measurements are more sensitive and can establish the scale factor with better precision.

The minimum detectable angular velocity in a single-shot measurement of the proposed technique is 1074.8 deg/s (18.76 rad/s), based on the asymptotic scale factor of 11.63 fs/(deg/s). However, as we discussed in *Section*1.4.2 the minimum angular velocity could be efficiently decreased as $1/n$ by estimating the accumulated Sagnac-induced temporal shift over n roundtrips. Thus, the resolution of the setup is limited by the memory of the oscilloscope, which allows to record $n =\sim$ 392000 consecutive roundtrips, providing the total resolution of 2.74 mdeg/s (47.9 μrad/s). However, the increased resolution comes at the cost of the decreased data frequency by n time and is estimated to a value of $\sim$ 38 Hz.

To characterise the gyroscope performance we calculate the Signal-to-Noise Ratio (SNR) as a squared ratio of the mean value μ and the standard deviation σ :

$$SNR = 10log[(\frac{\mu}{\sigma})^2] = 20log(\frac{\mu}{\sigma}) \tag{2.8}$$

In order to estimate the gyroscopic performance of the proposed setup, we calculate the SNR for an angular speed of 1 deg/s in a single-shot regime (without applying averaging techniques). Thus, the mean value μ is the temporal shift per roundtrip at the angular velocity of 1 deg/s, while the standard deviation is the pulse-to-pulse variation of the pulse temporal position of the reference measurements and equals 7.15 ps. The resulting SNR is -55.8 dB. Such a low value was expected due to the low resolution of the measurements equipment compared to the Sagnac effect. However, the accumulation of the Sagnac effect will add an additional term $10log(n^2)$ into the eq. 2.8, where n is the number of accumulated roundtrips. For the presented measurements with averaging over 1000

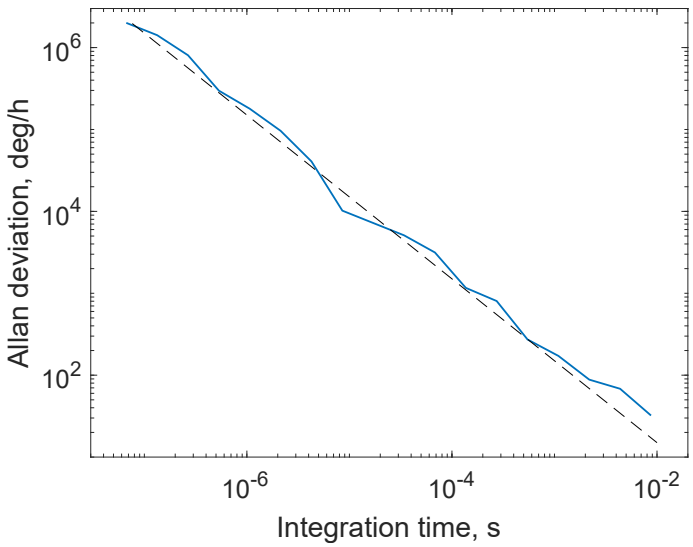

Figure 2.21: Allan deviation of the pulse-to-pulse temporal change between consecutive pulses during the reference measurements. Dashed line represents the 1/t trend.

roundtrips, the SNR is 4.2 dB which is enough to distinguish the signal from noises.

To estimate the main parameters of the gyroscope we calculated the Allan deviation. As we introduced earlier, the Allan deviation is usually calculated for the beat-note frequency at a constant angular velocity to estimate the limiting perfomance of the gyro. The constant angular velocity is necessary in order to obtain the beat-note frequency. Since our measurement technique is completely different, we calculated the Allan deviation of the pulse-to-pulse variation on the temporal separation between counter-propagating pulses, converted into angular velocity by using the experimental scale factor, for the reference measurements. The applied constant angular velocity will induce an additional temporal shift, which is the same per each roundtrip in the ideal case. This additional term will be cancelled as can be seen in the eq. 1.23. Thus, the approach we used is equivalent to the traditional methods to estimate the Allan deviation.

Figure 2.21 demonstrates the calculated Allan deviation. The maximum integration time was limited by the memory of the oscilloscope to 8.7 ms. The Allan deviation has a strong 1/t downward trend for longer integration time, where t is the integration time. This dynamics is expected since the pulse dynamics occur at much smaller time scales than the resolution of the measurement equipment, and a wide averaging window is necessary for the increased resolution. On the other hand, the rapid temporal fluctuations of the pulses, such as timing jitter, are averaging out at long integration times and only long-term fluctuations could be observed (e.g. environmental perturbations). The resulting bias instability is 32.2 deg/h at an integration time of 8.7 ms. The high integration time indicates that this approach is preferred to operate at low data frequencies in order to achieve the highest angular resolution. Unfortunately, we are not able to measure the Angular Random Walk (ARW), which is the Allan deviation at the integration time of 1 s, due to the limited memory of the oscilloscope. Nevertheless, we estimate the ARW from

the Allan deviation at the maximum integration time and multiply by $\sqrt{1s/8.7ms} = 10.68$, considering $\sqrt{t}$ upward trend of the Allan deviation. Hence, the upper limit of the ARW is estimated to 343.8 deg/$\sqrt{h}$.

In conclusion, we want to highlight that the proposed approach is linear and easy to implement and provides the real-time gyroscopic measurements. This technique is also capable to measure dynamics angular rotations implemented by a stepper motor. However, due to the relatively low response time of the photodetector, this approach is more suitable for measuring slow-variable angular rotations which are accumulated over many roundtrips. Unfortunately, this approach has a relatively low performance compared to the traditional optical gyroscopes, however the increased temporal shift due to the Sagnac effect makes the ultrashort pulses attractive for further investigation of gyroscopic measurements.

Interferometric measurements

Generally, the interferometric techniques are based on the measurements of the Sagnac-induced phase shift. By combining both counter-propagating beams at the output from the laser cavity an interferometric pattern can be achieved, from which a relative phase and its variations could be extracted. This approach demonstrates higher sensitivity compared to the temporal measurements, which can be understood from the phase-time relation 1.4. In other words, a temporal shift, equivalent to one wavelength temporal period ($t = \lambda/c$), translocates the interferometric pattern by the phase of 2π. This interferometric technique have been used to experimentally investigate the internal dynamics of solitons molecules [182; 189]. In this *Section* we evaluate the phase shift between counter-propagating pulses in the bidirectional mode-locked fibre laser by using the Dispersive Fourier Transform. To extract the relative phase information we followed the technique, discussed in *Section* 1.6.2.

Figure 2.22(a) demonstrates the experimental setup for the interferometric measurements of the Sagnac effect. The output radiation from both counter-propagating directions is combined in the optical coupler. To obtain an interferometric pattern of counter-propagating pulses, their temporal space should be adjusted in the range, given by the eq. 1.29. Then, both pulses temporally broaden in the DFT line and are registered by a 50 GHz photodiode, connected to a 33 GHz digital storage oscilloscope. The DFT line consists of 11 km of dispersion compensating fibre and has a GDD of -1200 ps/nm/km. The spectral resolution of the DFT measurements, based on the used measuring equipment, is 0.02 nm. The resolution of the phase retrieval, limited by the measuring equipment and the SNR, was 1 μrad. More discussion on the resolution of the phase extraction in the presence of noises is presented in *Appendix* A.

In these measurements, we adjusted the polarisation controllers in the laser cavity to generate mode-locked pulses in opposite directions with identical repetition rates. In

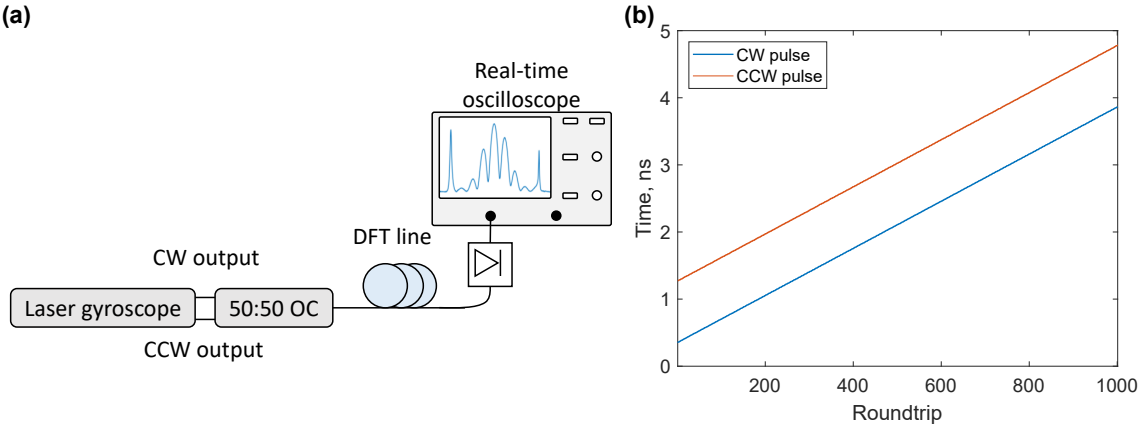

Figure 2.22: **(a)** The experimental setup of the interferometric measurements of the Sagnac phase shift. OC - optical coupler. **(b)** The spatio-temporal dynamics of counter-propagating pulses with matched repetition rates at rest.

the time domain, the matched repetition rates of counter-propagating pulses mean that the temporal spacing between the pulses is constant over time, which is necessary for the continuous detection of their interference. Thus, the generation regime with unsynchronised repetition rates could not be applied for the phase measurements via the DFT technique. Figure 2.22(b) presents an example of the spatio-temporal dynamics of the counter-propagating pulses with matched repetition rates at rest. For this generation regime we revealed two different dynamics of the relative phase between the counter-propagated pulses: when the counter-propagating pulses inherit a continuously changing relative phase; another dynamics we observed is when the counter-propagating pulse are fully locked with a fixed relative phase. Both regimes experienced different responses to the applied angular velocity which we are going to discuss below.

Generation of counter-propagating ultrashort pulses with frequency offset

In this section, we investigate the gyroscopic response of the relative phase of the counter-propagating pulses in the bidirectional mode-locked laser to the rotation exposure. In analogue with spatio-temporal measurements, we firstly provided reference measurements when the gyroscope platform was at rest. Figure 2.23(a) demonstrate the dynamics of the interferometric pattern of counter-propagating pulses recorded via the DFT. The remarkable characteristic of this generation regime is that the relative phase was constantly changing during the reference measurements. The change of the relative phase is presented as a tilt of the modulation of the interference over the roundtrips and corresponds to the beating between the CEO frequencies of counter-propagating pulses as $\Delta f = f_{CEO}^{CW} - f_{CEO}^{CW} = \frac{\Delta\phi}{2\pi} f_{rep}$. Note, that the relative temporal spacing remained constant from pulse-to-pulse. Thus, in the frequency domain, both counter-propagating frequency combs have an equal separation between each lines but have an offset relative to each other.

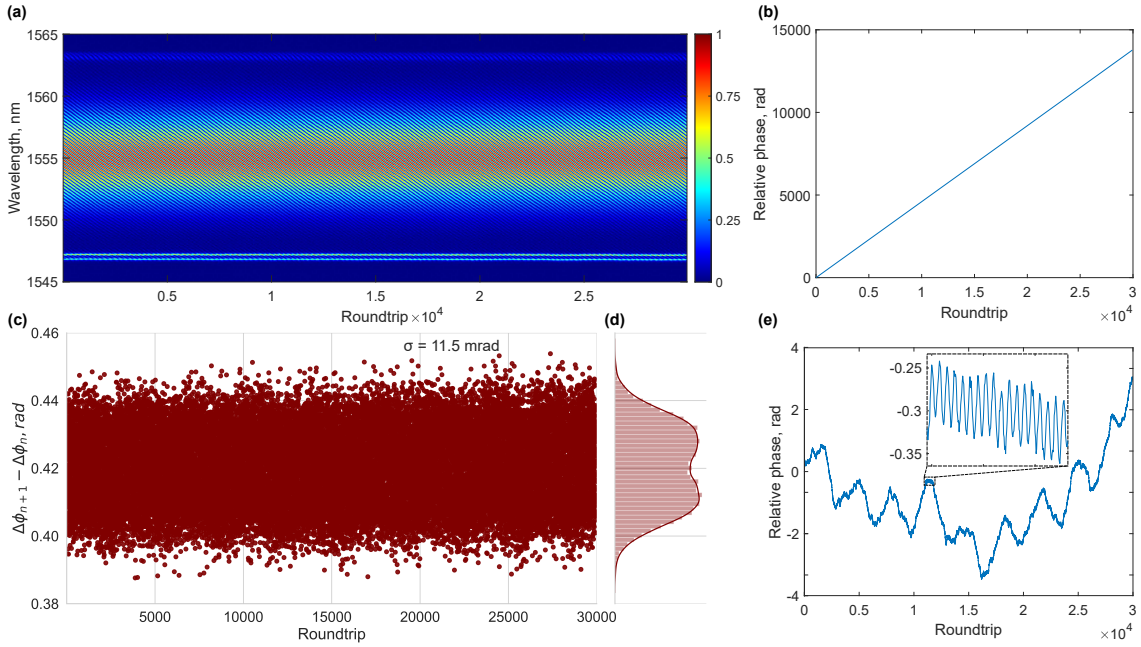

Figure 2.23: **(a)** The spectral dynamics of the interference of counter-propagating pulses recorded with the DFT. The incline of the spectral modulation corresponds to the changing relative phase of the counter-propagating beams. **(b)** The dynamics of the relative phase, evaluated from the DFT measurements. *(c)* The pulse-to-pulse change of the relative phase with average phase slippage of 0.42 rad and standard deviation of 11.5 mrad with **(d)** corresponding probability density function. **(e)** The dynamics of the relative phase after we subtracted the average phase slippage of 0.42 rad.

Figure 2.23(b) presents the relative phase dynamics, obtained from the corresponding single-shot DFT spectra. The pulse-to-pulse variation of the relative phase, which is the differentiation of the relative phase over roundtrips, is shown in Fig. 2.23(c) with the corresponding Probability Density Function (PDF) in Fig. 2.23(d). The average phase slip ϕ_{slip} we observed is 0.42 rad with a standard deviation of 11.5 mrad. The standard deviation of the phase measurement limits the minimum relative phase, which we can distinguish from the laser phase noise, and, hence, provide a resolution of the further gyroscopic measurements. In the frequency domain, the phase slippage of the relative phase corresponds to the frequency offset between counter-propagating combs of $\Delta f = 1$ MHz. Additionally, the standard deviation can be represented as a width of the Δf frequency and was estimated to be 27.5 kHz. The two-peak structure indicates a strange attractor for the synchronisation of counter-propagating pulses.

Figure 2.23(e) demonstrates the dynamics of the relative phase after subtraction of the average phase slippage ϕ_{slip} for each roundtrip, representing a phase bias from the average phase slippage. A strong frequency oscillation was observed with an amplitude of ∼0.5 rad with a periodicity of ∼30 thousand roundtrips (2 ms). Small oscillations of the relative phase in a range of 0.06 rad with a time period of 15 roundtrips are shown in the inset at Fig. 2.23(e). These phase oscillations have similar temporal periods to the presented in the previous *Section* on pulse build-up dynamics. Note, that this dynamics is accumulated

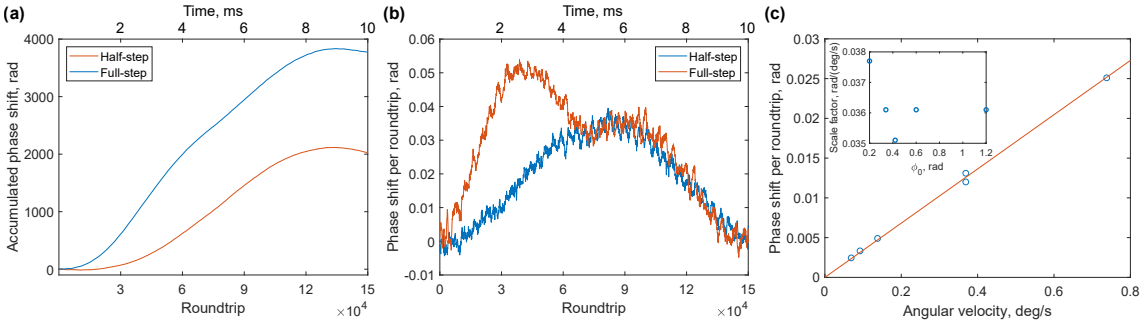

Figure 2.24: **(a)** The accumulated Sagnac-induced phase shift between the counter-propagating pulses when the stepper motor was set to produce 100 steps per second (10 ms or 150000 roundtrips per step) with full-step (blue line) and half-step size (orange line). **(b)** The corresponding differentiation of the accumulated phase shift with averaging window of 100 roundtrips. **(c)** The relation between the average shift of the relative phase per roundtrip and the applied angular velocity (blue dots) with linear approximation (orange line). Inset: The relation between the experimental scale factor and the average phase slippage ϕ_{slip}.

through roundtrip. In other words, if 0.5 phase is accumulated through 15 thousand roundtrips it corresponds only to the deviation of 33.3 μrad per roundtrip (80 Hz). The deviation of the relative phase may arise due to noises inherited from the mode-locked generation such as intensity noises and fluctuations of the surrounding conditions.

According to the Sagnac effect, the angular movements induce an additional phase shift between the counter-propagating pulse, and in other words, change the angle of the tilt of the interferometric trace. Analogically to the spatio temporal measurements, to estimate the Sagnac induced phase shift we subtracted the average pulse-to-pulse average phase shift, obtained from the reference measurements, from the obtained results on the gyroscopic measurements. Figure 2.24(a) presents the dynamics of the relative phase when the gyroscope experienced rotation movements from the stepper motor at speed of 100 steps per second (10 ms per step). As expected, similar to the spatio-temporal measurement, the relative phase was accumulated over roundtrips due to the Sagnac effect (eq. 1.5). To resolve the profile of the rotation movements, we differentiate the accumulated phase with an averaging window of 100 roundtrips, which is shown in Fig. 2.24(b). The two-peak profile of the step is a feature of stepper motors and arise due to the relatively long time between charging consecutive coils, which force the motor to rotate. This profile is resolved due to the higher resolution of the phase measurements and more narrow average window, compared to the spatio-temporal measurements of the Sagnac effect. Notably, that the relative pulse separation did not change during the angular rotation of the laser platform, as it is expected similar to the spatio-temporal measurements since the Sagnac effect manifests as a temporal delay between opposite directed pulses. That also lead to the conclusion that the counter-propagating pulses always collided in the saturable absorber even when the angular velocity was applied to the platform. We refer these observations to the synchronisation dynamics between counter-propagating pulses and the effect of the

colliding mode-locking.

The experimentally obtained relation between the average phase shift per roundtrip and the applied angular velocity is shown in Fig. 2.24(c). The scale factor is linearly approximated to a value of 0.0361 rad/(deg/s). Taking into account the standard deviation of the relative phase dynamics, the resolution of the gyroscopic measurement is 318.6 mdeg/s (5.56 μrad/s). The SNR of the single-shot measurements is 9.9 dB. Unlike the spatio-temporal approach, the scale factor did not depend on the pulse parameters such as the phase slippage. The Inset in Fig. 2.24(c) demonstrates the obtained scale factor at different values of the reference pulse-to-pulse phase slippage. Moreover, due to the periodicity of the interferometric pattern, the phase shift per roundtrip of π and higher could not be undoubtedly estimated. This limits the maximum measured angular velocity to a value of 87 deg/s (1.5 rad/s).

The experimentally obtained scale factor diverges from a theoretically evaluated value of 1.1 mrad/(deg/s) using the Sagnac eq. 1.5. Similar to the spatio-temporal approach, this discrepancy from the classic Sagnac equations can be caused by the intracavity anomalous dispersion and the unique properties of the ultrashort pulses. However, the enhancement factor of 32 is much smaller compared to the one obtained via the spatio-temporal measurements. The reduction in the enhancement factor is due to the synchronisation dynamics between counter-propagating pulses and the effect of the colliding mode-locking. Moreover, we also observed that during the angular rotations the accumulated phase difference tended to return back to the initial condition, restricting the continuous measurements of the angular velocity. This can be understood as follows: the applied angular rotations induce perturbation to the synchronisation dynamics between counter-propagating pulses and the colliding mode-locking, which in turn compel the counter-propagating pulses to return back into initial conditions in order to maintain the conditions, imposed by the colliding mode-locking.

At the same time, the presented scale factor is slightly smaller but comparable to the one demonstrated in Ref. [266]. The disagreement with previous results is mostly due to the different types of used motors and the slippage between the motor and the gyroscopic platform. Moreover, here we evaluate the relative phase with a more advanced technique, which allows us to evaluate the relative phase in a single-shot regime with higher precision.

Figure 2.25 presents the calculated Allan deviation of the pulse-to-pulse phase change of the pulse train. Similar to the spatio-temporal measurements, the Allan deviation was estimated for the reference measurements, which represent the lowest phase noises of the generation regime and limit the overall gyroscopic performance of the used setup. A small peak of the Allan deviation at low integration time corresponds to the oscillation noises [56] due to the phase oscillations shown in Fig. 2.23(e). The minimum Allan deviation of 24.2 deg/h, which is the bias instability by the definition, is observed at the integration time of 0.14 ms, indicating the optimised data rate of around 7.1 kHz. After that minimum point, the Allan deviation starts to slowly increase due to the pulse dynamics in the

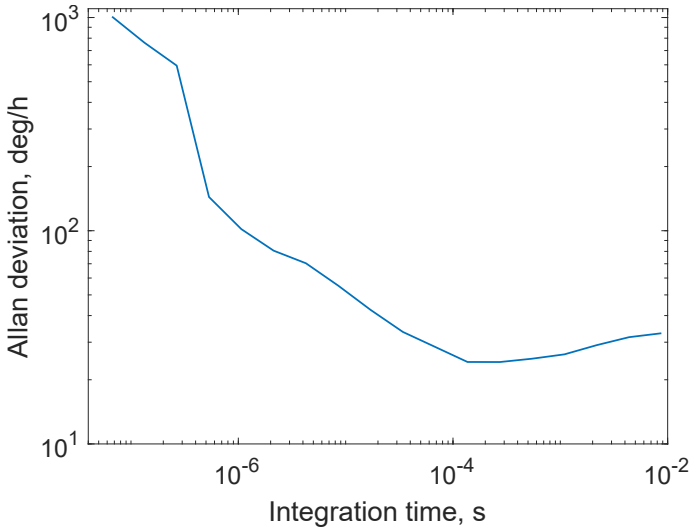

Figure 2.25: Allan deviation of the pulse-to-pulse phase change between consecutive pulses during the reference measurements.

laser cavity. No strong trends have been observed from the Allan deviation due to the complex phase dynamics of counter-propagating pulses. Using the same approach as in the spatio-temporal measurements, from the Allan deviation the ARW is estimated to be 353.5 deg/$\sqrt{h}$.

As expected, the phase measurements inherit much better gyroscopic performance at higher data rates, compared to the spatio-temporal technique. By using the whole memory of the oscilloscope, the resolution can potentially reach 0.8 μdeg/s. However, the drawback of this approach is that the relative phase experiences strong fluctuations during the angular rotation of the platform and had a strong tendency to return to the original phase slippage due to the colliding mode-locking, strongly limits the application of the proposed method for robust and continuous detection of dynamics angular velocity. Additionally, the synchronisation between counter-propagating pulses significantly reduces the enhancement factor compared to the one we observed during the spatio-temporal measurements by directly estimating the Sagnac-induced temporal shift. Moreover, the phase measurements are sensitive to the fluctuations of the CEO frequency and are more sensitive to the environmental perturbations, requiring stabilisation of the laser cavity. On the other hand, we demonstrated that the DFT interferometry is a more accurate tool for sensing applications.

Generation of counter-propagating ultrashort pulses with fixed relative phase

This generation regime features fully-locked frequency combs in opposite directions. Figure 2.26(a) shows the spectral dynamics recorded via the DFT techniques when the laser gyro is at rest. Dissimilar to the previous generation regime, no tilt in the spectral modulation has been observed. The absence of the phase slippage indicates that the frequency combs in opposite directions are fully locked (i.e. the counter-propagating frequency combs

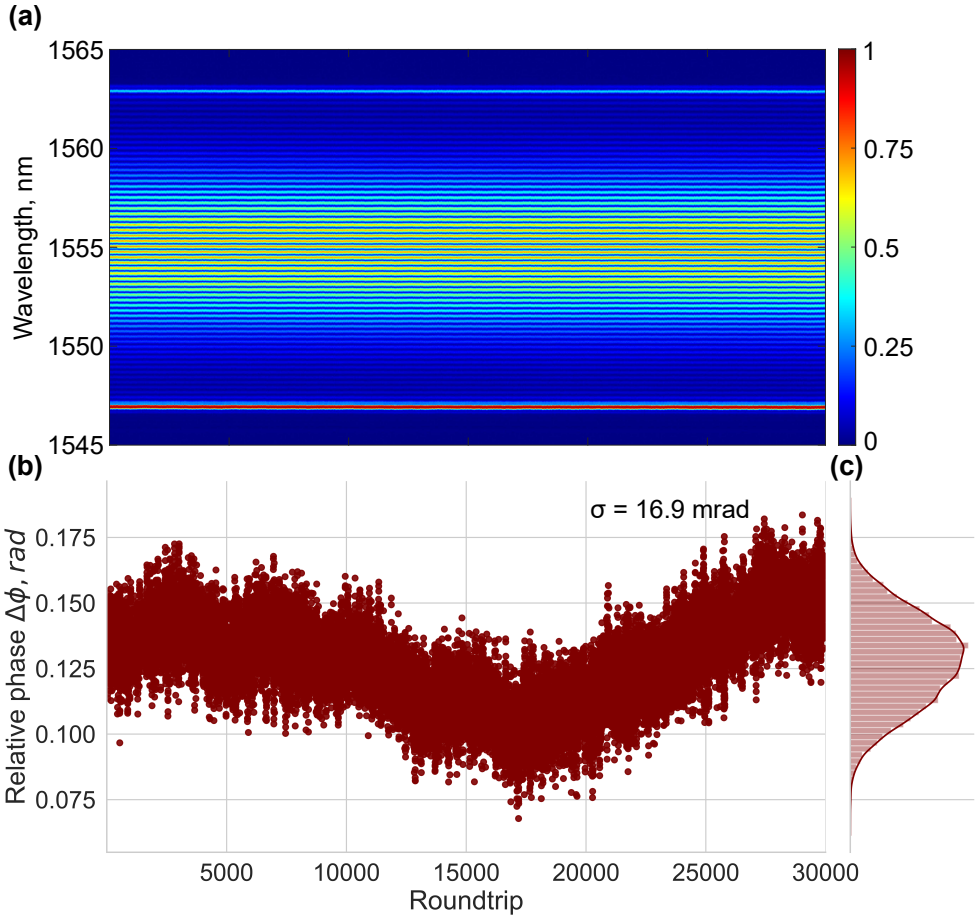

Figure 2.26: **(a)** The spectral dynamics of the interference of counter-propagating pulses recorded with the DFT. **(b)** The dynamics of the relative phase, evaluated from the DFT measurements with **(c)** corresponding probability density function.

are matching since the repetition frequency is the same and the relative CEO frequency equals zero). The corresponding relative phase, extracted from the DFT data, is demonstrated in Fig. 2.26(b) with the corresponding PDF shown in Fig. 2.26(c). This generation regime produces much more stable ultrashort pulses with a standard deviation of the relative phase of 16.9 mrad. The increased stability of the pulses may origin from the mechanism of full-locking of counter-propagating pulse, which forces the counter-propagating pulses to maintain their characteristics for the laser generation. Additionally, since the relative CEO frequency is zero, the counter-propagating pulses always collide in the cavity with the same relative phase.

We also observed that this generation regime can exhibit more complex dynamics of the phase synchronisation between counter-propagating pulses with strong time-phase oscillations, which is demonstrated in *Appendix* C. These time-phase oscillations can be mitigating by carefully adjusting the intracavity PCs.

To evaluate the gyroscopic measurements, we firstly measured the reference measurements to determine the initial relative phase between the counter-propagating pulses, which corresponds to the zero velocity. Figure 2.27(a) demonstrates the dynamics of the

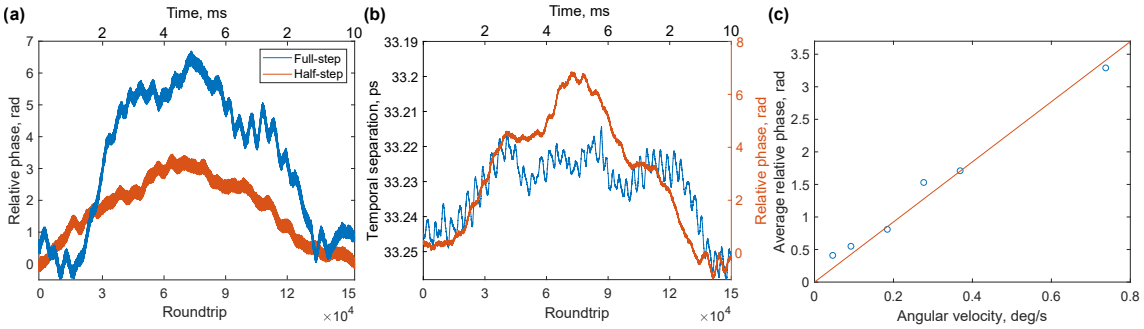

Figure 2.27: **(a)** The Sagnac-induced phase shift between the counter-propagating pulses with full-step (blue line) and half-step size (orange line). **(b)** The dynamics of the relative phase and the relative temporal spacing between the counter-propagating pulses with averaging window of 1000 roundtrips. For both measurements the stepper motor was set to produce 100 steps per second (10 ms or 150000 roundtrips per step) **(c)** The relation between the average shift of the relative phase per roundtrip and the applied angular velocity (blue dots) with linear approximation (orange line).

relative phase under exposure of dynamic angular rotation on the laser platform. Dissimilar to the previous operation regime, the angular movements were not accumulated through roundtrips. Hence, after each step of the motor, the laser pulses returned to the initial synchronised state. Hence, this generation regime does not require differentiation of the relative dynamics in order to estimate the real-time angular velocity. Moreover, the phase response to the applied angular velocity is significantly increased compared to the previous measurements. As we observe in the previous phase measurements, the few-peak structure of the motor step is also preserved.

As we discussed before, it is possible to extract the relative temporal separation between the pulses from the interferometric pattern. The resolution of the extracted temporal spacing with the zero-pudding method can achieve values of 7.7 fs and 0.24 fs for a single-shot regime and for an averaging over 1000 roundtrips. The data on the relative pulse spacing with a moving averaging window of 1000 roundtrips is plotted in Fig. 2.27(b). Strong oscillations in the temporal spacing mostly refer to the complex synchronisation dynamics, similar to the one shown in *Appendix* C. The average temporal shift per step is 11.5 fs, which is close to the one observed by using the spatio-temporal approach. This results demonstrate that the counter-propagating pulses were shifted relative to each other, similar to the observation via the spatio-temporal technique.

On top of the temporal separation in Fig. 2.27(b) we include the relative phase data. According to the phase-time eq. 1.4, the average temporal shift induces a shift of the relative phase by 13.5 rad, while the observed experimental result is 3.29 rad. This divergence arises due to the synchronisation dynamics of the counter-propagating pulses similar to the lock-in effect, which constrains the Sagnac-induced variations in the parameters of the counter-propagating pulses for gyroscopic measurements. Additionally, similar to the reference measurements, presented in *Appendix* C, the divergence between the phase and temporal domains is the feature of this unique generation regime for its self-sustaining.

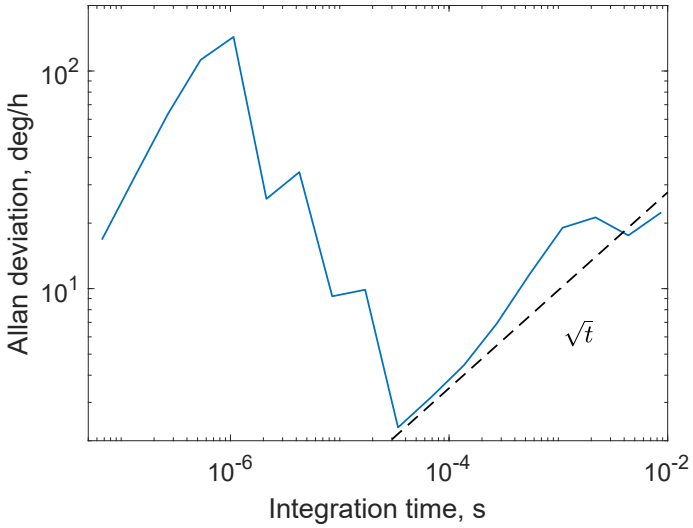

Figure 2.28: Allan deviation of the relative phase dynamics between consecutive pulses during the reference measurements.

Moreover, we observed that under rotation exposure on the laser platform, the counter-propagating frequency combs can transit into the previously described generation regime with the relative CEO frequency offset.

Figure 2.27(c) demonstrates the relation between the average phase shift and the applied angular velocity. The experimental scale factor, obtained from the linear approximation, is 4.62 rad/(deg/s). Similar to the previous measurements, this scale factor substantially exceeds the theoretical value. According to the standard deviation of the relative phase of 16.9 mrad, the minimum resolvable angular velocity in a single-shot regime is 3.66 mdeg/s (63.9 μrad/s). However, since the phase is not accumulated from each roundtrip, the resolution can be increasing by $1/\sqrt{n}$, where n is a number of roundtrips of the averaging window.

The Allan deviation of the relative phase dynamics is shown in Fig. 2.28. A strong peak of the Allan deviation at a small integration time relates to the sinusoidal noises due to the strong phase oscillation at high frequencies, demonstrated in C. The bias instability is 2.3 deg/h, derived from the lowest value of the Allan deviation at the integration time of 34.1 μs (29.3 kHz). After the minimum point, the Allan deviation starts to increase at a pace of $\sqrt{t}$. This trend is known as a rate random walk, which is the exponentially correlated noise with long correlation time [56]. The Allan deviation at the highest integration time is 22.4 deg/h, which corresponds to the ARW of 239.6 deg/$\sqrt{h}$. The bias instability is by an order of magnitude lower than the previously presented measurements, indicating a better performance of the gyroscope. This is achieved due to higher enhancement factor. Moreover, the lower integration time of the bias instability confirms that this generation regime is more eligible for the detection of dynamic angular rotations.

Similar to the previous phase measurements, the phase shift per step cannot exceed π. However, during these measurements, the pulse-to-pulse phase change is related to the

angular acceleration. Thus, the maximum angular acceleration can be defined as:

$$\Omega_{max} = \pi/(S \cdot T_{rep}) \tag{2.9}$$

, where S is the scale factor and T_{rep} is the time period of the pulse train. Taking into account the obtained scale factor and the time period of 66.67 ns, the maximum angular acceleration is restricted by a value of 10.2 Mdeg/s^2. Note that the maximum acceleration is inversely proportional to the scale factor. So, the maximum angular acceleration can be further increased by decreasing the length of the laser cavity, which will affect both components of the denominator in the equation. However, this will also lead to the lower sensitivity of the gyroscopic measurements.

From the physical point of view, the maximum recognisable angular velocity is not limited in the setup. However, at a high angular velocity, the Sagnac-induced temporal shift may increase the inter-pulse separation so the interferometric pattern could not be resolved. The range of the temporal spacing between the pulses can be obtained by using the eq. 1.29 and for the given pulse is ≈170 ps. For the obtained scale factor the maximum angular velocity is limited by the value of $43.4 \cdot 10^3$ deg/s, which substantially exceeds the required range of applied angular velocities.

To conclude we would like to note that this regime is more sensitive in a single-shot detection of the gyroscopic effect due to the higher scale factor, compared to the previously shown generation regime with varying relative phase. On the other side, the Sagnac effect is not accumulated through roundtrips for this generation regime. By considering the resolution of both measurements and their dependence on the number of averaging roundtrips, we can infer that the generation regime in this *Section* is preferred when the required data frequency of the gyroscopic measurements surpasses 2 kHz. In addition, we also would like to note that the relative phase dynamics for this generation regime is more robust, yet still fluctuating due to the synchronisation dynamics between the counter-propagating pulses.

2.4 Summary

This *Chapter* has been dedicated to the development of the bidirectional mode-locked fibre lasers and their applications for gyroscopic measurements. We started by discussing the up-to-date cavity setups to achieve bidirectional mode-locking generation, emphasizing their advantages and limitations. Then, we presented the formation dynamics of counter-propagating pulses in the ring bidirectional mode-locked fibre laser. The presented experimental results demonstrate numerous complex non-linear dynamics, which affect the resulting generation regime. The existence of numerous phenomena and events indicates the potential of bidirectional ultrafast laser platforms to serve as an efficient test-bed for the investigation of complex dynamics in non-linear systems in general. This complex

dynamics can lead to a partial or full synchronisation of counter-propagating pulses in the bidirectional mode-locked laser. The understanding of underlying processes during pulse formation and stable mode-locking generation is essential for practical applications, transforming bidirectional ultrafast lasers into robust and versatile tools for gyroscopy and spectroscopy and a range of emerging applications.

In this *Chapter* we included a historical development and comprehensive analysis of the gyroscopic measurements in bidirectional mode-locked lasers. We also presented our results on measuring the dynamic angular velocities, provided by the stepper motor, with the use of the real-time measurement techniques. The spatio-temporal technique demonstrates the lowest resolution of the gyroscopic measurements due to the relatively long response time of the used photodetectors compared to the Sagnac-induced temporal shift. However, the experimentally obtained scale factor of 11.63 fs/(deg/s) is significantly enhanced compared to the classical Sagnac equations, which is an essential feature of the ultrashort pulses. We also demonstrated that no lock-in effect was observed for the counter-propagating pulses with different repetition rates. However, due to the colliding mode-locking, the scale factor of the gyroscopic measurements is strongly affected by the initial divergence rate between the counter-propagating pulses, while at a low divergence rate the pulses can be synchronised and transit into the generation regime with matched repetition rates.

Another approach for measuring the Sagnac effect, we demonstrated here, is based on the evaluation of the relative phase between the counter-propagating pulses. As expected, this interferometric method has a better resolution compared to the measurements in the time domain. We revealed that the pulses experience various phase responses to the angular movements, depending on the degree of synchronisation between the counter-propagating pulses. While the regime with synchronised repetition rates and varying relative phase has a lower scale factor and the angular resolution as a consequence, compared to the regime with constant relative phase, the Sagnac-induced phase shift is accumulated through roundtrips. Thus, the first regime is more suitable for sensitive detection at long time scales (data rates below 2 kHz) due to the accumulated effect, the other regime is preferred for measurements of dynamically varying angular velocity at data frequency above 2 kHz. The general drawback of both generations with matched repetition rates is that the colliding mode-locking hampers the temporal shift induced by the angular movements, limiting its overall performance for robust and continuous detection of angular velocity. Moreover, the phase measurements are sensitive to the fluctuation of the CEO phase between the counter-propagating pulses.

It is worth noting, that the experimentally obtained scale factor significantly exceeds the theoretical values, indicating a great potential of ultrashort pulses for gyroscopic measurements. Though the phase measurements of the Sagnac effect are more sensitive, this approach can be applied only for the bidirectional pulsed generation with the matched repetition rates, which inherits complex synchronisation dynamics and strictly constrain

to achieve a high enhancement factor. On the other hand, the spatio-temporal measurements demonstrated a higher enhancement factor by using the unsynchronised generation of ultrashort pulse, but this approach does not have a sufficient resolution. An eligible approach to achieve more reliable gyroscopic measurements with higher resolution is to measure the relative phase, given by the temporal shift as achieved by using the spatio-temporal technique, while the synchronisation dynamics of the counter-propagating pulses is strongly mitigated or, even, completely avoided. Thereby, we discuss other approaches to overcome these obstacles in the following *Chapters*.

Chapter 3

Gyroscopic Measurements in a Uni-directional Mode-locked Fibre Laser

In the previous *Chapter* we introduced experimental results on the Sagnac effect in a bidirectional mode-locked fibre laser by using the Dispersive Fourier Transform (DFT) technique. As found, ultrashort pulses experience a significantly increased response to the applied angular rotations, compared to the theoretical values based on the classic Sagnac equations, while the usage of the DFT allowed single-shot measurements with high precision. However, the colliding mode-locking and synchronisation dynamics of counter-propagating pulses in bidirectional mode-locked lasers strictly limit continuous gyroscopic measurements since the relative phase tends to return to its initial state. Considering this obstacle it is desirable to avoid this complex dynamics by exploiting other approaches.

In this *Chapter* we propose a novel approach to estimate the pulse-to-pulse phase shift of a pulse train, generated by a uni-directional mode-locked laser, using an external Mach-Zehnder Interferometer (MZI). The external MZI with unequal arms allows recording interference of consecutive pulses of the pulse train via the DFT, the relative phase of which corresponds to pulse-to-pulse phase changes. These pulse-to-pulse phase changes are further extracted from the interferometric pattern by using the method, proposed in the previous *Chapters*. This data on the pulse-to-pulse phase changes can be further used to characterise the phase stability of a mode-locked laser or, if the angular rotations are applied, to evaluate the Sagnac-induced phase shift. The description of the operational principle and the experimental setup is discussed in the *Section* 3.1. This technique allows achieving much higher data rates in the MHz region compared to the traditional methods for characterisation of the pulse phase, which are limited by 100 kHz [273; 274; 275] and also involve nonlinear conversion steps, limiting applicable peak power and pulse duration.

In the previous *Chapter*, we and other works on gyroscopic measurements in ultrafast lasers indicated that the performance of ultrafast gyroscopes is mostly limited by the

stability of the Carrier-Envelope Offset (CEO) phase. Thus, in *Section* 3.2 we firstly applied the proposed method to evaluate the phase dynamics of the pulse train from an Erbium-doped mode-locked fibre laser. We were able to detect phase oscillations of the output pulses, governed by fluctuations in the pulse intensity due to the Kerr-induced self-phase modulation. Measurements of the phase dynamics of an ultrashort pulse train are crucial for many applications, which require precision characterisation of the pulses such as frequency comb generation, metrology, high-field physics, and sensing applications. A comprehensive discussion on the advantages and limitations of the proposed technique is also presented.

In the case of applying angular velocity to the laser cavity, the pulse-to-pulse phase shift will acquire an additional phase shift related to the Sagnac effect. Thus, the proposed method is also can be used as a gyroscopic platform. In *Section* 3.3 we present the experimental results on the gyroscopic measurements, proving that this setup can serve for precise measurements of dynamics angular velocities. Moreover, we confirm that this approach is able to achieve better performance and lacks the disadvantages inherent in bidirectional laser cavity setups.

3.1 Experimental methodology and setup

In the *Introduction* we discussed how the CEO phase of a pulse train manifests in the temporal and frequency domains. We also indicated the significance of the CEO phase for high-field physics, attosecond science, and for precision measurements such as frequency metrology, optical clocks, and laser gyroscopes. Thus, it is crucial to detect and investigate the CEO phase dynamics of a pulse train.

The first attempt to evaluate the Carrier-Envelope Offset (CEO) phase was realised in work [157] by L. Xu in 1996. The phase slippage was obtained from the second-order cross-correlation of the consecutive pulses. However, cross-correlation is a time-consuming technique and cannot achieve single-shot measurements to characterise the phase evolution, providing only averaging phase slippage over a long period of time. Similar approaches to retrieve the phase change have been also described in other works [86; 276]. As we discussed in *Section* 1.5.2 the absolute value of the pulse-to-pulse phase slippage can be measured by the $f-2f$ interferometer, which also provide averaged value at data rates up to 100 kHz [274]. On the other hand, the above-threshold ionization technique is able to provide single-shot measurements, but the maximum achieved up-to-date data rate constituted 100 kHz [273]. Moreover, these traditional methods for absolute measurements of the CEO phase involve non-linear conversion steps, limiting applicable peak power and pulse duration. In Ref. [277] Authors have demonstrated that by retrieving the relative phase between consecutive pulses from the interferogram, it is possible to reconstruct the carrier-envelope phase. However, their spectral measurements did not allow them to achieve an evaluation of the relative phase with high resolution and data rates. To enable

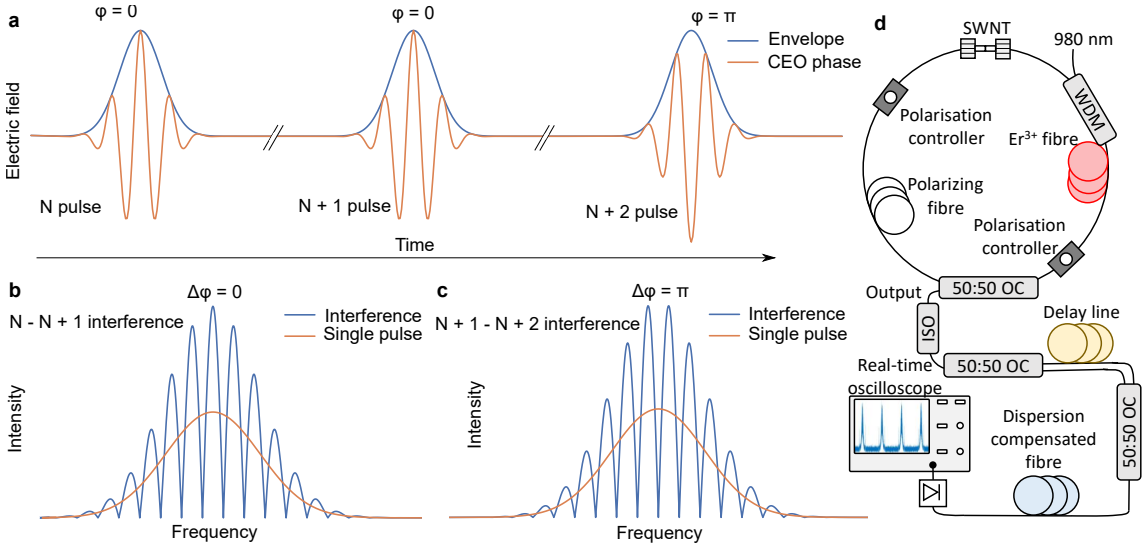

Figure 3.1: (**a**) An ultrashort pulse train with the carrier and envelope profiles. Spectrum of interference between (**b**) $N - N + 1$ and (**c**) $N + 1 - N + 2$ pulses with indicated relative phase between the pulses. (**d**) The measurement setup for evaluation of the phase dynamics of the pulse train generated in the mode-locked ring fiber laser. SWNT - single-walled carbon nanotubes, ISO - optical isolator, OC - optical coupler.

single-shot detection of absolute phase difference at high data rates, here we propose to apply the DFT technique to retrieve the phase changes from the interference of consecutive pulses. The main advantage of using the DFT technique is that it allows observing the single-shot spectra of each consecutive interference of a pulse train with a repetition rate of up to hundreds of MHz. Knowing the pulse slippage between each consecutive pulse, it is possible to reconstruct the total phase evolution.

Figure 3.1 demonstrates the operational basis for the evaluation of the phase dynamics of the pulse train from the interferogram. Figure 3.1(a) schematically shows train of three pulses, whose phases are 0, 0, and π. Figures 3.1(b) and (c) demonstrate spectral interference of N and N + 1, and N + 1 and N + 2 pulse pairs, correspondingly. As seen in Fig. 3.1(b) and (c), such sequential spectral interferograms contain the information on the phase slippage between the consecutive pulses, which is the CEO phase by the definition. Thus, by recording the single-shot interferogram between consecutive pulses we are able to reconstruct the complete pulse-to-pulse phase evolution of the pulse train.

The Erbium-doped fibre laser we used is the same we described in *Section* 2.2.1 and is shown in Figures 3.1(d). By adjusting the Polarisation Controllers (PC) we achieved a unidirectional generation in the CW direction with the average output power of 1 mW. The all-fibre MZI was realised via two 3-dB fibre couplers with an additional section of SMF-28 fibre in a delay arm. The length of the delay arm of the interferometer was 13.3 m which equals the cavity length. Therefore, the pulse train was delayed in one interferometer arm by one round-trip time. This allowed continuous recording of the interference of two consecutive pulses, similar to Fig. 3.1(a-c). The influence of the surrounding temperature fluctuations was negligible over the measured time scales.

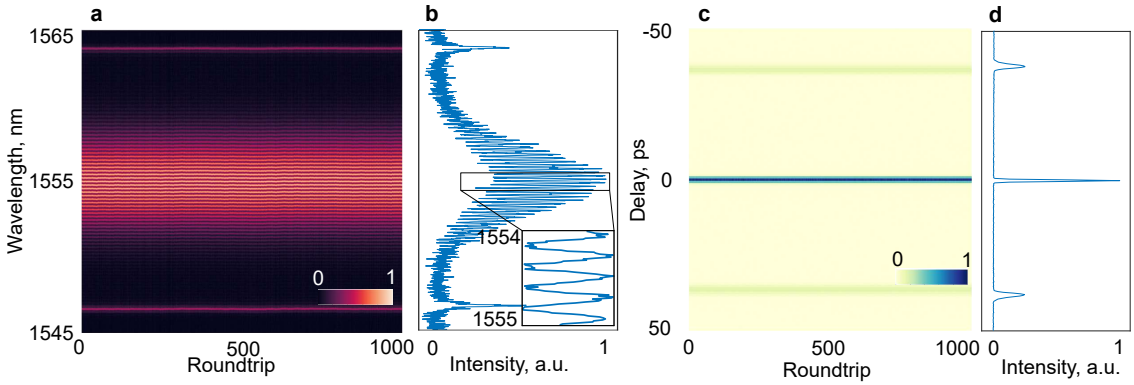

Figure 3.2: (**a**) Measured DFT spectra and (**c**) corresponding field autocorrelation function. Cross-section of (**b**) the DFT spectra and (**d**) the field autocorrelation function.

3.2 Phase dynamics of a pulse train

As we discussed, it is important firstly to evaluate the CEO phase dynamics of a pulse train. These measurements serve as phase noise of the laser, defining the performance of the gyroscope based on the setup. In the experiments, we have recorded 26.2 ms of consecutive interferograms, which correspond to around 390 000 round trips. Figure 3.2(a) demonstrates recorded single-shot spectral evolution of the interference over 1000 consecutive round trips. A typical cross-section of the DFT spectra is shown in Fig.3.2(b). Strong spectral modulation, depicted in more details in the inset in Fig. 3.2(b), indicates persistent interference between consecutive pulses. Figure 3.2(c) presents the corresponding 1000 round trips of the numerically obtained field Autocorrelation function (ACF). Figure 3.2(d) shows the autocorrelation function cross-section that reveals the presence of two pulses, separated by 36.5 ps.

By applying the fast Fourier Transform to the single-shot DFT spectra and exploiting the methodology for the relative phase evaluation described in *Section* 1.6.2, we retrieved an overall picture of the relative phase evolution, shown in Fig. 3.3. Since the pulse accumulates an additional phase shift due to the dispersion in the delay line of the MZI (0.239 ps/nm for 13 meters of SMF-28 fibre), the reference level could not be uniquely determined. Therefore, we assumed the value at the beginning of the recording as a zero reference level. As in the previous phase measurements, the resolution of the phase retrieval from the DFT spectra is estimated to a value of 1 mrad. More discussion on the resolution of the DFT measurements and the phase retrieval is presented in *Appendix* A.

Numerically, the recorded relative phase between the N and N + 1 pulses can be described as:

$$\Delta\phi = \phi_{N+1} - \phi_N - \delta\phi_{delay} \tag{3.1}$$

where $\delta\phi_{delay}$ is the additional phase accumulated by the delayed pulse in the delay arm of the interferometer. This additional phase is constant in time but is susceptible to environmental perturbations. To further minimise the temperature fluctuations on the

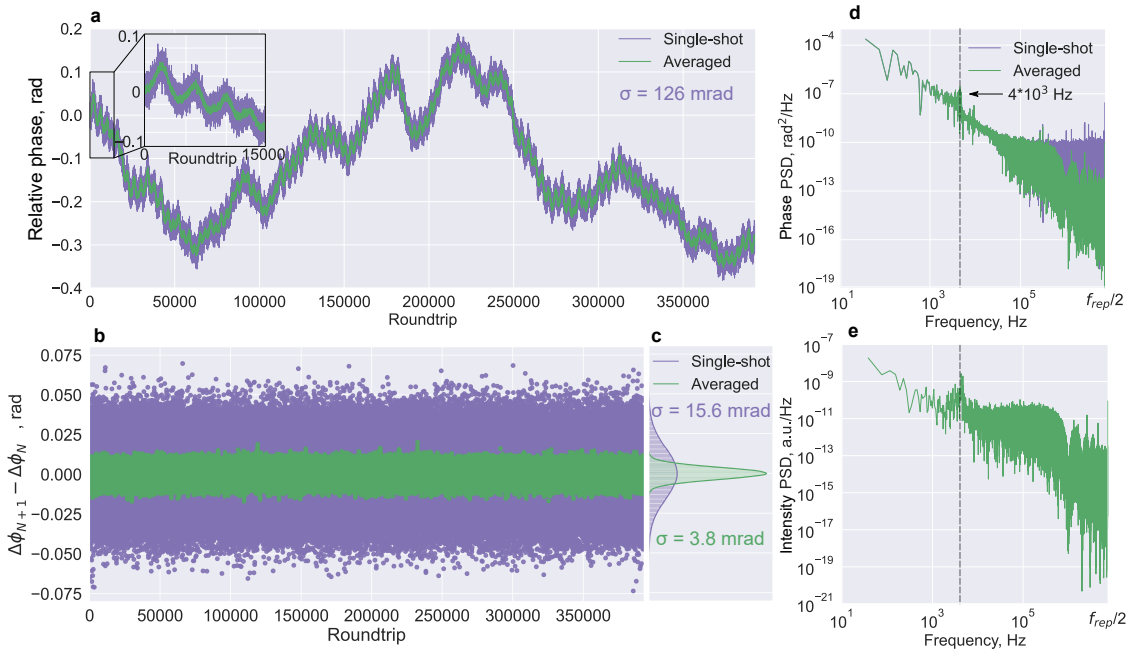

Figure 3.3: (**a**) Relative phase drift with the standard deviation of 126 mrad. Inset: crop of the first 15000 roundtrips that illustrates the phase oscillation of the pulse. (**b**) Pulse-to-pulse phase deviation with (**c**) probability density function. Power spectral density (PSD) of (**d**) the phase evolution and (**e**) the pulse intensity with indication of frequencies responsible for phase oscillations. All figures: violet - single shot; green - averaged with a moving window of 15 roundtrips.

$\delta\phi_{delay}$ we covered the delayed line into a foam box. Thereby, the absolute value of the pulse-to-pulse phase slippage remains unknown, the method is able to provide the variation (i.e. stability) of the phase slippage in time. In principle, the dispersion in the fibre interferometer can be compensated by implementing a dispersion-less delay line such as vacuum chamber [86; 157] and the absolute value of the CEO phase could be measured.

Figure 3.3(a) provides information on the changes of the pulse-to-pulse phase and characterises the short-term stability of the laser. As shown, the CEO phase tends to strongly fluctuate over time, which is expected for a free-running laser. The standard deviation of the relative phase change was observed to be 126 mrad. In the frequency domain, the standard deviation is transformed to the fluctuation of the CEO frequency of ∼300 kHz. In the temporal domain, this would correspond to the timing jitter of the pulse train of 132.6 as. Figure 3.3(b) shows the differentiation of the relative phase, representing the change of the phase slip for consecutive pulses. The standard deviation of the phase slip was 15.6 mrad, which corresponds to the timing jitter of 16.5 as at the central wavelength of 1555 nm. For the results with a moving averaging window of $n = 15$ roundtrips, the standard deviation and timing jitter reduced down to 3.8 mrad and 4 as, respectively. The corresponding histogram and the Probability Density Function (PDF), depicted in Fig. 3.3(c), obey the normal distribution law. The standard deviation decreases by $\sqrt{n}$ obeying the normal distribution, confirming the noise nature of the fluctuations in CEO phase.

The inset in Fig. 3.3(a) illustrates the phase oscillation dynamics of the output pulses zoomed over the first 15 000 round trips. The phase oscillates in the range of 50 mrad. The observed frequency of the phase oscillations corresponds to a peak at 4.6 kHz with 3-dB width of 570 Hz and 23 dB signal-to-noise ratio, as shown in the Power Spectral Density (PSD) in Fig. 3.3(d). The minimum frequency of the PSD is inversely proportional to the temporal span of the oscilloscope and corresponds to ∼39 Hz, limited by the storage memory of the oscilloscope. Figure 3.3(e) shows the PSD of the pulse intensity derived from the interference pattern. Frequency spikes at around 4.6 kHz observed in both PSDs support our assumption that the phase oscillations were caused by the pulse energy variations due to the Kerr-induced self-phase modulation [120; 152]. Pulses of different intensities experience different optical paths, and an additional phase shift, owing to the non-linear refractive index. The acquired non-linear phase could be obtained as [225]:

$$\phi_{NL} = n_2 k L |E^2| \tag{3.2}$$

where n_2 is the non-linear refractive index, L is the optical paths, E is the electric field, and $k = 2\pi/\lambda$ is the wavenumber with λ is the central wavelength. Owing to the pulse characteristics and using the above equation, the phase fluctuations of 50 mrad corresponds to the fluctuations of the pulse peak power of 1.2%. This result is in good agreement with experimental observations, which indicate about fluctuation of the pulse peak power of 1.6%. These oscillations were mediated by pump power instabilities and gain medium dynamics [278]. Note, a substantial suppression of noises at the frequency range higher than 100 kHz for the averaged values, which allows further increase of the phase resolution of the setup at a price of a reduced data frequency.

Additionally, the interferogram also provides information on the temporal separation between the pulses. Firstly, these fluctuations of the temporal spacing between consecutive pulses provide information on the timing jitter of the pulse train. Secondly, the data on the pulse separation could be used in addition to the phase measurements, for example, to evaluate the Sagnac effect in the temporal domain. However, the resolution of the temporal measurements is significantly lower compared to the phase measurements. The experimental results of the temporal pulse spacing are presented in *Appendix* D. We would like to note that the temporal spacing may vary each time we switch on the laser due to small differences in the central wavelength of the laser generation.

This novel approach possesses a simple setup, which is able to characterise the pulse-to-pulse stability of the CEO phase with the data frequency up to the MHz range. This method allowed observations of weak oscillations at 4 kHz of the output pulse phase that refers to the fluctuations in the pulse energy. The provided measurements are crucial for further application of the ultrafast laser for gyroscopic phase measurements, setting the uncertainty level and the resolution consequently.

This method, based on the recording of single-shot spectra using the DFT technique,

provides ∼40 times more accurate measurements than a similar approach, based on the spectrally and spatially resolved interferometry [277]. Moreover, this technique inherits several advantages compared to the most established methods for the absolute characterisation of the CEO frequency, including much higher data rates, a simpler linear setup with no limitations to input peak power or pulse duration. Besides, this method could be successfully expanded for other types of ultrashort pulses (e.g. dissipative solitons, similaritons, soliton molecules, and *etc.*), since the underlying physics and the numerical approach remain the same.

This technique could be supplemented by combination with other traditional methods of the CEO measurements, such as $f - 2f$ interferometer or above-threshold ionization method. While the traditional technique can unambiguously determine the reference level and provide measurements at a longer time scale, the DFT-based technique can characterise pulse-to-pulse dynamics of the CEO phase at MHz data frequency. Increased data rates and single-shot measurements are crucial for the investigation of field-driven dynamics in atoms [279], ion-ion coincidence imaging [280; 281], time-resolved photo-electron spectroscopy [282]. Additionally, the presented method allows a simple realisation of the cross-interference between two pulse trains, where the first laser is stabilised and serves as a reference level for the second laser or when the second laser is under investigation.

Importantly, as we discuss in *Appendix* A, the resolution of the method can be further increased by increasing the spectral resolution of the DFT or by increasing the Signal-to-Noise Ratio (SNR) via amplified-DFT [283]. An additional increase of the sensitivity can be achieved by suppressing the noises by averaging over longer round trip windrows. However, such improvement in sensitivity would come at a price of reduced data acquisition frequency. In addition, the increased resolution and the increased SNR will provide better resolution on the temporal separation between the pulses. Maintaining the all-fibre setup, a temperature-insensitive fibre interferometer can be used to eliminate the temperature fluctuations for the long-term operation [284]. We believe that the proposed method has a great potential to pave a novel avenue for phase-based applications at high data rates, including but not limited to high-field physics, imaging, optical coherence tomography, and sensing applications.

3.3 Gyroscopic Measurements

By using the same experimental setup and placing the laser on the rotational platform we provided gyroscopic measurements. Due to the angular rotation, in eq. 3.1 the N + 1 pulse will have an additional phase shift associated with the Sagnac effect compared to the previous N pulse, delayed in the interferometer. Since this technique registers pulse-to-pulse variations of the pulse phase (differential phase shift), the Sagnac-induced phase shift can not be accumulated through roundtrips. For example, in the case of a constant angular velocity, the relative phase will be shifted by a constant value from the reference

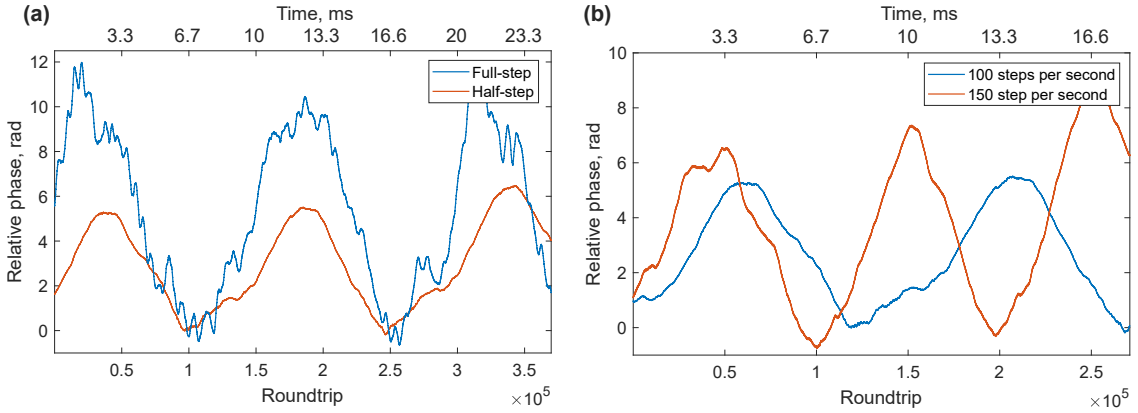

Figure 3.4: (**a**) Relative phase dynamics under rotational exposure by a stepper motor with full-step (blue line) and half-step size (orange line) at 100 steps per second (150 000 roundtrips or 10 ms per step). (**b**) Relative phase dynamics under rotational exposure by a stepper motor set to produce 100 steps per second (blue line) and 150 steps per second (100 000 roundtrips or 15 ms per step; orange line) at half-step size.

measurements, which is related to the Sagnac effect. Hence, the setup is operating similar to the one discussed in *Chapter* 2.3.2, resembling passive optical gyroscopes. Moreover, the setup should work in the same way if the rotational platform would rotate the delay arm of the MZI, inducing the Sagnac phase shift to the N pulse. Since only one pulse experiences angular rotations and accumulates the Sagnac phase, the total sensitivity is reduced by a factor of two compared to the classic Sagnac equation 1.5.

Similar to previous results, firstly we provided the reference measurements to determine the relative phase corresponding to the zero angular velocity. Figure 3.4(a) demonstrates the relative phase dynamics under the rotational exposure, applied by the stepper motor with full step and half-step sizes at 100 steps per second (150 000 roundtrips or 10 ms per step). This corresponds to the average angular velocity of the platform of 0.74 deg/s and 0.37 deg/s accordingly. The average phase shift per step is 4.27 rad and 2.11 rad, which corresponds to the angular shifts of 7.38 mdeg and 3.69 mdeg, respectively. The step profile is similar to the discussed in the previous *Chapters*. More information on the operational principles of the stepper motor is presented in *Chapter* 2.3.2.

The phase dynamics with different value of steps per second is shown in Fig. 3.4(b). The motor was set to produce 100 steps per second (150 000 roundtrips or 10 ms per step) and 150 steps per second (100 000 roundtrips or 6.67 ms per step). The observations provide a good temporal agreement between the set temporal duration of the step and the observed duration of the motor step cycle. These results confirm that by using this technique it is possible to observe continuously changing angular rotations. In addition, we did not observe any influence of the applied angular rotations on the pulse behaviour inside the laser cavity, as was observed in bidirectional mode-locked lasers and discussed in the previous *Chapter*.

We would like to note that the differentiation of the relative phase over time will provide information on the angular acceleration of the rotating platform. However, due to strong

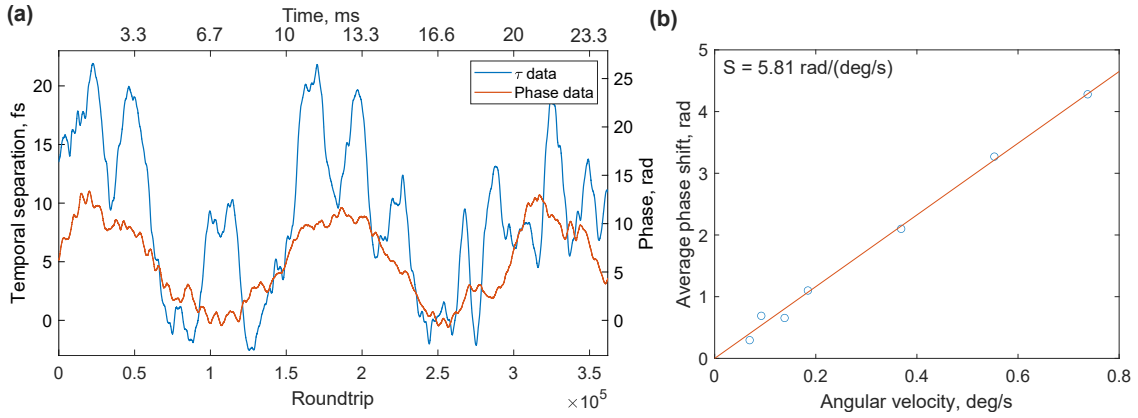

Figure 3.5: (**a**) Comparison of the data of the relative phase and the relative temporal separation between the pulses with a moving averaging window of 5 000 roundtrips extracted from the interferometric pattern. Phase data was converted to the temporal domain by using the phase-time relation. The motor was set to produce 100 steps per second at full-step size (150 000 roundtrips or 10 ms per step). (**b**) Experimentally obtained scale factor of 11.57 rad/(deg/s).

fluctuations of the CEO phase of the free-running laser, the acceleration information has a significant noises and should be highly averaged. The corresponding results on the angular acceleration of the platform, rotated by the stepper motor, are presented in *Appendix* D.2. Nonetheless, this experimental setup has the potency to simultaneously operate as an accelerometer.

Figure 3.5(a) presents the data on the relative phase and the relative temporal separation between the pulses extracted from the same interferometric pattern when the stepper motor was set to produce 100 steps per second at the full-step size. The phase data was transformed into the temporal domain by using the phase-time relation 1.4. Due to the low resolution of the temporal measurements of 7.7 fs, we used a moving averaging window with size of 5 000 roundtrips. Both measurements follow the step profile of the motor. However, some disagreement between both measurements and the strong oscillations of the temporal data are referred to the low temporal resolution of the measurements and significant timing jitter of the pulse train, shown in *Appendix* D.1.

The experimental relation between the applied average velocity and the average phase shift we observed during the experiment is shown in Fig. 3.5(b). The angular rotations were applied in the range from 69.1 mdeg/s (150 steps per second with 1/16 step size) up to 0.74 deg/s (100 full steps per second). The scale factor was estimated to be 5.81 rad/(deg/s) by using a linear approximation. This provides the resolution of the gyroscopic measurements of 21.7 mdeg/s (378.7 μrad/s). In the temporal domain, the scale factor is approximated to a value of 4.9 fs/(deg/s), based on the phase-time relation 1.4. This value is close to the observed in previous *Sections* 2.3.2 in the bidirectional fibre laser (11.63 fs/(deg/s) and 11.5 fs/(deg/s) for the spatio-temporal measurements and for phase-based measurements correspondingly), noting that the Sagnac response is two times smaller due to the unidirectional operation of the laser during these measurements.

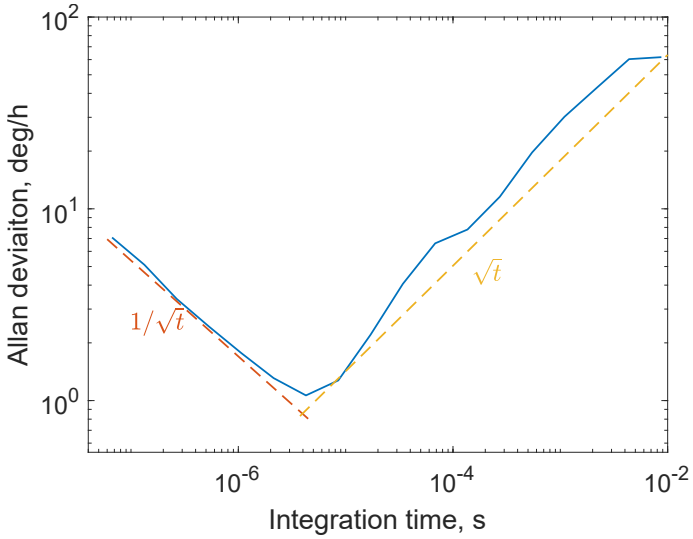

Figure 3.6: Allan deviation of the relative phase dynamics between consecutive pulses during the reference measurements.

The results of the Sagnac phase measurements are strongly affected by the fluctuations of the CEO phase, which we presented in the previous *Section* 3.2. To estimate the contribution of these fluctuations we calculated the Signal-to-Noise Ratio (SNR) using the eq. 2.8. For the angular velocity at 1 deg/s and the standard deviation of the phase noise of 126 mrad, the SNR is 33.3 dB and significantly exceeds the SNR of the bidirectional setups.

Further on, the gyroscope performance was assessed by calculating the Allan deviation of the CEO phase dynamics. The calculated Allan deviation of the phase dynamics is plotted in Fig. 3.6. Allan deviation has a downward trend proportional to $1/\sqrt{t}$ due to the averaging of the noises up to the integration time of 4.27 μs. This integration time corresponds to the bias instability of 1.06 deg/h at the data frequency of 234.2 kHz, when the gyroscopic setup can achieve the highest angular resolution before the fluctuations of the CEO phase start to dominate at longer time scales. This bias instability is two-fold better than the best results we achieved in a bidirectional setup. The same upward trend of $\sqrt{t}$ of Allan deviations as shown in previous *Chapter* is observed here, after the extremum point. Following the upward trend of Allan deviation, the Angular Random Walk (ARW) is estimated to a value of 661 deg/$\sqrt{h}$. Such a high value of the ARW is attributed to the significant fluctuations of the CEO phase in free-running mode-locked fibre lasers.

The calculated Allan deviation has only two strong trends, which are attributes of the noises during the measurements. These observations confirm that this setup is less susceptible to the complex pulse dynamics inside the unidirectional mode-locked fibre laser under rotation exposure, compared to the bidirectional counterparts.

Similar to the previous results, the maximum angular velocity which could be measured is limited by the maximum pulse spacing at which the interferometric pattern could be observed (eq. 1.29). For the range of the pulse spacing of 170 ps and the experimental

scale factor of 4.9 fs/(deg/s), the maximum applied angular velocity should not exceed 34.710^3 deg/s.

At the same time, the maximum pulse-to-pulse phase change should be smaller than π to avoid uncertainties in our measurements. This limits the maximum angular acceleration of the laser platform and can be calculated by using the eq. 2.9, giving a value of 8.11 Mdeg/s^2. As in the active gyroscopes based on bidirectional mode-locked lasers, the maximum angular acceleration could be increased by using the laser with a lower timing period of the pulse train, which comes at the cost of the lower sensitivity of angular velocity measurements.

The Sagnac response of the setup could be further two-fold improved by placing the delay arm of the MZI on the rotation platform in opposite direction to the pulse, circulating in the laser cavity. While the N pulse will accumulate the positive Sagnac shift, the N + 1 pulse acquires the Sagnac shift of different signs such that their relative phase will have a doubled Sagnac phase shift, also improving the SNR by 6 dB.

The disadvantage of the proposed gyroscope configurations is that it requires an additional passive interferometer in supplement to the mode-locked laser. The limitation to achieve higher angular sensitivity is strongly dependent on the stability of the CEO phase of the used ultrafast laser. On the other hand, the transition from bidirectional to unidirectional operation regime is a substantial step since the bidirectional mode-locked lasers have much more sophisticated cavity designs and still require further investigations for reliable application in precision measurements.

3.4 Summary

This *Chapter* was dedicated to overpassing the main obstacle of bidirectional mode-locked fibre laser such as the complex synchronisation dynamics of counter-propagating pulses under applied angular rotations. To realise this goal we proposed to use a unidirectional mode-locked fibre laser with an additional external unbalanced Mach-Zehnder Interferometer for continuous recording of the interferometric patterns between consecutive pulses. The external MZI allowed us to observe pulse-to-pulse variations of the pulse phase, which in the case of angular rotations will accumulate additional phase shifts associated with the Sagnac effect.

First of all, we would like to note that such an experimental setup turns out to be a powerful tool to investigate pulse-to-pulse variations of the pulse phase, which can find many applications beyond gyroscopic measurements. Compared to the traditional techniques for phase characterisation, this technique is able to operate at much higher data rates up to hundreds of MHz. So, we characterised the phase stability of the pulse train, generated by the free-running mode-locked laser, used for further gyroscopic applications. We were able to detect subtle phase oscillations related to the Kerr non-linearity due to the instabilities of the pump laser. As the main disadvantage, the demonstrated technique

is not able to detect the absolute values of the CEO phase due to the dispersion in the delay arm of the MZI. However, this obstacle could be eliminated by using a dispersionless optical path in the interferometer. A similar technique have been used to observe the temporal dynamics of the pulse during the self-starting process [285]. Though we presented a novel way to register phase dynamics of the pulse train and demonstrated proof-of-principle, such an approach requires further investigation and direct comparison with traditional techniques.

After characterising the phase stability of the pulse train of the used ultrafast fibre laser, we investigated the performance of the proposed setup for gyroscopic measurements. As expected, the proposed setup is able to detect the Sagnac phase shift. The proposed gyroscope design resembles a passive optical gyroscope, where the variation of the Sagnac phase shift through consecutive roundtrips is estimated. The scale factor is nearly twice as small as in bidirectional setup, which provides a good agreement since only one pulse accumulated the Sagnac phase shift. The estimated SNR is 33.3 dB with the angular resolution of 21.7 mdeg/s (0.38 μrad/s). The lower bias instability at the higher data frequency compared to the results achieved by using the bidirectional mode-locked fibre lasers, indicate that this setup has a higher potential for gyroscopic measurements. Moreover, unidirectional mode-locked lasers completely lack of the lock-in effect or synchronisation dynamics and their usage significantly simplifies the total setup owing to a much simpler cavity design compared to the bidirectional mode-locked lasers.

A similar setup could be obtained for gyroscopic measurements if the delay line of the MZI is placed on the rotational platform (passive gyroscope configuration). Moreover, by placing the delay arm on the rotation platform in opposite direction to the pulse, circulating in the laser cavity, it is possible to increase the Sagnac response of the setup by two times. However, the phase fluctuations will still preserve. We also would like to note, that the delay arm of the MZI also introduces additional noises inherent to optical gyroscopes such as the Kerr-induced phase noise, temperature fluctuations, and vibrations. However, its noises could be efficiently reduced in an active feedback loop [276].

The limiting factor for the long-term gyroscopic measurements is the high value of the ARW due to the strong fluctuations of the CEO phase. While the techniques for stabilisation of the CEO phase in unidirectional mode-locked lasers are well studied, it is not obvious if they could be effectively combined with mode-locked laser under rotation exposure. Hence, other techniques for mitigation of the CEO phase fluctuations should be implemented. In the following *Chapter* we consider another approach where we significantly reduce the problem of the phase fluctuations.

Chapter 4

Passive Gyroscope based on Ultrashort Pulses

In the previous *Chapters*, as well as in Ref. [214; 266], key findings indicated that the gyroscopic measurements are mostly limited by the fluctuations of the Carrier-Envelope Offset (CEO) phase of a pulse train. One of the straightforward conclusions is to actively and passively stabilise the frequency comb by the well-known methods [286; 287]. While passive stabilisation can decrease the effect of environmental fluctuations for a long time operation, precise active stabilisation of mode-locked generation is not so obvious, since the Sagnac-induced frequency offset hinders the applicability of the traditional active stabilisation techniques based on a feedback loop. So, other more sophisticated methods for stabilisation of the mode-locked generation should be proposed. In any case, to increase the sensitivity and performance of gyroscopes based on ultrafast lasers it is desirable to provide measurements that would be free from CEO phase fluctuations.

The generation of ultrashort pulses which would not suffer from the CEO frequency fluctuations is not a trivial task. One of the approaches is the difference frequency generation, which results in 'offset-free' pulses due to subtraction of the offset frequency during the non-linear process [288]. However, the whole process is cumbersome with resulting pulses at the central wavelength in the mid-infrared region which is not the best choice for gyroscopic measurements. In this *Chapter*, to cancel the fluctuation of the CEO phase we propose to use an external Mach-Zehnder Interferometer (MZI), placed on the rotation platform, representing a passive gyroscope. It is the first time, to for the best of our knowledge, the passive gyroscope operates on the basis of ultrashort pulse train. Here, we experimentally demonstrate that this approach is free from fluctuation of the CEO phase and lacks any synchronisation dynamics or lock-in effect while inheriting all the advantages of the ultrashort pulses for gyroscopic measurements, shown in previous *Chapters*. Moreover, the most prevailing technique for evaluation of the Sagnac effect in traditional Fibre-Optic Gyroscope (FOG) is the phase measurements, which allow us to assume that the combination of the ultrashort pulse train with the DFT interferometry would be the

most beneficial to be exploited in the passive gyroscope configuration.

4.1 Experimental setup

Figure 4.1 presents an experimental design of the passive gyroscope. The used Erbium-doped mode-locked fibre is the same as was presented in *Section* 2.2.1. The laser was operating in a unidirectional regime and produced almost bandwidth-limited ultrashort pulses with the duration of ∼570 fs at the repetition rate of 15 MHz and average output power of ∼1 mW. The output pulses were divided into two arms of the MZI, placed on the rotation platform. An additional polarisation controller was placed in one arm of the MZI to match the state of polarisation of both pulse replicas for achieving high modulation depths of the interferometric pattern. Both arms of the interferometer have almost equal lengths with a difference of a few millimeters in order to observe the interferometric pattern as given by the Eq. 1.29. To achieve higher Sagnac phase shift between both channels, we placed both interferometer's arms on the rotational platform in opposite direction, which increased the gyroscopic response by a factor of two. Moreover, this also decreases the influence of the temperature fluctuations on the measurements, since both arms were located at the same place. To further decrease the environmental fluctuations we covered the fibre coils of the interferometer with a foam box. Then, both arms are combined in the following coupler and the pulses were propagated through the dispersive line. The dispersive line is the 11 km of dispersive compensated fibre with total accumulated dispersion of -1200 ps/nm. Then the interferogram was recorded via 50 GHz photodiode and 33 GHz digital storage oscilloscope. The spectral resolution of the DFT is 0.02 nm and the resolution of the phase retrieval was estimated to a value of ∼1 mrad. More discussion on the DFT resolution in the presence of noises is presented in *Appendix* A.

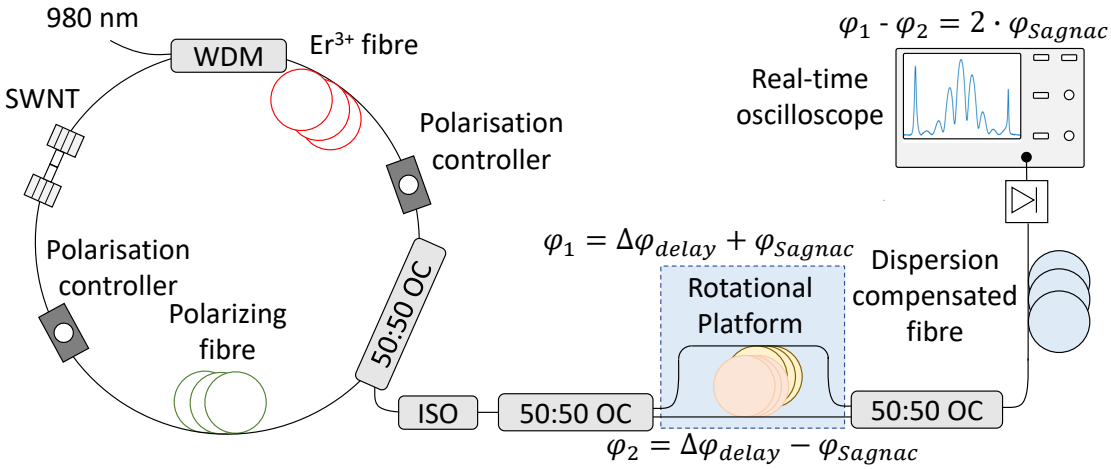

Figure 4.1: Experimental setup of the passive gyroscope based on ultrashort pulses. The passive gyroscope is realised as a Mach-Zehnder interferometer with equal arm lengths, placed on the rotational platform. SWNT - single-walled carbon nanotubes, ISO - optical isolator, OC - optical coupler.

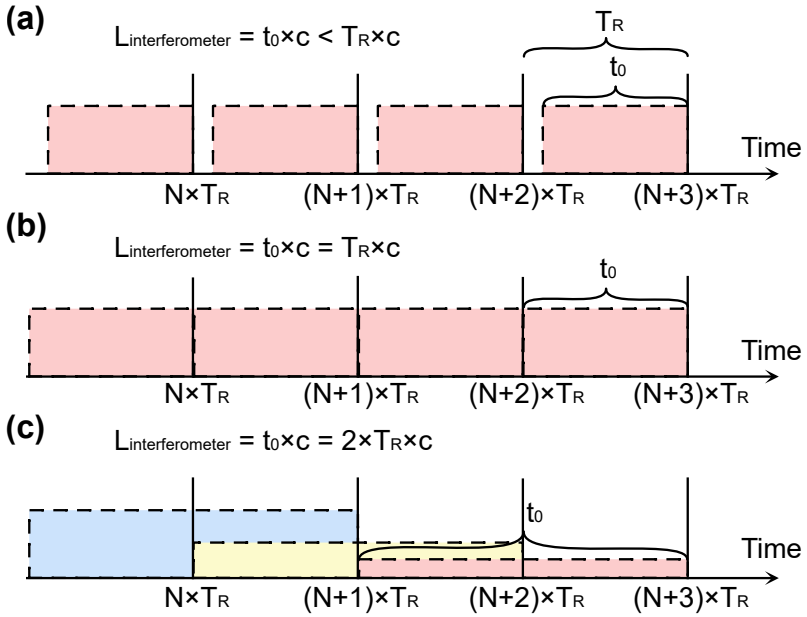

Figure 4.2: Schematic illustration of the pulse train. The shaded areas represent the time when the pulses accumulate the Sagnac effect while propagating in the interferometer. The data presented for the three cases: **(a)** length of the interferometer arms is smaller than the length of the laser cavity, **(b)** length of the interferometer arms is equal to the length of the laser cavity, **(c)** length of the interferometer arms is twice the length of the laser cavity. c is the speed of light.

The total length of each arm of the interferometer is 12.7 m. The length of the MZI was chosen to be close to the length of the laser cavity so that only one pulse is circulating inside the interferometer. If the length of the interferometer arms is shorter than the laser cavity, then it induces periodic time intervals when the gyroscopic effect is not measured. This is schematically illustrated in Fig. 4.2(a), where the unshaded area corresponds to the time intervals when the gyroscopic effect is not accumulated by the pulses. Thus, such configuration should be avoided. The case when the length of the interferometer arms is equal to the length of the laser cavity is shown in Fig. 4.2(b) and it can be seen that each pulse provides unique data on the Sagnac effect inside the interferometer. If the length of the interferometer is longer than the laser cavity (e.g. twice as long as the laser cavity as shown in Fig. 4.2(c)), then several pulses will circulate inside the interferometer and they would not provide unique data, but increase the data rate of the measurements.

Here we would like to note, that there is a conceptual limit between the data rate and the resolution of the gyroscopic measurement. Due to the physical limitations of the speed of light, the pulses cannot propagate through the interferometer at a higher speed than declared by the speed of light. Hence, for a certain amount of time, e.g. the time period between consecutive pulses in our case, the pulses can propagate through a limited optical path. Since the Sagnac effect is directly dependent on the total area covered by the optical pulses, its value is limited by the time period when the pulses propagate through the interferometer. This leads to a trade-off between the accuracy and the data rate of

the gyroscopic measurements. Thus, the interferometer with longer arms will not affect the single-shot resolution of the gyroscopic but will increase the gyroscope performance at a longer integration time.

At the same time, the length of both arms of the interferometer should be close in order to observe the interferometric pattern as given by the Eq. 1.29. The rotation platform has a circular shape with a radius of 0.315 m. The resulting area of the gyroscope is 2 m^2, which is slightly higher than for active gyroscope, discussed above, due to the slightly higher radius of the platform and the fact that all fibre was efficiently coiled on the platform in the circular shape.

The main advantage of this passive gyro setup is that it is free from the phase fluctuations of the incoming pulses. Owing to the fact that the pulse interferes with itself, the fluctuations of the input pulse phase are canceled out and do not affect the relative phase, extracted from the interferogram. Numerically, the phase of the pulse in each direction is $\phi_1 = \delta\phi + \phi_{delay1} + \phi_{Sagnac}$ and $\phi_2 = \delta\phi + \phi_{delay2} - \phi_{Sagnac}$, where $\delta\phi$ is the phase of the pulse at the input of the MZI, ϕ_{delay1} and ϕ_{delay2} is the accumulated phase in the different arms of the MZI and ϕ_{Sagnac} is the phase shift associated with the Sagnac effect (the sign depends on the direction of the angular rotation). The resulting relative phase is the difference between the phase of each pulse $\Delta\phi = \phi_1 - \phi_2 = \phi_{delay1} - \phi_{delay2} + 2\phi_{Sagnac} = \Delta\phi_{delay} + 2\phi_{Sagnac}$. Note, in case if only one arm of the interferometer is placed on the rotation platform, the Sagnac phase response will not be multiplied by a factor of two. The phase component $\Delta\phi_{delay}$ is responsible for the difference between the lengths of both arms of the interferometers and, ideally, remains constant over time. But, since the optical path can fluctuate over time, this phase term is the main source of fluctuations of the measurements. Additionally, the delay phase also depends on the carrier wavelength of the beam. However, the effect of the fluctuations of the central wavelength on the measurements is significantly reduced due to the small mismatch between the arms of the MZI. The fluctuation of the central wavelength can induce additional fluctuations to the obtained relative phase as we discussed in the *Appendix* A.

Another source of fluctuations is related to the classical non-reciprocal effects such as the Kerr effect. If the coupling ratio changes in time, the pulses will acquire different non-linear shifts and result in varying Δ_{delay} in time. The non-reciprocal fluctuations are arisen due to fluctuations of the division ratio of the optical coupler, which fluctuates with temperature. In addition, the division ratio of the optical fibre coupler is dependent on wavelength, which imposes restrictions on the stability of the central wavelength of the laser source.

Thus, the variations of the relative phase in such a measurement setup are mostly related to the acquired Sagnac phase shift, while the influence of noises are significantly compared to the previously shown setup. Therefore, we anticipate that this setup should operate in a similar manner as demonstrated in a previous *Chapter* with elimination of the problem of CEO phase fluctuations.

4.2 Gyroscopic measurements

The reference DFT measurements when the rotational platform is at rest are shown in Fig. 4.3(a). The interference with high modulation depths evidences the presence of two pulses. Figure 4.3(b) demonstrates the calculated relative phase dynamics with the corresponding Probability Density Function (PDF). To extract the information from the interferometric pattern we used the same procedure as described in *Section* 1.6.2. The standard deviation was 7.3 mrad that is equivalent to 8.7 as timing jitter at the central wavelength of 1555 nm. The standard deviation defines the smallest relative phase changes distinguished from the noises and represents the resolution of the proposed passive gyroscope. The lower value of the standard deviation, compared to the measurements in the active gyroscope with an external MZI, confirms that the oscillations of the CEO phase were efficiently suppressed, indicating a better potential for precise measurements. The residual fluctuations of the relative phase are related to the noises mentioned above.

We would like to note that the standard deviation in this setup is comparable to the numerically obtained value at the given Signal-to-Noise Ratio (SNR) of the measured DFT spectra, as discussed in the Appendix A. Moreover, at this limit, the fluctuations of the carrier wavelength are also converted into phase fluctuations due to the uncertainty in the determination of the central frequency (Appendix A). Nonetheless, the standard deviation, and the minimum resolution as a consecutive, could be further enhanced by $\sqrt{n}$ by averaging over n roundtrips, obeying the normal distribution for noises.

Figure 4.3 demonstrates the relative timing separation between the pulses from the MZI with a moving averaging window of 100 round trips, providing the temporal resolution of 0.7 fs. The average temporal separation is 4.35 ps with a standard deviation of 0.94 fs. The much lower value of standard deviation compared to the data from a uni-directional gyroscope, shown in *Appendix* D.1, evidences that this setup does not suffer from the timing jitter of the laser source. This result is expected since the timing jitter is converted into a temporal fluctuation of the arriving time of the pulse to the interferometer input, which does not significantly affect the measurements of the relative phase. However, due to the time-frequency duality of the DFT measurements, the timing jitter can induce uncertainties to the determination of the central wavelength of the interferometric pattern, converting to the fluctuations of the relative phase (Appendix A). However, that effect is not significant.

The timing jitter of the laser source can also affect the measurements of the platform acceleration, but its effect is sufficiently weak since the timing jitter is neglecting compared to the round trip time period. The uncertainty of the angular acceleration measurements due to timing jitter of the laser source can be estimated as $\Omega_{jitter} = \tau_{jitter}/T_{rep}$, where Ω_{jitter} is the uncertainty in the measurements of the angular acceleration due to the timing jitter, τ_{jitter} is the timing jitter and T_{rep} is the pulse timing period. So, the induced uncertainty in the measurements of 1% is caused by the timing jitter of 666.7 ps, which

is by several orders of magnitude lower than the timing jitter of free-running mode-locked fibre lasers.

To compare the influence of the external perturbations on the laser source in the passive gyroscope and the active gyroscope (*Chapter* 3), we recorded the relative phase dynamics in both configurations under vibration exposure, shown in Fig. 4.4(a). The vibrations were implemented as a soft mechanical shock in the plane perpendicular to the platform. Both setups experienced increased fluctuations of the relative phase compared to the reference measurements. The corresponding standard deviations are 364.6 mrad and 132.8 mrad for the active and passive gyroscope, respectively. It can be clearly seen, that

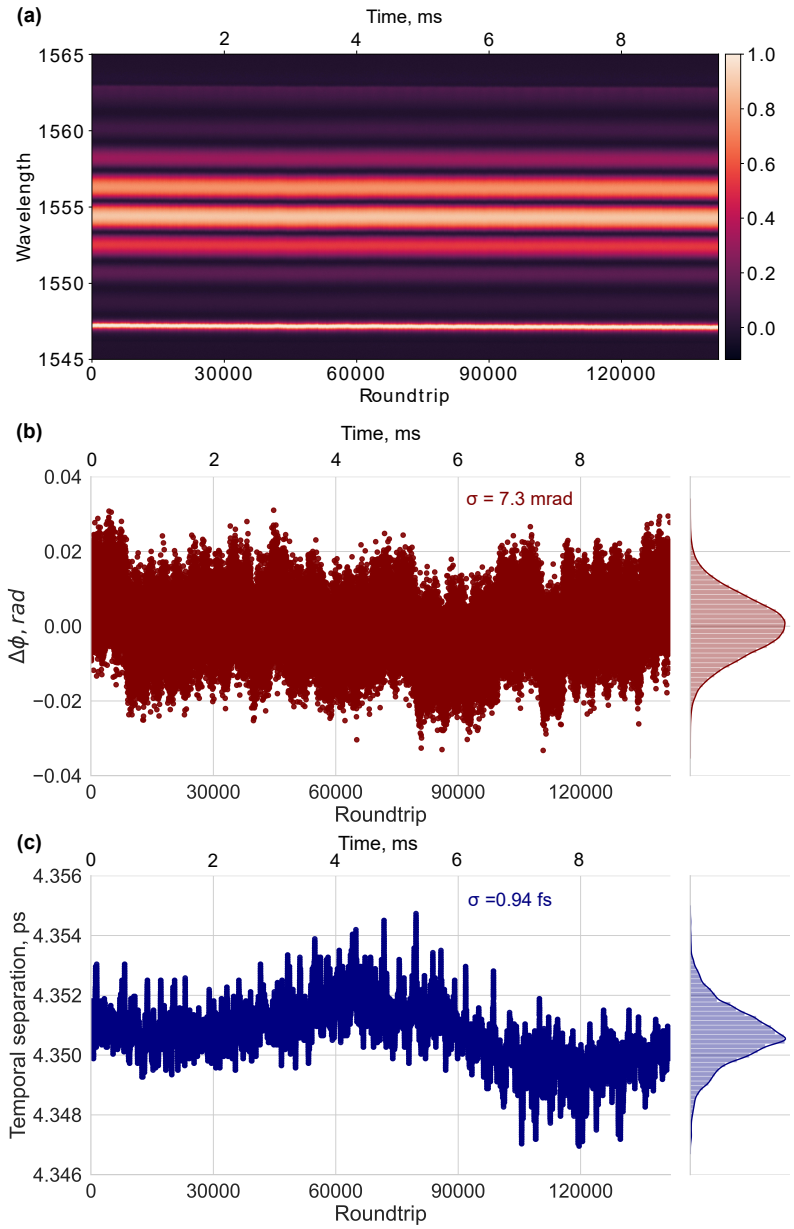

Figure 4.3: **(a)** The DFT measured spectra from balanced Mach-Zehnder-interferometer at rest. **(b)** The single-shot extracted relative phase with corresponding probability density function. The standard deviation of the relative phase is 7.3 mrad. **(c)** Temporal separation between the pulses with moving averaging window of 100 roundtrips.

the fluctuations are more pronounced in the active gyro setup. This is expected since in the active gyroscope the mechanical perturbations are directly converted into movements of the platform. The fluctuations of the relative phase in the passive configuration are mostly referred to the fluctuations of the central wavelength of the incoming pulses (the relation between the fluctuations of the central wavelength and the extracted relative phase we present in *Appendix* A). The corresponding Power Spectral Density (PSD) is shown in Fig. 4.4(b). A strong peak of the phase oscillations in the active gyroscope at frequencies in the kHz range is clearly visible, which is completely eliminated in the passive gyro. These oscillations refer to the fast fluctuations of the CEO phase. Moreover, the PSD of the passive gyroscope configuration is lower than the PSD of the active gyroscope throughout the entire frequency range presented. These results confirm that the proposed gyroscope design in this *Chapter* is less sensitive to the perturbation of the laser source, compared to the setup discussed in the *Chapter* 3. Thus, the proposed passive gyroscope is not highly affected by the perturbations and the stability, as a consequence, of the laser source.

The dynamics of the relative phase of the output pulses from the MZI during rotation exposure are shown in Fig. 4.5(a). The stepper motor was set to produce 300 steps per second (50 000 roundtrips or 3.33 ms per step) at the full-step size and half-step size. The average phase shift per step is 47.22 rad and 23.08 rad, which corresponds to the average angular velocity of the motor of 2.14 deg/s (7.14 mdeg per step) and 1.07 deg/s (3.57 mdeg per step), respectively. The step profile does not inherit complex profile due to higher angular velocity, which enforces the coils of the stepper motor to switch faster. Figure 4.5(b) present the phase measurements at different speeds of the stepper motor. The motor was set to produce 300 steps per second 200 steps per second (75 000 roundtrips or 5 ms per step). The obtained average shift at 200 full steps per

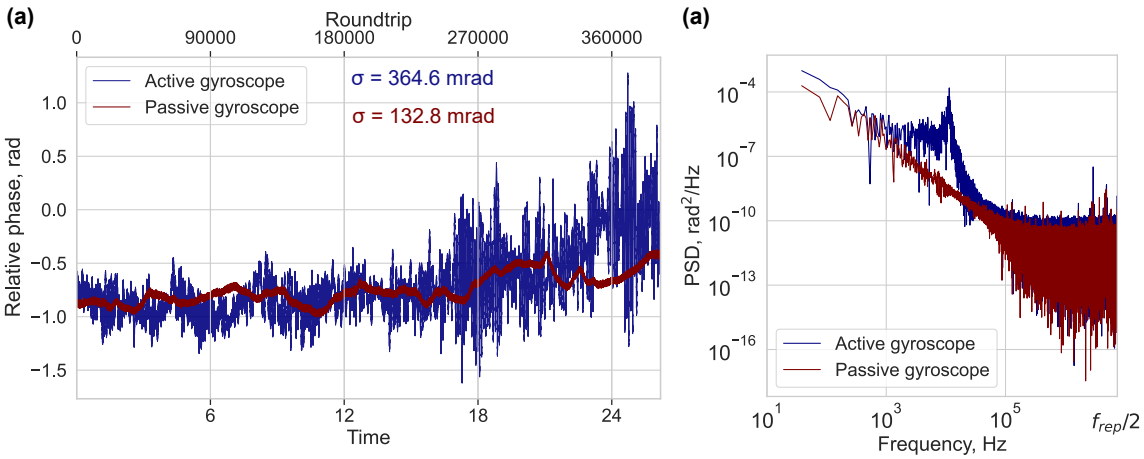

Figure 4.4: **(a)** Relative phase dynamics of the pulses in the active (blue line) and passive (red line) gyroscope configuration under vibration exposure with standard deviation of 364.6 mrad and 132.8 mrad, respectively. **(b)** The corresponding power spectral density of the phase evolution during vibration exposure.

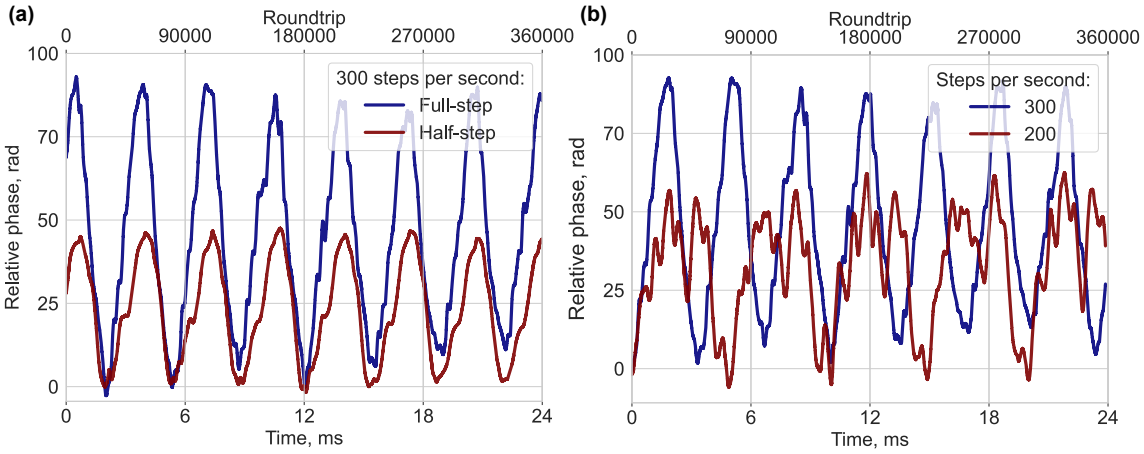

Figure 4.5: (**a**) Relative phase dynamics under rotational exposure by a stepper motor with full-step (blue line) and half-step size (red line) at 300 steps per second (50 000 roundtrips or 3.33 ms per step). (**b**) Relative phase dynamics under rotational exposure by a stepper motor, set to produce 300 steps per second (blue line) and 200 steps per second (75 000 roundtrips or 5 ms per step; red line) at full-step size.

second is 32.73 rad. The observations provide a good temporal agreement between the set temporal duration of the step and the observed duration of the motor step cycle. The motor step at the setting of 200 steps per second starts to experience a complex two-peak angular profile, but as we will demonstrate later, this can be resolved due to higher resolution of this setup compared to the previous results. As expected, the presented passive gyroscope configuration does not have any synchronisation dynamics or lock-in effect. These observations confirm that ultrashort pulses could be effectively used for gyroscopic measurement in a passive configuration.

Comparison of the data on the relative phase and the relative temporal position between the pulses at the output of the MZI, extracted from the same interferometric pattern, is shown in Fig. 4.6(a). To plot the relative phase in the time domain we transformed the phase data by using the phase-time relation 1.4. While the single-shot resolution of the temporal measurements of 7.7 fs is the same as in the previous *Chapters*, due to the mitigation of the timing jitter of the laser source both data demonstrate a good agreement even without averaging. The average temporal shift is 39.82 fs, corresponding to a disagreement with the phase data of only 4%. Such a good agreement between both measurements supports our results on gyroscopic measurements. Furthermore, both data of relative phase data and temporal measurements can be simultaneously used to increase the total resolution of the setup.

The scale factor of the passive gyroscope configuration was estimated from a linear approximation between the applied average angular velocity and the observed average shift of the relative phase depicted in Fig. 4.6(b). The applied angular rotation was ranging from 89.3 mdeg/s (200 steps per second at 1/16 step size) up to 2.14 deg/s (300 full steps per second). The resulting scale factor is 21.98 rad/(deg/s) or 18.02 fs/(deg/s) using the phase-time relation 1.4, which is closed to the observed scale factors in previous

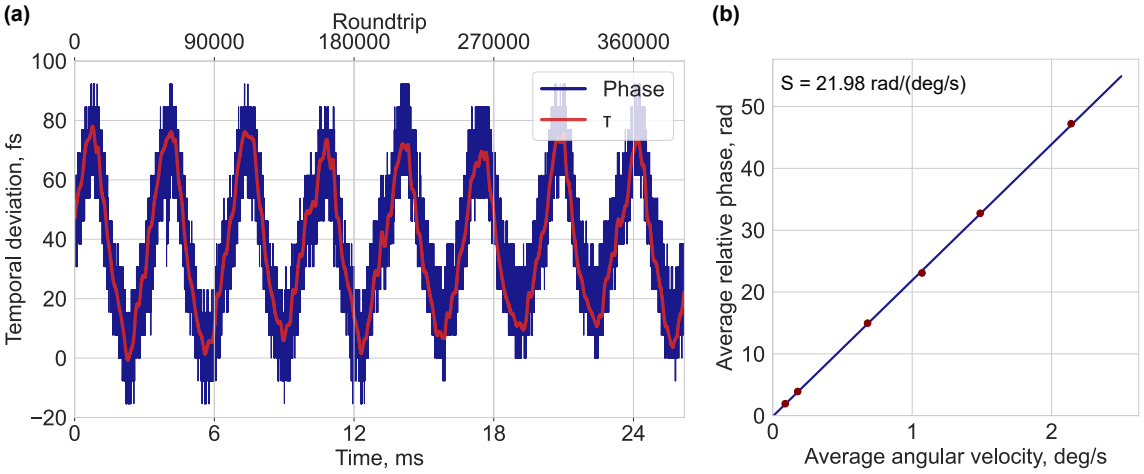

Figure 4.6: (**a**) Dynamics of the relative phase (red line) and the relative temporal separation (blue line) between the pulses from the interferometer extracted from the same interferometric pattern. The phase data was converted to the temporal domain by using the phase-time relation. The motor was set to produce 300 steps per second at full-step size (50 000 roundtrips or 3.33 ms per step). (**b**) The experimentally obtained relation between applied average angular velocity and the observed average shift in relative phase with linear approximation. The resulting scale factor is 21.98 rad/(deg/s).

Chapter, considering the slightly higher total area of the passive gyroscope.

As was discussed before, the maximum detectable angular velocity is limited by the range of inter-pulse temporal separation when the interferometric pattern is preserved. This temporal range can be estimated to be ≈170 ps by using eq. 1.29. For the experimentally obtained scale factor of 18.02 fs/(deg/s), the maximum velocity is limited by 9.0410^3 deg/s. The maximum observable angular velocity could be further increased proportionally to the spectral resolution of the DFT.

Additionally, restrictions are applied for the maximum angular acceleration of the platform. The acceleration of the platform could be calculated by differentiation of the data on angular velocity over roundtrips and presented in Fig. 4.7. The single-shot resolution of the acceleration is defined by the eq. D.1 to 4.98 kdeg/s^2. The resolution is increased by an order of magnitude compared to the previous results due to the higher scale factor and lower standard deviation of the phase measurements. However, this resolution is not enough to measure the acceleration of the stepper motor and we used a moving averaging window over 10 000 roundtrips which provide the resolution of ∼5 deg/s^2. The theoretical average acceleration during the first half of the step cycle is 2571.4 deg/s^2 while the experimentally obtained value is 2253.5 deg/s^2. The error between these two results is mostly due to the step profile of the stepper motor. This can be seen from Fig. 4.7, that the step cycle has the acceleration with a positive sign of longer time duration than the half of the cycle and longer than a further deceleration of the platform. The resulting average acceleration per step is -12.7013 deg/s^2, which is close to zero with a residual mistake of around 0.56% related to the mean value of acceleration. The measurements of angular acceleration are significant as they provide more information about the dynamics

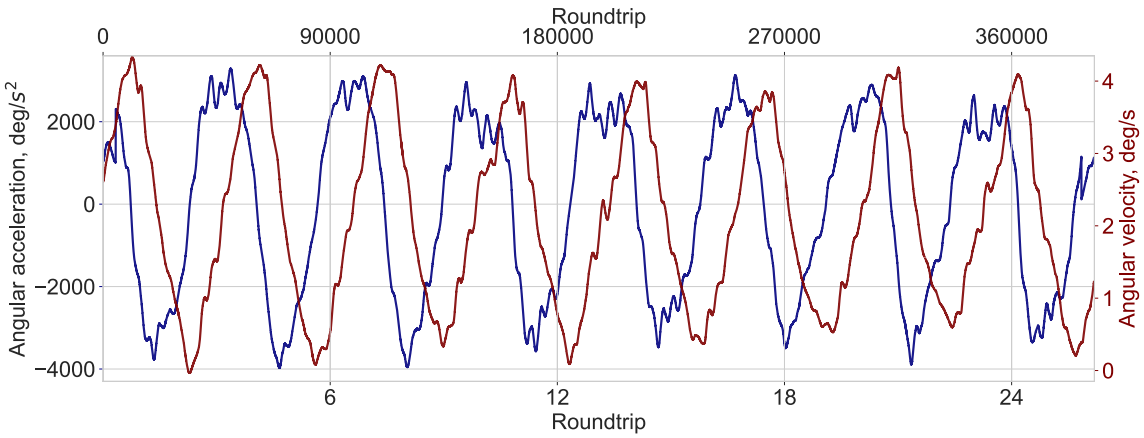

Figure 4.7: Angular acceleration (blue line) and angular velocity (red line) of the laser platform during rotation exposure by the stepper motor. The motor was set to produce 300 full steps per second (50 000 roundtrips or 3.33 ms per step). The acceleration was obtained by differentiating the velocity over a window of 10 000 roundtrips to increase the resolution.

of the platform.

Similar to previous results, the maximum applied angular acceleration is restricted to the value of 2.14 Mdeg/s^2 using the eq. 2.9. As in active gyroscopes, the maximum angular acceleration could be increased by using the laser with a higher repetition rate, but dissimilar to active gyroscopes, this approach will not affect the resolution of the angular velocity measurements in a passive gyroscope configuration. Moreover, the higher repetition rate of the ultrafast laser source will also result in a higher data frequency of the gyroscopic measurements. Thus, for more precise measurements of the angular acceleration, laser sources with a lower timing period between pulses are preferred.

Finally, we estimate the performance of the proposed passive gyroscope for measurements of angular velocities. The angular velocity resolution in single-shot measurements is estimated to be 0.33 mdeg/s (5.8 μrad/s), based on the scale factor of 21.98 rad/(deg/s) and the standard deviation of the reference measurements of 7.3 mrad. Due to the strong mitigation of the CEO phase noise, the resolution is increased by two orders of magnitudes compared to the results of unidirectional gyroscopic measurements. The calculated Signal-to-Noise Ratio (SNR) from eq. 2.8 is also significantly improved from 33.3 dB up to 69.6 dB.

For the full description of the gyroscope performance, we calculated Allan deviation and demonstrate it in Fig. 4.8. Calculated Allan deviation shows two strong trends, which are related to the noises of the system. The minimum Allan deviation of 0.06 deg/h, which is the bias instability, is observed at the integration time of 17.07 μs. So, the maximum resolution could be achieved at the data rate of 58.6 kHz. The lower bias instability confirms that the proposed passive gyroscope is able to provide almost 50 times more accurate resolution of the angular rotation than the best results achieved in the previous measurements. The higher integration time is explained by the fact that the

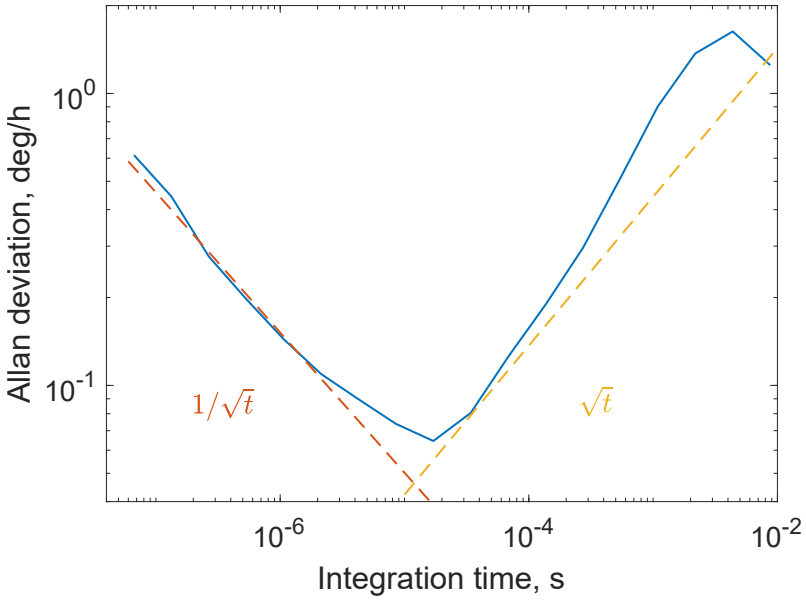

Figure 4.8: Allan deviation of the relative phase dynamics in a passive gyroscope during the reference measurements.

noises of the measurement equipment could be averaged more efficiently over a longer time period before the noises with long correlation time start to dominate [56]. However, Allan deviation of these measurements at the integration time of 4.27 μs, where the minimum of Allan deviation was observed in the unidirectional gyroscope presented in *Chapter* 3, is 0.09 deg/h which is also by an order of magnitude more accurate. The estimated Angular Random Walk (ARW) is 13.38 deg/$\sqrt{h}$. The significantly decreased value of the ARW is achieved due to the mitigation of the long-term fluctuations of the CEO phase.

Such a low value of the bias instability is close to meet the requirements for laser gyros used for navigation purposes [37; 208]. Additionally, the presented here passive gyro is able to provide the measurements at data rate by orders of magnitude higher than even the fastest commercially available gyroscopes. We would like to note that this is the first realisation of a passive gyroscope based on ultrashort pulses for demonstration of the possibilities of the proposed setup, while many improvements can be implemented for further enhancement of the gyroscope performance. For example, the gyro performance can be further increased by providing active and passive stabilisation of both the laser source and the arms of the interferometer. Through stabilising technique, we estimate that Allan deviation will follow the downward trend as $1/\sqrt{t}$ until the integration time of around 1 s with estimated bias instability of $\sim$ 0.27 mdeg/h. At integration time longer than 1 s residual noises, which could not be eliminated by the feedback loop, start to dominate. Moreover, the stabilisation will also significantly reduce the value of the ARW.

For a comprehensive analysis of the proposed gyro configuration for further improvement, we should consider the interferometer with longer optical paths. The longer arms of the MZI will increase the scale factor and benefit the angular velocity resolution without affecting the data rate. Considering the Sagnac eq. 1.5 for the phase shift, the scale factor

increases proportionally to the total area of the fibre coil, which increases as L^2. However, if we consider the same form factor of the interferometer, the scale factor will increase proportionally to the first order of the length. Moreover, to account for the additional noise induced by higher gyro length, we provided an estimation for the case if the scale factor will increase proportionally to the $\sqrt{L}$. Thus, a typical length of fibre optic gyroscope of 500 m will provide the bias instability of less than $5 \cdot 10^{-5}$ deg/h for a passive gyroscope with the same form factor.

At the same time, if the arms of the interferometer are longer than the laser cavity, several pulses will circulate inside the MZI as we discussed above and schematically shown in Fig. 4.2(c). Several circulating pulses in the interferometer arms will not contain completely unique data and, as a sequence, will not affect the total gyroscopic resolution, but will provide higher data rates and more obtained data. More data points could be averaged to increase the resolution and lower the integration time at which the bias instability occurs. Additionally, the higher data rate will also benefit the resolution of the angular acceleration measurements. Thus, mode-locked lasers with high repetition rates (e.g. harmonic mode-locking [241; 289; 290] or microcavities [291; 292]) are very attractive for further applications as a laser source. Such lasers inherit worse stability performance compared to more traditional mode-locked fibre lasers, but as we demonstrated, the passive gyroscope configuration is less dependent on the input pulse parameters. However, the upper limit of the applicable data rate is set by the DFT measurements, which is limited by ∼40 MHz in our measurements.

The performance of the proposed gyroscope can be also increased by using polarisation-maintaining fibre, which is commonly used in passive optics gyroscopes. Moreover, a temperature-insensitive interferometer, shown in Ref. [284], can substantially decrease the ARW and provide better performance over the long time scales.

The disadvantage of passive gyroscope configurations is that they require an additional passive interferometer in supplement to the laser source. On the other hand, such configuration does not suffer from the main source of noises discussed in the previous *Chapters* while inherent all the advantages of using the ultrashort pulses. Moreover, this approach requires a unidirectional mode-locked laser, which is well studied to perform accurate measurements in many applications.

4.3 Summary

In this *Chapter*, we implemented a passive optic gyroscope, operating on the basis of ultrashort pulses. The passive gyroscope is realised in a simple all-fibre design, consisted of the balanced MZI and a uni-directional free-running mode-locked fibre laser. We confirmed that the passive gyro configuration lacks the main limitation of active gyroscopes such as fluctuations of the CEO phase and timing jitter. Thus, we experimentally confirm our conjecture that the passive gyro configuration is less dependent on the stability

performance of the used laser source.

This *Chapter* also contains the gyroscopic measurements in the proposed setup. The results demonstrated good agreement with the previous *Chapters*. Moreover, the relative phase data has an excellent agreement with the data on temporal separation, extracted from the same interferometric pattern. The experimentally obtained scale factor is 21.98 rad/(deg/s) is higher than the one we observe in uni-directional gyroscope considering the higher total area of the passive gyroscope. The agreement between the results in passive and active gyroscope configurations using different real-time measurement techniques (spatio-temporal and the DFT) provides a conclusion that the increased response of the ultrashort pulses to the angular movements is a general phenomenon and should be further investigated.

The suppression of the CEO phase allows us to increase the single-shot resolution of the passive gyroscope down to 0.33 mdeg/s (5.8 μrad/s) and achieve the SNR of 69.6 dB. The bias instability of 0.06 deg/h is achieved at the integration time of 17.07 μs, which corresponds to the optimal data frequency of 58.6 kHz. The ARW constituted 13.38 deg/$\sqrt{h}$. These results on significantly improved gyroscope performance help us to conclude that our goal of the *Chapter* to eliminate the problem of the CEO phase fluctuations have been successfully achieved. At the same time, the passive gyro preserves all the advantages, indicated in previous *Chapters*. Moreover, this setup can operate at higher data rates without affecting the angular resolution. If a better resolution of the angular acceleration or a higher data rate is required, the laser sources with repetition rates from hundreds of MHz up to tens of GHz could be used. However, this would require a further optimisation of the DFT measurements.

Further works should consider passive and active stabilisation of the laser source and the passive interferometer. The scale factor and the gyroscope performance could be also increased by using longer arms in the MZI. We estimated that these amendments can reduce the bias instability below $5 \cdot 10^{-5}$ deg/h. Furthermore, the usage of polarisation-maintaining fibre or temperature-insensitive fibre will also benefit the bias instability and the ARW. The gyro performance with the proposed measuring technique could also benefit from the simultaneous extraction of the relative phase and the relative temporal spacing between the pulses.

Chapter 5

Overall discussion and conclusion

Laser development has a significant impact on the modern world we live in today. Modern lasers deliver versatile optical parameters and play a crucial role in various interdisciplinary fields, ranging from material processing to communications and optical clocks. Of particular interest are the mode-locked lasers, which generate a particularly stable train of ultrashort pulses. Nowadays, mode-locked lasers have proven their unparalleled performance and reached their maturity to benefit society by impacting science, medicine, and industry, by substituting the lasers with continuous-wave generation. Despite this progress, the growing demands of modern technologies require further improvements, pushing the investigation of mode-locked lasers into new applications. In the thesis, we have explored the niche of gyroscopic measurements and interferometry in general, by combining recent development in conjugate areas such as fast electronics and ultrafast lasers. The combination of both these areas allows achieving new insights on gyroscopic measurements and other applications based on phase measurements in general.

We started the thesis by providing a historical perspective of gyroscopes and up-to-date setups, which use ultrashort pulses. While different works on ultrafast gyroscopic measurements exploit different types of ultrashort pulses and measuring techniques, they all are based on bidirectional mode-locked lasers. Thus, we firstly investigated bidirectional mode-locked fibre laser and the inter-cavity behaviour of counter-propagating pulses by using the single-shot spectral and intensity measurement techniques. The experimental results revealed the complex dynamics of counter-propagating pulses, which highlight the significance of colliding mode-locking and the sophistication of bidirectional lasers. The experimental observations are particularly important due to the lack of efficient numerical models. These experimental results on the spectral evolution of pulses deepen the knowledge of soliton collisions in non-linear systems. From a practical point of view, the results provide a better understanding of pulse interactions inside the cavity, benefiting the further design of bidirectional mode-locked fibre lasers and their optimisation for intracavity measurements.

We observed three different generation regimes in the bidirectional mode-locked fibre laser. With the use of the Dispersive Fourier Transform (DFT) technique, we were able

to particularly investigate two generation regimes with the matched repetition rates: with partially-locked frequency combs with different Carrier-Envelope Offset (CEO) frequency; and fully-locked counter-propagating frequency combs with matched CEO frequencies. Each of the generation regimes inherits unique complex synchronisation dynamics between counter-propagating pulses. Moreover, we observed that the generation of fully-locked counter-propagating frequency combs experiences much lower phase fluctuations than the same laser operating in the uni-directional regime (*Chapter* 3). This can be understood as a self-stabilisation of the frequency combs due to the colliding mode-locking. However, some residual oscillations in the CEO phase may preserve due to the synchronisation dynamics.

Further on, in *Chapter* 2 we investigated each of the generation regimes for the gyroscopic measurements by rotating the bidirectional fibre laser. We demonstrated that the response of ultrashort pulses to the angular rotations is significantly enhanced compared to the classic Sagnac equations and affected by the generation regime. Interestingly, for the generation regime with the unsynchronised repetition rates of the counter-propagating pulses, we observed that the scale factor is dependant on the difference between repetition rates. While this phenomenon resembles the lock-in effect, it does not limit the minimum detectable angular velocity. Unfortunately, due to the mismatch in the repetition rates of counter-propagating pulses of this generation regime, we were not able to provide the DFT measurements, both for investigating the generation regime and to provide phase-based gyroscopic measurements with better resolution than the spatio-temporal technique.

Although all the observed generation regimes are sensitive to the applied angular rotations, the synchronisation dynamics strictly limit their applicability to provide continuous and reliable detection of the Sagnac effect. This principal problem could be solved by mitigating the influence of the colliding mode-locking on the pulse synchronisation dynamics while designing the cavity setup. However, at the same time in order to achieve the continuous interference of the counter-propagating pulses via the DFT, both pulses should have exactly matched repetition rates, restricting the design of the laser cavity.

To achieve more reliable detection of the Sagnac effect in *Chapter* 3 we decided to transit from a bidirectional to a uni-directional cavity setup. The move away from the traditional bidirectional setups for gyroscopic measurements is a conceptual step and allows to significantly simplify the overall gyro setup. We proposed a novel technique to measure single-shot pulse-to-pulse phase slippage. The proposed setup conjoins the principles of the first attempts to detect the CEO phase and the DFT interferometry. In terms of gyroscopic application, such a setup exhibits the two-fold lower bias instability at the lower integration time compared to the results achieved in the bidirectional ultrafast gyroscope, while lacking the synchronisation dynamics or lock-in effect. The main limitation for the precision phase measurements was imposed by the fluctuations of the CEO phase of the free-running mode-locked laser. An evident solution is the phase stabilisation of the output pulses down to sub milliradian level. However, the active feedback loop will

interfere with changes in the output pulses imposed by the Sagnac effect in the presence of angular movements. This is a conceptual limitation and requires further investigation to achieve high stability in the presence of angular rotations. Aside from the gyroscopic capabilities, this setup for the single-shot phase measurements is a powerful tool to investigate the pulse-to-pulse phase evolution and the stability of the pulse train and can be potentially spread for many phase-based applications. While this setup was demonstrated to confirm the proof of principle, with further amendments it would be able to detect the absolute measurements of the CEO phase and to potentially substitute the traditional techniques.

Since the stabilisation of an active bidirectional ultrafast gyroscope is a non-trivial task, we decided to explore the passive gyro configuration. While it seems a straightforward solution, it was the first demonstration of a passive gyroscope operating on the ultrashort pulses. The lack of works on passive ultrafast gyroscopes is due to the reason that the previous works have been mostly focused on the beat-note measurement technique, which cannot be applied in passive gyro configuration. Our suggestion to investigate the passive gyroscope was supported by the fact that the phase measurement of the Sagnac effect is the dominating technique in passive gyroscopes. Hence, the ultrashort pulse interferometry via the DFT interferometry is the perfect tool for gyroscopic measurements in the passive gyro configuration. Indeed, we experimentally confirmed that the passive gyroscope inherits all the previously obtained benefits of using the ultrashort pulses such as increased response to the Sagnac effect and high data rates. And what is even more important, the main advantage of the ultrafast passive gyroscope is that it is not sensitive to the fluctuations of the CEO phase of the input pulse train. Thus, we conclude that passive ultrafast gyroscope based on the DFT interferometry is the best choice for exploiting the ultrashort pulses in order to achieve the best performance at the highest available data frequencies. The drawbacks of this setup are typical for passive gyroscopes. First, the passive configuration requires both the laser source and the passive interferometer. However, this implementation and its stabilisation still are much easier compared to the bidirectional mode-locked lasers. The second drawback is that the Sagnac-induced phase shift is not accumulated through roundtrips in passive gyro configurations. This limitation can be compensating by constructing the passive interferometer with long arms, the length of which can reach several kilometers in traditional fibre optic gyroscopes.

The summary of the achieved performances by using the various gyro setups during the project and comparison to other works is shown in Table 5.1. As shown, the achieved performance during this project significantly surpasses the previously demonstrated results on gyroscopic measurements based on ultrafast fibre lasers. The previous works on gyroscopic measurements based on ultrashort pulses mostly used traditional techniques for the detection of the Sagnac effect. Such approaches do not allow to extract the entire potential of ultrashort pulses. Compared to the previous works based on real-time measurement techniques, we achieved a better resolution at higher data frequency by im-

Table 5.1: Summary of the presented gyroscope performances with comparison to other ultrafast gyroscopes.

Cavity configuration	Gyroscope length/area	Measurement method	Scale factor	Single-shot resolution	Bias instability / Integration time	Stability performance	Advantages	Disadvantages
Bidirectional mode-locked gyroscope with different repetition rates	13.5 m / 1.2 m^2	time delay	11.63 fs/(deg/s)	1074.8 deg/s 18.76 rad/s	32.2 deg/h 8.7 ms	Angular random walk 343.8 deg/$\sqrt{h}$	Simple setup Accumulation of the Sagnac effect	Low angular resolution Require bidirectional laser
Bidirectional mode-locked gyroscope partially-locked generation	13.5 m / 1.2 m^2	DFT interferometry	0.0361 rad/(deg/s)	318.6 mdeg/s 5.5 mrad/s	24.2 deg/h 0.14 ms	Angular random walk 353.5 deg/$\sqrt{h}$	High data rate Accumulation of the Sagnac effect	Require bidirectional laser Synchronisation dynamics of pulses
Bidirectional mode-locked gyroscope fully-locked generation	13.5 m / 1.2 m^2	DFT interferometry	3.79 fs/(deg/s) 4.62 rad/(deg/s)	3.66 mdeg/s 63.9 μrad/s	2.3 deg/h 34.1 μs	Angular random walk 239.6 deg/$\sqrt{h}$	High data rate	Require bidirectional laser Synchronisation dynamics of pulses
Uni-directional mode-locked gyroscope with unbalanced MZI	13.5 m / 1.2 m^2	DFT interferometry	4.77 fs/(deg/s) 5.81 rad/(deg/s)	21.69 mdeg/s 378.5 μrad/s	1.06 deg/h 4.27 μs	Angular random walk 661 deg/$\sqrt{h}$	Do not require bidirectional mode-locked laser	Strong fluctuations of the CEO phase
Passive gyroscope with balanced MZI	13.5 m / 1.2 m^2	DFT interferometry	18.02 fs/(deg/s) 21.98 rad/(deg/s)	0.33 mdeg/s 5.8 μrad/s	0.06 deg/h 17.07 μs	Angular random walk 13.38 deg/$\sqrt{h}$	Do not require bidirectional mode-locked laser	
Bidirectional mode-locked gyroscope [214]	4.59 m / 0.79 m^2	beat-note	6.95 kHz/(deg/s)	-	100 deg/h $>$ 1 s	beat-not standard deviation 193 Hz	Well-established and simple method	Low stability due to fluctuation of the CEO frequency
Bidirectional mode-locked gyroscope based on generation of dark solitons [264]	69.5 m / 5.22 m^2	beat-note	3.31 kHz/(deg/s)	-	183.8 deg/h $>$ 1 s	zero bias drift 72 Hz	Better stability of dark solitons and simple method	Sophisticated generation regime
Bidirectional mode-locked gyroscope with different repetition rates [266]	13.5 m / 1.2 m^2	time delay	0.885 ns/(deg/s)	-	79.6 deg/h 666.7 μs	Timing jitter $<$ 0.8 ps	Simple setup Accumulation of the Sagnac effect	Low angular resolution Require bidirectional laser
Bidirectional mode-locked gyroscope with partially-locked generation [266]	13.5 m / 1.2 m^2	DFT interferometry	0.017 kHz/(deg/s)	-	25.9 deg/h 333.3 μs	-	High data rate Accumulation of the Sagnac effect	Sensitivity to the CEO phase Require bidirectional laser
Bidirectional mode-locked Ti:sapphire laser [25]	4 m / 1 m^2	beat-note	57.3 kHz/(deg/s)	-	0.05 deg/h $>$ 1 s	-	Well-established and simple method	Require bidirectional mode-locked bulk laser

proving the method for phase extraction and investigated the gyro performance in different gyro configurations.

In the Table 5.1 we also included the comparison to the best-achieved results on gyro performance in bulk bidirectional mode-locked laser. While bulk ultrafast gyroscope has a slightly better performance than our first demonstration of the passive ultrafast gyro, the methods we used allow obtaining data rates by orders of magnitudes higher, while further optimisation of the passive gyro setup has a strong potential to overcome the performance of the bulk competitors.

The presented summary Table 5.1 allows us to conclude that passive fibre gyroscope, based on ultrashort pulses with phase measurements via the DFT interferometry, is the best candidate to provide high angular resolution at high data rates. But, is the performance of the ultrafast fibre gyroscope, demonstrated in this project, sufficient enough to compete with traditional laser gyroscopes based on the continuous-wave generation? Unfortunately, not at the presented stage of development. And further investigations is required in order to maximise and optimise the performance of ultrafast gyroscopes to compete with traditional optical gyroscopes. However, even at the presented stage of development, ultrafast gyroscopes significantly surpass by orders of magnitude the data frequencies of their competitors. This feature can be used in applications that require high data frequencies alongside with high accuracy. Additionally, this feature allows to simultaneously record the data on the angular acceleration of the platform. The proposed phase measurement techniques could be also widely expanded to such applications as measurements of refractive index, air flow, acoustic noises, displacement measurements, and scatterometry [25]. Additionally, the proposed methodology could be also used as a laser vibrometer to investigate vibration frequencies in the MHz range.

Below we provide our assumptions and suggestions for further investigations which should be considered in order to improve the performance of the DFT interferometry and the demonstrated ultrafast gyroscopes. In general, a lot of further amendments and studies should take place in order to extract the full potential of the proposed system. The first and the most important is to further investigate the response of optical wave packets such as ultrashort pulses to the applied angular rotations. In this project, we have indicated that ultrashort pulses have a significantly increased response to the applied angular movements compared to the expected values obtained from the classic Sagnac equations. These observations have been confirmed by using the spatio-temporal and the DFT measurements in both passive and active gyroscope configurations. Only a few works have investigated the propagation of wave packets in moving media with anomalous dispersion and these works have indicated that ultrashort wave packets may experience an additional phase shift in supplement to the classic Sagnac equations. This provides a further enhancement of the scale factor in the gyroscope with the same form factor and highlights the potential of the ultrashort pulses for gyroscopic measurements. The following works are necessary to comprehensively study this enhancement factor for various

types of ultrashort pulses with different parameters, propagating in a dispersive media in the presence of the non-linear effects.

From the engineering point of view, optimisation of the laser source and passive interferometer will significantly benefit the overall performance. First of all, a passive interferometer with longer arm lengths should be considered since the Sagnac effect is linearly proportional to the optical length of propagation (if the same form factor is considered). In traditional Fibre-Optic Gyroscope (FOG) the length of interferometer typically ranges from 0.5 km up to 2 km, which is 40-150 times longer than the interferometer presented in the *Chapter* 4. This approach will significantly benefit the gyroscope performance at longer time scales. However, the peculiarities of soliton propagation in optical fibres should be taken into account. Additionally, the DFT line can be implemented inside the passive interferometer and serve as the interferometer's arms.

Another significant aspect of the ultrafast passive gyroscope is a proper choice of a source of ultrashort pulses. As we stated before, laser sources with higher repetition rates will result in a higher data rate of the gyroscopic measurements, which could be converted into lower integration time or improvement of the bias instability. Additionally, this will increase the accuracy of measurements of angular acceleration. From this perspective, lasers with high repetition rates such as semiconductor lasers, electro-optic lasers, harmonic lasers, and lasers based on microcavities could be a perfect choice. Nevertheless, regarding the gyroscope resolution, the central wavelength of the laser source should be stabilised, which is well studied for uni-directional mode-locked laser and could be efficiently implemented.

As was previously mentioned, the division ratio of the optical couplers and the length of the passive interferometer should be stabilised to achieve higher performance at longer time scales. In addition, some established techniques from traditional FOG, summarized in Ref.[21], could be successfully adopted for ultrafast gyroscopes. Last but not least, a more advanced optical fibre should be also used in order to suppress polarisation and intensity instabilities, and temperature fluctuations.

Another essential element is the optimisation of the DFT measurements. As we discussed in *Appendix* A, an improvement in the accuracy of the phase retrieval could be achieved by increasing the SNR of the DFT signal. The resulting SNR of the provided measurements is mostly limited by three constituents: SNR of the laser used, losses in the interferometer and in the DFT line, and noises of the measuring equipment. The SNR of the laser source depends on the intracavity losses and the generation regime and has been discussed in *Chapter* 1.5.2. The losses of the interferometer arise due to two couplers and several fibre splices and could not be mitigated. However, in our experiments, we used only one output from the interferometer, while the simultaneous use of both outputs can benefit the overall performance of the phase retrieval accuracy. Additional losses are preserved during the pulse propagation in the dispersive media and could be minimised by using an optimised setup with optimised dispersion for achieving the desirable resolution

(e.g. the length of the DFT fibre coil). At the first glance, the SNR could be improved by increasing the input power. Unfortunately, the input power should be limited in order to avoid fibre non-linearities and preserve the original pulse spectrum. The solution is to use an amplifier, based on the stimulated Raman scattering, which does not induce spectral changes to the pulse under investigation [196]. Our simulation also demonstrated that it would be possible to achieve continuous phase measurements with adequate resolution at GHz data rates by optimising the measuring setup. Moreover, other techniques for phase retrieval should be investigated. For example, if the temporal pulse separation is relatively small, their relative phase will directly affect the total spectral energy recorded via the DFT, which can be used to ease the process of the phase retrieval in a presence of noises.

We also would like to note, that the data, contained in the interferometric pattern such as the pulse separation, the relative phase, and the amplitude ratio, could be simultaneously retrieved and used to increase the efficacy of the approach. The usage of this entire data on the pulses along with more advanced data processing techniques such as machine learning will allow to further increase the accuracy of the phase retrieval.

Thus, we provided a general investigation on the usage of ultrashort pulses with the DFT technique for phase measurements and gyroscopic measurements particularly. This thesis has significantly developed the ultrafast fibre gyroscopes and the DFT interferometry by demonstrating a range of setups for evaluation of the Sagnac effect and by significantly advancing the current state-of-the-art performance. All the gyroscopic setups demonstrated an increased response of the ultrashort pulses to the applied angular movements. We indicated the pros and cons of the proposed technique and provided recommendations for further investigations and potential applications. Meeting all indicated improvements with further research will allow ultrafast gyroscopes to contend with the established optical gyroscopes and even to surpass their performances. We hope that the work detailed in the thesis will contribute to the development of ultrafast lasers and gyroscopes. We also anticipate that this project highlighted the potency of the DFT interferometry and its application will expand to other phase-based measurements, where high accuracy and data rates are required.

References

[1] K. Kieu and M. Mansuripur, "All-fiber bidirectional passively mode-locked ring laser," *Optics Letters*, vol. 33, no. 1, pp. 64–66, 2008. 7, 53, 54, 57

[2] N. Abdukerim, M. I. Kayes, A. Rekik, and M. Rochette, "Bidirectional mode-locked thulium-doped fiber laser," *Applied Optics*, vol. 57, no. 25, pp. 7198–7202, 2018. 7, 53, 54

[3] C. Ouyang, P. Shum, K. Wu, J. H. Wong, H. Q. Lam, and S. Aditya, "Bidirectional passively mode-locked soliton fiber laser with a four-port circulator," *Optics Letters*, vol. 36, no. 11, pp. 2089–2091, 2011. 7, 54

[4] A. A. Krylov, D. S. Chernykh, N. R. Arutyunyan, V. V. Grebenyukov, A. S. Pozharov, and E. D. Obraztsova, "Generation regimes of bidirectional hybridly mode-locked ultrashort pulse erbium-doped all-fiber ring laser with a distributed polarizer," *Applied Optics*, vol. 55, no. 15, pp. 4201–4209, 2016. 7, 54, 55

[5] M. Chernysheva, M. Al Araimi, H. Kbashi, R. Arif, S. V. Sergeyev, and A. Rozhin, "Isolator-free switchable uni-and bidirectional hybrid mode-locked erbium-doped fiber laser," *Optics Express*, vol. 24, no. 14, pp. 15721–15729, 2016. 7, 54, 55, 57, 63, 72, 86

[6] Y. Ma, B. Xu, H. Ishii, F. Meng, Y. Nakajima, I. Matsushima, T. R. Schibli, Z. Zhang, and K. Minoshima, "Low-noise 750 mhz spaced ytterbium fiber frequency combs," *Optics letters*, vol. 43, no. 17, pp. 4136–4139, 2018. 17

[7] J. F. Wagner and A. Trierenberg, "The machine of bohnenberger," in *The History of Theoretical, Material and Computational Mechanics-Mathematics Meets Mechanics and Engineering*, pp. 81–100, Springer, 2014. 21

[8] L. Foucault, "Sur les phénomènes d'orientation des corps tournants entraînés par un axe fixe à la surface de la terre," *CR Acad. Sci*, vol. 35, p. 424, 1852. 21

[9] J. B. Scarborough, *The Gyroscope*. Interscience Publ., 1958. 21

[10] W. R. Johnson, "Description of an apparatus called the rotascope, for exhibiting several phenomena and illustrating certain laws of rotary motion," *American Journal of Science and Arts (1820-1879)*, vol. 21, no. 2, p. 264B, 1832. 21

[11] G. Sagnac, "L'ether lumineux demontre par l'effet du vent relatif d'ether dans un interferometre en rotation uniforme," *Comptes Rendus*, 1913. 22

[12] G. SAGNAC, "Sur la preuve de la realite de l'ether lumineux par l'experience de l'interferographe tournant," *C. R. Acad. Sci.*, vol. 157, pp. 1410–1413, 1913. 22

[13] M. Laue, "Über einen versuch zur optik der bewegten körper," *Münchener Sitzungsberichte*, vol. 12, pp. 405–412, 1911. 22

[14] W. Pauli, *Theory of relativity*. Courier Corporation, 2013. 22

[15] W. M. Macek and D. T. M. Davis, "Rotation rate sensing with traveling-wave ring lasers," *Applied Physics Letters*, 1963. 22

[16] C. Hadziioannou, P. Gaebler, U. Schreiber, J. Wassermann, and H. Igel, "Examining ambient noise using colocated measurements of rotational and translational motion," *Journal of Seismology*, vol. 16, no. 4, pp. 787–796, 2012. 23

[17] K. U. Schreiber, T. Klügel, J.-P. R. Wells, R. B. Hurst, and A. Gebauer, "How to detect the chandler and the annual wobble of the earth with a large ring laser gyroscope," *Physical Review Letters*, vol. 107, p. 173904, Oct 2011. 23

[18] F. A. Karwacki, M. Shishkov, Z. Hasan, M. Sanzari, and Hong-Ling Cui, "Optical biasing of a ring laser gyroscope with a quantum well mirror," in *IEEE 1998 Position Location and Navigation Symposium (Cat. No.98CH36153)*, pp. 161–168, 1998. 24

[19] J. A. Geen, "Dithered ring laser gyroscope with residual lock-in error compensation," 1986. US Patent 4,606,637. 24

[20] H. Kanamori, H. Yokota, G. Tanaka, M. Watanabe, Y. Ishiguro, I. Yoshida, T. Kakii, S. Itoh, Y. Asano, and S. Tanaka, "Transmission characteristics and reliability of pure-silica-core single-mode fibers," *Journal of lightwave technology*, vol. 4, no. 8, pp. 1144–1150, 1986. 24

[21] V. Passaro, A. Cuccovillo, L. Vaiani, M. De Carlo, and C. E. Campanella, "Gyroscope technology and applications: A review in the industrial perspective," *Sensors*, vol. 17, no. 10, p. 2284, 2017. 24, 30, 138

[22] H. J. Arditty and H. C. Lefevre, "Sagnac effect in fiber gyroscopes," *Optics letters*, vol. 6, no. 8, pp. 401–403, 1981. 25

[23] A. Tartaglia, "General relativistic corrections to the sagnac effect," *Physical Review D*, vol. 58, no. 6, p. 064009, 1998. 25

[24] A. Ori and J. E. Avron, "Generalized sagnac-wang-fizeau formula," *Physical Review A*, vol. 94, p. 063837, Dec 2016. 25

[25] L. Arissian and J.-C. Diels, "Intracavity phase interferometry: frequency combs sensor inside a laser cavity," *Laser & Photonics Reviews*, vol. 8, no. 6, pp. 799–826, 2014. 26, 84, 89, 136, 137

[26] A. Kaplan and P. Meystre, "Enhancement of the sagnac effect due to nonlinearly induced nonreciprocity," *Optics Letters*, vol. 6, no. 12, pp. 590–592, 1981. 26

[27] L. V. Hau, S. E. Harris, Z. Dutton, and C. H. Behroozi, "Light speed reduction to 17 metres per second in an ultracold atomic gas," *Nature*, vol. 397, no. 6720, pp. 594–598, 1999. 26

[28] U. Leonhardt and P. Piwnicki, "Ultrahigh sensitivity of slow-light gyroscope," *Physical Review A*, vol. 62, no. 5, p. 055801, 2000. 26, 93

[29] M. S. Shahriar, G. S. Pati, R. Tripathi, V. Gopal, M. Messall, and K. Salit, "Ultrahigh enhancement in absolute and relative rotation sensing using fast and slow light," *Physical review A*, vol. 75, p. 053807, May 2007. 26, 93

[30] D. D. Smith, H. Chang, L. Arissian, and J. C. Diels, "Dispersion-enhanced laser gyroscope," *Physical Review A*, vol. 78, p. 053824, Nov 2008. 26, 93

[31] P. Eliseev, "Theory of nonlinear sagnac effect," *Opto-Electronics Review*, vol. 16, no. 2, pp. 118 – 123, 2008. 26

[32] J. Hendrie, M. Lenzner, H. Afkhamiardakani, J. C. Diels, and L. Arissian, "Impact of resonant dispersion on the sensitivity of intracavity phase interferometry and laser gyros," *Optics Express*, vol. 24, no. 26, pp. 30402–30410, 2016. 26, 93

[33] H. N. Yum, M. Salit, J. Yablon, K. Salit, Y. Wang, and M. S. Shahriar, "Superluminal ring laser for hypersensitive sensing," *Optics Express*, vol. 18, pp. 17658–17665, Aug 2010. 26

[34] T. Qin, J. Yang, F. Zhang, Y. Chen, D. Shen, W. Liu, L. Chen, X. Jiang, X. Chen, and W. Wan, "Fast-and slow-light-enhanced light drag in a moving microcavity," *Communications Physics*, vol. 3, no. 1, pp. 1–8, 2020. 26, 94

[35] M. J. Grant and M. J. F. Digonnet, "Enhanced rotation sensing and exceptional points in a parity–time-symmetric coupled-ring gyroscope," *Optics Letters*, vol. 45, pp. 6538–6541, Dec 2020. 26

[36] G. Stedman, "Ring-laser tests of fundamental physics and geophysics," *Reports on progress in physics*, vol. 60, no. 6, p. 615, 1997. 28

[37] W. Chow, J. Gea-Banacloche, L. Pedrotti, V. Sanders, W. Schleich, and M. Scully, "The ring laser gyro," *Reviews of Modern Physics*, vol. 57, no. 1, p. 61, 1985. 28, 130

[38] K. U. Schreiber and J.-P. R. Wells, "Invited review article: Large ring lasers for rotation sensing," *Review of Scientific Instruments*, vol. 84, no. 4, p. 041101, 2013. 28

[39] S. Ezekiel and S. Balsamo, "Passive ring resonator laser gyroscope," *Applied Physics Letters*, vol. 30, no. 9, pp. 478–480, 1977. 28

[40] J. Li, M.-G. Suh, and K. Vahala, "Microresonator brillouin gyroscope," *Optica*, vol. 4, pp. 346–348, Mar 2017. 28, 89

[41] Y.-H. Lai, M.-G. Suh, Y.-K. Lu, B. Shen, Q.-F. Yang, H. Wang, J. Li, S. H. Lee, K. Y. Yang, and K. Vahala, "Earth rotation measured by a chip-scale ring laser gyroscope," *Nature Photonics*, pp. 1–5, 2020. 28

[42] G. A. Sanders, S. J. Sanders, L. K. Strandjord, T. Qiu, J. Wu, M. Smiciklas, D. Mead, S. Mosor, A. Arrizon, W. Ho, *et al.*, "Fiber optic gyro development at honeywell," in *Fiber Optic Sensors and Applications XIII*, vol. 9852, p. 985207, International Society for Optics and Photonics, 2016. 28

[43] U. Hochuli, P. Haldemann, and H. Li, "Factors influencing the relative frequency stabiltiy of he–ne laser structures," *Review of Scientific Instruments*, vol. 45, no. 11, pp. 1378–1381, 1974. 29

[44] W. E. Ahearn and R. E. Horstmann, "Nondestructive analysis for he–ne lasers," *IBM Journal of Research and Development*, vol. 23, no. 2, pp. 128–131, 1979. 29

[45] F. Aronowitz, "Fundamentals of the ring laser gyro," *Optical gyros and their application*, vol. 339, 1999. 29

[46] D. M. Shupe, "Thermally induced nonreciprocity in the fiber-optic interferometer," *Applied Optics*, vol. 19, pp. 654–655, Mar 1980. 29

[47] K. Hotate and K. Tabe, "Drift of an optical fiber gyroscope caused by the faraday effect: influence of the earth's magnetic field," *Applied Optics*, vol. 25, pp. 1086–1092, Apr 1986. 29

[48] V. Logozinskii, "Magnetically induced non-faraday nonreciprocity in a fiber-optic gyroscope," *Journal of Communications Technology and Electronics*, vol. 51, no. 7, pp. 836–840, 2006. 29

[49] T. Saida and K. Hotate, "General formula describing drift of interferometer fiber-optic gyro due to faraday effect: Reduction of the drift in twin-depo-i-fog," *Journal of Lightwave Technology*, vol. 17, p. 222, Feb 1999. 29

[50] S. Ezekiel, J. Davis, and R. Hellwarth, "Intensity dependent nonreciprocal phase shift in a fiberoptic gyroscope," in *Fiber-Optic Rotation Sensors and Related Technologies*, pp. 332–336, Springer, 1982. 29

[51] H. K. Kim, M. J. F. Digonnet, and G. S. Kino, "Air-core photonic-bandgap fiber-optic gyroscope," *Journal of Lightwave Technology*, vol. 24, p. 3169, Aug 2006. 29

[52] U. K. Schreiber, C. H. Rowe, D. N. Wright, S. J. Cooper, and G. E. Stedman, "Precision stabilization of the optical frequency in a large ring laser gyroscope," *Applied Optics*, vol. 37, pp. 8371–8381, Dec 1998. 29

[53] K. U. Schreiber, A. Gebauer, and J.-P. R. Wells, "Long-term frequency stabilization of a 16 m^2 ring laser gyroscope," *Optics Letters*, vol. 37, pp. 1925–1927, Jun 2012. 29

[54] Z. Wang, Y. Yang, P. Lu, R. Luo, Y. Li, D. Zhao, C. Peng, and Z. Li, "Dual-polarization interferometric fiber-optic gyroscope with an ultra-simple configuration," *Optics Letters*, vol. 39, pp. 2463–2466, Apr 2014. 29

[55] J. A. Bucaro, H. D. Dardy, and E. F. Carome, "Optical fiber acoustic sensor," *Applied Optics*, vol. 16, pp. 1761–1762, Jul 1977. 29

[56] "Ieee standard specification format guide and test procedure for single-axis interferometric fiber optic gyros," *IEEE Std 952-1997*, pp. 1–84, 1998. 30, 100, 104, 130

[57] O. J. Woodman, "An introduction to inertial navigation," tech. rep., University of Cambridge, Computer Laboratory, 2007. 30

[58] M. Tur, E. Shafir, and K. Blotekjaer, "Source-induced noise in optical systems driven by low-coherence sources," *Journal of Lightwave Technology*, vol. 8, no. 2, pp. 183–189, 1990. 30

[59] L. K. Strandjord, T. Qiu, J. Wu, T. Ohnstein, and G. A. Sanders, "Resonator fiber optic gyro progress including observation of navigation grade angle random walk," in *OFS2012 22nd International Conference on Optical Fiber Sensors*, vol. 8421, p. 842109, International Society for Optics and Photonics, 2012. 30

[60] K. Karki, V. Fedorov, D. Martyshkin, and S. Mirov, "High energy (0.8 j) mechanically q-switched 2.94 μm er: Yag laser," *Optics Express*, vol. 29, no. 3, pp. 4287–4295, 2021. 30

[61] L. Hargrove, R. L. Fork, and M. Pollack, "Locking of he–ne laser modes induced by synchronous intracavity modulation," *Applied Physics Letters*, vol. 5, no. 1, pp. 4–5, 1964. 30, 33

[62] U. Morgner, F. X. Kärtner, S. H. Cho, Y. Chen, H. A. Haus, J. G. Fujimoto, E. P. Ippen, V. Scheuer, G. Angelow, and T. Tschudi, "Sub-two-cycle pulses from a kerr-lens mode-locked ti:sapphire laser," *Optics Letters*, vol. 24, pp. 411–413, Mar 1999. 30, 33

[63] J. Sotor and G. Sobon, "24 fs and 3 nJ pulse generation from a simple, all polarization maintaining er-doped fiber laser," *Laser Physics Letters*, vol. 13, p. 125102, nov 2016. 30

[64] C. N. Danson, C. Haefner, J. Bromage, T. Butcher, J.-C. F. Chanteloup, E. A. Chowdhury, A. Galvanauskas, L. A. Gizzi, J. Hein, D. I. Hillier, *et al.*, "Petawatt and exawatt class lasers worldwide," *High Power Laser Science and Engineering*, vol. 7, 2019. 31

[65] T. Brabec and F. Krausz, "Intense few-cycle laser fields: Frontiers of nonlinear optics," *Reviews of Modern Physics*, vol. 72, no. 2, p. 545, 2000. 31

[66] A. Di Piazza, C. Müller, K. Hatsagortsyan, and C. H. Keitel, "Extremely high-intensity laser interactions with fundamental quantum systems," *Reviews of Modern Physics*, vol. 84, no. 3, p. 1177, 2012. 31

[67] P. Zhang, S. Bulanov, D. Seipt, A. Arefiev, and A. Thomas, "Relativistic plasma physics in supercritical fields," *Physics of Plasmas*, vol. 27, no. 5, p. 050601, 2020. 31

[68] S. A. Diddams, "The evolving optical frequency comb," *JOSA B*, vol. 27, no. 11, pp. B51–B62, 2010. 31

[69] I. Coddington, N. Newbury, , and W. Swann, "Dual-comb spectroscopy," *Optica*, 2016. 31

[70] N. Picqué and T. W. Hänsch, "Frequency comb spectroscopy," *Nature Photonics*, vol. 13, no. 3, pp. 146–157, 2019. 31

[71] T. Udem, R. Holzwarth, and T. W. Hänsch, "Optical frequency metrology," *Nature*, vol. 416, no. 6877, p. 233, 2002. 31

[72] P. Gaal, M. B. Raschke, K. Reimann, and M. Woerner, "Measuring optical frequencies in the 0–40 THz range with non-synchronized electro–optic sampling," *Nature Photonics*, 2007. 31

[73] H. Leopardi, J. Davila-Rodriguez, F. Quinlan, J. Olson, J. A. Sherman, S. A. Diddams, and T. M. Fortier, "Single-branch er:fiber frequency comb for precision optical metrology with 10^{-18} fractional instability," *Optica*, vol. 4, pp. 879–885, Aug 2017. 31

[74] T. Udem, J. Reichert, R. Holzwarth, and T. W. Hänsch, "Accurate measurement of large optical frequency differences with a mode-locked laser," *Optics Letters*, vol. 24, pp. 881–883, Jul 1999. 31, 43

[75] S. A. Diddams, D. J. Jones, J. Ye, S. T. Cundiff, J. L. Hall, J. K. Ranka, R. S. Windeler, R. Holzwarth, T. Udem, and T. W. Hänsch, "Direct link between microwave and optical frequencies with a 300 thz femtosecond laser comb," *Physical review letters*, vol. 84, no. 22, p. 5102, 2000. 31

[76] H. Margolis, G. Barwood, G. Huang, H. Klein, S. Lea, K. Szymaniec, and P. Gill, "Hertz-level measurement of the optical clock frequency in a single 88sr+ ion," *Science*, vol. 306, no. 5700, pp. 1355–1358, 2004. 31

[77] M. Murphy, T. Udem, R. Holzwarth, A. Sizmann, L. Pasquini, C. Araujo-Hauck, H. Dekker, S. D'Odorico, M. Fischer, T. Hänsch, *et al.*, "High-precision wavelength calibration of astronomical spectrographs with laser frequency combs," *Monthly Notices of the Royal Astronomical Society*, vol. 380, no. 2, pp. 839–847, 2007. 31

[78] D. A. Braje, M. S. Kirchner, S. Osterman, T. Fortier, and S. Diddams, "Astronomical spectrograph calibration with broad-spectrum frequency combs," *The European Physical Journal D*, vol. 48, no. 1, pp. 57–66, 2008. 31

[79] M.-G. Suh, X. Yi, Y.-H. Lai, S. Leifer, I. S. Grudinin, G. Vasisht, E. C. Martin, M. P. Fitzgerald, G. Doppmann, J. Wang, *et al.*, "Searching for exoplanets using a microresonator astrocomb," *Nature photonics*, vol. 13, no. 1, pp. 25–30, 2019. 31

[80] M. R. Leahy-Hoppa, J. Miragliotta, R. Osiander, J. Burnett, Y. Dikmelik, C. McEnnis, and J. B. Spicer, "Ultrafast laser-based spectroscopy and sensing: applications in libs, cars, and thz spectroscopy," *Sensors*, vol. 10, no. 5, pp. 4342–4372, 2010. 31

[81] A. O. Chernutsky, D. A. Dvoretskiy, I. O. Orekhov, S. G. Sazonkin, Y. Z. Ososkov, L. K. Denisov, K. V. Stepanov, A. A. Zhirnov, A. B. Pnev, and V. E. Karasik, "High-spatial-resolution distributed temperature sensing system based on a mode-locked fiber laser," in *2020 International Conference Laser Optics (ICLO)*, pp. 1–1, IEEE, 2020. 31

[82] M. E. Fermann, A. Galvanauskas, and G. Sucha, *Ultrafast lasers: technology and applications*, vol. 80. CRC Press, 2002. 32

[83] H. A. Haus, "Mode-locking of lasers," *IEEE Journal of Selected Topics in Quantum Electronics*, vol. 6, no. 6, pp. 1173–1185, 2000. 32, 33

[84] G. P. Agrawal, "Optical pulse propagation in doped fiber amplifiers," *Physical Review A*, vol. 44, no. 11, p. 7493, 1991. 32

[85] G. Agrawal, "Nonlinear fiber optics, 1–629 academic press," *San Diego*, 1989. 32

[86] D. J. Jones, S. A. Diddams, J. K. Ranka, A. Stentz, R. S. Windeler, J. L. Hall, and S. T. Cundiff, "Carrier-envelope phase control of femtosecond mode-locked lasers

and direct optical frequency synthesis," *Science*, vol. 288, no. 5466, pp. 635–639, 2000. 33, 44, 109, 112

[87] C. Spielmann, N. Burnett, S. Sartania, R. Koppitsch, M. Schnürer, C. Kan, M. Lenzner, P. Wobrauschek, and F. Krausz, "Generation of coherent x-rays in the water window using 5-femtosecond laser pulses," *Science*, vol. 278, no. 5338, pp. 661–664, 1997. 33

[88] C. G. Durfee III, A. R. Rundquist, S. Backus, C. Herne, M. M. Murnane, and H. C. Kapteyn, "Phase matching of high-order harmonics in hollow waveguides," *Physical Review Letters*, vol. 83, no. 11, p. 2187, 1999. 33

[89] P. Kryukov and V. Letokhov, "Fluctuation mechanism of ultrashort pulse generation by laser with saturable absorber," *IEEE Journal of Quantum Electronics*, vol. 8, no. 10, pp. 766–782, 1972. 33

[90] W. Glenn, "The fluctuation model of a passively mode-locked laser," *IEEE Journal of Quantum Electronics*, vol. 11, no. 1, pp. 8–17, 1975. 33

[91] E. P. Ippen, "Principles of passive mode locking," *Applied Physics B*, vol. 58, no. 3, pp. 159–170, 1994. 33

[92] D. Kuizenga and A. Siegman, "Fm and am mode locking of the homogeneous laser - part i: Theory," *IEEE Journal of Quantum Electronics*, vol. 6, no. 11, pp. 694–708, 1970. 33

[93] U. Keller, K. J. Weingarten, F. X. Kartner, D. Kopf, B. Braun, I. D. Jung, R. Fluck, C. Honninger, N. Matuschek, and J. Aus der Au, "Semiconductor saturable absorber mirrors (sesam's) for femtosecond to nanosecond pulse generation in solid-state lasers," *IEEE Journal of Selected Topics in Quantum Electronics*, vol. 2, no. 3, pp. 435–453, 1996. 35

[94] H. W. Mocker and R. Collins, "Mode competition and self-locking effects in a q-switched ruby laser," *Applied Physics Letters*, vol. 7, no. 10, pp. 270–273, 1965. 35

[95] W. Glenn, M. Brienza, and A. DeMaria, "Mode locking of an organic dye laser," *Applied Physics Letters*, vol. 12, no. 2, pp. 54–56, 1968. 35

[96] U. Keller, D. Miller, G. Boyd, T. Chiu, J. Ferguson, and M. Asom, "Solid-state low-loss intracavity saturable absorber for nd: Ylf lasers: an antiresonant semiconductor fabry–perot saturable absorber," *Optics letters*, vol. 17, no. 7, pp. 505–507, 1992. 35

[97] V. Liverini, S. Schön, R. Grange, M. Haiml, S. Zeller, and U. Keller, "Low-loss gainnas saturable absorber mode locking a 1.3-μ m solid-state laser," *Applied Physics Letters*, vol. 84, no. 20, pp. 4002–4004, 2004. 35

[98] O. Okhotnikov, A. Grudinin, and M. Pessa, "Ultra-fast fibre laser systems based on sesam technology: new horizons and applications," *New journal of physics*, vol. 6, no. 1, p. 177, 2004. 35

[99] S. Y. Set, H. Yaguchi, Y. Tanaka, and M. Jablonski, "Laser mode locking using a saturable absorber incorporating carbon nanotubes," *Journal of lightwave Technology*, vol. 22, no. 1, p. 51, 2004. 35

[100] V. A. Margulis and T. Sizikova, "Theoretical study of third-order nonlinear optical response of semiconductor carbon nanotubes," *Physica B: Condensed Matter*, vol. 245, no. 2, pp. 173–189, 1998. 35

[101] M. Chernysheva, A. Bednyakova, M. Al Araimi, R. C. Howe, G. Hu, T. Hasan, A. Gambetta, G. Galzerano, M. Rümmeli, and A. Rozhin, "Double-wall carbon nanotube hybrid mode-locker in tm-doped fibre laser: A novel mechanism for robust bound-state solitons generation," *Scientific Reports*, vol. 7, p. 44314, 2017. 35

[102] H. Zhang, D. Tang, L. Zhao, Q. Bao, and K. Loh, "Large energy mode locking of an erbium-doped fiber laser with atomic layer graphene," *Optics Express*, vol. 17, no. 20, pp. 17630–17635, 2009. 35

[103] A. Martinez and Z. Sun, "Nanotube and graphene saturable absorbers for fibre lasers," *Nature Photonics*, vol. 7, no. 11, pp. 842–845, 2013. 35

[104] C. Zhao, H. Zhang, X. Qi, Y. Chen, Z. Wang, S. Wen, and D. Tang, "Ultrashort pulse generation by a topological insulator based saturable absorber," *Applied Physics Letters*, vol. 101, no. 21, p. 211106, 2012. 35

[105] G. Zhao, S. Han, A. Wang, Y. Wu, M. Zhao, Z. Wang, and X. Hao, ""chemical weathering" exfoliation of atom-thick transition metal dichalcogenides and their ultrafast saturable absorption properties," *Advanced Functional Materials*, vol. 25, no. 33, pp. 5292–5299, 2015. 35

[106] R. I. Woodward and E. J. Kelleher, "2d saturable absorbers for fibre lasers," *Applied Sciences*, vol. 5, no. 4, pp. 1440–1456, 2015. 35

[107] X. Jiang, S. Liu, W. Liang, S. Luo, Z. He, Y. Ge, H. Wang, R. Cao, F. Zhang, Q. Wen, *et al.*, "Broadband nonlinear photonics in few-layer mxene ti3c2tx (t= f, o, or oh)," *Laser & Photonics Reviews*, vol. 12, no. 2, p. 1700229, 2018. 35

[108] Y. I. Jhon, J. Koo, B. Anasori, M. Seo, J. H. Lee, Y. Gogotsi, and Y. M. Jhon, "Metallic mxene saturable absorber for femtosecond mode-locked lasers," *Advanced Materials*, vol. 29, no. 40, p. 1702496, 2017. 35

[109] Y. Chen, G. Jiang, S. Chen, Z. Guo, X. Yu, C. Zhao, H. Zhang, Q. Bao, S. Wen, D. Tang, *et al.*, "Mechanically exfoliated black phosphorus as a new saturable

absorber for both q-switching and mode-locking laser operation," *Optics Express*, vol. 23, no. 10, pp. 12823–12833, 2015. 35

[110] Z. Qin, G. Xie, C. Zhao, S. Wen, P. Yuan, and L. Qian, "Mid-infrared mode-locked pulse generation with multilayer black phosphorus as saturable absorber," *Optics Letters*, vol. 41, no. 1, pp. 56–59, 2016. 35

[111] J. Wang, A. Coillet, O. Demichel, Z. Wang, D. Rego, A. Bouhelier, P. Grelu, and B. Cluzel, "Saturable plasmonic metasurfaces for laser mode locking," *Light: Science & Applications*, vol. 9, no. 1, pp. 1–9, 2020. 35

[112] A. Owyoung, R. Hellwarth, and N. George, "Intensity-induced changes in optical polarizations in glasses," *Physical Review B*, vol. 5, no. 2, p. 628, 1972. 36

[113] K. Tamura, E. Ippen, H. Haus, and L. Nelson, "77-fs pulse generation from a stretched-pulse mode-locked all-fiber ring laser," *Optics letters*, vol. 18, no. 13, pp. 1080–1082, 1993. 36

[114] N. Doran and D. Wood, "Nonlinear-optical loop mirror," *Optics Letters*, vol. 13, no. 1, pp. 56–58, 1988. 36

[115] I. N. Duling, "All-fiber ring soliton laser mode locked with a nonlinear mirror," *Optics letters*, vol. 16, no. 8, pp. 539–541, 1991. 36

[116] D. E. Spence, P. N. Kean, and W. Sibbett, "60-fsec pulse generation from a self-mode-locked ti: sapphire laser," *Optics letters*, vol. 16, no. 1, pp. 42–44, 1991. 36

[117] M. E. Fermann, F. Haberl, M. Hofer, and H. Hochreiter, "Nonlinear amplifying loop mirror," *Optics Letters*, vol. 15, no. 13, pp. 752–754, 1990. 36

[118] C. Kim, K. Jung, K. Kieu, and J. Kim, "Low timing jitter and intensity noise from a soliton er-fiber laser mode-locked by a fiber taper carbon nanotube saturable absorber," *Optics express*, vol. 20, no. 28, pp. 29524–29530, 2012. 37

[119] S. Kim, Y. Kim, J. Park, S. Han, S. Park, Y.-J. Kim, and S.-W. Kim, "Hybrid mode-locked er-doped fiber femtosecond oscillator with 156 mw output power," *Optics express*, vol. 20, no. 14, pp. 15054–15060, 2012. 37

[120] J. Kim and Y. Song, "Ultralow-noise mode-locked fiber lasers and frequency combs: principles, status, and applications," *Advances in Optics and Photonics*, vol. 8, no. 3, pp. 465–540, 2016. 37, 43, 85, 113

[121] P. Grelu and N. Akhmediev, "Dissipative solitons for mode-locked lasers," *Nature Photonics*, vol. 6, no. 2, p. 84, 2012. 38, 39

[122] L. F. Mollenauer, R. H. Stolen, and J. P. Gordon, "Experimental observation of picosecond pulse narrowing and solitons in optical fibers," *Physical Review Letters*, 1980. 37

[123] L. F. Mollenauer and R. H. Stolen, "The soliton laser," *Optics News*, vol. 10, no. 6, pp. 20_2–21, 1984. 37

[124] S. Kelly, "Characteristic sideband instability of periodically amplified average soliton," *Electronics Letters*, vol. 28, no. 8, pp. 806–807, 1992. 38, 74, 78

[125] W. Tomlinson, R. H. Stolen, and A. M. Johnson, "Optical wave breaking of pulses in nonlinear optical fibers," *Optics letters*, vol. 10, no. 9, pp. 457–459, 1985. 38

[126] S. K.Turitsyn, B. G.Bale, and M. P.Fedoruk, "Dispersion-managed solitons in fibre systems and lasers," *Physics Reports*, 2012. 38

[127] L. Nugent-Glandorf, T. A. Johnson, Y. Kobayashi, and S. A. Diddams, "Impact of dispersion on amplitude and frequency noise in a yb-fiber laser comb," *Optics letters*, vol. 36, no. 9, pp. 1578–1580, 2011. 39

[128] Y. Song, C. Kim, K. Jung, H. Kim, and J. Kim, "Timing jitter optimization of mode-locked yb-fiber lasers toward the attosecond regime," *Optics express*, vol. 19, no. 15, pp. 14518–14525, 2011. 39

[129] B. Oktem, C. Ülgüdür, and F. Ö. Ilday, "Soliton–similariton fibre laser," *Nature Photonics*, vol. 4, no. 5, pp. 307–311, 2010. 39

[130] D. Anderson, M. Desaix, M. Lisak, and M. L. Quiroga-Teixeiro, "Wave breaking in nonlinear-optical fibers," *JOSA B*, vol. 9, no. 8, pp. 1358–1361, 1992. 39

[131] F. Ilday, J. Buckley, W. Clark, and F. Wise, "Self-similar evolution of parabolic pulses in a laser," *Physical review letters*, vol. 92, no. 21, p. 213902, 2004. 39

[132] A. Chong, J. Buckley, W. Renninger, and F. Wise, "All-normal-dispersion femtosecond fiber laser," *Optics express*, vol. 14, no. 21, pp. 10095–10100, 2006. 39

[133] Y. S. Kivshar and B. Luther-Davies, "Dark optical solitons: physics and applications," *Physics Reports*, vol. 298, no. 2-3, pp. 81–197, 1998. 39

[134] H. Zhang, D. Tang, L. Zhao, and X. Wu, "Dark pulse emission of a fiber laser," *Physical Review A*, vol. 80, no. 4, p. 045803, 2009. 39, 85

[135] D. Tang, J. Guo, Y. Song, H. Zhang, L. Zhao, and D. Shen, "Dark soliton fiber lasers," *Optics express*, vol. 22, no. 16, pp. 19831–19837, 2014. 39

[136] W. Zhao and E. Bourkoff, "Propagation properties of dark solitons," *Optics Letters*, vol. 14, pp. 703–705, Jul 1989. 39, 85

[137] Y. Chen and J. Atai, "Absorption and amplification of dark solitons," *Optics Letters*, vol. 16, pp. 1933–1935, Dec 1991. 39, 85

[138] W. Zhao and E. Bourkoff, "Interactions between dark solitons," *Optics Letters*, vol. 14, pp. 1371–1373, Dec 1989. 39, 85

[139] K. Sala, G. Kenney-Wallace, and G. Hall, "Cw autocorrelation measurements of picosecond laser pulses," *IEEE Journal of Quantum Electronics*, vol. 16, no. 9, pp. 990–996, 1980. 40

[140] R. Stolen and C. Lin, "Self-phase-modulation in silica optical fibers," *Physical Review A*, vol. 17, no. 4, p. 1448, 1978. 40

[141] R. Trebino, *Frequency-Resolved Optical Gating: The Measurement of Ultrashort Laser Pulses: The Measurement of Ultrashort Laser Pulses*. Springer Science & Business Media, 2000. 40

[142] D. J. Kane and R. Trebino, "Characterization of arbitrary femtosecond pulses using frequency-resolved optical gating," *IEEE Journal of Quantum Electronics*, vol. 29, no. 2, pp. 571–579, 1993. 40

[143] S. Akturk, M. Kimmel, P. O'Shea, and R. Trebino, "Measuring pulse-front tilt in ultrashort pulses using grenouille," *Optics Express*, vol. 11, pp. 491–501, Mar 2003. 40

[144] C. Iaconis and I. A. Walmsley, "Spectral phase interferometry for direct electric-field reconstruction of ultrashort optical pulses," *Optics Letters*, vol. 23, pp. 792–794, May 1998. 40

[145] F. X. Kärtner, U. Morgner, T. Schibli, R. Ell, H. A. Haus, J. G. Fujimoto, and E. P. Ippen, "Few-cycle pulses directly from a laser," *Few-cycle laser pulse generation and its applications*, pp. 73–136, 2004. 40

[146] D. Von der Linde, "Characterization of the noise in continuously operating mode-locked lasers," *Applied Physics B*, vol. 39, no. 4, pp. 201–217, 1986. 41, 42

[147] H. A. Haus and A. Mecozzi, "Noise of mode-locked lasers," *IEEE Journal of Quantum Electronics*, vol. 29, no. 3, pp. 983–996, 1993. 41

[148] D. Hou, C.-C. Lee, Z. Yang, and T. Schibli, "Timing jitter characterization of mode-locked lasers with¡ 1 zs/ $\sqrt{Hz}$ resolution using a simple optical heterodyne technique," *Optics Letters*, vol. 40, no. 13, pp. 2985–2988, 2015. 41

[149] K. Jung and J. Kim, "Characterization of timing jitter spectra in free-running mode-locked lasers with 340 db dynamic range over 10 decades of fourier frequency," *Optics Letters*, vol. 40, pp. 316–319, Feb 2015. 41

[150] R. Paschotta, "Noise in laser technology: Part 1: Intensity and phase noise," *Optik & Photonik*, vol. 4, no. 2, pp. 48–50, 2009. 42

[151] D. E. McCumber, "Intensity fluctuations in the output of cw laser oscillators. i," *Physical Review*, vol. 141, pp. 306–322, Jan 1966. 42

[152] R. Paschotta, "Noise of mode-locked lasers (part ii): timing jitter and other fluctuations," *Applied Physics B*, vol. 79, no. 2, pp. 163–173, 2004. 42, 113

[153] D. W. Allan, "Statistics of atomic frequency standards," *Proceedings of the IEEE*, vol. 54, no. 2, pp. 221–230, 1966. 42

[154] D. Kwon, I. Jeon, W.-K. Lee, M.-S. Heo, and J. Kim, "Generation of multiple ultrastable optical frequency combs from an all-fiber photonic platform," *Science Advances*, vol. 6, no. 13, p. eaax4457, 2020. 43

[155] D. Kwon and J. Kim, "All-fiber interferometer-based repetition-rate stabilization of mode-locked lasers to 10^{-14}-level frequency instability and 1-fs-level jitter over 1 s," *Optics letters*, vol. 42, no. 24, pp. 5186–5189, 2017. 43

[156] X. Xie, R. Bouchand, D. Nicolodi, M. Giunta, W. Hänsel, M. Lezius, A. Joshi, S. Datta, C. Alexandre, M. Lours, *et al.*, "Photonic microwave signals with zeptosecond-level absolute timing noise," *Nature Photonics*, vol. 11, no. 1, pp. 44–47, 2017. 43

[157] L. Xu, C. Spielmann, A. Poppe, T. Brabec, F. Krausz, and T. W. Hänsch, "Route to phase control of ultrashort light pulses," *Optics Letters*, vol. 21, pp. 2008–2010, Dec 1996. 43, 109, 112

[158] I. Hartl, G. Imeshev, M. E. Fermann, C. Langrock, and M. M. Fejer, "Integrated self-referenced frequency-comb laser based on a combination of fiber and waveguide technology," *Optics Express*, vol. 13, pp. 6490–6496, Aug 2005. 43

[159] T. Wittmann, B. Horvath, W. Helml, M. G. Schätzel, X. Gu, A. L. Cavalieri, G. Paulus, and R. Kienberger, "Single-shot carrier–envelope phase measurement of few-cycle laser pulses," *Nature Physics*, vol. 5, no. 5, pp. 357–362, 2009. 43

[160] A. Baltuška, T. Udem, M. Uiberacker, M. Hentschel, E. Goulielmakis, C. Gohle, R. Holzwarth, V. S. Yakovlev, A. Scrinzi, T. W. Hänsch, *et al.*, "Attosecond control of electronic processes by intense light fields," *Nature*, vol. 421, no. 6923, pp. 611–615, 2003. 43

[161] R. Gowda, N. Nguyen, J.-C. Diels, R. A. Norwood, N. Peyghambarian, and K. Kieu, "All-fiber bidirectional optical parametric oscillator for precision sensing," *Optics Letters*, vol. 40, no. 9, pp. 2033–2036, 2015. 43, 84, 87

[162] B. R. Washburn, W. C. Swann, and N. R. Newbury, "Response dynamics of the frequency comb output from a femtosecond fiber laser," *Optics Express*, vol. 13, pp. 10622–10633, Dec 2005. 43

[163] N. R. Newbury and W. C. Swann, "Low-noise fiber-laser frequency combs," *JOSA B*, vol. 24, no. 8, pp. 1756–1770, 2007. 43

[164] L. Nugent-Glandorf, T. A. Johnson, Y. Kobayashi, and S. A. Diddams, "Impact of dispersion on amplitude and frequency noise in a yb-fiber laser comb," *Optics Letters*, vol. 36, pp. 1578–1580, May 2011. 43

[165] J. K. Wahlstrand, J. T. Willits, C. R. Menyuk, and S. T. Cundiff, "The quantum-limited comb lineshape of a mode-locked laser: Fundamental limits on frequency uncertainty," *Optics Express*, vol. 16, pp. 18624–18630, Nov 2008. 43

[166] S. A. Diddams, T. Udem, J. Bergquist, E. Curtis, R. Drullinger, L. Hollberg, W. M. Itano, W. Lee, C. Oates, K. Vogel, *et al.*, "An optical clock based on a single trapped 199hg+ ion," *Science*, vol. 293, no. 5531, pp. 825–828, 2001. 44

[167] D. Churkin, S. Sugavanam, N. Tarasov, S. Khorev, S. Smirnov, S. Kobtsev, and S. Turitsyn, "Stochasticity, periodicity and localized light structures in partially mode-locked fibre lasers," *Nature Communications*, vol. 6, p. 7004, 2015. 44, 45, 46

[168] N. Tarasov, S. Sugavanam, and D. Churkin, "Spatio-temporal generation regimes in quasi-cw raman fiber lasers," *Optics express*, vol. 23, no. 19, pp. 24189–24194, 2015. 45

[169] S. Sugavanam, N. Tarasov, and D. V. Churkin, "Real-time intensity domain characterization of fibre lasers using spatio-temporal dynamics," *Applied Sciences*, vol. 6, no. 3, p. 65, 2016. 45

[170] E. Turitsyna, S. Smirnov, S. Sugavanam, N. Tarasov, X. Shu, S. Babin, E. Podivilov, D. Churkin, G. Falkovich, and S. Turitsyn, "The laminar–turbulent transition in a fibre laser," *Nature Photonics*, vol. 7, no. 10, p. 783, 2013. 46

[171] S. Birkholz, E. T. J. Nibbering, C. Brée, S. Skupin, A. Demircan, G. Genty, and G. Steinmeyer, "Spatiotemporal rogue events in optical multiple filamentation," *Physical Review Letters*, vol. 111, p. 243903, Dec 2013. 46

[172] G. Herink, B. Jalali, C. Ropers, and D. Solli, "Resolving the build-up of femtosecond mode-locking with single-shot spectroscopy at 90 mhz frame rate," *Nature Photonics*, vol. 10, no. 5, p. 321, 2016. 46, 50, 58, 61, 62, 63, 65, 68

[173] J. Peng, M. Sorokina, S. Sugavanam, N. Tarasov, D. V. Churkin, S. K. Turitsyn, and H. Zeng, "Real-time observation of dissipative soliton formation in nonlinear

polarization rotation mode-locked fibre lasers," *Communications Physics*, vol. 1, no. 1, p. 20, 2018. 46, 50, 62, 63, 65, 72, 78

[174] B. H. Kolner and M. Nazarathy, "Temporal imaging with a time lens," *Optics letters*, vol. 14, no. 12, pp. 630–632, 1989. 46

[175] M. Närhi, B. Wetzel, C. Billet, S. Toenger, T. Sylvestre, J.-M. Merolla, R. Morandotti, F. Dias, G. Genty, and J. M. Dudley, "Real-time measurements of spontaneous breathers and rogue wave events in optical fibre modulation instability," *Nature communications*, vol. 7, no. 1, pp. 1–9, 2016. 46

[176] A. Tikan, S. Bielawski, C. Szwaj, S. Randoux, and P. Suret, "Single-shot measurement of phase and amplitude by using a heterodyne time-lens system and ultrafast digital time-holography," *Nature Photonics*, vol. 12, no. 4, p. 228, 2018. 46

[177] A. Lebel, A. Tikan, S. Randoux, P. Suret, and F. Copie, "Single-shot observation of breathers from noise-induced modulation instability using heterodyne temporal imaging," *Optics Letters*, vol. 46, no. 2, pp. 298–301, 2021. 46

[178] K. Goda and B. Jalali, "Dispersive fourier transformation for fast continuous single-shot measurements," *Nature Photonics*, vol. 7, no. 2, p. 102, 2013. 46, 48

[179] A. Mahjoubfar, D. V. Churkin, S. Barland, N. Broderick, S. K. Turitsyn, and B. Jalali, "Time stretch and its applications," *Nature Photonics*, vol. 11, no. 6, p. 341, 2017. 46, 47

[180] S. Yegnanarayanan, P. Trinh, and B. Jalali, "Recirculating photonic filter: a wavelength-selective time delay for phased-array antennas and wavelength code-division multiple access," *Optics Letters*, vol. 21, no. 10, pp. 740–742, 1996. 47

[181] E. D. Diebold, N. K. Hon, Z. Tan, J. Chou, T. Sienicki, C. Wang, and B. Jalali, "Giant tunable optical dispersion using chromo-modal excitation of a multimode waveguide," *Optics express*, vol. 19, no. 24, pp. 23809–23817, 2011. 47

[182] Z. Wang, K. Nithyanandan, A. Coillet, P. Tchofo-Dinda, and P. Grelu, "Optical soliton molecular complexes in a passively mode-locked fibre laser," *Nature Communications*, vol. 10, no. 1, p. 830, 2019. 48, 50, 56, 72, 75, 96, 174

[183] Y. Cao, L. Gao, S. Wabnitz, H. Ran, L. Kong, and T. Zhu, "Experimental revealing of asynchronous transient-soliton buildup dynamics," *Optics & Laser Technology*, vol. 133, p. 106512, 2021. 50

[184] X. Wang, X. Ren, J. Peng, X. Shen, K. Huang, M. Yan, and H. Zeng, "On the q-switching bunch dynamics in the build-up of stretched-pulse mode-locking," *Optics express*, vol. 27, no. 3, pp. 2747–2753, 2019. 50

[185] Y. Luo, R. Xia, P. P. Shum, W. Ni, Y. Liu, H. Q. Lam, Q. Sun, X. Tang, and L. Zhao, "Real-time dynamics of soliton triplets in fiber lasers," *Photonics Research*, vol. 8, no. 6, pp. 884–891, 2020. 50

[186] M. Liu, Z.-W. Wei, H. Li, T.-J. Li, A.-P. Luo, W.-C. Xu, and Z.-C. Luo, "Visualizing the "invisible" soliton pulsation in an ultrafast laser," *Laser & Photonics Reviews*, vol. 14, no. 4, p. 1900317, 2020. 50

[187] J. Peng, S. Boscolo, Z. Zhao, and H. Zeng, "Breathing dissipative solitons in mode-locked fiber lasers," *Science Advances*, vol. 5, no. 11, p. eaax1110, 2019. 50

[188] C. Lapre, C. Billet, F. Meng, P. Ryczkowski, T. Sylvestre, C. Finot, G. Genty, and J. M. Dudley, "Real-time characterization of spectral instabilities in a mode-locked fibre laser exhibiting soliton-similariton dynamics," *Scientific Reports*, vol. 9, no. 1, pp. 1–12, 2019. 50, 58, 72

[189] G. Herink, F. Kurtz, B. Jalali, D. Solli, and C. Ropers, "Real-time spectral interferometry probes the internal dynamics of femtosecond soliton molecules," *Science*, vol. 356, no. 6333, pp. 50–54, 2017. 50, 56, 96, 174

[190] P. Ryczkowski, M. Närhi, C. Billet, J.-M. Merolla, G. Genty, and J. M. Dudley, "Real-time full-field characterization of transient dissipative soliton dynamics in a mode-locked laser," *Nature Photonics*, vol. 12, no. 4, p. 221, 2018. 50, 58, 72, 81

[191] M. H. Asghari, Y. Park, and J. Azaña, "Complex-field measurement of ultrafast dynamic optical waveforms based on real-time spectral interferometry," *Optics Express*, vol. 18, no. 16, pp. 16526–16538, 2010. 50

[192] J. Hammer, P. Hosseini, C. R. Menyuk, P. S. J. Russell, and N. Y. Joly, "Single-shot reconstruction of spectral amplitude and phase in a fiber ring cavity at a 80 mhz repetition rate," *Optics letters*, vol. 41, no. 20, pp. 4641–4644, 2016. 50

[193] G. Pu, L. Yi, L. Zhang, C. Luo, Z. Li, and W. Hu, "Intelligent control of mode-locked femtosecond pulses by time-stretch-assisted real-time spectral analysis," *Light: Science & Applications*, vol. 9, no. 1, pp. 1–8, 2020. 50

[194] F. Meng and J. M. Dudley, "Toward a self-driving ultrafast fiber laser," *Light, science & applications*, vol. 9, 2020. 50

[195] L. Salmela, M. Hary, J. M. Dudley, and G. Genty, "Full-field prediction of supercontinuum generation dynamics," in *AI and Optical Data Sciences II*, vol. 11703, p. 1170314, International Society for Optics and Photonics, 2021. 50

[196] K. Goda, K. K. Tsia, and B. Jalali, "Amplified dispersive fourier-transform imaging for ultrafast displacement sensing and barcode reading," *Applied Physics Letters*, vol. 93, no. 13, p. 131109, 2008. 50, 139

[197] T. T. Wong, A. K. Lau, K. K. Wong, and K. K. Tsia, "Optical time-stretch confocal microscopy at 1 μm," *Optics Letters*, vol. 37, no. 16, pp. 3330–3332, 2012. 50

[198] K. Goda, K. Tsia, and B. Jalali, "Serial time-encoded amplified imaging for real-time observation of fast dynamic phenomena," *Nature*, vol. 458, no. 7242, pp. 1145–1149, 2009. 50

[199] K. Goda, A. Ayazi, D. R. Gossett, J. Sadasivam, C. K. Lonappan, E. Sollier, A. M. Fard, S. C. Hur, J. Adam, C. Murray, C. Wang, N. Brackbill, D. Di Carlo, and B. Jalali, "High-throughput single-microparticle imaging flow analyzer," *Proceedings of the National Academy of Sciences*, vol. 109, no. 29, pp. 11630–11635, 2012. 50

[200] Y. Jiang, S. Karpf, and B. Jalali, "Time-stretch lidar as a spectrally scanned time-of-flight ranging camera," *Nature Photonics*, vol. 14, no. 1, pp. 14–18, 2020. 50

[201] R. Fork, B. Greene, and C. V. Shank, "Generation of optical pulses shorter than 0.1 psec by colliding pulse mode locking," *Applied Physics Letters*, vol. 38, no. 9, pp. 671–672, 1981. 53, 56

[202] N. Kuse, J. Jiang, C.-C. Lee, T. Schibli, and M. Fermann, "All polarization-maintaining er fiber-based optical frequency combs with nonlinear amplifying loop mirror," *Optics express*, vol. 24, no. 3, pp. 3095–3102, 2016. 53

[203] W. Hänsel, H. Hoogland, M. Giunta, S. Schmid, T. Steinmetz, R. Doubek, P. Mayer, S. Dobner, C. Cleff, M. Fischer, *et al.*, "All polarization-maintaining fiber laser architecture for robust femtosecond pulse generation," *Applied Physics B*, vol. 123, no. 1, p. 41, 2017. 53

[204] X. Yao, "Generation of bidirectional stretched pulses in a nanotube-mode-locked fiber laser," *Applied Optics*, vol. 53, no. 1, pp. 27–31, 2014. 53

[205] B. Li, J. Xing, D. Kwon, Y. Xie, N. Prakash, J. Kim, and S.-W. Huang, "Bidirectional mode-locked all-normal dispersion fiber laser," *Optica*, vol. 7, no. 8, pp. 961–964, 2020. 53

[206] D. Chernykh, A. Krylov, A. Levchenko, V. Grebenyukov, N. Arutunyan, A. Pozharov, E. Obraztsova, and E. Dianov, "Hybrid mode-locked erbium-doped all-fiber soliton laser with a distributed polarizer," *Applied optics*, vol. 53, no. 29, pp. 6654–6662, 2014. 55

[207] B. Atherton, S. Diddams, and J.-C. Diels, "Stabilization of a mode-locked ring laser gyroscope," in *Summaries of papers presented at the Conference on Lasers and Electro-Optics*, pp. 201–202, IEEE, 1996. 55

[208] A. Braga, J.-C. Diels, R. Jain, R. Kay, and L. Wang, "Bidirectional mode-locked fiber ring laser using self-regenerative, passively controlled, threshold gating," *Optics Letters*, vol. 35, pp. 2648–2650, Aug 2010. 55, 84, 89, 130

[209] L. Zhao, D. Tang, T. Cheng, and C. Lu, "Self-started unidirectional operation of a fibre ring soliton laser without an isolator," *Journal of Optics A: Pure and Applied Optics*, vol. 9, no. 5, p. 477, 2007. 55

[210] D. Li, D. Shen, L. Li, H. Chen, D. Tang, and L. Zhao, "Unidirectional dissipative soliton operation in an all-normal-dispersion yb-doped fiber laser without an isolator," *Applied Optics*, vol. 54, no. 26, pp. 7912–7916, 2015. 55

[211] I. Kudelin, S. Sugavanam, and M. Chernysheva, "Pulse-onset dynamics in a bidirectional mode-locked fibre laser via instabilities," *Communications Physics*, vol. 3, no. 1, pp. 1–10, 2020. 55, 64

[212] K. Krupa, K. Nithyanandan, and P. Grelu, "Vector dynamics of incoherent dissipative optical solitons," *Optica*, vol. 4, no. 10, pp. 1239–1244, 2017. 56

[213] Y. Wei, B. Li, X. Wei, Y. Yu, and K. K. Wong, "Ultrafast spectral dynamics of dual-color-soliton intracavity collision in a mode-locked fiber laser," *Applied Physics Letters*, vol. 112, no. 8, p. 081104, 2018. 56, 69

[214] A. A. Krylov, D. S. Chernykh, and E. D. Obraztsova, "Gyroscopic effect detection in the colliding-pulse hybridly mode-locked erbium-doped all-fiber ring soliton laser," *Optics Letters*, vol. 42, no. 13, pp. 2439–2442, 2017. 56, 63, 85, 86, 89, 120, 136

[215] Y. Yu, C. Kong, B. Li, J. Kang, Y.-X. Ren, Z.-C. Luo, and K. K. Wong, "Behavioral similarity of dissipative solitons in an ultrafast fiber laser," *Optics Letters*, vol. 44, no. 19, pp. 4813–4816, 2019. 56, 63, 65

[216] A. Afanas' ev, V. Volkov, V. Dritz, and B. Samson, "Interaction of counterpropagating self-induced transparency solitons," *Journal of Modern Optics*, vol. 37, no. 2, pp. 165–170, 1990. 56, 63, 64

[217] M. J. Shaw and B. W. Shore, "Collisions of counterpropagating optical solitons," *JOSA B*, vol. 8, no. 5, pp. 1127–1134, 1991. 56

[218] H. Afkhamiardakani and J.-C. Diels, "Controlling group and phase velocities in bidirectional mode-locked fiber lasers," *Opt. Lett.*, vol. 44, pp. 2903–2906, Jun 2019. 57

[219] K. Tai, A. Hasegawa, and A. Tomita, "Observation of modulational instability in optical fibers," *Physical review letters*, vol. 56, no. 2, p. 135, 1986. 60

[220] J. H. Nguyen, D. Luo, and R. G. Hulet, "Formation of matter-wave soliton trains by modulational instability," *Science*, vol. 356, no. 6336, pp. 422–426, 2017. 60

[221] D. R. Solli, G. Herink, B. Jalali, and C. Ropers, "Fluctuations and correlations in modulation instability," *Nature Photonics*, vol. 6, no. 7, pp. 463–468, 2012. 60

[222] T. B. Benjamin and J. E. Feir, "The disintegration of wave trains on deep water part 1. theory," *Journal of Fluid Mechanics*, vol. 27, no. 3, pp. 417–430, 1967. 60

[223] S. G. Thornhill and D. Ter Haar, "Langmuir turbulence and modulational instability," *Physics Reports*, vol. 43, no. 2, pp. 43–99, 1978. 60

[224] P. Kevrekidis and D. Frantzeskakis, "Pattern forming dynamical instabilities of bose–einstein condensates," *Modern Physics Letters B*, vol. 18, no. 05n06, pp. 173–202, 2004. 60

[225] G. P. Agrawal, "Nonlinear fiber optics," in *Nonlinear Science at the Dawn of the 21st Century*, pp. 195–211, Springer, 2000. 60, 63, 113

[226] Y. Du, M. Han, P. Cheng, and X. Shu, "Pulsating soliton with broadened kelly sidebands in an ultrafast fiber laser," *Optics Letters*, vol. 44, no. 16, pp. 4087–4090, 2019. 62, 78, 79

[227] X. Liu and Y. Cui, "Revealing the behavior of soliton buildup in a mode-locked laser," *Advanced Photonics*, vol. 1, no. 1, p. 016003, 2019. 62, 72, 78

[228] A. Pusch, J. M. Hamm, and O. Hess, "Controllable interaction of counterpropagating solitons in three-level media," *Physical Review A*, vol. 82, no. 2, p. 023805, 2010. 63, 64

[229] S. Sun, Z. Lin, W. Li, N. Zhu, and M. Li, "Time-stretch probing of ultra-fast soliton dynamics related to q-switched instabilities in mode-locked fiber laser," *Optics Express*, vol. 26, no. 16, pp. 20888–20901, 2018. 68, 70, 82

[230] L. Tartara, "Frequency shifting of femtosecond pulses by reflection at solitons," *IEEE Journal of Quantum Electronics*, vol. 48, no. 11, pp. 1439–1442, 2012. 69

[231] J. Gu, H. Guo, S. Wang, and X. Zeng, "Probe-controlled soliton frequency shift in the regime of optical event horizon," *Optics Express*, vol. 23, no. 17, pp. 22285–22290, 2015. 69

[232] V. L. Kalashnikov, E. Sorokin, and I. T. Sorokina, "Mechanisms of spectral shift in ultrashort-pulse laser oscillators," *JOSA B*, vol. 18, no. 11, pp. 1732–1741, 2001. 69

[233] M. Furdek, M. Bosiljevac, N. Skorin-Kapov, and Z. Šipuš, "Gain competition in optical amplifiers: a case study," in *The 33rd International Convention MIPRO*, pp. 467–472, IEEE, 2010. 69

[234] C. Hönninger, R. Paschotta, F. Morier-Genoud, M. Moser, and U. Keller, "Q-switching stability limits of continuous-wave passive mode locking," *JOSA B*, vol. 16, no. 1, pp. 46–56, 1999. 70

[235] F. X. Kaertner, L. R. Brovelli, D. Kopf, M. Kamp, I. G. Calasso, and U. Keller, "Control of solid state laser dynamics by semiconductor devices," *Optical Engineering*, vol. 34, no. 7, pp. 2024–2037, 1995. 70

[236] S. V. Sergeyev, "Vector self-pulsing in erbium-doped fiber lasers," *Optics letters*, vol. 41, no. 20, pp. 4700–4703, 2016. 70, 174

[237] H. Kbashi, S. V. Sergeyev, C. Mou, A. M. Garcia, M. A. Araimi, A. Rozhin, S. Kolpakov, and V. Kalashnikov, "Bright-dark rogue waves," *Annalen der Physik*, vol. 530, no. 5, p. 1700362, 2018. 70

[238] A. Schlatter, S. C. Zeller, R. Grange, R. Paschotta, and U. Keller, "Pulse-energy dynamics of passively mode-locked solid-state lasers above the q-switching threshold," *JOSA B*, vol. 21, no. 8, pp. 1469–1478, 2004. 70

[239] N. Pandit, D. Noske, S. Kelly, and J. Taylor, "Characteristic instability of fibre loop soliton lasers," *Electronics Letters*, vol. 28, no. 5, pp. 455–457, 1992. 74

[240] W. Loh, A. Grudinin, V. Afanasjev, and D. Payne, "Soliton interaction in the presence of a weak nonsoliton component," *Optics Letters*, vol. 19, no. 10, pp. 698–700, 1994. 74

[241] A. Grudinin and S. Gray, "Passive harmonic mode locking in soliton fiber lasers," *JOSA B*, vol. 14, no. 1, pp. 144–154, 1997. 74, 131

[242] I. Kudelin, "Collision dynamics of solitons in mode-locked fibre laser with net-anomalous dispersion," in *Real-time Measurements, Rogue Phenomena, and Single-Shot Applications VI*, vol. 11671, p. 116710C, International Society for Optics and Photonics, 2021. 74, 75, 91

[243] D. Tang, L.-M. Zhao, B. Zhao, and A. Liu, "Mechanism of multisoliton formation and soliton energy quantization in passively mode-locked fiber lasers," *Physical Review A*, vol. 72, no. 4, p. 043816, 2005. 74, 75

[244] W. H. Renninger, A. Chong, and F. W. Wise, "Area theorem and energy quantization for dissipative optical solitons," *JOSA B*, vol. 27, no. 10, pp. 1978–1982, 2010. 74, 75

[245] M. Erkintalo, G. Genty, and J. Dudley, "Giant dispersive wave generation through soliton collision," *Optics Letters*, vol. 35, no. 5, pp. 658–660, 2010. 74

[246] D. Tang, L. Zhao, and B. Zhao, "Soliton collapse and bunched noise-like pulse generation in a passively mode-locked fiber ring laser," *Optics Express*, vol. 13, no. 7, pp. 2289–2294, 2005. 75

[247] X. Liu, D. Popa, and N. Akhmediev, "Revealing the transition dynamics from q switching to mode locking in a soliton laser," *Physical Review Letters*, vol. 123, no. 9, p. 093901, 2019. 77

[248] Y. Cui and X. Liu, "Revelation of the birth and extinction dynamics of solitons in swnt-mode-locked fiber lasers," *Photonics Research*, vol. 7, no. 4, pp. 423–430, 2019. 78

[249] J. M. Soto-Crespo, M. Grapinet, P. Grelu, and N. Akhmediev, "Bifurcations and multiple-period soliton pulsations in a passively mode-locked fiber laser," *Physical Review E*, vol. 70, no. 6, p. 066612, 2004. 79

[250] E. N. Tsoy and N. Akhmediev, "Bifurcations from stationary to pulsating solitons in the cubic–quintic complex ginzburg–landau equation," *Physics Letters A*, vol. 343, no. 6, pp. 417–422, 2005. 79

[251] Y. Du, Z. Xu, and X. Shu, "Spatio-spectral dynamics of the pulsating dissipative solitons in a normal-dispersion fiber laser," *Optics Letters*, vol. 43, no. 15, pp. 3602–3605, 2018. 79

[252] Z.-W. Wei, M. Liu, S.-X. Ming, A.-P. Luo, W.-C. Xu, and Z.-C. Luo, "Pulsating soliton with chaotic behavior in a fiber laser," *Optics Letters*, vol. 43, no. 24, pp. 5965–5968, 2018. 79

[253] N. Akhmediev, J. M. Soto-Crespo, and G. Town, "Pulsating solitons, chaotic solitons, period doubling, and pulse coexistence in mode-locked lasers: Complex ginzburg-landau equation approach," *Physical Review E*, vol. 63, no. 5, p. 056602, 2001. 80

[254] J. M. Soto-Crespo and N. Akhmediev, "Soliton as strange attractor: nonlinear synchronization and chaos," *Physical Review Letters*, vol. 95, no. 2, p. 024101, 2005. 80

[255] I. Kudelin, S. Sugavanam, and M. Chernysheva, "Build-up dynamics in bidirectional soliton fiber lasers," *Photon. Res.*, vol. 8, pp. 776–780, Jun 2020. 80

[256] Q.-F. Yang, X. Yi, K. Y. Yang, and K. Vahala, "Counter-propagating solitons in microresonators," *Nature Photonics*, vol. 11, no. 9, p. 560, 2017. 80

[257] E. Desurvire, C. Giles, and J. R. Simpson, "Gain dynamics of erbium-doped fiber amplifiers," in *Fiber Laser Sources and Amplifiers*, vol. 1171, pp. 103–117, International Society for Optics and Photonics, 1990. 82

[258] J. Chesnoy, "Picosecond gyrolaser," *Optics Letters*, vol. 14, no. 18, pp. 990–992, 1989. 83

[259] M. L. Dennis, J.-C. M. Diels, and M. Lai, "Femtosecond ring dye laser: a potential new laser gyro," *Optics Letters*, vol. 16, pp. 529–531, Apr 1991. 84

[260] D. Gnass, N. Ernsting, and F. Schäfer, "Sagnac effect in the colliding-pulse-mode-locked dye ring laser," *Applied Physics B*, vol. 53, no. 2, pp. 119–120, 1991. 84

[261] M. Jeon, H. Jeong, and B. Y. Kim, "Mode-locked fiber laser gyroscope," *Optics Letters*, vol. 18, no. 4, pp. 320–322, 1993. 84

[262] B. W. Lee, H. J. Jeong, and B. Y. Kim, "High-sensitivity mode-locked fiber laser gyroscope," *Optics Letters*, vol. 22, pp. 129–131, Jan 1997. 84

[263] Jong Bum Hong, Yeong Bae Yeo, Bong Wan Lee, and Byoung Yoon Kim, "Phase sensitive detection for mode-locked fiber laser gyroscope," *IEEE Photonics Technology Letters*, vol. 11, no. 8, pp. 1030–1032, 1999. 84

[264] W. Zhang, L. Zhan, T. Xian, and L. Gao, "Bidirectional dark-soliton fiber lasers for high-sensitivity gyroscopic application," *Optics Letters*, vol. 44, pp. 4008–4011, Aug 2019. 85, 89, 136

[265] D. A. Dvoretskiy, S. G. Sazonkin, I. S. Kudelin, I. O. Orekhov, A. B. Pnev, V. E. Karasik, and L. K. Denisov, "Multibound soliton formation in an erbium-doped ring laser with a highly nonlinear resonator," *IEEE Photonics Technology Letters*, 2019. 86

[266] M. Chernysheva, S. Sugavanam, and S. Turitsyn, "Real-time observation of the optical sagnac effect in ultrafast bidirectional fibre lasers," *APL Photonics*, vol. 5, no. 1, p. 016104, 2020. 86, 90, 94, 100, 120, 136

[267] B. W. Lee, H. J. Jeong, and B. Y. Kim, "High-sensitivity mode-locked fiber laser gyroscope," *Optics Letters*, vol. 22, no. 2, pp. 129–131, 1997. 89

[268] A. A. Krylov, D. S. Chernykh, and E. D. Obraztsova, "Colliding-pulse hybridly mode-locked erbium-doped all-fiber soliton gyrolaser," *Laser Physics*, vol. 28, p. 015103, dec 2017. 89

[269] T. Kanna, M. Lakshmanan, P. T. Dinda, and N. Akhmediev, "Soliton collisions with shape change by intensity redistribution in mixed coupled nonlinear schrödinger equations," *Physical Review E*, vol. 73, no. 2, p. 026604, 2006. 91

[270] S. Gatz and J. Herrmann, "Soliton collision and soliton fusion in dispersive materials with a linear and quadratic intensity depending refraction index change," *IEEE journal of quantum electronics*, vol. 28, no. 7, pp. 1732–1738, 1992. 91

[271] R. Adler, "A study of locking phenomena in oscillators," *Proceedings of the IRE*, vol. 34, no. 6, pp. 351–357, 1946. 92

[272] Y. Zhang, N. Wang, H. Tian, H. Wang, W. Qiu, J. Wang, and P. Yuan, "A high sensitivity optical gyroscope based on slow light in coupled-resonator-induced transparency," *Physics Letters A*, vol. 372, no. 36, pp. 5848–5852, 2008. 93

[273] D. Hoff, F. J. Furch, T. Witting, K. Rühle, D. Adolph, A. M. Sayler, M. J. Vrakking, G. G. Paulus, and C. P. Schulz, "Continuous every-single-shot carrier-envelope phase measurement and control at 100 khz," *Optics Letters*, vol. 43, no. 16, pp. 3850–3853, 2018. 108, 109

[274] M. Natile, A. Golinelli, L. Lavenu, F. Guichard, M. Hanna, Y. Zaouter, R. Chiche, X. Chen, J. Hergott, W. Boutu, *et al.*, "Cep-stable high-energy ytterbium-doped fiber amplifier," *Optics Letters*, vol. 44, no. 16, pp. 3909–3912, 2019. 108, 109

[275] M. Kurucz, S. Tóth, R. Flender, L. Haizer, B. Kiss, B. Persielle, and E. Cormier, "Single-shot cep drift measurement at arbitrary repetition rate based on dispersive fourier transform," *Opt. Express*, vol. 27, pp. 13387–13399, Apr 2019. 108

[276] X. Zhang, G. Wu, M. Hu, and S. Xiong, "Stabilizing carrier-envelope offset frequency of a femtosecond laser using heterodyne interferometry," *Optics letters*, vol. 41, no. 18, pp. 4277–4280, 2016. 109, 119

[277] K. Osvay, M. Görbe, C. Grebing, and G. Steinmeyer, "Bandwidth-independent linear method for detection of the carrier-envelope offset phase," *Optics Letters*, vol. 32, pp. 3095–3097, Nov 2007. 109, 114

[278] K. Wu, P. P. Shum, S. Aditya, C. Ouyang, J. H. Wong, H. Q. Lam, and K. E. K. Lee, "Noise conversion from pump to the passively mode-locked fiber lasers at 1.5 μm," *Opt. Lett.*, vol. 37, pp. 1901–1903, Jun 2012. 113

[279] M. S. Schöffler, X. Xie, P. Wustelt, M. Möller, S. Roither, D. Kartashov, A. M. Sayler, A. Baltuska, G. G. Paulus, and M. Kitzler, "Laser-subcycle control of sequential double-ionization dynamics of helium," *Phys. Rev. A*, vol. 93, p. 063421, Jun 2016. 114

[280] J. Ullrich, R. Moshammer, A. Dorn, R. Dörner, L. P. H. Schmidt, and H. Schmidt-Böcking, "Recoil-ion and electron momentum spectroscopy: reaction-microscopes," *Reports on Progress in Physics*, vol. 66, pp. 1463–1545, aug 2003. 114

[281] J. Long, F. J. Furch, J. Durá, A. S. Tremsin, J. Vallerga, C. P. Schulz, A. Rouzée, and M. J. Vrakking, "Ion-ion coincidence imaging at high event rate using an in-vacuum pixel detector," *The Journal of chemical physics*, vol. 147, no. 1, p. 013919, 2017. 114

[282] M. I. Stockman, M. F. Kling, U. Kleineberg, and F. Krausz, "Attosecond nanoplasmonic-field microscope," *Nature Photonics*, vol. 1, no. 9, pp. 539–544, 2007. 114

[283] K. Goda, D. R. Solli, K. K. Tsia, and B. Jalali, "Theory of amplified dispersive fourier transformation," *Physical Review A*, vol. 80, no. 4, p. 043821, 2009. 114

[284] W. Zhu, E. R. N. Fokoua, Y. Chen, T. Bradley, M. N. Petrovich, F. Poletti, M. Zhao, D. J. Richardson, and R. Slavík, "Temperature insensitive fiber interferometry," *Optics Letters*, vol. 44, pp. 2768–2770, Jun 2019. 114, 131

[285] T. Xian, L. Zhan, W. Wang, W. Zhang, and L. Gao, "Real-time detection of transient roundtrip property in ultrafast lasers," in *CLEO: Science and Innovations*, pp. JW2F–19, Optical Society of America, 2020. 119

[286] B. R. Washburn, S. A. Diddams, N. R. Newbury, J. W. Nicholson, M. F. Yan, and C. G. Jørgensen, "Phase-locked, erbium-fiber-laser-based frequency comb in the near infrared," *Optics letters*, vol. 29, no. 3, pp. 250–252, 2004. 120

[287] A. Bartels, C. W. Oates, L. Hollberg, and S. A. Diddams, "Stabilization of femtosecond laser frequency combs with subhertz residual linewidths," *Optics letters*, vol. 29, no. 10, pp. 1081–1083, 2004. 120

[288] A. J. Lind, A. Kowligy, H. Timmers, F. C. Cruz, N. Nader, M. C. Silfies, T. K. Allison, and S. A. Diddams, "Mid-infrared frequency comb generation and spectroscopy with few-cycle pulses and χ (2) nonlinear optics," *Physical review letters*, vol. 124, no. 13, p. 133904, 2020. 120

[289] J.-M. Jiang, X.-J. Chen, Y.-X. Gao, M. Liu, Z.-A. Bai, A.-P. Luo, W.-C. Xu, and Z.-C. Luo, "Bidirectional ultrahigh-repetition-rate ultrafast fiber laser," *Optics & Laser Technology*, vol. 142, p. 107196, 2021. 131

[290] D. Korobko, D. Stoliarov, P. Itrin, M. Odnoblyudov, A. Petrov, and R. Gumenyuk, "Harmonic mode-locking fiber ring laser with a pulse repetition rate up to 12 ghz," *Optics & Laser Technology*, vol. 133, p. 106526, 2021. 131

[291] B. Shen, L. Chang, J. Liu, H. Wang, Q.-F. Yang, C. Xiang, R. N. Wang, J. He, T. Liu, W. Xie, *et al.*, "Integrated turnkey soliton microcombs," *Nature*, vol. 582, no. 7812, pp. 365–369, 2020. 131

[292] M.-G. Suh and K. Vahala, "Gigahertz-repetition-rate soliton microcombs," *Optica*, vol. 5, no. 1, pp. 65–66, 2018. 131

Appendix A

Dispersive Fourier Transform Measurements

A.1 Spectral resolution

As was discussed in the *Section* 1.6.2, the spectral resolution of the Dispersive Fourier Transform (DFT) measurements is limited by two factors if the higher order dispersion is neglected. The first limitation is related to the bandwidth of the used photodiode and the oscilloscope. In our experiments, the temporal resolution of the used equipment is t_{FWHM} = 25 ps, which results in the spectral resolution of the Dispersive Fourier Transform (DFT) of 0.0208 nm by using the eq. 1.26.

Another limitation factor of the spectral resolution is related to the Group Delay Dispersion (GDD) in analogy to the far-field spectral resolution in the spatial diffraction. This corresponds to the resolution of 0.1 nm, based on the eq. 1.27. In the temporal equivalent, this corresponds to the case when the first minimum of one diffracted wavelength coincides with the first minimum of the other wavelength. This is twice the Rayleigh criterion, which states that the two diffracted beams are resolvable when the separation between them is more than the first minimum of one of the diffracted beams. If the temporal separation between two diffracted wavelengths is lower than the Rayleigh criterion the diffracted light from each wavelength will overlap, decreasing the resulting modulation depth. The main conclusion from this discussion is that the obtained DFT measurements can provide the measurements with a resolution better than 0.1 nm at the cost of the lower modulation depth. This can be important for interferometric measurements with far-separated pulses.

Another limitation, which should be taken into account, is the uncertainty of the acquired Group Velocity Dispersion (GVD) ΔD. In the presence of the uncertainty in the GVD, the total resolution can be expressed as:

$$\delta\lambda_{GDD} = \frac{t_{FWHM}}{Dz} + \frac{\Delta Dz}{Dz}\Delta\lambda = \delta\lambda + \delta D\Delta\lambda \tag{A.1}$$

where $\delta\lambda_{GDD}$ is the spectral resolution in the presence of the GVD uncertainty, t_{FWHM} is the temporal resolution, D is the GVD, z is the length of the dispersive line, $\Delta\lambda$ is the wavelength offset from the central wavelength, and δD is the relative error of the GVD.

As can be seen, the DFT resolution degrades at the spectral wings of the pulse. Thus, the uncertainty in the GVD will compress or stretch the original optical depending on the sign of the uncertainty. We would like to note, that the initial chirp of the input pulse can be treated in the same way as the uncertainty of the GVD due to their similar effect on the pulse spectrum. Additionally, the resolution at the pulse spectral wings, recorded via the DFT, is also reduced by the higher-order dispersion as indicated in the eq. 1.25.

This GVD uncertainty can be experimentally evaluated by comparing the spectra, recorded by the DFT technique and optical spectrum analyser. In the absence of the GVD uncertainty and the higher-order dispersion, it would be possible to estimate the initial pulse chirp by comparing both spectra. Contrariwise, if the pulse is known to have a zero chirp, the comparison between both spectra will provide the data on the uncertainty of the GVD.

A.2 Determination of the central wavelength

The DFT technique provides measurements of only relative wavelengths, while the absolute central wavelength should be uniquely identified. In the steady state, the central wavelength can be easily identified by comparing the measured pulse spectrum from the DFT and the optical spectrum analyser.

Another way is to evaluate the time delay between the spatio-temporal and the DFT measurements. The time delay τ can be estimated as:

$$\tau = n(\lambda_0) \cdot z/c \tag{A.2}$$

where $n(\lambda_0)$ is the frequency-dependent refractive index of the fibre at the central wavelength of λ_0, z is the length of the dispersive line, and c is the speed of light in vacuum. This approach is appropriate to be used for a single-shot evaluation of the central wavelength. Moreover, this approach takes into account the time-frequency duality of the DFT technique: if the input pulse is delayed, the central wavelength of the DFT spectra will be shifted accordingly and could be misunderstood as a shift in the central frequency. Thus, the arriving time of a pulse is important in order to avoid this uncertainty. The drawback of this method is that the refractive index profile should be estimated with high accuracy since the fibre lengths, used in the DFT measurements, usually are several kilometers long. This technique allows to estimate the fluctuation of the central wavelength in the single-shot scale but this would require the data on the pulse spatio-temporal position.

Another method is the combination of both methods mentioned above. While the central wavelength at the steady state can be unambiguously defined by comparing with the spectrum obtained from the optical spectrum analyser, the measurements of the single-shot fluctuations of the central wavelength should take into the arriving time of the pulse.

A.3 Resolution of the phase extraction

In this Appendix, we also consider the resolution of the phase retrieval from the interferometric pattern depending on different parameters. To achieve that, we numerically simulated two-pulse interference with varying main parameters of ultrashort pulses and the DFT setup. The resolution or the mistake of the phase retrieval we estimated as a standard deviation from the true value, based on 10 000 samples for each simulation. Figure A.1(a) presented an exponential dependence of the phase resolution on the SNR with parameters similar to the one we used in our experiments. At the SNR of 60 dB, the standard deviation is slightly less than a mrad. Hence, it is crucial to provide the DFT measurements with high SNR for accurate phase retrieval.

Figure A.1(b) demonstrates the mistake of the phase retrieval depending on the amplitude ratio between two interfering beams. The amplitude ratio manifests as a modulation depth of the interferometric pattern and is sensitive to the noises. When the modulation depth reaches the level of noises, the noises can blur the interferometric pattern, impeding the phase extraction. While in our measures the amplitude ratio is close to 1, this may be significant for heterodyne detection when the local oscillator has significantly higher amplitudes. Moreover, as was stated before, the modulation depth tends to decrease when the modulation period of the interferometric pattern reaches the spectral resolution of the DFT measurements given by the eq. 1.27 (Rayleigh criterion). However, as shown in Fig. A.1(c), at high SNR the modulation depth does not play a crucial role and high accuracy is achievable.

The phase retrieval accuracy at various SNR and the spectral resolution of the DFT is shown in Fig. A.1(d). Since only the relation between the spectral resolution and the modulation period is relevant, we provided simulations as a number of data points (pixels) per modulation period. The crop, shown in Fig. A.1(e), demonstrates that high accuracy of the phase extraction could be achieved even with a low spectral resolution if the SNR remains high. This result is particularly important since it confirms that the phase could be extracted with high precision even by using a relatively slow oscilloscope and photodiode.

We also numerically simulated the influence of such parameters as the spectral width of the input pulses. The broader spectrum creates more data points for recording, but, our simulations did not show that this parameter has a significant impact on the phase retrieval procedure. However, at least two modulation periods should fit at the FWHM of the pulse spectra. Additionally, our simulations did not demonstrate a dependence of the phase retrieval resolution on the pulse separation, while the criteria given by the inequality 1.29 is fulfilled.

In the numerical results demonstrated above, we did not take into account the fluctuations of the central wavelength. However, strong fluctuations of the central wavelength can significantly degrade the results of the phase measurements. This can be numerically

expressed as:

$$\Delta\phi = 2\pi \frac{\Delta\lambda}{\lambda_{modulation}} = 2\pi\Delta\lambda\frac{c\tau}{\lambda_0^2} \tag{A.3}$$

where $\Delta\phi$ is the resulting phase error, $\Delta\lambda$ is the fluctuation of the central wavelength, and $\lambda_{modulation}$ is the modulation period of the interferometric pattern, c is the speed of light, τ is the temporal spacing between the pulses, and λ_0 is the central wavelength. This is a

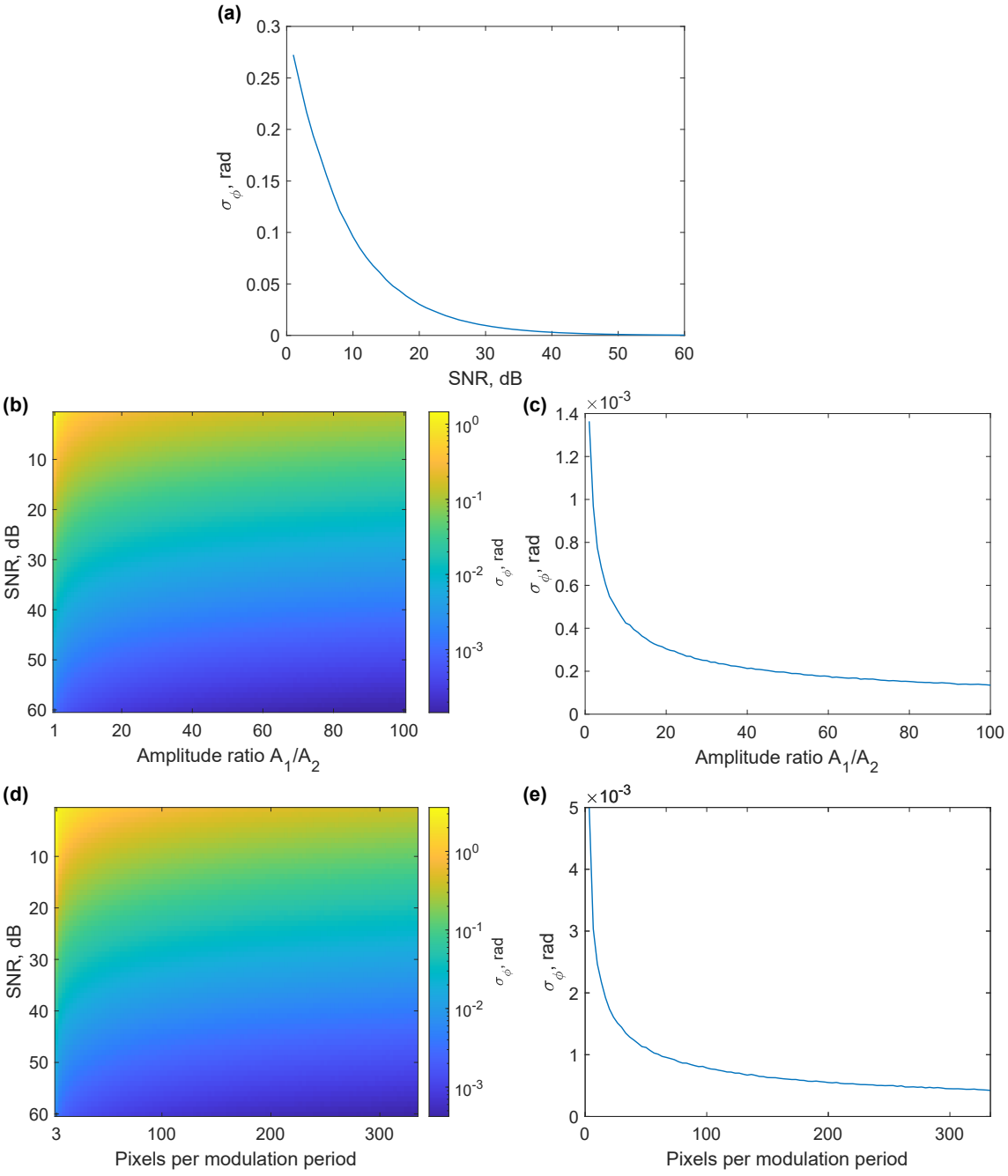

Figure A.1: Numerical estimation of the uncertainty of phase retrieval. **(a)** Standard deviation of the mistake of phase retrieval at different SNR. **(b)** Standard deviation of the mistake of phase retrieval at different SNR for various values of amplitude ratios between the two interfering beams with **(c)** corresponding crop at SNR of 60 dB. **(d)** Standard deviation of the mistake of phase retrieval at different SNR depending on the number of pixels per modulation period with **(e)** corresponding crop at SNR of 60 dB.

significant limitation especially if the interfering pulses have a high temporal separation. On the other hand, this effect can be reduced by providing a lower separation between the pulses. Additionally, due to the time-frequency duality, the temporal fluctuation of the arriving pulse will be converted into fluctuations in the central wavelength and results in the fluctuation of the extracted relative phase. Hence, to provide the highest resolution of the phase measurement, these fluctuations should be taken into account and numerically compensating by determining the central wavelength of the pulse spectrum and the spatio-temporal position of the pulse at each roundtrip.

All in all, the provided numerical simulations demonstrated that the high degree of accuracy even in a system with a low spectral resolution could be achieved by increasing the SNR, which is the main parameter for achieving high resolution of phase extraction. The resulting accuracy of the phase retrieval may also slightly vary depending on the input pulse characteristics such as chirp, spectral profile, and *etc.* These results are particularly important for further optimisation of the DFT setup for continuous measurement or the phase dynamics at high data rate and resolution. For example, by adjusting the separation between the pulses and using a spectral filter to crop the dispensable wings of the pulse spectra it would be possible to achieve phase retrieval at data rates in the GHz range. Due to the limited memory of the oscilloscope, the ease of the requirement to the temporal resolution (which is converted into spectral resolution during the DFT measurements) will allow the continuous observations of the phase evolution.

Appendix B

Pulse build-up dynamics in a bidirectional mode-locked laser with synchronised repetition rates

B.1 Evaluation of the central wavelength dynamics

In the *Appendix* A we introduced the importance of the determination of the pulse central wavelength for the DFT measurements. As a reference, we have used the spectra obtained by an optical spectrum analyser for the steady-state mode-locking generation. However, to estimate the central wavelength shift, one should compare the dynamics in the spatial domain and the DFT profiles. To identify the dynamics of the central wavelength we neglected the non-linear Kerr effect, which is significantly smaller than the effect of the dispersion, due to low pulse intensities during our experiments. Since both the cavity optical length and the DFT line are dispersive, it takes different time for different wavelengths to propagate through. The central wavelength drift results in a variation of the cavity roundtrip time owing to the intracavity GVD and lead to a temporal shift of the income pulse at the DFT line, which should be taken into account. Hence, to estimate the central wavelength drift from the DFT measurements, we need to exclude the contribution of the varying cavity round trip time, which can be obtained from the spatio-temporal dynamics. Once this contribution is removed, the wavelength drift can be estimated by using the known value of the dispersion of the DFT fibre span. In our experiments, the DFT line introduces the time delay of $t_{DFT} = 53.651$ μs at 1555 nm wavelength band. The mapping of the position of 1555 nm spectral component back to the recorded DFT is shown as a white line in the Fig 2.9(a). Therefore, the time mismatch between the DFT spectra and the corresponding delayed spatio-temporal intensity evolution trace, converted into wavelength domain by using the Eq. 1.25, demonstrates the deviation of the central wavelength drift in real-time (Fig. 2.9(b)).

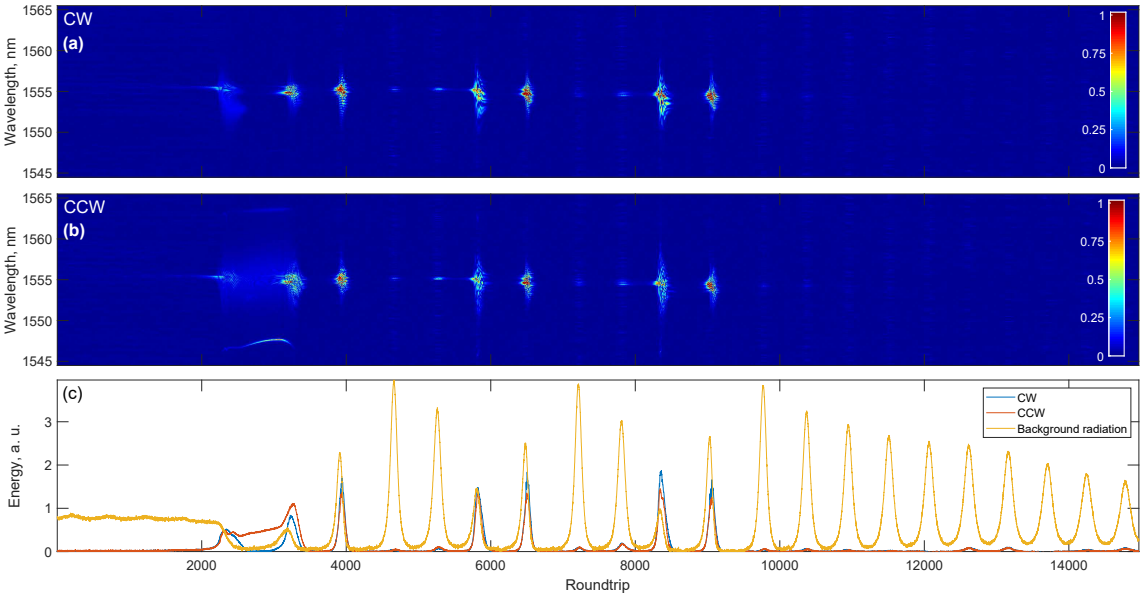

Figure B.1: The DFT spectra of the dynamics of the Q-switched instability in **a** the CW and the **b** CCW direction. **c** The energy dynamics during the Q-switched instability.

B.2 Q-switched instabilities dynamics

Figure B.1 demonstrate the Q-switched instability dynamics formed after the quasi-stable mode-locked generation. Dissimilar to other dynamics, more energy has been emitted in the CCW direction, while the CW pulse underwent a central wavelength shift and was annihilated shortly after. As was described in *Section* 2.2.3, after the break-up of the less energetic pulse, more energy was emitted in the counter-propagating direction and induce the instability dynamics. At the 10 thousandth roundtrip, the generation regime fully evolved into the traditional Q-switched operation regime without localised structures. The Q-switched generation experience decrease in the peak energy, while its duration started to increase.

B.3 The numerical autocorrelation function of multi-soliton complex in the clockwise direction excluding Kelly sidebands

Figure B.2 presents the numerical autocorrelation function of the clockwise direction during formation of multiple-solitons with excluded Kelly sidebands from our calculations. By comparing both graphs with included and excluded Kelly sidebands we can estimate their effect on the pulse dynamics and vice versa. It is worth noting the absence of strong surrounding quasi-continuous-waves at roundtrips close to 43.2 - 43.7, 44.2 - 44.7 and 45.2 - 45.7 thousand round trips are referred to the emitted dispersive waves.

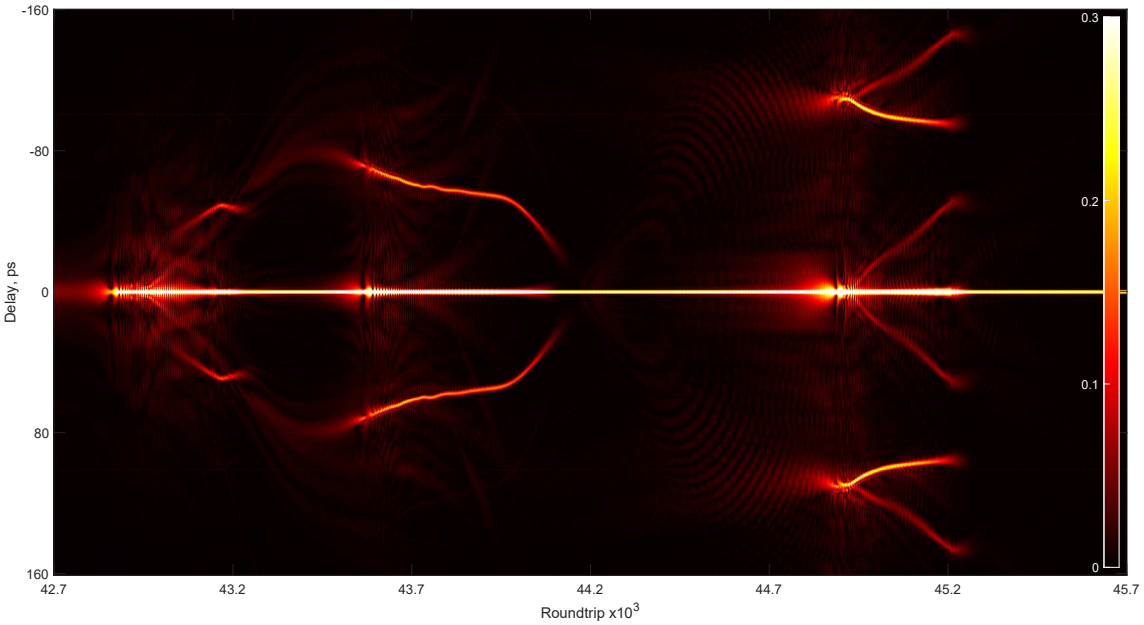

Figure B.2: **a** and **b** the DFT traces of the pulse formation in the CW and the CCW direction from a multi-soliton structures, respectively. **c** the pulse energy, and **d** the localisation parameter.

B.4 Build-up dynamics through multi-pulse formation

As shown in Fig. B.3, the multi-soliton was generated in a more energetic direction from a modulation of the quasi-continuous wave radiation (Q-switched generation). Notably, that the CCW direction had more energy than the CW direction due to particular adjustment of the polarisation controllers. A prerequisite for the multi-soliton generation is the presence of a residual excess energy after the intensity spike or the Q-switched instability, while the counter-propagating pulse lacks enough energy and it disappears shortly after the central wavelength shift. This dynamics clearly shows that stable bidirectional mode-locking generation have appeared only at the fifth time when the energy was more evenly distributed between both directions. Otherwise, the soliton undergoes the central wavelength shift and disappeared shortly after. Moreover, an additional burst of energy, similar to Q-switched instability, have been appeared each time before the formation of the pulse in the counter-propagating direction. Such bursts of energy and Q-switched instability served as redistributors of energy between opposite directions.

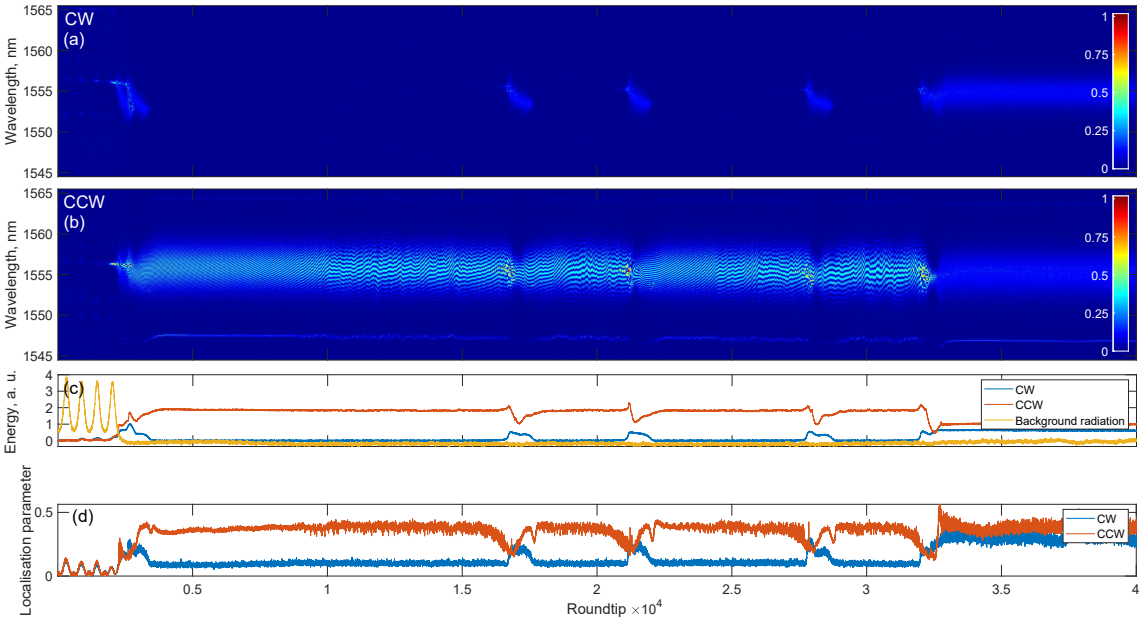

Figure B.3: **a** and **b** the DFT traces of the pulse formation in the CW and the CCW direction from a multi-soliton structures, respectively. **c** the pulse energy, and **d** the localisation parameter.

B.5 Final formation of the pulse in the counter-clockwise direction

Figure B.4 provides the measured DFT spectra and the corresponding ACF of the counter-clockwise pulse during the final formation of the stable bidirectional mode-locking generation. Note, that the pulse is originated from a residual pulse after the Q-switched instability with strong continuous-wave radiation. The theoretically calculated localisation value of 0.278 is close to the experimentally obtained value of 0.252. The drop in the localisation parameter near the 59.9 thousandth roundtrip is related to the formation of the side spikes. We also note a non-periodical fluctuation in localisation due to weak fluctuations of the pulse energy and spectra, but no spectral pulsations have been obtained in the CCW direction. The overall dynamics of the pulse formation in the CCW direction is similar to the CW direction.

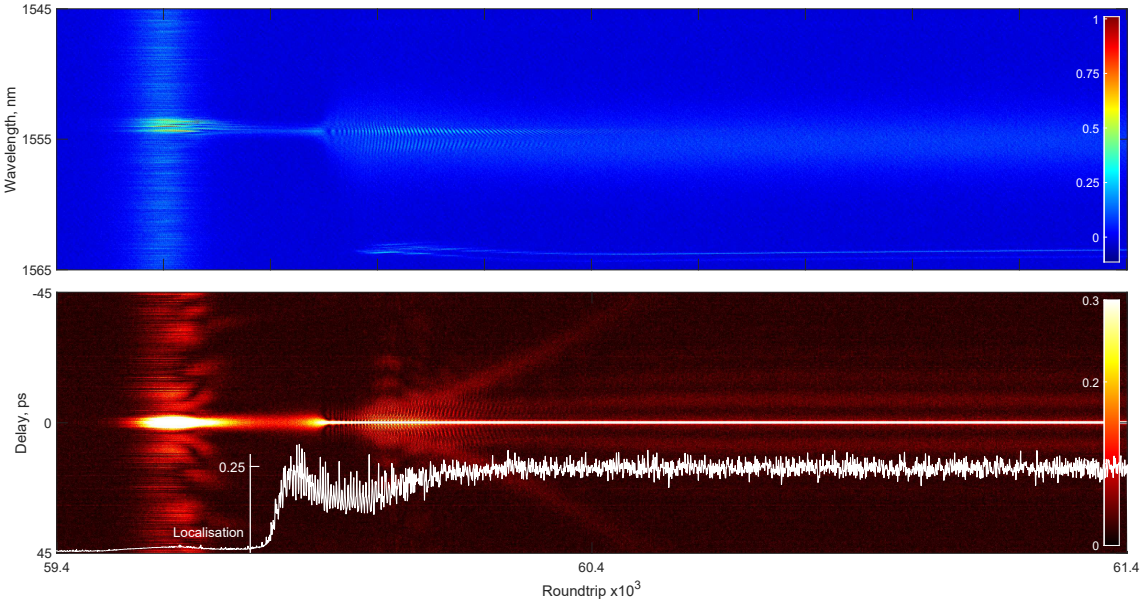

Figure B.4: Final formation of the counter-clockwise direction from a Q-switched-mode-locked instability: the measured DFT spectra and the corresponding ACF traces. In white the localisation parameter is shown.

Appendix C

Phase dynamics of fully-locked counter-propagated pulses

C.1 Phase-time oscillations

In this *Section* we present an oscillation dynamics of fully-locked counter-propagating pulses in the bidirectional mode-locked fibre laser. The spectral oscillations could be clearly seen from the inset in Fig. C.1(a). Figure C.1(b) demonstrate the extracted data on the temporal pulse separation and the relative phase. The period of both oscillations was 45 roundtrips, which is 3 μs. However, both oscillations were out of phase with a phase difference close to π. We plot the single period of the evolutionary trajectory of the phase-temporal dynamics in Fig. C.1(c-d). The deviation of the phase-time diagram from a perfect circular shape means that the phase and time components are not fully agreed through phase-time relation 1.4. As can be seen, the relative temporal spacing is varying in the range of 300 fs, while the phase has a range only of 0.4 rad. Thus, such oscillations indicate complex synchronisation dynamics of counter-propagated pulses.

Similar phase-time oscillations have been observed in soliton molecules in unidirectional lasers [182; 189]. These oscillations may arise as a self-adjusting of the unique bidirectional generation regime. Additionally, phase oscillation may be caused by the dynamics of the coupling strength between oscillator frequencies [236].

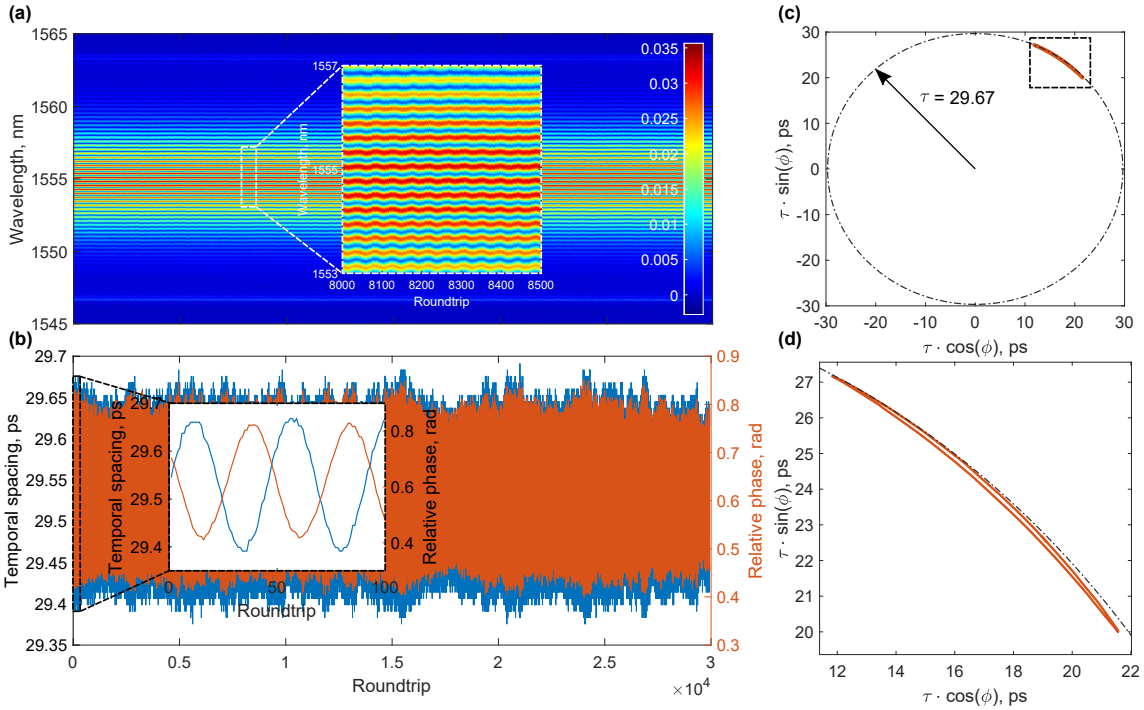

Figure C.1: **(a)** The DFT spectral dynamics of counter-propagating pulses. **(b)** The data on the inter-pulse separation and relative phase, extracted from the corresponding DFT spectra. **(c)** Phase time trajectory with **(d)** a zoom-in.

Appendix D

Interferometric measurements of pulse dynamics

D.1 Dynamics of temporal spacing between the consecutive pulses

Figure D.1 demonstrate the evolution of the temporal separation between consecutive pulses from the Mach-Zehnder Interferometer, which is directly related to the timing jitter of the used mode-locked free-running laser. This data correspond to the results, demonstrated in *Section* 3.2. The average time separation was 36.6 ps with a standard deviation of 19 fs. The resolution of the measurements was 7.7 fs, limited by the spectral window of the DFT measurements with the zero-padding. The temporal spacing has a slowly decreasing trend due to the temperature fluctuations.

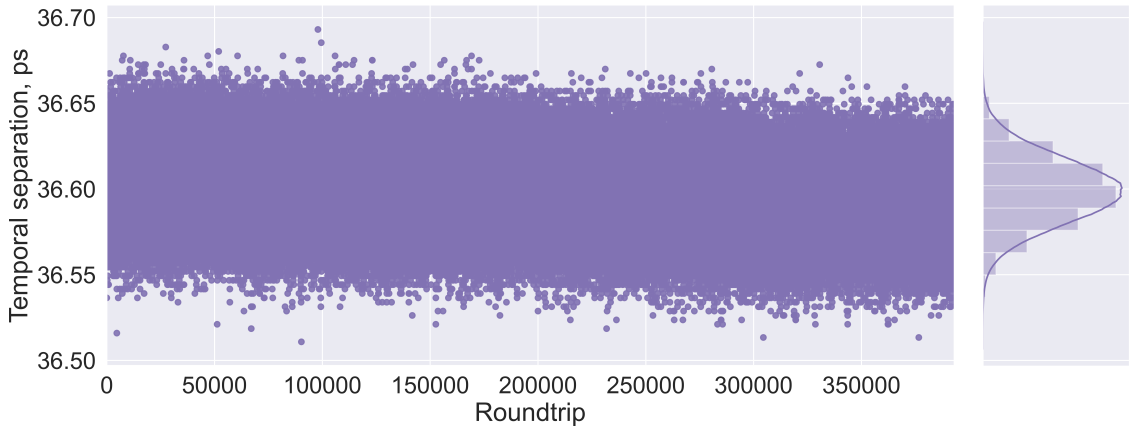

Figure D.1: Evolution of the temporal spacing between consecutive pulses with the corresponding probability density function.

D.2 Measurements of angular acceleration of the stepper motor

Figure D.2 provides the data on the angular velocity and the angular acceleration of the laser platform during the rotation exposure by the stepper motor. The motor was set to

produce 150 steps per second (100 000 roundtrips or 6.67 ms per step) at half-step size. The acceleration was obtained by differentiating the velocity over a window of 10 000 roundtrips to increase the resolution. The single shot resolution can be obtained by using the following equation:

$$\Omega_{min} = \sigma/(S \cdot T_{rep}) \tag{D.1}$$

where σ is the standard deviation, S is the scale factor and T_{rep} is the pulse repetition period. The calculated resolution is estimated to be 40.3 kdeg/s^2, while for the accumulated data over 10 000 roundtrips the resolution reduces down to 4 deg/s^2. The calculated average acceleration during the first half of the step cycle is 340.6 deg/s^2 which is close to the theoretically calculated of 332 deg/s^2. Theoretically, the mean acceleration during one step should be equals to zero which is confirmed by the experimental observations which result in an average acceleration over the step to -3.58 deg/s^2 or just 1.05% of the mean value.

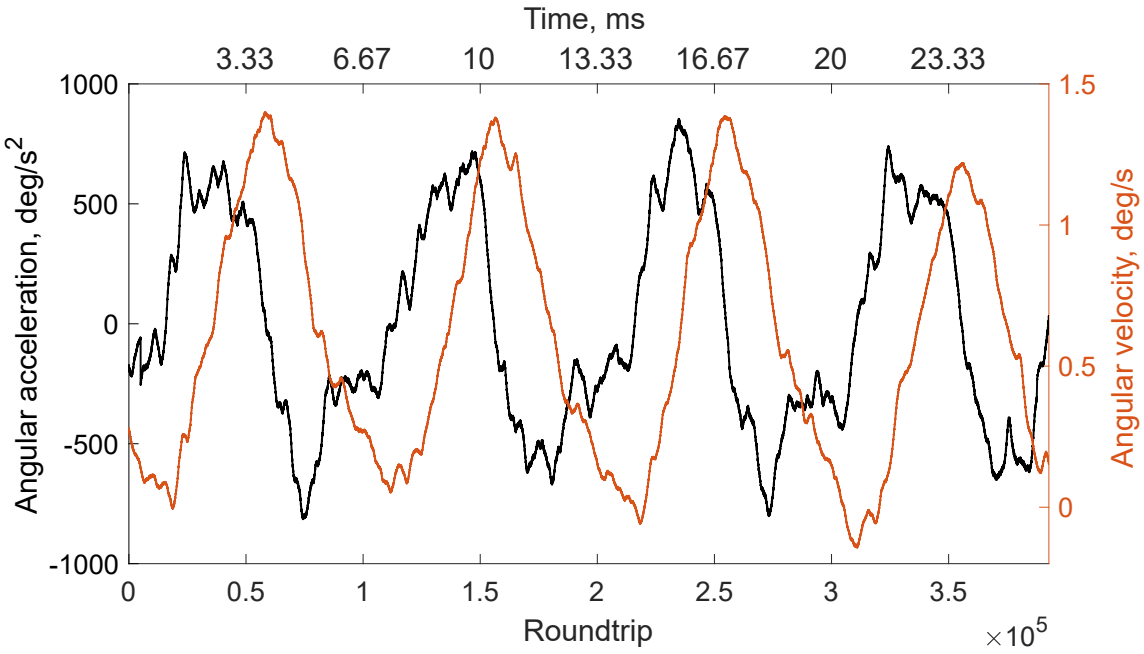

Figure D.2: Measurements of the angular acceleration (black line) and angular velocity (orange line) of the laser platform during rotation exposure by the stepper motor. The motor was set to produce 150 steps per second (100 000 roundtrips or 6.67 ms per step) at half-step size. The acceleration was obtained by differentiating the velocity over a window of 10 000 roundtrips to increase the resolution.